ISSN 1813-2065

Iraqi Journal of Applied Physics
IJAP

IRAQI JOURNAL OF APPLIED PHYSICS

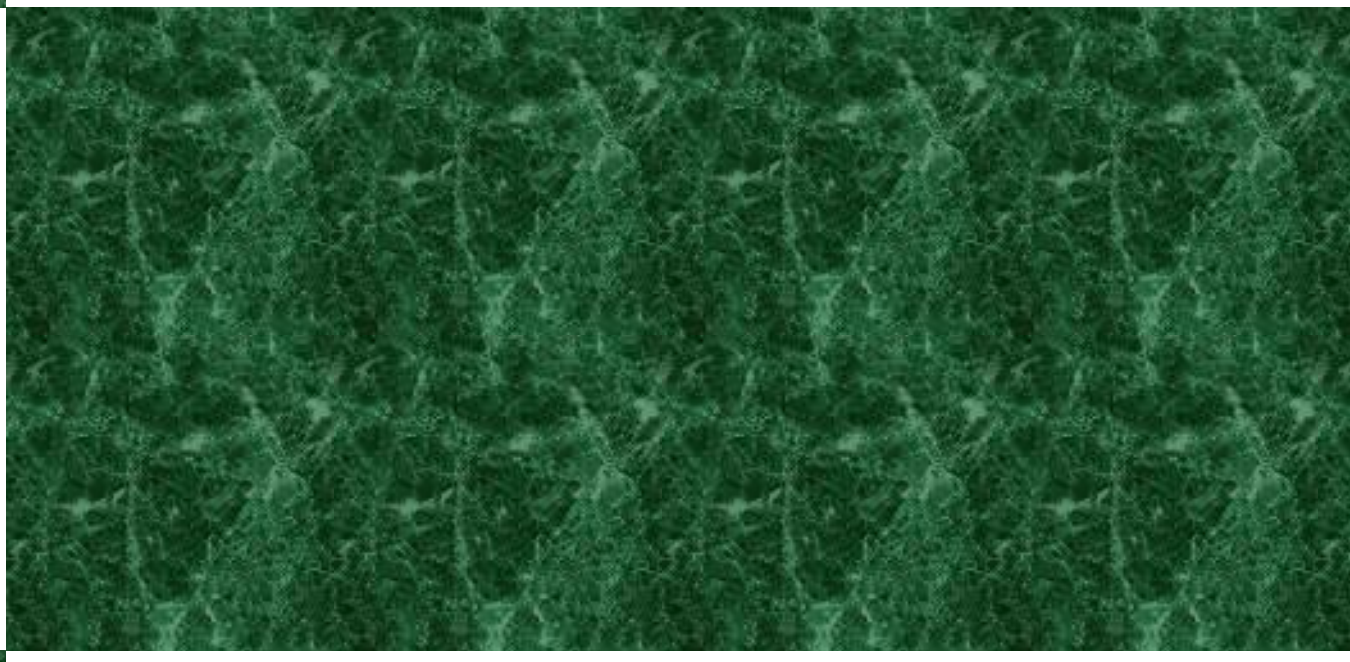

VOULME (20) ISSUE (3B) AUGUST 2024

Sponsored and Published by
American Quality for Scientific Publishing, Inc.

IRAQI JOURNAL OF APPLIED PHYSICS

The *Iraqi Journal of Applied Physics (IJAP)* is a peer reviewed journal of high quality devoted to the publication of original research papers from applied physics and their broad range of applications. IJAP publishes quality original research papers, comprehensive review articles, survey articles, book reviews, dissertation abstracts in physics and its applications in the broadest sense. It is intended that the journal may act as an interdisciplinary forum for Physics and its applications. Innovative applications and material that brings together diverse areas of Physics are particularly welcome. Review articles in selected areas are published from time to time. It aims to disseminate knowledge; provide a learned reference in the field; and establish channels of communication between academic and research experts, policy makers and executives in industry, commerce and investment institutions. IJAP is a quarterly specialized periodical dedicated to publishing original papers, letters and reviews in: Applied & Nonlinear Optics, Applied Mechanics & Thermodynamics, Digital & Optical Communications, Electronic Materials & Devices, Laser Physics & Applications, Plasma Physics & Applications, Quantum Physics & Spectroscopy, Semiconductors & Optoelectronics, Solid State Physics & Applications, Alternative & Renewable Energy, and Environmental Science & Technology. Sub-disciplines include Dielectrics, ferroelectrics, and multiferroics; Electrical discharges, plasmas, and plasma-surface interactions; Emerging, interdisciplinary, and other fields of applied physics; Energy and Sustainability; Magnetism, spintronics, and superconductivity; Organic-Inorganic systems, including organic electronics; Photonics, plasmonics, photovoltaics, optical phenomena, materials, and metamaterials; Physics of devices and sensors; Physics of materials, including electrical, thermal, mechanical and other properties; Physics of matter under extreme conditions; Physics of nanoscale, 2D materials, and low-dimensional systems; Physics of semiconductors; Quantum technology; Soft matter, fluids, and biophysics; Thin films, interfaces, and surfaces.

ISSN (Print): 1813-2065, ISSN (Online): 2309-1673

Editorial Office:
P. O. Box 88052, Baghdad 12631, IRAQ
Mobile: +964 7832 360 114 (Telegram, Viber, WhatsApp)
Website: www.ijap-iq.com
Emails: info@ijap-iq.com, editor_ijap@yahoo.co.uk, ijap.editor@gmail.com

SPONSORED AND PUBLISHED BY
AMERICAN QUALITY FOR SCIENTIFIC PUBLISHING INC.
1479 South De Gaulle Ct, Aurora, CO 80018, United States
Middle East office: aqsp.me, Email: info@aqsp.me

IRAQI JOURNAL OF APPLIED PHYSICS

INSTRUCTIONS TO AUTHORS

CONTRIBUTIONS

Contributions to be published in this journal should be original research works, i.e., those not already published or submitted for publication elsewhere, individual papers or letters to editor.
Manuscripts should be submitted to the editor at the mailing address:

Iraqi Journal of Applied Physics, Editorial Board, P. O. Box 88052, Baghdad 12631, IRAQ
Mobile: +964 7832 360 114 (Telegram, Viber, WhatsApp)
Website: www.ijap-iq.com
Email: info@ijap-iq.com, editor_ijap@yahoo.co.uk, ijap.editor@gmail.com

MANUSCRIPTS

Two hard copies or a soft Word copy on a CD or DVD should be submitted to the Editor in the following configuration:

- **One-column** Double-spaced one-side A4 size with 2.5 cm margins of all sides
- Times New Roman font (16pt bold for title, 14pt bold for names, 12pt bold for headings, 12pt regular for text)
- Manuscripts presented in English only are accepted.
- English abstract not exceed 150 words
- 4 keywords (at least) should be maintained on (PACS preferred)
- Author(s) should express all quantities in SI units
- Equations should be written in equation form (*italic* and symbolic) NOT in plain text
- Tables and Figures should be separated from text and placed in new pages after the references
- Charts should be indicated by the software used for generating them (e.g., Excel, MATLAB, Grapher, etc.)
- Figures and diagrams can be submitted in original colored forms for assessment and they will be returned to authors after provide printable copies
- Only original or high-resolution scanner photos are accepted
- For electronic submission, articles should be formatted with MS-Word software
- Figures, charts, photos, images or pictures **SHOULD NOT** be grouped in Word file
- Figure caption should be written as plan text **NOT** inside a text box

AUTHOR NAMES AND AFFILIATIONS

It is IJAP policy that all those who have participated significantly in the technical aspects of a paper be recognized as co-authors or cited in the acknowledgments. In the case of a paper with more than one author, correspondence concerning the paper will be sent to the first author unless staff is advised otherwise.
Author name should consist of first name, middle initial, last name. The author affiliation should consist of the following, as applicable, in the order noted:
- Company or college (with department name or company division), Postal address, City, Governorate or State, zip code, Country name, contacting telephone number, and e-mail

REFERENCES

The references should be brought at the end of the article, and numbered in the order of their appearance in the paper. The reference list should be cited in accordance with the following examples:
[1] F.H. Al-Berkdar, D.N. Raouf and F.H. Hamza, "A Line Tuned TEM_{00} Mode CW CO_2 Laser", *Iraqi J. Appl. Phys.*, 1(1) (20025) 8-10.
[2] W. Demtröder, **"Atoms, Molecules, and Photons"**, Springer-Verlag (Berlin, 2006), Ch. 4, p. 130.
[3] Y. Lee, S.A. Korpela and R. Horne, "Structure of Multi-Cellular Natural Convection in a Tall Vertical Annulus", Proceedings of 7th International Heat Transfer Conference, U. Grigul et al., eds., Hemisphere (NY), 2 (1982) 221–226.
[5] M. Hashish, "Waterjet Technology Development", High Pressure Technology, PVP-Vol. 406 (2000) 135-140.
[6] D.W. Watson, "Thermodynamic Analysis", ASME Paper No. 97-GT-288 (1997).
[7] Z. Cheng, "Vibrational Discrete Action Theory", Ph.D. thesis, Columbia University, USA (2021).

PROOFS

Authors will receive proofs of papers and are requested to return one corrected copy as a WORD file on a compact disc (CD) or by email. New materials inserted in the original text without Editor's permission may cause rejection of paper unless the handling editor is informed.

COPYRIGHT FORM

Author(s) will be asked to sign the IJAP Copyright Form and hence transfer copyrights of the article to the Journal soon after acceptance of it. This will ensure the widest possible dissemination of information.

OFFPRINTS

Authors will receive electronic offprint free of charge and any additional reprints can be ordered.

SUBSCRIPTION AND ORDERS

Annual fees (4 issues per year) of subscription are **50** US$ for individuals inside Iraq; **200** US$ for institutions inside Iraq; **100** US$ for individuals abroad; **300** US$ for institutions abroad.

Proceedings of 5th International Specialized Conference of Education College on Physics and Applied Sciences (5thICECAS24), 22-23 April 2024

Mustafa M. Abid
Adnan H. Mohammed

Department of Physics, College of Education, Mustansiriyah University, Baghdad, IRAQ

Output Power Dynamic Range in Presence of Semiconductor Optical Amplifier Dynamics

Injected current change can be done easily for simulating semiconductor optical amplifier (SOA) performance and even in experimental applications, require SOA use, so, our simulation focuses on the effects of injected current on saturation power under fast dynamics considerations included amplified spontaneous emission (ASE), carrier heating (CH), and spectral hole burning (SHB). For one segment model, the injected current that attain compression noise figure (NF) close saturation power, exploited to be used later into subsegment one of three segment model, achieved with three independently injected current. The procedure develops the saturation region to be more extended compared with the published researches. The results show that the fast dynamics must be taken into account. Also, -3dB for two configurations at a certain gain value referred to the stability in our simulation. CH and SHB reduce ASE effect, so, they must be taken account and as consequence the result will be close SOA real behavior.

Keywords: SOA; Saturation extension; Ultrafast dynamics; Noise
Received: 19 January 2024; Revised: 4 March 2024; Accepted: 4 April 2024

1. Introduction

Although the use of semiconductor optical amplifier (SOA) in linear amplification was limited and Er-doped fiber amplifiers are considered the suitable, SOA has advantages make it more suitable for optical communication in the future including the consumption of power is low, small footprint, wide bandwidth, and it accommodate wavelengths that EDFA cannot [1]. The aim of researchers at present to quest high gain, high-saturation power, low noise, and low cost [2]. There is a main drawback that occurs in SOA including the low saturation power. The latter limits the range at which the amplified signals are free distortion that is important when SOA is used as a component of multichannel amplifier. The gain saturation gives an image of SOA nonlinearities. For saturation, intense input signal undergoes smaller gain while the latter has larger gin for weaker gain. The saturation makes all power have the same power (all '1' symbols), i.e., SOA has a role as if power equalizer in a self-saturation regime as then it reduces the amplitude fluctuations. The letter can be got in ideal case if the gain recovery is fast enough [1]. To increase saturation output power, techniques like reducing the confinement factor [4], flared waveguides use [5], gain clamping [6], pump beams [7], and SOA can be contacted by a resistance that varied in order to increase the current density along the waveguide [8]. The mentioned techniques have disadvantages include the reducing the gain, fabrication cost increasing and complexities [9]. The segmented semiconductor optical amplifier (SOA) that is supplied with a one injected current, discussed so much theoretically and experimentally [1-3]. However, multielectrode SOA has been investigated as first-generation, the reducing of the noise figure (NF) or increasing the saturation power versus power (input or output) are taken into account [10]. Tailoring the carrier density profile for reducing NF has been explained in non- segmented SOA to control the distribution of carrier density while for segmented SOA, use injected current can be achieved by single source in conjunction with resister network [9]. The output dynamic range that gives indication of input dynamic range (IPDR) which turn on specifies the input power that amplified within it, in addition to, the data can be retrieved with free error. The segmented SOA that supplied with three independently injected current develop IPDR to be longer and serve the application with Datacom applications [10]. Also, the subdivision of SOA and supply it with different injected current assists to be the NF in less within the saturated region comparison with the single and multisegmented SOA that supply with one injected current. In other hand, that extension of saturation region makes the acceptable bit error rate in communication systems take place at input or output powers more than one segment mode [11]. The performance of bit error rate of PAM4 in SOA is extensively depended to supply independently by injected current to be swapped from low high and vice versa [9]. With advanced format of modulation signals, SOA is needed to scope their when used as amplifier for compensating the losses of multi- stage modulation and demodulation steps. Alike, the ideal case of SOA for formats mentioned latter amplify symbols with both small and large amplitudes. This presumably requires an SOA with a large input power dynamic range (IPDR). The IPDR defines the power range in which error-free amplification can be achieved [1]. A large IPDR and the low noise figure make the scoping of large and weak amplitude is possible [10].

The virtual division makes carrier density is determined by the current injected in SOA. So, the subsection is proposed to be perfect isolated and the diffusion of carrier density is not taken account [8]. Greater control of the carrier density profile could be achieved by improving the electrical isolation of the subsections to reduce the carrier diffusion. The improvement in saturation performance is also related to the ASE, as a higher level of power is required in order to supersede the effect of the ASE [12]. In this research, one segment model is used to choose the injected current for first subsection in three segment model. SOA is supplied by three independently injected currents to get extension of saturation region in presence fast dynamics and ASE effects. Consequently, there is no study has been discussed the improvement NF and saturation region in conjunction with SOA fast dynamic. We do not care to make a comparison of the saturation region extension obtained in two configurations with one segment model except for general explanation. Also, the pulse width on saturation region extension was discussed.

2. Simulation

To include compression (ε), amplified spontaneous emission (ASE) and loss (α) in addition to slow dynamics, then, the gain (g in m^{-1}) equation that expresses for the soon mentioned can be written as [13]:

$$\frac{\partial g}{\partial \tau} = \frac{g_o}{\tau_{cdp}} - \frac{g}{\tau_{eff}} - \frac{g}{E_{sat}} \frac{P(z,\tau)}{1+\varepsilon P(z,\tau)} \quad (1)$$

τ_{cdp} and τ_{eff} are is the carrier lifetime and gain recovery time, respectively while g_o and E_{sat} are the unsaturated gain and saturation energy. Rate equation of carrier density (N) is related to g by the following [2]

$$\frac{\partial N(z,\tau)}{\partial z} = \frac{I}{qV} - \frac{N}{\tau_{cdp}} - \frac{a\,\Gamma(N-N_0)P(z,\tau)}{aE_{sat}} \quad (2)$$

here $a\,\Gamma(N-N_0)$ represents g, $P(z,\tau)$ is the pulse power, I is the injected current, V is the active region volume, q represents the electronic charge and a is differential gain

Equation (1) can be expressed to take the integral formula in Eq. (3). The integrals $(\int_0^L g(z,\tau)\,\partial z)$ is the integrated gain at reduced time (τ), later, is expressed by $h(\tau)$. It can be determined by assisting the equation [3]

$$\frac{\partial P(z,\tau)}{\partial z} = [g(1-\varepsilon P) - \alpha]P(z,\tau) \quad (4)$$

to be written as

$$\int_0^L g\partial z = \int_{P_{in}}^{P_{out}} \frac{\partial P}{P} + \int_{P_{in}}^{P_{out}} \varepsilon \partial P + \alpha \int_0^L \partial z - \alpha\epsilon \int_0^L P\partial z$$

and more simplicity is written as

$$\int_0^L g\partial z = h(\tau) + \varepsilon P_{in}\left(e^{h(\tau)} - 1\right) + \alpha L - \alpha \int_0^L P\partial z \quad (5)$$

while the integral $\int_0^L Pg\partial z$ occurred at the last term in the R.H.S of Eq.(3) can be written as

$$\int_0^L Pg\partial z = \left(1+\varepsilon P(z,\tau)\right) \int_{P_{in}}^{P_{out}} \frac{\partial P}{P} + \alpha \int_0^L \partial z - \alpha\,\epsilon \int_0^L P\,\partial z \quad (6)$$

Now, substitute Eq. (4) and (5) into Eq. (6) to obtain Eq. (7), which can be simplified to Eq. (8). Equation (7) can be written in useful formula as in Eq. (9) that presents the integrated gain in presence slow, fast dynamics and loss in addition to ASE contribution. If all mentioned dynamics are presence, then, the solution does not available. To our knowledge, there are no published researches determine explicitly Eq. (9) as in our work. Neglecting the loss (α) into Eq. (9) reduce it to

$$\frac{dh}{d\tau} = \frac{1}{1+\varepsilon P_{in}e^h}\left\{\frac{h_o}{\tau_{cdp}} - \frac{h}{\tau_{eff}} - P_{in}e^h\left(\frac{\varepsilon}{\tau_{eff}} - \frac{1}{E_{sat}}\right) - P_{in}\left(\frac{\varepsilon}{\tau_{eff}} + \frac{1}{E_{sat}}\right) - \varepsilon\frac{dP_{in}}{d\tau}\left(e^{h(\tau)}+1\right)\right. \quad (10)$$

If ε and ASE are neglected, one can get well known equation that describes slow dynamics only [3]. The output power of subsection can be expressed by [4]

$$(\tau) = P_{in,k}(\tau)e^{h_k(\tau)} \quad (11)$$

k is index that refers to a subsection in multisession scheme, $P_{in,k}(\tau)$ represents the power profile of the input pulse and have a range to be -40dBm to 20 dBm in our work. $P_{out,k}(\tau)$ is the power profile of the output pulse at end a segment Eq. (9) is applied at each segment end after taking into account the following important considerations:

1. The diffusion of carrier density does not take into account at virtual proposed interfaces
2. The average out power at the first interface is taken as input power of the second segment.
3. The dynamics were presented in our simulation is absence the loss.
4. The injected currents for each segment are independent on the current that injected to the others.
5. The total injected current that is chosen to supply the first segment was the current that chevies a compression of the noise figure near the saturation region of single segment model.

3. Noise Figure in SOA

All amplifiers have noise; it cannot be avoided. Stimulated emission enables the amplification of incoming signal photons in any optically amplifying medium. However, a random and incoherent process known as carrier relaxation via Spontaneous emission (SE) will also take place [13,14]. Spontaneous emission events only add a detectable amount of noise power to the signal because they can emit a photon at any wavelength and in any direction or phase [15]. The following equation can be used to calculate the ASE noise's power within the SOA [16]

$$P_{ASE} = 2 \cdot n_{sp} \cdot h \cdot v \cdot (G-1) \cdot B_0 \quad (12)$$

where G is the gain at the optical frequency v, h symbolizes the Planck's constant, B_0 is the optical bandwidth, and n_{sp} represents the population inversion factor.

In ideal amplifier, n_{sp} is equal to 1, equivalent the complete inversion of the middle. Although, in the usual case, the population inversion is partial and

n_{sp}>1. Noise can be represented by an equation containing the three types of noise [17]:

$$NF = \&\frac{1}{G} + 2 \cdot n_{sp} \cdot \frac{G-1}{G} + \frac{h \cdot v \cdot B_0 \cdot n_{sp} \cdot P_{in} \cdot (G-1)}{P_{out}^2} + \frac{h \cdot v \cdot (2B_0 - B_e) \cdot n_{sp}^2 \cdot P_{in} \cdot (G-1)^2}{2 \cdot P_{out}^2} \quad (13)$$

Due to the low ASE power in comparison to the signal power, the final two portions can be ignored in practice. Alternatively, the spontaneous-spontaneous beat noise can be decreased by adding an optical filter to the output. NF can be rewritten as follows:

$$NF \approx \frac{1}{G} + 2 \cdot n_{sp} \cdot \frac{G-1}{G} \quad (14)$$

Since the spontaneous emission factor (n_{sp}) is always greater than 1, the smallest value of NF is obtained when n_{sp}=1. Therefore, NF of an ideal optical amplifier is 3dB for large gain values (G>>1). This is thought to have the least amount of NF. This implies that each time an optical signal is amplified, the signal to noise ratio is reduced by half [18].

To interpret the total noise figure (NF_T), it can be considered the amplifier as a chain of individual amplifier equivalent to virtual subsection and NF_T of the system is determined by NF in the initial subsection. The chain can be expressed as optical amplifier cascade and the Friis equation determine well this idea [21]

$$NF_T = NF_1 + \frac{NF_2 - 1}{g_1} + \frac{NF_3 - 1}{g_1 g_2} + \cdots + \frac{NF_m - 1}{g_m g_{m-1}} \quad (15)$$

NF_m and g_m are the NF and g of subsection m. A certain succeeded term reduces compared with the last because there are additional gain t each step. The commutative NF by each successive element is added which turn on reduce the magnitude as whole. So, the terms in the beginning have the significant contribution to NF_T.

3. Results and Discussion

The simulation is achieved by MATLAB Software and the used parameters determined in table (1). Since there are no published researches take into account the slow and fast dynamics together, so the parameters are assembled from many of published researches. The parameter is chosen such that the association of saturation region and compression noise is being verified and the important parameter that influence is the injected current that is carefully chosen, for slow dynamic ε=0, fast dynamic ε≠0 without and in presence ASE factor (τ_{eff}). To supply the three segments, we followed two configurations, the first and second are denoted by config.1 and config.2, respectively, as explained in table (2).

In three segment model as in our simulation, each sub segment is independently injected. The configuration in our research consist on three segment and injected currents are such that the first and the last section take higher and lower value respectively, while, the medium takes a middle value. To obtain the second configuration, the above can be reverse. Both schemes have carrier density distribution and NF depends on it such that takes minimum value if NF is high at the input while takes maximum value at final subsection. We attain the important requirement of eq. [NF_T] by choosing the current of first subsection that makes there is a compression noise close the saturation region.

Table (2) Two configurations used in the simulation

config.1			
I(mA)	260	140	80
P_{sat}(mW)	9.4	12.6	30..7
τ_{cdp}(ps)	390	292	120
config.1			
I(mA)	80	140	260
P_{sat}(mW)	30..7	12.6	9.4
τ_{cdp}(ps)	120	292	390

Each section is considered a new SOA of the same length. The amplitudes and powers determined for each segment will be utilized as input values for the subsequent segment's amplitude and power calculations. The final segment's output will be regarded as the SOA's output.

The compression noise is ranging from 5.65 to 4.99 dB for ASE dynamic and from -5.55 to 1.69 dB for ASE and ε dynamics. Both dynamics are in a range of P_{in} (-10 to 6.9 dBm), and ε can be reduced ASE effect to be lower comparison with presence ASE effect only as shown in Fig. (1). The latter features occur respectively in blue and red color. Due to mentioned, ε must be taken account because its effect on reduction ASE value, so, the result will be close SOA real behavior. In the simulation, it can be choice I=260mA and another injecting currents make them in sub segment 2 and 3 to be higher value in three segment model and we do not always capable to increased injected current as we desire. As a result, the compression noise is close the saturation region verified in our simulation.

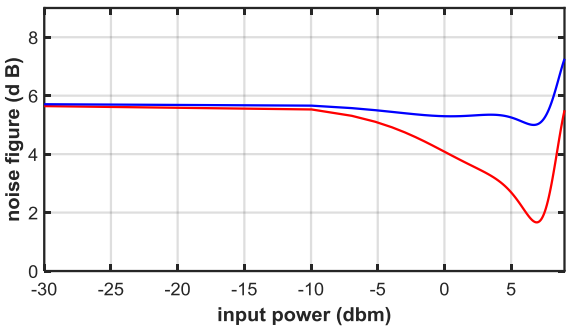

Fig. (1) Noise figure as a function of input power. ASE (red), ASE and ε (blue) for one segment

Figure (2) shows gain as a function of P_{out} for the three-segment SOA under different injected currents that increase towards the SOA end (The blue curve), and different injected currents that decrease towards the SOA end (red curve). We notice that gain behaves linearly at low power and decreases at high P_{out}, indicating the beginning of a saturation region, which turn of gets back to lower power that decreases as the pulse width decreases. The results for pulse width 0.1,

0.3, 0.5, 0.8, 1, and 1.5ps are, respectively, 6.97, 6, 5.8, 3.7, 4.1, and 3.66 dBm.

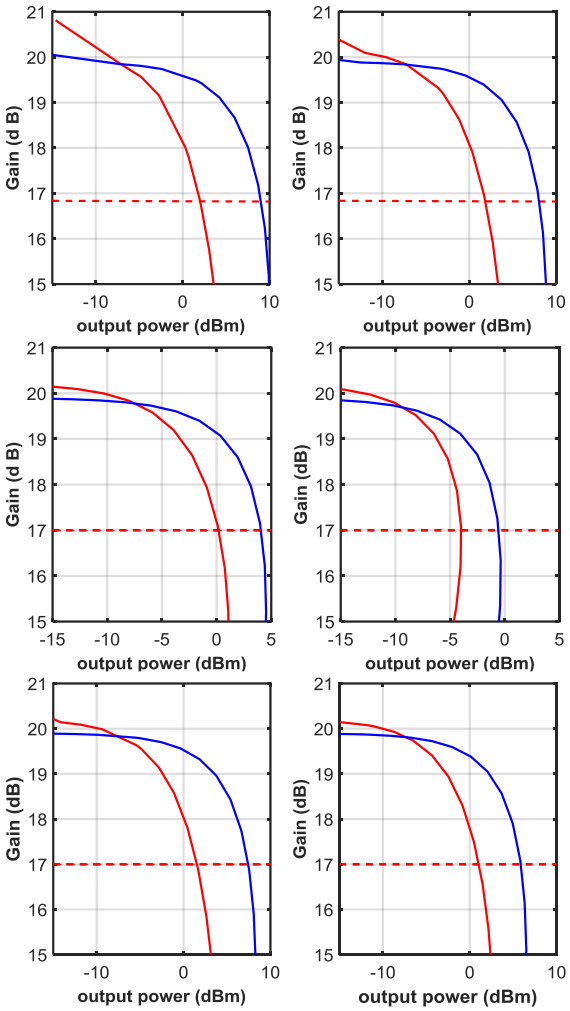

Fig. (2) Gain as a function of output power when the pulse width is: $\tau_p = 1.5\,ps$ upper left, $\tau_p = 1.0\,ps$ upper right, $\tau_p = 0.84\,ps$ middle left, $\tau_p = 0.5\,ps$ middle right, $\tau_p = 0.3\,ps$ the bottom of left, and $\tau_p = 0.1\,ps$ the bottom right. *ASE* effects and intraband are neglected

When the ASE effect is taken in respect Fig. (3), the width of saturation region increases compared to the previous form (slow dynamics only). The reason for this is the depletion of carriers due to spontaneous emission, while the width of the saturation region decreases (Fig. 2 and 3) as the pulse width decreases but in Fig. (3) when τ_p>0.5ps, the behavior is reversed and the saturation region starts to be decreased compared with it when τ_p<0.5ps. The reason is, effects ε and ASE are really existence but the occurrences and its effects decrease when the pulse τ_p>0.5ps, this behavior refers to that gain cannot be recovered fast enough within pulse width mentioned.

Figure (4) shows gain as a function of P_{out} when fast dynamic effects are taken (ε≠0) without ASE. The negligible of latter by making $\tau_{cdp} = \tau_{eff}$ makes blue color (config.1) and the second one (red color) get fast. There is no chance for ASE to prevent the fast gain recovery to get rapidly. As a result, the shifting towards the lower power will be less and one can be noted that there is no change from the slow dynamic as there is no significant change in the width of the saturation region, and the reason for this is the absence of the effects of ASE.

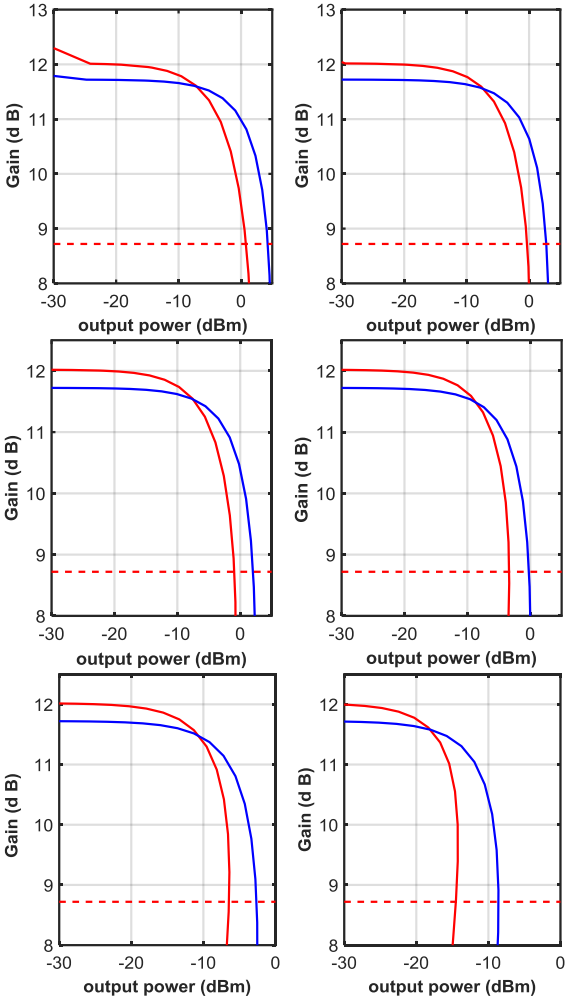

Fig. (3) Gain as a function of output power when the pulse width is: $\tau_p = 1.5$ ps upper left, $\tau_p = 1.0$ ps upper right, τ_p = 0.84 ps middle left, $\tau_p = 0.5$ ps middle right, $\tau_p = 0.3$ ps the bottom of left, and $\tau_p = 0.1$ ps the bottom of right. ASE effects taken, and intraband are neglected

Figure (5) shows gain as a function of P_{out} when fast dynamic effects are taken (ε≠0) without ASE. The gain recovery is fast when the pulse width 1, 0.84, and 0.5ps but is fester when the pulse width 300, and 500fs. The dependence of recovery on dynamics which turn on influences on pulse width makes the shifting is towards the lower power and is larger for femtosecond pulse width. In config. 1 (blue color), ASE is less compared with config. 2 (red color) because (NF_T=NF_1) as clearly determined by Eq. (15). So, the stimulated emission is dominant and -3dB gets fast. In config. 2, the mentioned behavior is reversed and ASE tries to prevent -3dB to get fast.

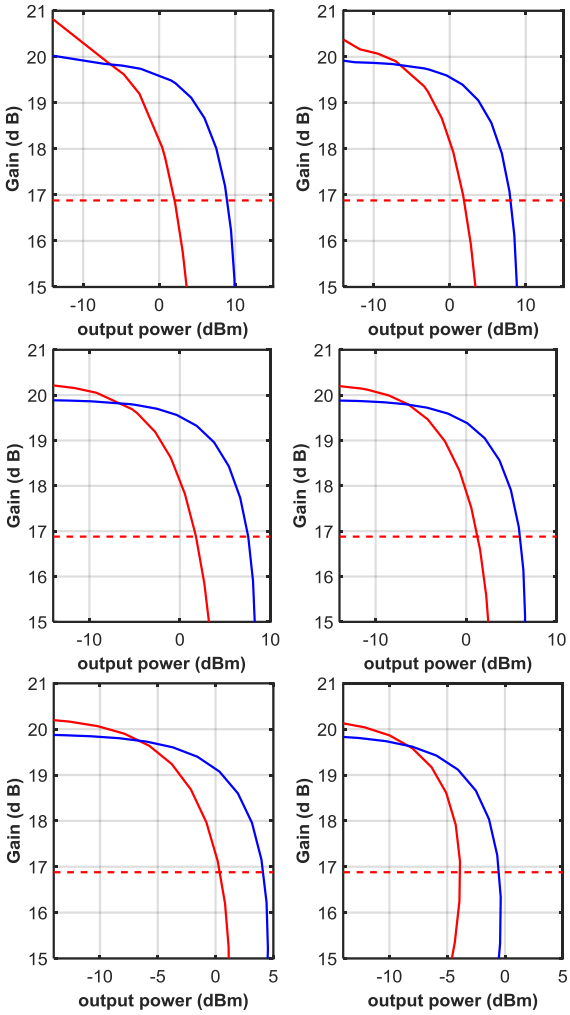

Fig. (4) Gain as a function of output power when the pulse width is: $\tau_p = 1.5\,ps$ upper left, $\tau_p = 1.0\,ps$ upper right, $\tau_p = 0.84\,ps$ middle left, $\tau_p = 0.5\,ps$ middle right, $\tau_p = 0.3\,ps$ the bottom of left, and $\tau_p = 0.1\,ps$ the bottom of right. *ASE* effects neglected, and intraband are taken

At a certain P_{in} then N at maximum value decreases with increasing P_{in} and this refers to there is a chance to induce depleted electrons at SOA beginning more than deep into SOA. If P_{in} decreases, the behavior is reversed and the chance is low. As a result, N has a symmetric special distribution while at high P_{in} then N becomes more asymmetrical. N is calculated at SOA rear of various P_{in} as shown in Fig. (6). Also, N decreases rapidly towards $N_{trans.}$ as P_{in} increases. Increasing N reduces NF and one cannot supply SOA indefinitely by injected current to improve NF due to ASE saturation and Auger recombination effects at high injected current. So, on can improve NF to be minimum with specific carrier density. The behavior of N with propagation distance (z) at high and low P_{in} explain, respectively, why does G decreasing takes places at high P_{out} of config. 1 and further of P_{out} of config. 2. So, the change of G in config. 1 starts to be less and depend on distribution N as shown in Fig. (6). In config.1, P_{in} that enter the second segment would represent P_{out} exciting from first one and its amplification depend on first segment injected current. The latter is large than other segments (second and third). G is inevitable but differs in config. 1 that is smaller than into second and smallest into third one. Since, G in first (config. 1) does suffer low NF according to Eq. (15). So, the saturation of config. 1 is larger compared with the other. Concerning on config. 2, NF of first segment is larger than second and third as sequence of Eq. (15). As a result, G for first one is the smallest than the others.

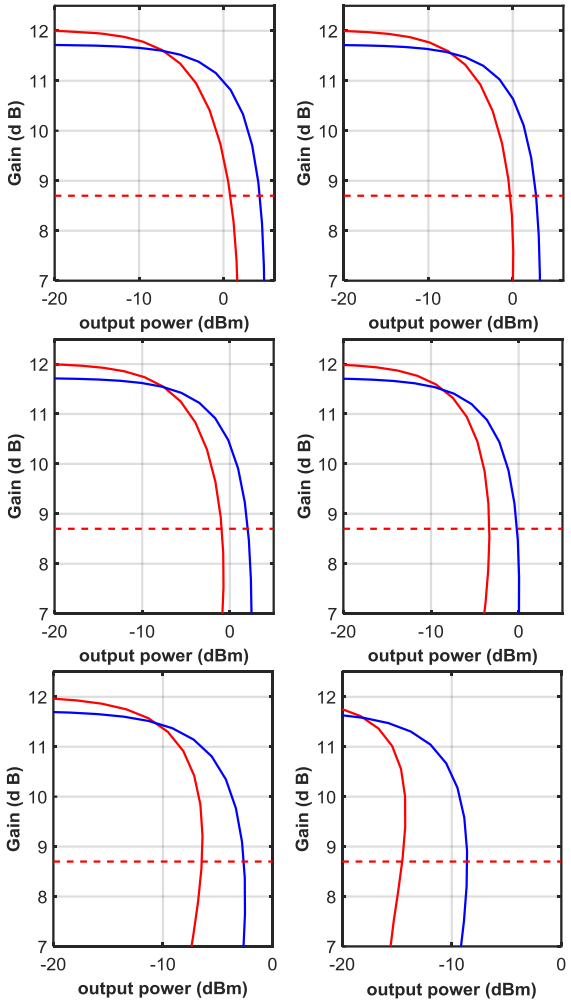

Fig. (5) Gain as a function of output power when the pulse width is: $\tau_p = 1.5\,ps$ upper left, $\tau p = 1.0\,ps$ upper right, $\tau_p = 0.84\,ps$ middle left, $\tau_p = 0.5\,ps$ middle right, $\tau_p = 0.3\,ps$ the bottom of left, and $\tau_p = 0.1\,ps$ the bottom of right. *ASE* effects and intraband are taken

The SOA gain saturation provides much insight into the improvements offered by the multi-section SOA. One can compare the one-segment model (dashed line) and the lamped current in two configurations (red and blue line), as shown in Fig. (7). For low output powers below -10dBm, the unsaturated gain for the one-segment model (dash line) and the lamped SOA is taken to be 20 dB. The SOA gain decreases as output increases referred to that saturation start to be the is gain less and less to

obtain output power at which the gain is 3 dB lower than the unsaturated value. The single-section SOA has $P_{out(sat.)}$= 6 dBm, whereas for multi-section (red line) SOA is $P_{out(sat.)}$= 1.8 dBm and when three-segment SOA under different injected currents increases towards the SOA end (blue color), the output saturation power increases to be $P_{out(sat.)}$= 7.6 dBm.

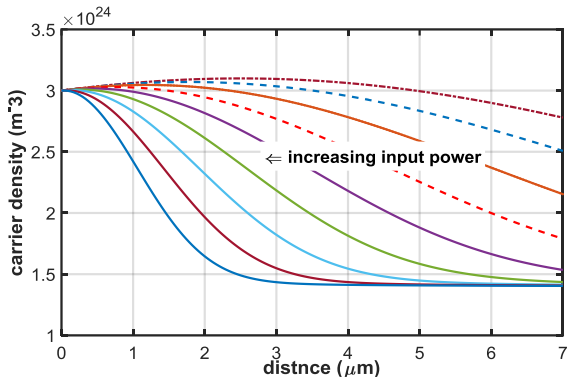

Fig. (6) Carrier density as a function of propagation distance at various input power

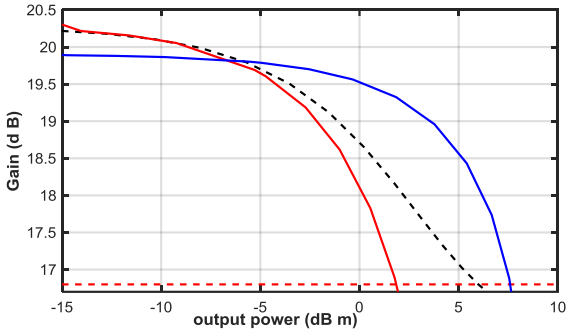

Fig. (7) Gain as a function of output power for one segment model (dashed line) when the pulse width is: $\tau p = 1.0\ ps$ and for lamped current of two configurations (red and blue line). ASE effects and fast dynamics are neglected

4. Conclusion

One segment model that occurs noise compression at a certain injected current can be considered the best for designing three-segment model that is supplied independently by three injected currents. As well as, one segment model aids to attain the important requirement to avoid the damages of NF_T into three segment model by making NF to be equivalent NF_T. These considerations make saturation region extension to be large and can use in many applications, such as PAM4. Also, the presence of fast dynamics can be influenced, so, it must take into account to simulate SOA.

References

[1] A. Crottini et al., "Noise figure improvement in semiconductor optical amplifiers by holding beam at transparency scheme", *IEEE Photon. Technol. Lett.*, 17(5) (2005) 977-979.

[2] T.W. Berg, "The dynamics of semiconductor optical amplifiers: Modeling and applications", *Opt. Photon. News*, 14(7) (2003) 42-48.

[3] A. Sobhanan et al., "Semiconductor optical amplifiers: recent advances and applications", *Adv. Opt. Photon.*, 14(3) (2022) 571-651.

[4] M.J. Connelly, "Wideband semiconductor optical amplifier steady-state numerical model", *IEEE J. Quantum Electron.*, 37(3) (2001) 439-447.

[5] R. Brenot et al., "Experimental study of the impact of optical confinement on saturation effects in SOA", in Optical Fiber Communication Conference (2005), Optica Publ. Group, p. OME50.

[6] G. Bendelli et al., "A new structure for high-power TW-SLA (Travelling wave semiconductor laser amplifier)", *IEEE Photon. Technol. Lett.*, 3(1) (1991) 42-44.

[7] G. Giuliani and D. D'Alessandro, "Noise analysis of conventional and gain-clamped semiconductor optical amplifiers", *J. Lightwave Technol.*, 18(9) (2000) 1256.

[8] M. Yoshino and K. Inoue, "Improvement of saturation output power in a semiconductor laser amplifier through pumping light injection", *IEEE Photon. Technol. Lett.*, 8(1) (1996) 58-59.

[9] S. Saini et al., "A semiconductor optical amplifier with high saturation power, low noise figure and low polarization dependent gain over the C-band", in 17th Annual Meeting of the IEEE Lasers and Electro-Optics Society (2004) vol. 1, IEEE, pp. 102-103.

[10] K. Carney et al., "Method to improve the noise figure and saturation power in multi-contact semiconductor optical amplifiers: simulation and experiment", *Opt. Exp.*, 21(6) (2013) 7180-7195.

[11] R. Bonk et al., "Linear semiconductor optical amplifiers for amplification of advanced modulation formats", *Opt. Exp.*, 20(9) (2012) 9657-9672.

[12] S.P.Ó Dúill, P. Landais and L.P. Barry, "Estimation of the performance improvement of pre-amplified PAM4 systems when using multi-section semiconductor optical amplifiers", *Appl. Sci.*, 7 (2017) 9-908.

[13] R. Lennox et al., "Impact of bias current distribution on the noise figure and power saturation of a multicontact semiconductor optical amplifier", *Opt. Lett.*, 36(13) (2011) 2521-2523.

[14] P.P. Baveja et al., "Self-phase modulation in semiconductor optical amplifiers: impact of amplified spontaneous emission", *IEEE J. Quantum Electron.*, 46(9) (2010) 1396-1403.

[15] M. Ueffing, "Direct amplification of femtosecond pulses", LMU (München, 2018).

[16] V. Agarwal and M. Agrawal, "Characterization and optimization of semiconductor optical amplifier for ultra-high speed applications: a review", in 2018 Conference on Signal Processing and Communication Engineering Systems (SPACES) (2018), IEEE, pp. 215-218.

[17] K. Obermann et al., "Noise characteristics of semiconductor-optical amplifiers used for

wavelength conversion via cross-gain and cross-phase modulation", *IEEE Photon. Technol. Lett.*, 9(3) (1997) 312-314.
[18] H.G. Shiraz, "The principles of semiconductor laser diodes and amplifiers", Imperial College Press (London, 2004).
[19] Y. Said, H. Rezig and A. Bouallegue, "Analysis of noise effects in long semiconductor optical amplifiers", *Open Opt. J.*, 2(1) (2008).
[20] Y. Yamamoto and K. Inoue, "Noise in amplifiers", *J. Lightwave Technol.*, 21(11) (2003) 2895-2915.
[21] E.A. Alquda and A.M. Matarneh, "Comprehensive investigation modeling for semiconductor optical amplifier (SOA)", *Jordan. J. Comput. Inform. Technol.*, 1(1) (2015).
[22] A. Kotb, K.E. Zoiros and C. Guo, "Numerical investigation of an all-optical logic OR gate at 80 Gb/s with a dual pump–probe semiconductor optical amplifier (SOA)-assisted Mach–Zehnder interferometer (MZI)", *J. Computat. Electron.*, 18 (2019) 271-278.
[23] G.P. Agrawal and N.A. Olsson, "Self-phase modulation and spectral broadening of optical pulses in semiconductor laser amplifiers", *IEEE J. Quantum Electron.*, 25(11) (1989) 2297-2306.

$$\frac{\partial}{\partial\tau}\int_0^L g\partial z = \frac{g_o L}{\tau_{cdp}} - \frac{1}{\tau_{eff}}\int_0^L g\partial z - \frac{1}{E_{sat}}\int_0^L \frac{Pg\partial z}{1+\varepsilon P(z,\tau)} \quad (3)$$

$$\frac{\partial}{\partial\tau}\left[h(\tau) + \varepsilon P_{in}\left(e^{h(\tau)}-1\right) + \alpha L - \alpha\int_0^L P\partial z\right] = \frac{g_o L}{\tau_{cdp}} - \frac{1}{\tau_{eff}}\left[h(\tau) + \varepsilon P_{in}\left(e^{h(\tau)}-1\right) + \alpha L - \alpha\int_0^L P\partial z\right] + \frac{1}{E_{sat}}\left[\int_0^L \frac{(1+\varepsilon P(z,\tau))\int_{P_{in}}^{P_{out}}\frac{\partial P}{P} + \alpha\int_0^L \partial z - \alpha\epsilon\int_0^L P\,\partial z}{1+\varepsilon P(z,\tau)}\right] \quad (7)$$

$$\frac{\partial h(\tau)}{\partial\tau} + \frac{\partial}{\partial\tau}\left(\varepsilon P_{in}\, e^{h(\tau)}\right) - \frac{\partial}{\partial\tau}\varepsilon P_{in} + \alpha L - \frac{\partial}{\partial\tau}\left(\alpha\int_0^L P\partial z\right) = \frac{g_o L}{\tau_{cdp}} - \frac{h(\tau)}{\tau_{eff}} + \frac{\varepsilon P_{in}\, e^{h(\tau)}}{\tau_{eff}} - \frac{\varepsilon P_{in}}{\tau_{eff}} + \frac{\alpha L}{\tau_{eff}} - \frac{\alpha\int_0^L P\partial z}{\tau_{eff}} + \frac{P_{in}\left(e^{h(\tau)}-1\right)}{E_{sat}} + (1+\varepsilon P(z,\tau))^{-1}\ \alpha\int_0^L \partial z\ - (1+\varepsilon P(z,\tau))^{-1}\,\alpha\,\epsilon\int_0^L P\,\partial z \quad (8)$$

$$\frac{dh}{d\tau} = \frac{1}{1+\varepsilon P_{in}e^{h}}\left\{\frac{h_o}{\tau_{cdp}} - \frac{h}{\tau_{eff}} - P_{in}e^{h}\left(\frac{\varepsilon}{\tau_{eff}} - \frac{1}{E_{sat}}\right) - P_{in}\left(\frac{\varepsilon}{\tau_{eff}} + \frac{1}{E_{sat}}\right) + \alpha\left(\frac{L}{\tau_{eff}} + \frac{1}{E_{sat}} - L\right) - \varepsilon\frac{dP_{in}}{d\tau}\left(e^{h(\tau)} + 1\right) - \frac{\alpha\int_0^L P\partial z)}{\tau_{eff}} + \frac{\alpha\,\epsilon\int_0^L P\partial z)}{E_{sat}(1+\varepsilon P(z,\tau))} + \alpha\int_0^L P\,\partial z \quad (9)$$

Table (1) Parameters that were used in our simulation [19]

Parameters	Symbol	Value and unit
SOA region length	LE from [11]	700 μm
Width	W	3×10^{-6} m
Height	H	80×10^{-9} m
Confinement factor	Γ	0.3
Pulse width	τ_p from [20]	varied
Current	I	varied
Carrier life time	τ_{cdp}	292 ps
Effective gain recovery	τ_{eff} from [12]	20 ps
Differential gain	a	2.78×10^{-20} m^{-2}
Carrier density at transparency	No	1.4×10^{24} m^{-3}
Carrier density used	N	3×10^{24} m^{-3}
Saturation energy	East	3.74 pJ
Compression factors due to CH	ϵ_{CH}	0.2 W^{-1}
Compression factors due to SHB	ϵ_{SHB}	0.2 W^{-1}
Nonradioactive recombination coefficient	A	1.5×10^{8}
Bimolecular recombination coefficient	B	10×10^{-16}
Auger recombination coefficient	C	3×10^{-41}

Proceedings of 5th International Specialized Conference of Education College on Physics and Applied Sciences (5thICECAS24), 22-23 April 2024

Wedian K. Abad [1]
Hassan H. Darwoysh [2]
Ahmed N. Abd [3]

[1] *University of Technology-Iraq*
[2] *Department of Physics, College of Education, Mustansiriyah University, Baghdad, IRAQ*
[3] *Department of Physics, Faculty of Science, Mustansiriyah University, Baghdad, IRAQ*

A Simple and Economical Method to Prepare Cu/CuO/Cu_2O NPs for Biomedical Applications

In the current study, Cu/copper oxide nanoparticles (NPs) has been produced by simple chemical method. The structural and spectroscopic characteristics of these nanoparticles were determined. The material has monoclinic diffraction pattern and there was no indication on the presence of any additional impurities. The successful formation of copper oxide was confirmed by the vibrational mode of Cu-O bond at 400-700 1/cm. The surface plasmon resonance (SPR) of Cu/copper oxide at 220nm is responsible for the narrow absorption peak. The band gap energy of Cu/copper oxide NPs reached 4.6eV. Four bacterial strains and one strain of fungus were used to test the anti-bacterial and antifungal properties of copper and oxide. The Cu/CuO/Cu_2O showed an inhibiting effect on bacteria more than fungi.

Keywords: Nanoparticles; Copper oxides; Optical properties; Antibacterial activity
Received: 19 January 2024; Revised: 4 March 2024; Accepted: 4 April 2024

1. Introduction

The various metal nanoparticles (NPs) are involved in a wide range of biological and biochemical processes. Copper oxide possesses qualities that make it antimicrobial, antibacterial, antifungal, gas sensing, biocidal, superconductive, catalytic, and optical material [1-4]. CuO NPs is a p-type semiconductor and has optical band gap of about 1.7 eV [5,6]. A number of chemical, physical, and biological procedures can be used to produce CuO NPs [,8]. Antimicrobial resistance (AMR) is a global hazard to human progress and health [9]. Urgent multi-sectoral action is needed to achieve the sustainable development goals (SDGs) [10]. It is not unexpected to see that nanotechnology is being used in medicine increasingly frequently to tackle the antibiotic resistance threat [11-14]. Infections can be treated in a number of methods using NPs [15]. To strengthen their physiochemical action against bacteria that are resistant to medication, they can be coupled with currently available antimicrobials [16-18]. Ion Cu NPs cause toxicity inside of bacterial cells when they come into contact with them, leading to a variety of malfunctions and finally leading to cell death. This results in a multitude of problems, including cell death. The Cu NPs are capable of penetrate the bacterial cell through the cell membrane because of their small particle size. Cu ions are efficiently drawn by carboxylic and amine groups in the bacterial cell membrane. The toxicity of Cu NPs is greatly impacted by the form and size of the particles [19]. Reactive oxygen species (ROS) that Cu NPs accumulates can damage cell membranes and cause immediate cellular toxicity [20]. Due to its high redox potential, copper can produce Cu ions, which can be used as an electron donor or acceptor. These ions collect superoxide and hydroxyl radicals, which makes them extremely hazardous for bacterial cells and causes oxidative stress. These ROS production can affect how bacteria reproduce their DNA, divide their cells, and regulate their metabolism. Degradation of mitochondria, and other proteins channels found in the bacterial cell membrane is facilitated by CuNPs-mediated toxicity in bacterial cells. The precise mechanism underlying anti-bacterial action is still being researched. The following graphic (Fig. 1) illustrates a potential anti-bacterial mechanism of CuNPs [21].

The aim of this study is to prepare copper oxide nanoparticles from copper iodide in a simple and inexpensive method and then verify the properties of the prepared material and its effectiveness against microbial.

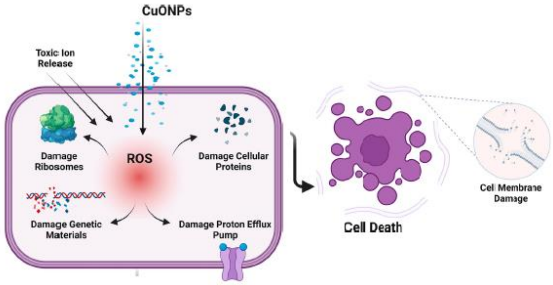

Fig. (1) Probable antimicrobial mechanism of Cu/CuO/Cu_2O NPs

2. Experimental Part

The Cu/CuO/Cu_2O NPs have been produced by simple chemical method. First, 1.0 g of CuI was dissolved in 100 ml ethanol. Second, 50 ml of NaOH (2M) was added to the CuI solution. Finally, both solutions were mixed by magnetic stirrer at room temperature for one hour, as shown in Fig. (2a). The crystallographic structure of Cu/CuO/Cu_2O NPs was determined by x-ray diffraction (XRD) patterns, the spectroscopic analysis of Cu/CuO/Cu_2O NPs was performed within the range of 200-1100 nm by a UV–visible spectrophotometer, and the surface topography of the prepared samples was determined by atomic force microscopy (AFM). The Fourier-transform infrared (FTIR) spectroscopy was used to determine chemical bonds in the wavenumber range of 400-4000 cm^{-1}. Finally, the antibacterial and antifungal activities of Cu/CuO/Cu_2O NPs were studied. The Mueller-Hinton agar medium plates were used for the test, which was conducted using the well diffusion method. A clean, well-sterilized cutter was sued to form well with a 6 mm diameter on the plates. Using clean, sterile cotton swabs, the bacteria suspension was applied uniformly to the Mueller-Hinton agar culture medium, and after the plates had dried, 100 ml of the Cu/CuO/Cu_2O NPs solution was added to the wells. Once the incubator reached 37°C, the plates were left there for one day, then the inhibitory zone's circumference around the well was determined in millimeters, according to Fig. (2b).

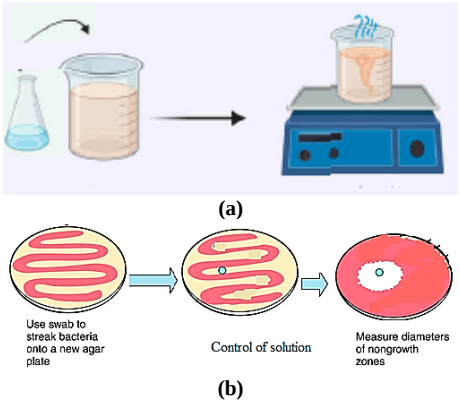

Fig (2) (a) The creation of copper oxide NPs graphically, and (b) schematic diagram of cultivation of bacteria and fungi

3. Results and Discussion

XRD pattern was used to verify the crystalline structure of Cu/CuO/Cu_2O NPs, as can be shown in Fig. (3). The four primary distinctive XRD peaks, which correspond to Bragg's reflections at (311), (002), (331) and (200) for Cu_2O, Cu/CuO/Cu_2O and Cu, respectively. The findings clearly support the Cu/CuO/Cu_2O NPs synthesis. There are no other contaminants found in the Cu/CuO/Cu_2O NPs diffraction pattern. The results of this study were in agreement with Cu_2O JCPDS card no. 34-1254, Cu/CuO/Cu_2O JCPDS card no. 45-0937 and Cu JCPDS card no. 02-1225. It guarantees the purity of the resulting Cu/CuO/Cu_2O NPs [22-26].

AFM was used to study the surface topography of prepared film. It can be noticed from Fig. (4) that the grains are different in size where the maximum size is about 88.9 nm. Also, the grain size is ranging from very small size (<100 nm) to others may reach to 1 µm.

Figure (5) depicts the transmission spectra of Cu/CuO/Cu_2O NPs formed chemically. The Cu/CuO/Cu_2O NPs have shown a relatively narrow peak of absorption at 220 nm, which is most likely due to Cu/CuO/Cu_2O semiconductor surface plasmon resonance (SPR) excitation [27]. The energy band gap (E_g) of the Cu/CuO/Cu_2O NPs was determined to be 4.6 eV using the Tauc's equation [28,29], as shown in Fig. (6), where the value of E_g was larger than value of bulk structure (2.1eV) because decreasing particle size causes to increase energy band gap (E_g) [25,29]. The Cu/CuO/Cu_2O NPs might be used as an ideal solar harvester and a powerful photocatalyst for environmental cleanup [29,30].

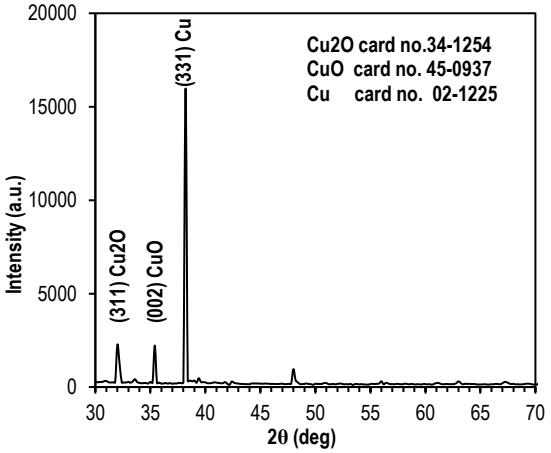

Fig. (3) XRD pattern of Cu/CuO/Cu_2O sample

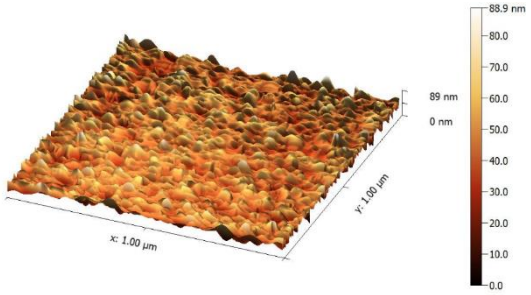

Fig. (4) AFM image of the synthesized Cu/CuO/Cu_2O NPs

In FTIR analysis, the bands at wavenumbers 3443 and 1625 cm^{-1} as well as the peak at 2360 cm^{-1} are generated by airborne CO_2 due to O-H (hydroxyl) bond. The N-H bond vibration is thought to be responsible for the peak at 1523 cm^{-1}. The peaks at 1083 and 1205 cm^{-1} were created by vibration modes of C=O and C=H bonds and O-H bond, respectively. Bands seen at 485cm^{-1} (Cu-O symmetric stretching), at 669 cm^{-1} (Cu-O asymmetric stretching), and at 750 cm^{-1} (wagging) correspondingly can be used to identify the characteristic Cu/CuO/Cu_2O bond

frequencies in Cu/CuO/Cu_2O NPs. The formation of Cu/CuO/Cu_2O NPs is evidently the result of an electrostatic interaction between Cu ions and electron-rich amino, ketonic C=O, and alcoholic OH groups, as shown in Fig. (7) [31,32].

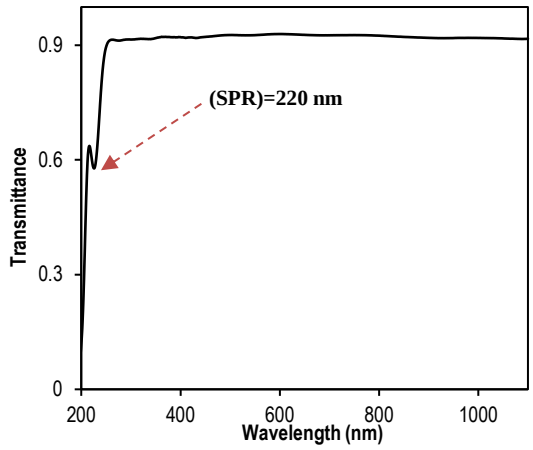

Fig. (5) Transmission spectrum of Cu/CuO/Cu_2O NPs

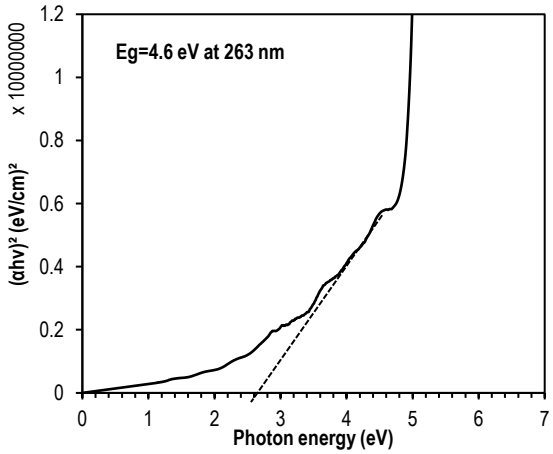

Fig. (6) Determination of energy band gap of the prepared sample

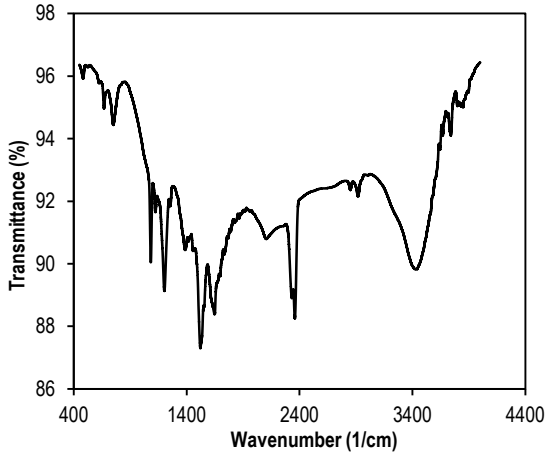

Fig. (7) FTIR spectrum of copper oxide nanoparticles

A well-diffusion assay, which makes use of disks impregnated with anti-biotics or nanoparticles, is frequently used to measure the bacterial susceptibility to these agents. The wells were filled with the prepared Cu/CuO/Cu_2O NPs suspension. To allow for diffusion, the samples were initially incubated for 15min at 4°C, then for 24h at 37°C. After the incubation period, the inhibition zone encircling the well was regarded as a successful test result. The copper oxide NPs were tested at various concentrations (100%) for their ability to inhibit *S. epidermidis*, *S. aureus* and *Klebsiella*, *Escherichia coli* strains, as well as one fungal strain. Figure (8) depicts this impact. Bacteria (such as *E. coli*) have been seen to have inhibition ratios as large as 14 mm in diameter. Although Cu/CuO/Cu_2O NPs inhibited *S. epidermidis* at the highest rate (13mm). This was caused by the bacteria's cellular wall construction. This was caused by the bacteria's cellular wall construction.

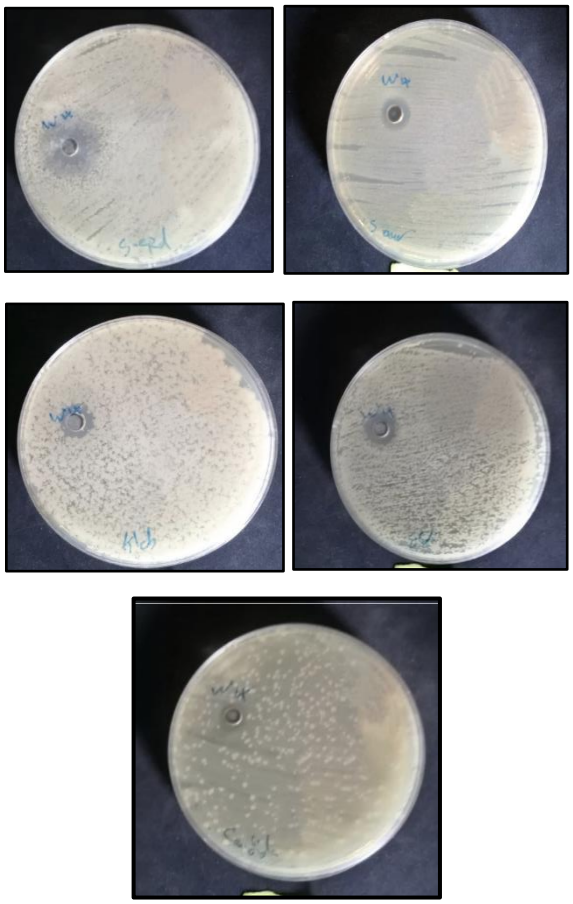

Fig. (8) Growth-inhibition zone of Cu/CuO/Cu_2O NPs

Given that bacterial death has characteristics comparable to nanoparticles in terms of stability, volume and concentration to the growing medium that extends the duration for interaction between nanoparticles and bacteria, the strain of fungi, in contrast, recorded 10mm, as depicted in Fig. (9). Many theories exist to explain how nanoparticles can prevent bacterial development. When the surface to volume ratio increases by a factor of nano millions, there is a general shift in the optical characteristics structure [33]. The majority of bacterial cell membranes have microscopic pores called stomata.

However, in order to have an impact on bacterial development by altering cellular function, the nanostructures must penetrate or pass through those membranes and remain there for a long enough period of time [34]. Despite the fact that researchers have developed a variety of strategies, each one is based on the same fundamental idea: The negative charge on the surface of bacterial cells can be attracted to the positive charge of nanoparticles, causing an accumulation of particles on the membrane of cell. As a result, the bacteria's membrane processes, including permeability, respiration, and electron transfer, are stopped [35-37]. The bacterial membrane's physical and chemical characteristics have changed, resulting in this damage. The positive ions can be released from the nanoparticles inside the cell and connected to the ribosome of bacteria to prevent protein forming or to attach those nanoparticles to the bacteria's genetic material to stop it from proliferating. The DNA would be ruined, and cell death would result [38-43].

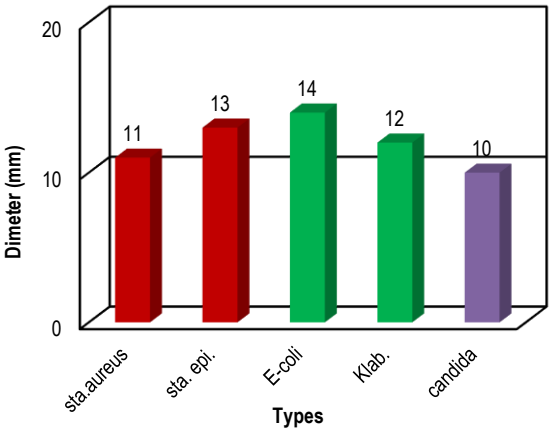

Fig. (9) Diameter of inhibition zone

4. Conclusion

The findings of this study demonstrated that copper oxide nanoparticles could be produced chemically simply by reacting sodium hydroxide with copper iodide. The significant copper ion adsorption to bacterial cells, which results in concentration-dependent anti-bacterial efficacy, is the primary cause of the anti-bacterial mechanism, where copper oxide nanoparticles may replace several anti-biotics. The material has high transmittance in visible and IR region reaching 91% and this makes it suitable for solar cells as window layer.

References

[1] A.V. Singh et al., "Biological Synthesis of Copper Oxide Nano Particles Using Escherichia Coli", *Curr. Nanosci.*, 6(4) (2010) 365-369.

[2] S. Yedurkar, C. Maurya and P. Mahanwar, "A Biological Approach for the Synthesis of Copper Oxide NPs by Ixora coccinea Leaf Extract", *J. Mater. Enviro. Sci. Com.*, 8 (2017) 1173-1178.

[3] R. Vijay Kumar et al., "Preparation and Characterization of Nanocrystalline Copper Oxide Embedded in Poly(Vinyl Alcohol) and its Effect on Crystal Growth of Copper Oxide", *Langmuir*, 17 (2001) 1406-1410.

[4] A.J. Yin et al., "Fabrication of Highly Ordered Metallic Nanowire Arrays by Electrodeposition", *Appl. Phys. Lett.*, 79 (2001) 1039-1041.

[5] H. Wang et al., "Preparation of Cu/CuO/Cu_2O NPs by Microwave Irradiation", *J. Cryst. Growth*, 244 (2002) 88-94.

[6] L. Argueta-Figueroa et al., "Synthesis, characterization and antibacterial activity of copper, nickel and bimetallic Cu–Ni nanoparticles for potential use in dental materials", Prog. Nat. Sci.: Mater. Int., 24(4) (2014) 321-328.

[7] S.M. Ahmed et al., "The implementation of National Action Plan (NAP) on Antimicrobial Resistance (AMR) in Bangladesh: Challenges and lessons learned from a cross-sectional qualitative study", *Antibiotics*, 11(5) (2022) 690.

[8] O.A. Hammadi, "Production of Nanopowders from Physical Vapor Deposited Films on Nonmetallic Substrates by Conjunctional Freezing-Assisted Ultrasonic Extraction Method", *Proc. IMechE, Part N, J. Nanomater. Nanoeng. Nanosys.*, 232(4) (2018) 135-140.

[9] M. Kumar, A. Curtis and C. Hoskins, "Application of nanoparticle technologies in the combat against anti-microbial resistance", *Pharmaceutics*, 10(1) (2018) 11.

[10] A.H. Hashem et al., "Biomedical applications of mycosynthesized selenium NPs using penicillium expansum ATTC 36200", *Biol. Trace Element Res.*, 199(10) (2021) 3998-4008.

[11] M.H. Hassoni et al., "Invention and Description of p-Cu/CuO/Cu_2O /n-Si (200°C) Heterojunction for Photodiode Applications", *J. Global Pharma Technol.*, 11 (2019) 601-606.

[12] M.A. Hameed, S.H. Faisal, R.H. Turki, "Characterization of Multilayer Highly-Pure Metal Oxide Structures Prepared by DC Reactive Magnetron Sputtering Technique", *Iraqi J. Appl. Phys.*, 16(4) (2020) 25-30

[13] B. Liu and H.C. Zeng, "Mesoscale organization of Cu/CuO/Cu_2O nanoribbons: formation of dandelions", *J. Am. Chem. Soc.*, 126(26) (2004) 8124-8125.

[14] S. Marouzi, Z. Sabouri and M. Darroudi, "Greener synthesis and medical applications of metal oxide NPs", *Ceram. Int.*, 47(14) (2021) 19632-19650.

[15] M. Hasanin et al., "*in vitro* improvement and rooting of banana plantlets using antifungal nanocomposite based on myco-synthesized copper oxide NPs and starch", *Biomass Conver. Biorefin.*, 13 (2023) 8865-8875.

[16] M. Hasanin et al., "Ecofriendly synthesis of biosynthesized copper NPs with starch-based nanocomposite Antimicrobial, antioxidant, and anticancer activities", *Biol. Trace Element Res.*, 200(5) (2022) 2099-2112.

[17] A.M. Shehabeldine et al., "Multifunctional silver NPs based on chitosan: Anti-bacterial, antibiofilm, antifungal, antioxidant, and wound-healing activities", *J. Fungi*, 8(6) (2022) 612.

[18] H. Abou-Yousef et al., "Biocompatible hydrogel based on aldehyde-functionalized cellulose and chitosan for potential control drug release", *Sustain. Chem. Pharm.*, 21 (2022) 100419.

[19] S.A. Akintelu et al., "Green Synthesis of Copper Oxide NPs for Biomedical Application and Environmental Remediation", *Heliyon*, 6(7) (2020) e04508.
[20] P. Sutradhar, M. Saha and D. Maiti, "Microwave Synthesis of Copper Oxide NPs Using Tea Leaf and Coffee Powder Extracts and its Anti-bacterial Activity", *J. Nanostruct. Chem.*, 4 (2014) 86.
[21] M. Ikram et al., "Dye degradation performance, bactericidal behavior and molecular docking analysis of Cu-doped TiO_2 nanoparticles", *RSC Adv.*, 10(41) (2020) 24215-24233.
[22] J. Fang and Y. Xuan, "Investigation of optical absorption and photothermal conversion characteristics of binary Cu/CuO/Cu_2O/ZnO nanofluids", *RSC Adv.*, 7(88) (2017) 56023-56033.
[23] A.A. Badawy et al., "Efficacy assessment of biosynthesized copper oxide NPs (Cu/CuO/Cu_2O NPs) on stored grain insects and their impacts on morphological and physiological traits of wheat (triticum aestivum l.) plant", *Biology*, 10(3) (2021) 233.
[24] T.I. Shaheen, A. Fouda and S.S. Salem, "Integration of cotton fabrics with biosynthesized Cu/CuO/Cu_2O NPs for bactericidal activity in the terms of their cytotoxicity assessment", *Ind. Eng. Chem. Res.*, 60(4) (2021) 1553-1563.
[25] E.M. Ali et al., "Green Synthesis, Characterization and Antimicrobial activity of Cu/CuO/Cu_2O NPs Derived from *Hibiscus sabdariffa* a plant and CuCl", *J. Phys.: Conf. Ser.*, 1963 (2021) 012092.
[26] A.M. Hameed and M.A. Hameed, "Highly-Pure Nanostructured Metal Oxide Multilayer Structure Prepared by DC Reactive Magnetron Sputtering Technique", *Iraqi J. Appl. Phys.*, 18(4) (2022) 9-14.
[27] A. Bhaumik et al., "Significant enhancement of optical absorption through nano-structuring of copper based oxide semi-conductors: possible future materials for solar energy applications", *Phys. Chem. Chem. Phys.*, 16(22) (2014) 11054-11066.
[28] G. Varughese et al., "Characterisation and optical studies of copper oxide nanostructures doped with lanthanum ions", *Adv. Mater. Sci. Eng.*, 14(4) (2014) 49-60.
[29] A.M. Hameed and M.A. Hameed, "Spectroscopic characteristics of highly pure metal oxide nanostructures prepared by DC reactive magnetron sputtering technique", *Emerg. Mater.*, 6 (2022) 627-633.
[30] V. Vellora, T. Padil and M. Cernik, "Green synthesis of copper oxide NPs using gum karaya as a biotemplate and their anti-bacterial application", *Int. J. Nanomed.*, 8 (2013) 889-898.
[31] C. Ashok, K. Venkateswara Rao and C. Shilpa Chakra, "Structural analysis of Cu/CuO/Cu_2O nanomaterials prepared by novel microwave assisted method", *J. Atoms Molecules*, 4(5) (2014) 803-806.
[32] S. Iravani, "Green synthesis of metal NPs using plants", *Green Chem.*, 13(10) (2011) 2638-2650.
[33] F. Buazar et al., "Biofabrication of highly pure copper oxide NPs using wheat seed extract and their catalytic activity: A mechanistic approach", *J. Green Process. Synth.*, 8 (2019) 691-702.
[34] F. Ahmadi and A.H. Kordestany, "Investigation on silver retention in different organs and oxidative stress enzymes in male broile fed diet supplemented with powder of nano silver", *J. Toxicol. Sci.*, 3 (2011) 28-35.
[35] P.V. Asharani et al., "Toxicity of silver NPs in zebrafish models", *J. Nanotech.*, 19 (2008) 255102.
[36] S. Naz et al., "Synthesis, biomedical applications, and toxicity of CuO nanoparticles", *Appl. Microbiol. Biotech.*, 107 (2023) 1039-1061.
[37] S. Kim et al., "Oxidative stress-dependent toxicity of silver NPs in human hepatoma cells", *J. Toxicol. in vitro*, 23 (2009) 1076-1084.
[38] A. Rani et al., "Exploring the antibacterial and antibiofilm potential of copper oxide nanoparticles biosynthesized using *Centratherum punctatum* leaf extract", *South African J. Botany*, 164 (2024) 1-8.
[39] N.N. Hussein and M.M. Khadum, "Evaluation of the Biosynthesized Silver Nano-particles Effects on Biofilm Formation", *J. Appl. Sci. Nanotech.*, 1(1) (2021) 23-31.
[40] W.K. Abad, A.N. Abd and N.F. Habubi, "Synthesis of Ag_2O Nano-particles via Fresh Pomegranate Peel Extract for Bioapplications", *Nano Biomed. Eng.*, 15(4) (2023) 363-368.
[41] R.H. Hussein, A.A. Taha and O.M. Abdulhusein, "Study of Bio-logical Activities of Magnetic Iron Oxide Nano-particles Prepared by Co-Precipitation Method", *J. Appl. Sci. Nanotech.*, 1(2) (2021) 37-48.
[42] E. Ansarifard et al., "Evaluation of antimicrobial and antibiofilm activities of copper oxide nanoparticles within soft denture liners against oral pathogens", *Bioinorg. Chem. Appl.*, 2021 (2021) 9939275.
[43] M.Y. Ali et al., "Rapid Synthesis of SeO_2 NPs and Their Activity against Clinica Isolates (Gram positive, Gram negative, and Fungi)", *Nano World J.*, 9(3) (2023) 89-93.

Proceedings of 5th International Specialized Conference of Education College on Physics and Applied Sciences (5thICECAS24), 22-23 April 2024

Preparation and Characterization of Ag/CdTeQDs/PS/c-Si/Ag Heterojunction for Photodetector Applications

Hala R. Hassan
Mohammed J.M. Ali
Ahmed N. Abd

Department of Physics, College of Science, University of Mustainsiriyah, Baghdad, IRAQ

In this study, pure cadmium telluride (CdTe) nanoparticles and porous silicon were synthesized selectively by using the laser ablation method with distilled water and a laser energy of not more than 480 mJ and a maximum number of pulses of 300. Practical studies have shown that the material behaves like a quantum dot and porous silicon bases were prepared with a current density of 15 mA/cm^2 and an etching period of 10 min. When a quantum dot is deposited on the porous silicon, an increase in the spectral responsivity of 0.65 A/W was clearly observed.

Keywords: Porous silicon; Laser ablation; Cadmium telluride; Photodetectors
Received: 19 January 2024; Revised: 4 March 2024; Accepted: 4 April 2024

1. Introduction

Electronics and optoelectronic devices use transition metal chalcogenides (TMCs) such as ZnSe, ZnS, , CuSe, CdS, CdTe, and CdSe, among others. Cadmium chalcogenide materials like CdS, CdSe, and CdTe are the most important because they are used so often in electrical injection lasers, photodetectors, solar cells, and high-performance optoelectronic devices [1-3]. The straightforward formula for binary metal monochalcogenides is MX, where M stands for metal and X for chalcogen. The MX is a compound semiconductor, meaning that solar energy may be converted into electrical energy due to its appropriate bandgap (E_g). CdTe single crystal is good for thermoelectric, optoelectronic, photodetector, and solar cell applications because it has a straight bandgap energy of 1.5 eV [4-6]. Over 90% of the light that hits CdTe is absorbed, and its crystal structure is a type of cubic zinc blend with a very sharp absorption edge [7,8]. Research on CdTe that has been doped with zinc (Zn) and manganese (Mn) shows photorefractive properties and the link between lattice strain and a nonzero piezoelectric field [9,10]. Zone melting, the Bridgman method, traveling heaters, and epitaxial growth can all be used to generate pure CdTe crystals [11]. In the infrared spectrum, CdTe has an electro-optic coefficient that is approximately three times greater than that of InP and GaAs [12-14]. If CdTe can be alloyed with zinc (Zn), it will improve the optical devices' switch-off time for electro-optic modulators [15,16]. For application in spectroscopic gamma-ray detectors, alloying CdTe with ZnTe can modify the bandgap and lattice parameters [17]. CdTe is utilized as an absorbent layer with perfect stoichiometry and a thickness of only a few microns in the production of solar cells [18,19].

In this research, CdTe QDs were prepared for the purpose of spreading them into the pores of porous silicon and increasing the spectral response of the photodetector.

2. Experimental Part

CdTe nanoparticles preparation by laser ablation in distilled water mirror-like single crystal (4-16 Ω.cm), 508 µm thick and (100) n-type silicon wafers were cleaned, cut into 1.5×1.5 cm^2 rectangles and then chemically treated with HF. Using a thermal resistive technique, 1 µm thick silver ohmic contacts were deposited on the backsides of the wafer, and an anti-acidic wax layer was subsequently added to protect this electrode during electrochemical etching. By photoelectrochemically etching the silicon samples in a 1:1 mixture of HF (46%) - ethanol (absolute) solution using 10 mA/cm^2 current density for 15 minutes at room temperature, the porous layer was obtained. The silicon samples underwent anodization before being washed out with deionized water for ten minutes and dried with tungsten lamb. Teflon electrochemical etching cell employing an Au grid was used in the current study and is shown in Fig. (1). The etched area was adjusted to be around 0.789 cm^2.

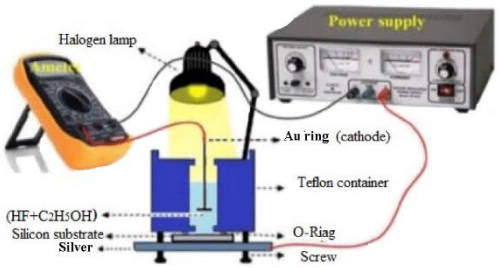

Fig. (1) Illustration of PECE setup for porous Si at various current densities, with 10 min of etching time, and 48% HF

Figure (2) depicts a three-dimensional topographic representation of porous silicon, exhibiting a pyramid-like morphology with dimensions of 73 nm, uniformly scattered across the entirety of the surface. The pyramidal morphology is indicative of an elevated surface roughness resulting from the process of anodization. The significant level of surface roughness exhibited by porous silicon suggests its potential as an anti-reflection coating, as the presence of a textured surface can effectively minimize light reflection. Moreover, the phenomenon of scattering in porous silicon can be attributed to the presence of surface roughness in relation to the thickness of the porous layer [20,21].

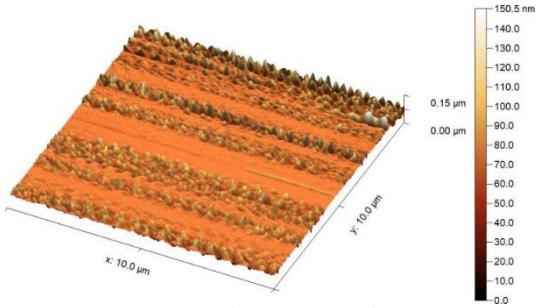

Fig. (2) A 3D AFM image of porous silicon fabricated under the conditions of a current density of 10 mA/cm^2 and an etching time of 10 minutes

A Nicolet 380 Fourier-transform infrared (FTIR) spectrometer was used to measure the FTIR spectrum from 400 cm^{-1} to 4000 cm^{-1}. This range encompasses the fundamental vibration frequencies of the primary bonding groups found in various materials, including those based on silica, refer to Fig. (3). The significant infrared (IR) peaks that have been discovered are Si-Si, Si-H, Si-OH, and CH_2, which are positioned at wavenumbers of 534, 910, 1077, and 2938 cm^{-1}, respectively [22]. The obtained peak positions were compared with those reported in other research, and a significant level of agreement was observed. In the context of photodetector applications, it is imperative for the uppermost layer to possess a low reflectivity characteristic.

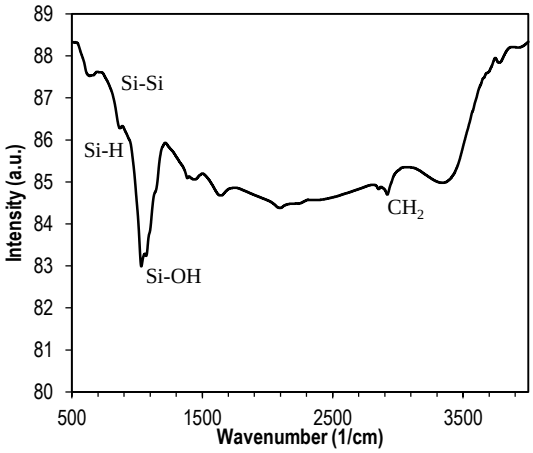

Fig. (3) FTIR spectrum of porous silicon fabricated under the conditions of current density of 10 mA/cm^2 and an etching time of 10 min

CdTe nanoparticles were synthesized by the process of laser ablation. High-purity CdTe material, in the form of a pellet of 1 cm in diameter and 4 mm in thickness, was produced by laser ablation in deionized water of 99.99% purity. The synthesis was performed at room temperature. The CdTe target was positioned at the base of the glass piker, and a solution containing colloidal CdTe nanoparticles was prepared to fill the vessel, ensuring a volume of 10 ml more than that of the target. The colloidal solution was generated through the process of irradiating a CdTe pellet using a HUAFEI 7 ns pulsed Nd:YAG laser with a wavelength of 1064 nm. A positive 16 cm lens was employed to focus the laser beam onto the target. The laser energy 480 mJ and pulse ablation (300) were set to carry out this experiment. The laser ablation in a liquid system is depicted in Fig. (4) as a simplified schematic diagram.

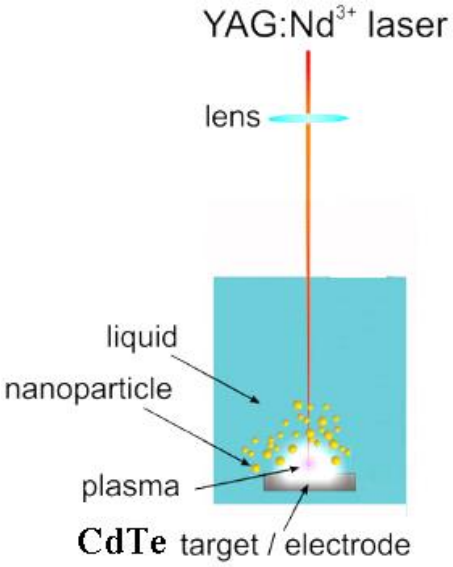

Fig. (4) Laser ablation in a liquid system. Inset is fresh colloidal CdTe NPs

The investigation focused on examining the structural, morphological, and optical properties of

porous silicon and CdSe nanoparticles. This was achieved by the utilization of a Shimadzu XRD-6000 X-ray diffractometer (CuK), and a Shimadzu SL174 PL spectrophotometer, and the techniques employed in this study include FTIR spectroscopy, JEOL JSM-5600 scanning electron microscopy, Philips CM10 pw 6020 transmission electron microscopy, Angstrom AA 3000 atomic force microscopy, and Cary 100 Conc plus UV-visible spectrophotometer. The colloidal CdTe NPs with a concentration of around 50 µL were embedded in porous silicon by drop casting technique. The photosensitivity was measured by utilizing a monochromator and the power was calibrated using a Sanwa silicon powermeter.

The observation of a diffraction peak at approximately 23.9° in Fig. (5) corresponds to the (111) plane of a cubic phase structure. The XRD patterns consistently exhibit a pronounced orientation along the [111] direction, which is indicative of the zinc-blende crystal structure. The obtained results were compared to the JCPDS card 75-2086 (cubic) for CdTe [23]. The situation is reversed when it comes to the width of the peak. The observed phenomenon can be ascribed to the growth of crystallites characterized by larger dimensions, which can be attributed to enhanced atomic mobility.

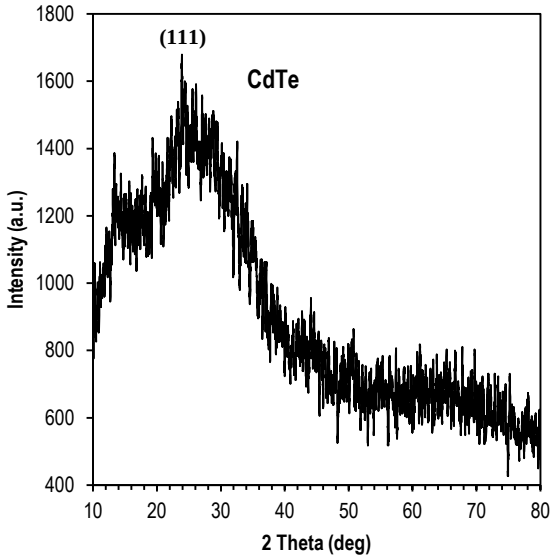

Fig. (5) XRD pattern of CdTe thin film prepared in this work

The parameters determined by XRD investigations have been displayed in table (1). The determination of the crystallite size (D) in the samples was performed using the Debye-Scherrer formula, and the obtained values are presented in table (1)

$$D_{ave} = \frac{0.9\lambda}{\beta cos\theta} \quad (1)$$

where β is the full-width at half maximum (FWHM), which is determined throughout the measurement of radial angles

The microstrain (η) can be calculated using the following equation [23]

$$\eta = \frac{\beta cos\theta}{4} \quad (2)$$

The density of the dislocation abstractions is the number of lines that take off the unit of area in that crystal. This is the ratio between the total length of all lines of extraction and the volume of crystal (Williamson and Smallmans) [24]:

$$\delta = \frac{1}{D_{ave}^2} \quad (3)$$

Table (1) Structural parameters of CdTe QDs

2θ (deg)	FWHM (deg)	hkl plane	D (nm)	η	σ (line/m²)
23.9	0.5	(111)	16.15	21.44	38.32

The utilization of AFM for surface topology analysis provides a means to obtain microscopic details regarding the surface structure of thin films. This technique enables the generation of topographic representations that accurately represent the surface relief [25]. In this study, AFM was utilized to observe and analyze the topographical features of the surface. Figure (6) illustrates the surface topography of the CdTe material, which was synthesized through the process of laser ablation in liquid and subsequently deposited onto a glass substrate. The average size measures approximately 8.42 nm, while the root mean square (RMS) values for roughness are estimated to be around 18.95 nm and 2.25 nm, accordingly. The homogeneity and uniformity of the surface can be inferred from the significant differences in the average and root mean square values of the roughness.

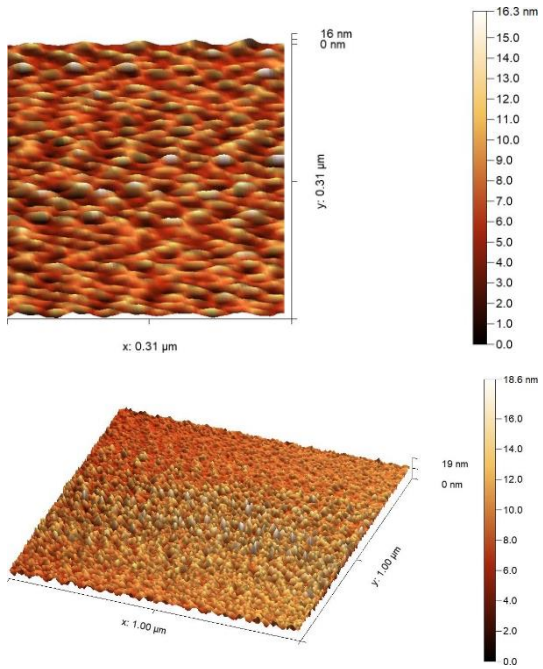

Fig. (6) 2D and 3D AFM images for CdTe thin film

The FTIR characterization of the sample, as displayed in Fig. (7), reveals the presence of characteristic stretching vibrations associated with O–H bonds, which occur within the spectral range of

3.447 cm^{-1}. The intense peak observed at a wavenumber of 1644 cm^{-1} may correspond to the stretching vibrations associated with the carbonyl group (C=O). The absorption spectra of the CdTe quantum dots (QDs) were detected at approximately 744 cm^{-1}, indicating the occurrence of bond formation between Cd^{+2} and Te^{-2}, thereby validating the formation of CdTe QDs. A novel spectral feature was detected at approximately 1137 cm^{-1}, attributed to the vibrational stretching of carbonyl groups (C–O). The observation suggests the potential existence of carbon dioxide within the laboratory [26-28].

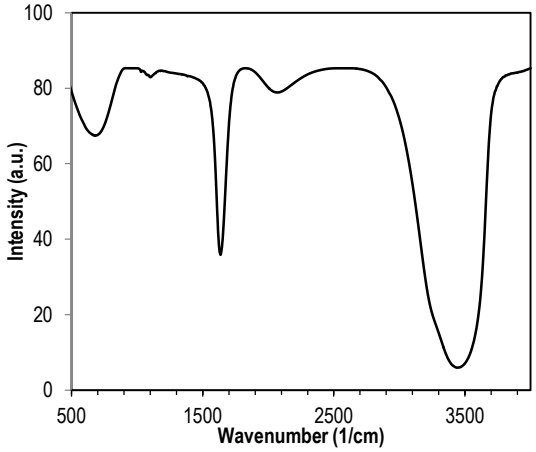

Fig. (7) FTIR spectrum of pure CdTe QDS

The interest pertains to UV-visible absorption spectra where an investigation of colloidal CdTe quantum dots (QDs) was conducted, as displayed in Fig. (8). The sample shows a well-pronounced absorption maximum. The absorption spectrum exhibits an absorption band edge at approximately 200 nm. The calculated band gap is about 3.1 eV. The band gap values of CdTe quantum dots exhibit a significant increase in comparison to bulk CdTe, as a result of the quantum confinement effect [29,30]. This effect is responsible for the observed high band gap values.

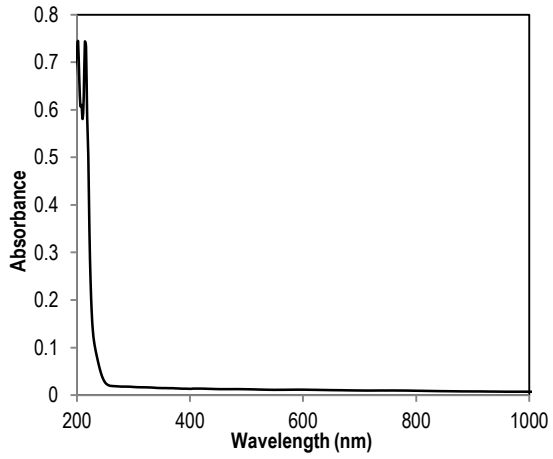

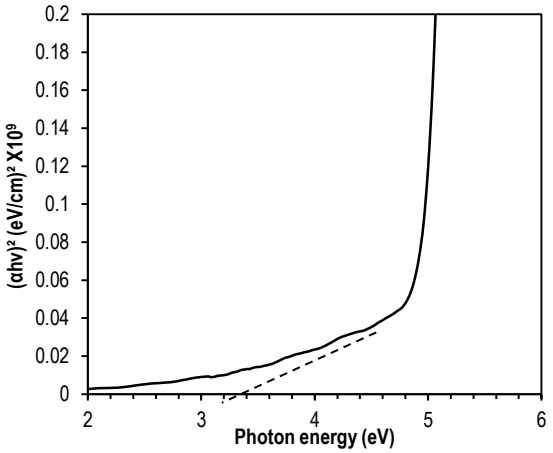

Fig. (8) (a) UV-Vis absorption spectrum of CdTe quantum dots (QDs) and (b) the relationship between $(\alpha h\nu)^2$ vs and photon energy

One of the most crucial factors that affect photodetector is (I-V) in dark and bight To determine the type of hybrid junction prepared and to clarify the reasons for generating photocurrent in reverse bias, in other words, the ability of the hybrid junction to generate an electron-hole. Figure (9) displays the current's fluctuation versus the applied voltage for both forward and reverse biasing throughout the device, in both light and dark conditions.

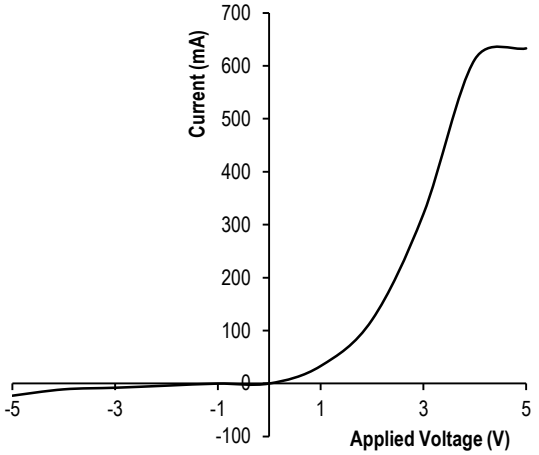

Fig. (9) Current-voltage (I-V) characteristics in dark for both reverse and forward for Ag/CdTe QDs/PS /c-Si/Ag

As observed in Fig. (6), the device Ag/CdTe Q_{Ds}/PS /c-Si/Ag was fabricated using pulsed laser ablation, from the information presented in Fig. (10), it is evident that the observed current value of Ag/CdTe Q_{Ds}/PS /c-Si/Ag structure may be attributed to the defects that have been induced on the surface of the deposited CdTe QDs on the cleaned (porous silicon). The observed phenomenon can be attributed to the presence of forward dark current resulting from the majority carriers, as well as the injection of majority carriers caused by the applied voltage. These factors collectively contribute to a decrease in the built-in potential, as well as a reduction in the depletion layer. Therefore, it is possible to observe three distinct regimes.

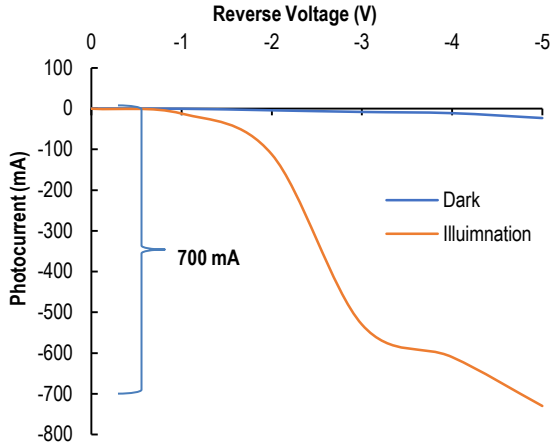

Fig. (10) Current-voltage (I-V) characteristic of the Ag/CdTe QDs/PS /c-Si/Ag under both forward and reverse bias conditions while being subjected to illumination

The first regime corresponds to the recombination current, where the concentration of the generated current exceeds the intrinsic concentration (n_i), resulting in $np > n_i^2$ and leading to the recombination process [31]. In the context of higher voltages, it was observed that the bending region, this is the second regime exhibited variation in response to variations in the series resistance. In the context of reverse current behavior, a crucial parameter that distinguishes diodes from one another is the "dark saturation current" (I_0). I_0 is a measurement of the amount of recombination that occurs in a device. Larger recombination in a diode will result in a larger I_0. This phenomenon demonstrates the generation of electron-hole pairs under conditions of low biasing. Conversely, under high reverse voltage, the minority carriers may undergo a reverse transition across the surface layer of the junction [32,33]. The experimental results indicate that the photocurrent of the Ag/CdTe QDs/PS /c-Si/Ag device was measured to be 700 mA when a voltage of -5V was applied. This photocurrent is influenced by the morphology and structural properties of the PSi-layer, including parameters such as layer thickness and porosity, as depicted in Fig. (7).

The investigation of spectral responsivity in structures is conducted within the wavelength range of 400-900nm, utilizing a 5V bias. The calculation of spectral responsivity is performed using the equation (4) [30]:

$$R_{\lambda} = I_{Ph} / P_{(A/W)} \quad (4)$$

where I_{ph} represents the photocurrent, while P denotes the input power

The structure referred to as Ag/CdTe QDs/PS/c-Si/Ag comprises of two heterojunctions. The initial heterojunction exists between the CdTe layer and porous silicon (CdTe/PSi), while the subsequent heterojunction is formed between the porous silicon layer and (substrate) crystalline silicon (PSi/Si). Consequently, there are two depletions zones in the Ag/CdTe QDs/PS/c-Si/Ag. The spectral responsivity of the Ag/CdTe QDs/PS/c-Si/Ag structures is plotted as a function of wavelength displays in Fig. (11). The curve's spectral responsivity is composed of a single peak of the response. The first peak is due to the absorption edge of CdTe nanoparticles at 700 nm, and the second area can be attributed to the absorption edge of porous silicon occurring at a wavelength of 750nm. This peak reflects the superposition of the two vertices.

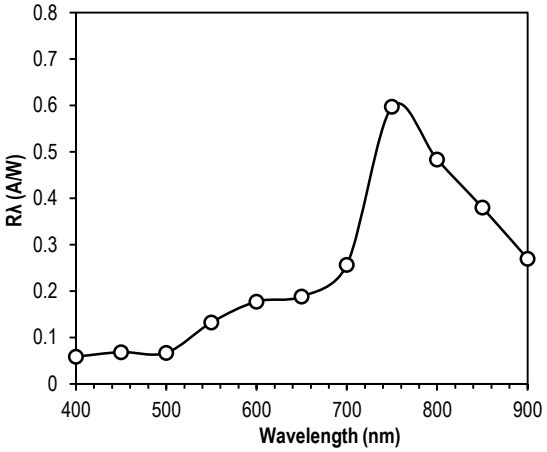

Fig. (11) Spectral responsivity of CdTe/PSi/n-Si photodetectors as a function of wavelength

4. Conclusion

In conclusion, it can be seen that the aforementioned points support the notion that the topic at hand is deserving of further investigation and analysis. A nanostructure heterojunction photodetector, consisting of CdTe and PSi materials, was successfully fabricated through the employment of pulsed laser ablation in water (PLAL) technique and photoelectrochemical etching respectively. The spectral responsivity of the photodetector is approximately 0.65 A/W. This be attributed to the enhancement of light absorption, the increase in depletion width and diffusion length, the surface defect states were minimized, or the potential approach to enhance the carrier collection efficiency is through an increase in its value.

References

[1] V. Dzhagan et al., "Phonon Raman spectra of colloidal CdTe nanocrystals: effect of size, non-stoichiometry and ligand exchange", *Nanoscale Res. Lett.*, 6 (2011) 79.

[2] J.J. Loferski, "Theoretical considerations governing the choice of the optimum semiconductor for photovoltaic solar energy conversion", *J. Appl. Phys.*, 27 (1956) 777.

[3] O.A. Hammadi et al., "Electrical and spectral characterization of CdS/Si heterojunction prepared by plasma-induced bonding", *Opt. Quantum Electron.*, 48(8) (2016) 375-381.

[4] N.E. Naji et al., "Characterization of CdSe/Si Heterostructures Synthesized by Plasma-Induced

Bonding Technique", *Iraqi J. Appl. Phys.*, 18(1) (2022) 21-26.
[5] T. Takahashi, K. Nakazawa, S. Watanabe, G. Sato, T. Mitani, et al., *SLAC-PUB*- 11147, 2005.
[6] S.H. Faisal and M.A. Hameed, "Heterojunction Solar Cell Based on Highly-Pure Nanopowders Prepared by DC Reactive Magnetron Sputtering", *Iraqi J. Appl. Phys.*, 16(3) (2020) 27-32.
[7] Z.R. Khan, M. Zulfequar and M.S. Khan, "Structural, optical, photoluminescence, dielectric and electrical studies of vacuum-evaporated CdTe thin films", *Bull. Mater. Sci.*, 35 (2012) 169–174.
[8] K.P. O'Donnell and P.G. Middleton, "Bandgaps of widegap II-VIs, temperature dependence", in: R. Bhargara (Ed.), INSPEC, Institute of Electrical Engineers, London, U.K., 1997, pp. 33–36.
[9] R.B. Bylsma et al., "Photorefractive properties of doped cadmium telluride", *Appl. Phys. Lett.*, 51 (12) (1987) 889–891.
[10] E.A. Latief, A.T. Mohi and A.N. Abd, "Effect of Natural Dye on the Spectral Response of the Heterojunction Ag/ZnO/Ps/Si/Ag for Photodetector Application", *Int. J. Nanosci.*, 22(6) (2023) 2350048.
[11] M. Hage-Ali and P. Siffert, "Growth methods of CdTe nuclear detector materials", in: T.E. Schlesinger, R.B. James (Eds.), Semiconductors for Room Temperature Nuclear Detector Applications, vol. 43, Academic Press, San Diego, CA, USA, 1995, pp. 219–257.
[12] C.J. Johnson, "Electrooptic effect in CdTe at 23.35 and 27.95 microns", *Proc. IEEE*, 56 (1968) 1719.
[13] C.J. Johnson, G.H. Sherma and R. Weil, "Far infrared measurement of the dielectric properties of GaAs and CdTe at 300 K and 8 K", *Appl. Opt.*, 8 (1969) 1667–1671.
[14] R.B. Bylsma et al., "Photorefractive properties of doped cadmium telluride", *Appl. Phys. Lett.*, 51 (12) (1987) 889.
[15] A. Milani et al., "Characterization of electro-optic shielding effect in bulk CdTe: in crystals", *J. Cryst. Growth*, 214 (2000) 913.
[16] A. Zappettini et al., "Sub-nanosecond all-optical switching in CdZnTe", *J. Cryst. Growth*, 214 (2000) 866.
[17] T.E. Schlesinger et al., "Cadmium zinc telluride and its use as a nuclear radiation detector material", *Mater. Sci. Eng.*, 32 (2001) 103.
[18] N. Yellin and S. Szapiro, "Vapor transport of nonstoichiometric CdTe in closed ampoules", *J. Cryst. Growth*, 69 (1984) 555.
[19] K. Matsune et al., "15% efficiency CdS/CdTe thin film solar cells using CdS layers doped with metal organic compounds", *Sol. Ener. Mater. Sol. Cells*, 90 (2006) 3108–3114
[20] A. Ramizy et al., *Appl. Sur.Sci.*, 257 (2011) 6112.
[21] O.A. Hamadi, "Characteristics of CdO-Si Heterostructure Produced by Plasma-Induced Bonding Technique", Proc. IMechE, Part L, J. Mater.: Design & Appl., 222 (2008) 65-71.
[22] K.A. Salman, Z. Hassan and K. Omar, *Int. J. Electrochem. Sci.*, 7 (2012) 376.
[23] F.H. Siyanaki et al., "The effect of substrate rotation rate on physical properties of cadmium telluride films prepared by a glancing angle deposition method", *Thin Solid Films*, 577 (2015) 128–133.
[24] M.A. Faraj, M.A. Jabbar and A.N. Abd , "Bismuth oxide aqueous colloidal NPS obtained by a green synthesis inhibit candida albicans", *AIP Conf. Proc.*, 2834 (2023) 090009.
[25] H. Hernandez-Contreras, C. Mejia-Garcia and G. Contreras-Puente, *Thin Solid Films*, 203 (2004) 451-452.
[26] M.S. Abd El-sadek and S. Moorthy Babu, *Curr. Appl. Phys.*, 11 (2011) 926–932.
[27] K.Z. Yahiya et al., "Optical and electrical properties of selenium-antimony heterojunction formed on silicon substrate", *Sharjah Univ. J. Pure Appl. Sci.*, 4(2) (2007) 1-11.
[28] R.H. Turki and M.A. Hameed, "Spectral and Electrical Characteristics of Nanostructured NiO/TiO_2 Heterojunction Fabricated by DC Reactive Magnetron Sputtering", *Iraqi J. Appl. Phys.*, 16(3) (2020) 39-42.
[29] N.F. Habubi et al., "Improving the photoresponse of porous silicon for solar cell applications by embedding of CdTe nanoparticles", *Indian J. Pure Appl. Phys.*, 53 (2015) 718.
[30] O.A. Hamadi, "Characterization of SiC/Si Heterojunction Fabricated by Plasma-Induced Growth of Nanostructured Silicon Carbide Layer on Silicon Surface", *Iraqi J. Appl. Phys.*, 12(2) (2016) 9-13.
[31] B.J. Alwan, A.N. Abd and N.H. Zaki, "Inhibitory effect of lithium oxide nanoparticle produced by green synthesis method", *AIP Conf. Proc.*, 2834 (2003) 090012.
[32] A.N. Abd, "Improved photoresponse of porous silicon photodetectors by embedding CdS nanoparticles", *World Sci. News*, 19 (2015) 32.
[33] O.A. Hamadi, "Effect of Annealing on the Electrical Characteristics of CdO-Si Heterostructure Produced by Plasma-Induced Bonding Technique", Iraqi J. Appl. Phys., 4(3) (2008) 34-37.

Proceedings of 5th International Specialized Conference of Education College on Physics and Applied Sciences (5thICECAS24), 22-23 April 2024

Effect of Yttrium Doping on Structural and Microscopic Characteristics of Barium Titanate

Musaab R. Feza'a
Abbas K. Saadon

Department of Physics, College of Education for Pure Science - Ibn Al-Haitham, University of Baghdad, Baghdad, IRAQ

In this research, barium titanate ($BaTiO_3$) (BT) prepared doped with yttrium ion $Ba_{1-x}Y_xTiO_3$ (with x= 0, 5, 10, 15, 20, 30 wt.%) by solid-state reactions method. Samples were pressed into pellets and sintered at 1200°C for 2 hours in air. The structural and microstructural characteristics of samples were investigated. The formation of a tetragonal phase of BT doped with Y^{3+} was revealed and it became less clear with increasing Y^{3+} concentration. Average crystallite size was 43nm at x= 0 and decreased with increasing Y^{3+} to reach 21nm at x=5 wt.%, and then it starts to fluctuate. Adding Y^{3+} to BT changes density 3.52 to 3.09 g/cm^3 for x=15-30 wt.% as well as porosity increased to reach 47%. Average grain size increases with increasing Y^{3+} concentration to be 0.199–0.361µm.

Keywords: Barium titanate; Yttrium; X-ray diffraction; Microscopic properties
Received: 19 January 2024; Revised: 4 March 2024; Accepted: 4 April 2024

1. Introduction

Barium titanate ($BaTiO_3$) is interesting ceramic complex. It has good piezoelectric and ferroelectric properties at Curie temperature, that's used in electric and electronic devices because it can transfer from paraelectric to ferroelectric [1,2]. $BaTiO_3$ is used in various industrial applications such as capacity and multi-layers alternative sources [3,4]. Furthermore, $BaTiO_3$ is used in many applications that need high density materials with good dielectric constant and low loss factor [5]. The ferroelectric ceramic $BaTiO_3$ has more interesting properties because it contains one oxide material. As well, $BaTiO_3$ has tetragonal symmetry with natural molarity. To reach maximum dielectric $BaTiO_3$, transport at room temperatures by doping materials on the $BaTiO_3$ dielectric is very sensitive to temperature, field intensity and frequency [6-8]. The $BaTiO_3$ powder is doped with many materials to produce materials with good performance, grain size and electrical properties as ceramic materials. In addition, the dielectric properties of $BaTiO_3$ depend largely on grain growth during sintering as well as on percentage concentration of doping material [9-11]. One of the main characteristic of $BaTiO_3$ ceramic is good homogeneity with suitable added material and sintering time [10-14]. Yttrium oxide (Y_2O_3) is a dopant material using to produce low-cost multilayer ceramic capacitor [15]. Y^{+3} was used with barium to improve the dielectric properties with target conductivity and permittivity. On the other hand, it enhances the thermal stability of $BaTiO_3$ and exchanges the lattice parameters and hence causes shifting in Curie temperature. Y^{+3} is used to decrease the sintering temperature of $BaTiO_3$ due to high melting temperature of Y_2O_3 [16]. The radius of Y^{+3} ion is about 0.9Å, so, it lies between 1.61Å of Ba^{+2} and 0.605Å of Ti^{4+}. Therefore, the Y^{3+} may be used to replace Ba^{2+} or Ti^{4+} in the $BaTiO_3$ lattice. This indicates why Y^{3+} may enhance the life of multi-layer ceramic capacitor. Additionally, dielectric properties depend on the doping materials, preparing method, microscopic structure of $BaTiO_3$, melting point and electrical properties of doping materials [17]. Addition of Y_2O_3 with different concentrations has reasonable effect on the structural, morphological, electrical and optical characteristic of $BaTiO_3$. Increasing the concentration of Y_2O_3 used for doping of $BaTio_3$ causes to decrease average grain size.

In this work, pure barium titanate (BT) doped with yttrium ions (Y^{3+}) was preparing at different concentrations and used a reaction method of solid state. To understand the role of yttrium addition, the prepared samples are analyzed and studied the compositional and microstructural properties of the preparing samples.

2. Experimental methods

To prepare $BaTiO_3$, $BaCO_3$ (99.5%), TiO_2 (99.9%) and Y_2O_3 (99.9%) were used for the solid state reaction method according to chemical equilibrium equation

$$BaCO_3 + TiO_2 \rightarrow BaTiO_3 + CO_2$$

Next, the materials were mixed and grinded for 5 hours. The mixture was placed in alumina pot and fired at 1200°C for 2 hours in air using electric oven to produce $BaTiO_3$. The $BatiO_3$ powder was produced with average grain size of 1 µm. The powder was mixed with Y_2O_3 using for 4 hours in

ethanol, then dried at 80°C for 5 hours to leave the powder without ethanol. The product was mixed with PVA to form discs under pressure of 5 tons with diameters of 15mm and thickness of 3mm. these samples were sintered at 1250°C for 2 hours in air.

X-ray diffraction (XRD) was used to study the crystalline structure of all prepared samples (pure and Y_2O_5-doped $BaTiO_3$) using x-ray diffractometer with Cu-target (λ=1.54Å) in the diffraction angle 2θ range of 10°-80° with scan velocity (8°/min). Data of crystalline structure of $BaTiO_3$ were obtained from ICDD no. 01-074-1958. The microstructure of pure and doped $BaTiO_3$ powders was evaluated using an INSPECT scanning electron microscope (SEM).

3. Results and Discussion

XRD patterns of pure $BaTiO_3$, pure Y_2O_3 and $BaTiO_3$ doped with Y^{+3} ions at different concentrations ($Ba_{1-x}Y_xTiO_3$) (x=0, 5, 10, 15, 20, 30 wt.%) are shown in figures (1) and (2). Results show that the prepared samples are perovskite, and diffraction peaks are appeared in (001), (101), (111), (002), (200) and (210) planes, which correspond to 2θ of 22.34°, 31.72°, 39.07°, 45.80°, 45.53° and 50.92°, respectively. The diffraction peaks were matched to the JCPDS no. 01-0740-1958, which confirms that the structure is tetragonal. All samples except x=30 wt.% show pseudo-cubic structure, which agree with reference [12]. The melting of yttrium in $BiTiO_3$ powder lead to limit the tetragonal structure of $BaTiO_3$ according to [16]. The ferroelectricity of $BaTiO_3$ decreases strongly when the grain size is less than 7µm, and the structure changes from tetragonal into pseudo-cubic. In general phase transitions were a combined of tetragonal and cubic structure, where a pseudo-cubic has been observed, in agreement with reference [16]. The XRD pattern of $BaTiO_3$ powder indicates a tetragonal structure while $BaTiO_3$ doped with Y^{3+} ions showed a decrease in the tetragonality structure at high concentration of Y^{3+}, and it matches with reference [20]. In addition, it was found that diffraction pattern of $BaTiO_3$ powder was doped with Y^{3+} ion showed a double peak at about 45°, which indicates the presence of a tetragonal ferroelectric phase with crystal planes of (002) and (200). This indicates a distortion and shift towards higher angles which causes an increase in the lattice parameters.

This confirms the incorporation of Y^{3+} ions in the sites of barium (Ba) in $BaTiO_3$ lattice, which leads to increase the size of crystal lattice [20]. The parameters of the tetragonal structure were calculated from the values of miller indices (hkl) and the interplanar spacing (d) using the relation [21]:

$$\frac{1}{d2} = \frac{h2+k2}{a2} + \frac{l2}{c2} \quad (1)$$

The average grain size (D) of the prepared samples was measured for peaks on (002) and (200) planes using the Debye-Scherrer formula [21,22]:

$$D = \frac{0.9\lambda}{\beta cos\theta} \quad (2)$$

where λ=1.54Å is x-ray wavelength, β is the full-width at half-maximum (FWHM), and θ is Bragg's diffraction angle

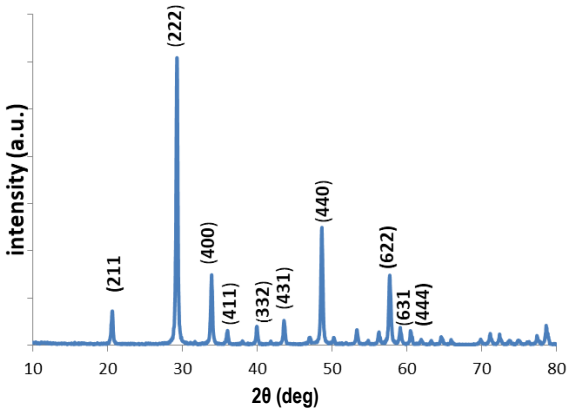

Fig. (1) XRD pattern of Y_2O_3

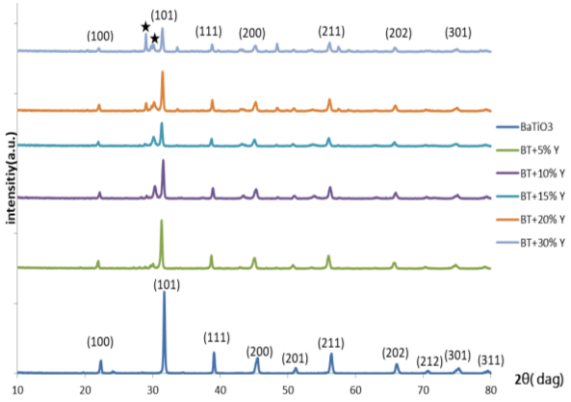

Fig. (2) XRD patterns of yttrium-doped $BaTiO_3$ ceramics

The crystal lattice parameters (a, b, and c), as well as crystallite size (D_{sh}), were calculated using equations (1) and (2) and shown in table (1). The crystallite size of $BaTiO_3$ decreases with Y^{3+} addition up to x=5 wt.%, after which the crystallite size increases with increasing yttrium concentration up to 10 wt.%, and the unit cell size also increases. This confirms that when sintering at relatively low temperatures (1200°C), the lattice parameters of the tetragonal structure are affected by defects and impurities [23,24]. The XRD analysis indicated the formation of the perovskite phase, improved crystallinity of yttrium-doped $BaTiO_3$, and change in the lattice parameter (c). It is clear evident of the incorporation of the Y^{3+} ions into Ba sites, and the Y^{3+} ions can replace Ti sites [20,25]. With the formation of oxygen vacancies, grains grow and hence grain boundaries are diffused depending on impurities, sintering temperature and crystal orientation. The unit cell size is calculated by multiplying ($a^2.c$), as shown in table (1). Additionally, incorporation of Y^{3+} ions into $BaTiO_3$

lattice enhances the tetragonal structure in $BaTiO_3$ matrix, which increases the unit cell size from 63.39Å^3 at x=0 to 66.069Å^3 at x=30%. The lattice parameters (a,c) were increasing with increasing Y^{3+} concentration due to the difference in the ionic radii and electronic density of the Y^{3+}. This type of expansion was observed when zirconium was added to the matrix of tetragonal structure of $BaTiO_3$ [26,27]. The strain of the crystal lattice causes an expansion for diffraction peaks of the material as a result of defects and impurities, depending on Williamson-Hall formula [26].

$$W_{hkl} = W_{crystal} + W_{strain} \quad (3)$$

where W_{hkl} is the intensity of the FWHM, which is related to the strain of crystal lattice and crystalline size, and W_{strain} is the strain of the crystal lattice that causes the expansion of the diffraction peaks. It is calculated by [26]:

$$W_{strain} = 4\varepsilon \tan\theta \quad (4)$$

Substituting this into Eq. (3), we get

$$W_{hkl}\cos\theta = \frac{0.9\lambda}{D} + 4\varepsilon \sin\theta \quad (5)$$

The W-H plotted of $W_{hkl}\cos\theta$ versus $4\sin\theta$ for $BaTiO_3$ doped with Y^{3+} are shown in Fig. (3). The average crystallite size and the lattice strain were calculated using the slope and y-interception of linear part. The crystallite size and crystal lattice strain were obtained from equations (4) and (5), and the values are shown in table (1). Debye-Scherrer analysis and Williamson Hall showed that the crystallite size and crystal lattice strain of the prepared samples follow the same trend [26].

The tolerance factor Goldschmidt (t) is a geometric factor used as an indicator of the stability and deformation of crystalline structure, that is, to describe the perovskite structure ABO_3, and because a large different in the ionic radii of ions between A and B sites, this makes the perovskite structure ABO_3 more stable and it is much more difficult for ions to transfer to sites and producing corresponding drift resistance. One of good characteristics of perovskite structure was its strongest abilities to accept additions in both A-site and B-site. The first description of the perovskite tolerance factor (t) was given by Goldschmidt in 1926. The ABO_3 expression was given as [28,31]

$$t = \frac{(r_A + r_O)}{\sqrt{2}\,(r_B + r_O)} \quad (6)$$

where r_A, r_O and r_B are ionic radii of cation A site, oxygen ion, and cation B-site, respectively

In addition, Goldschmidt proposal is a formula that describes stability of perovskite structure. The tolerance factor (t) for a stable perovskite structure ranges within $0.77 \le t \le 1.10$, and was found for $BaTiO_3$ ceramic in our work is 0.992. This indicates that there is a slight distortion in the crystal structure as

r_A (Ba^{2+}) = 1.61Å, r_B (Ti^{4+}) = 0.605Å, r_O (O^{2-}) = 1.4Å, when yttrium (Y^{3+}) [r(Y^{3+}) = 0.9Å] is added to $BaTiO_3$, it leads to a decrease in the tolerance factor (t), whose values for pure $BaTiO_3$ and Y^{3+}-doped $BaTiO_3$ are shown in table (2), which ranges from 0.992 to 1.007. This indicates that A and B sites are occupied by largest and smallest ions, and the sites with difference division would be occupied by the medium ions. This use of tolerance factor to evaluate ions at different locations was only a qualitative measures [29].

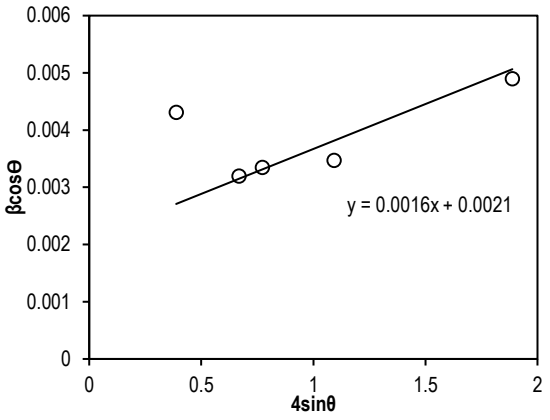

$BaTiO_3$

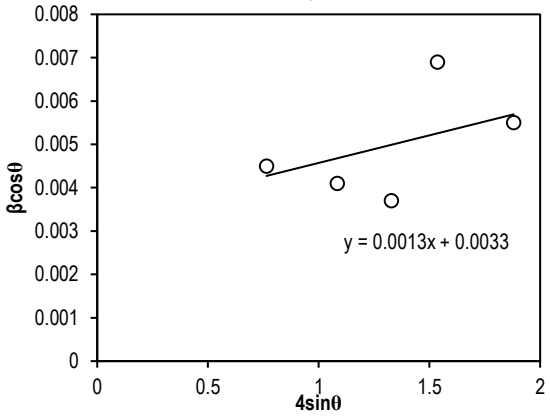

5 wt.% Y^{3+}-doped $BaTiO_3$

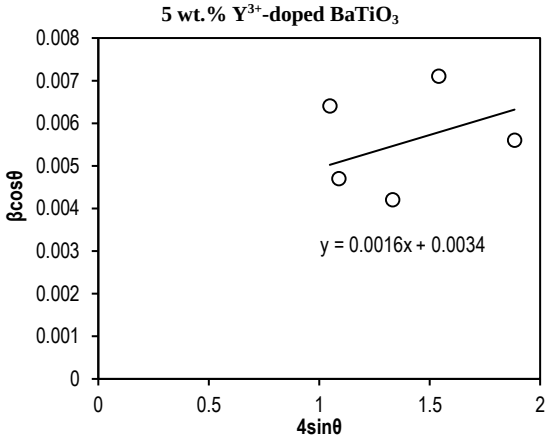

10 wt.% Y^{3+}-doped $BaTiO_3$

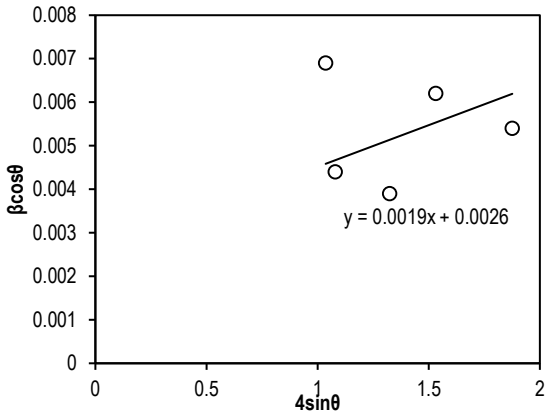

15 wt.% Y^{3+}-doped $BaTiO_3$

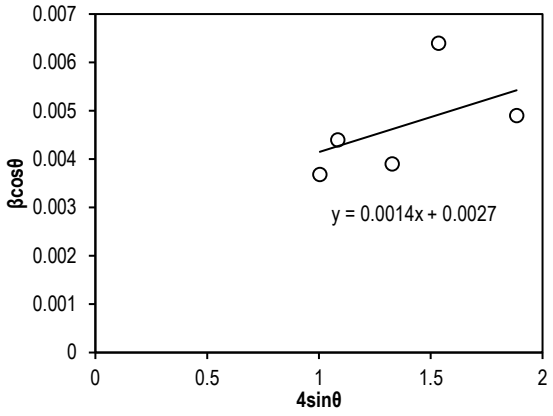

20 wt.% Y^{3+}-doped $BaTiO_3$

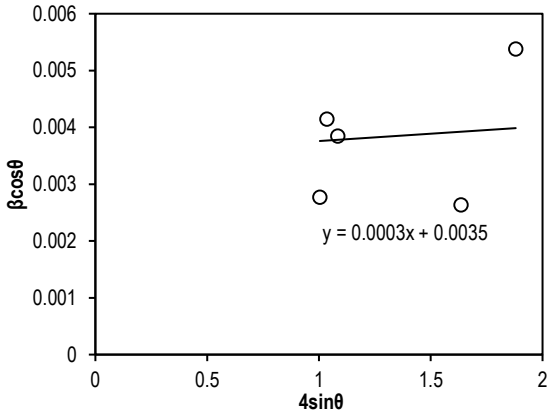

30 wt.% Y^{3+}-doped $BaTiO_3$

Fig. (3) W-H plots of $BaTiO_3$ ceramics

Figure (4) shows the microstructure of pure $BaTiO_3$, Y^{3+}-doped $BaTiO_3$ and sintered at 1250°C for 2 hours. The SEM images showed the surface morphology of the samples with a hexagonal structure, good facets, and grains with distinct boundaries, those are clustered.

From Fig. (4a), it can be noticed that grains are agglomerated, but figures (4b) and (4c) refer to the mechanism of layer formation. The average grain size for pure $BaTiO_3$ ceramic is 0.199µm, while for the Y^{3+}-doped $BaTiO_3$ samples (x=20, 30 wt.%), the average grain size increased to 0.336µm at x=20 wt.%, and 0.361µm at x=30 wt.%, as shown in figures (4a,b,c) and table (2). This is consistent with the results of references [30,32]. The effects of liquid-phase sintering, grain boundary diffusion and defect reaction, which plays an important role in enhancing the grain growth kinetics, are clear. The highest value for the average grain size was found to be 0.361µm at x=30 wt.%, and the porosity is also high.

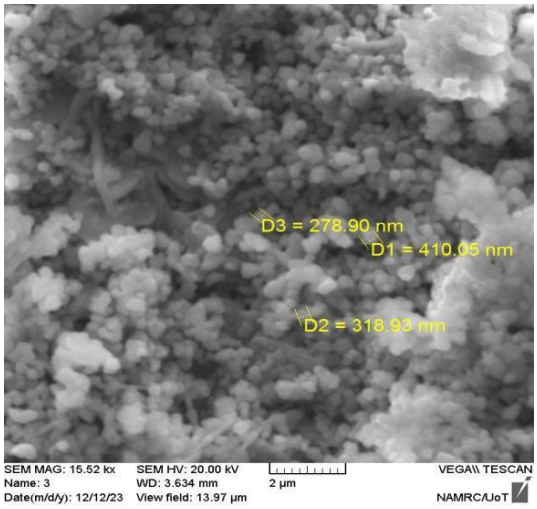

(a)

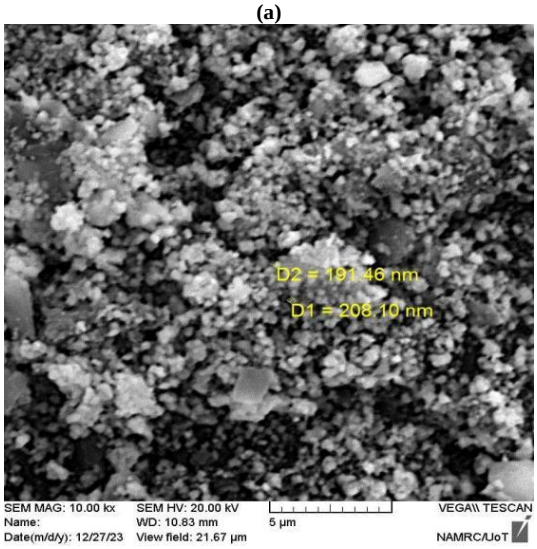

(b)

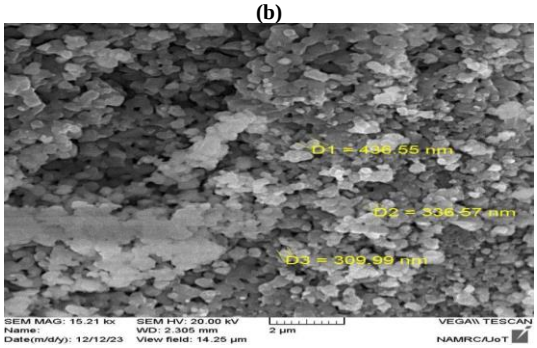

(c)

Fig. (4) SEM of yttrium-doped $BaTiO_3$ (a) x=0, (b) x=20%, and (c) x=30%

4. Conclusion

Barium titanate ($BaTiO_3$) ceramics were successfully prepared and doped with yttrium (Y^{3+}) ions at different concentrations (0, 5, 10, 15, 20, and

30 wt.%) using solid state reaction method. The effect of Y^{3+} ions on the microstructure and structural properties of the prepared samples was revealed. The structure of the prepared samples is tetragonal and pseudo-cubic. The crystallite size of prepared $BaTiO_3$ samples was decreased with increasing yttrium ions concentration up to 5 wt.% after which the crystallite size increased and good grain growth was observed for the doped samples. The average grain size of the doped samples was comparable to $BaTiO_3$ ceramic (0.199-0.365µm).

References

[1] M. Biglar et al., "Optimal configuration of Piezoelectric sensors and actuators for active vibration control of a plate using a genetic algorithm", *Acta Mech.*, 226(10) (2015) 3462-3462.

[2] M.M. Vijatovic, J.D Bobic and B.D. Stojanovic, "History and challenges of barium titanate", Pt. 11 *Sci. Sinter.*, 40 (2008) 235-252.

[3] C. Miot, C. Proust and E. Husson, "Dense ceramics of $BaTiO_3$ produced from powders prepared by a chemical process", *J. Euro. Ceram. Soc.*, 15 (1995) 11631170.

[4] C.F. Kao and W.D. Yang, "Preparation of barium titanate strontium titanate Powder from citrate precursor", *Appl. Organomet. Chem.*, 13 (1999) 370-383.

[5] B. Ertug, "The overview of the electrical Properties of barium titanate", *Amer. J. Eng. Res.*, 2(8) (2013) 1-7.

[6] K. Uchino, **"Ferroelectric Device"**, Marcel Dekker, Inc. (New York, 2000).

[7] W. Heywang and H. Thomann, "Positive temperature coefficient resistor in electronic ceramics", London and New York (1991).

[8] D. Hennings "Barium titanate based ceramics materials for dielectric use", *Int. J. High Technol. Ceram.*, 3 (1987) 91-111.

[9] M.N. Rahaman and R. Manalert, "Grain boundary mobility of $BaTiO_3$ doped with aliovalent cations", *J. Euro. Ceram. Soc.*, 18 (1998) 1063-1071.

[10] S.-K. Chiang, W.-E. Lee and D.W. Ready, "Core-shell structure in doped $BaTiO_3$", *Am. Ceram. Bull.*, 66 (1987) 1230.

[11] M. Kohn, "Preparation of small-grain and large grained ceramics from Nb-doped $BaTiO_3$", *J. Am. Ceram. Soc.*, 54 (1971) 452-454.

[12] S. Islam et al., "Effect of Yttrium doping on structural, electrical and optical properties of barium titanate", *Ceramics*, 8 (2022) el0529.

[13] W. Xuefe et al., "Effect of Yttrium (Y) substitution on the structure and dielectric properties of $BaTiO_3$", 49(69) (2023) 9042-9051.

[14] D. Mehraj et al., "Probing of dielectric and ferroelectric Properties of yttrium doped barium titanate ceramics", 7(4) (2018).

[15] A. Alshoaibi et al., "Insights into the Impact of Yttrium Doping at the Ba and Ti sites of $BaTiO_3$ on the electron structures and optical properties", *A first principles study* (2020).

[16] K. Park et al., "Doping behaviors of dysprosium yttrium and holmium in $BaTiO_3$ ceramics", *J. Euro. Ceram. Soc.*, 29 (2009).

[17] C. Kim et al., "Role of yttrium and magnesium in the formation of core-shell structure of $BeTiO_3$ grains in MLCG", *J. Fur. Cavam.*, 50(C28) (2008) 1213-1219.

[18] A.K. Saadon, "The effect of Silica SiO_2, on the Dielectric and Physical properties of Mn-Ni Ferrite", *Ibn Al-Haitham J. Pure Appl. Sci.*, 25(3) (2012) 188-191.

[19] A.K. Saadon, "Studying the effect of Zirconia on some Physical properties of Porcelain", *Ibn Al-Haitham J. Pure Appl. Sci.*, 29(3) (2016) 46-53.

[20] M. Tihtih et al., "Role of A-site (Sr), B-site (Y), and A,B sites (Sr,Y) substitution in Lead-free $BaTiO_3$ ceramic compounds: structural, optical, microstructure, mechanical and Thermal conductivity Properties", *Ceram. Int.*, 49 (2023) 1947-1959.

[21] A.K. Saodon, "Study of the effect of eO_2 on the structural properties of cadmium ferrites", *Ener. Proc.*, 157 (2019) 561-567.

[22] A.K. Saadon, A.M. Mhayyal and K.A. Jasim, "Effect of $BaTiO_3$ mixture on the structural electrical properties and morphology for PET/$BaTiO_3$ composites", *AIP Conf. Proc.*, 2307(1) (2020) 020014.

[23] G. Qi et al., "Yttrium Doping Behavior in $BaTiO_3$ Ceramics at different Sintered Temperatures", *Mater. Chem. Phys.*, 82 (2003) 423-427.

[24] D.H. Jumaah and A.K. Saadon, "Prepared and measuring the structural and dielectric properties of $PbTiO_3$ and $PbZrO_3$", *AIP Conf. Proc.*, 2123(1) (2019) 020056.

[25] A.K. Saadon, "Preparation and study of some Electrical properties of Mn-Ni $FeZO_4$", *Ibn Al-Haitham J. Pure Appl. Sci.*, 26(3) (2013) 69-76.

[26] M. Reda, E.L. Dek and S.I. Arman, "Improvement of ferroelectric properties via Zr Doping in $BaTiO_3$ Nanoparticles", *Mater. Sci. Mater. Electron.*, 33 (2022) 16753-16776.

[27] K.A. Jasim, "Synthesis and study the structural, and electrical and mechanical properties of high temperature superconductor $Tl_{0.5}Pb_{0.5}Ba_2Ca_{u-1}Cu_{n-x}Ni_xO_{2n+3}$ substituted with nickel oxide for n=39", *Ibn Al-Haitham J. Pure Appl. Sci.*, 31(3) (2018).

[28] W.J. Choi et al., "Effect of charge compensation change on the crystal structure: Grain growth Behavior, and Dielectric Properties in the La_2O_3-doped $BaTiO_3$ system

with $MnCO_3$ addition", *J. Alloys Comp.*, 916 (2022) 165388.
[29] E. Hannachi et al., "Impact of Tin oxide on the structure Features and Radiation shielding Response of Some ABO_3 Perovskites ceramics (A=Ca, Sr, Ba, B=Ti)", *Appl. Phys. A: Mater. Sci. Process.*, 127 (2021) 970.
[30] S.N. Rahman et al., "Techno-computational and applied sciences, comparative studies of cerium and zirconium doped barium titanate", *Int. Assoc. Sci. Innov. Res.*, (2014) 15-19.
[31] R.S. Al-Khafaji and K.A. Jasim, "Dependence the microstructure specifications of earth metal lanthanum La substituted $Bi_2Ba_2CaCu_{2-x}La_xO_{8+\delta}$ on cation vacancies", *AIMS Mater. Sci.*, 8(4) (2021) 550-559.
[32] A.W. Watan et al., "Preparation and Physical Properties of Doped $CdBa_{2-x}Sr_xCa_2Cu_3O_{8+\delta}$ Compound", *Ener. Proc.*, 119 (2017) 466-472.

Table (1) Structural parameters of Y^{3+}-doped $BaTiO_3$ samples

$BaTiO_3$ sample (%)	Lattice parameters (a=b) (Å)	c (Å)	c/a	Cell volume $(Å)^3$	D_{sh}	D_{W-H}	ε_{sh} x10^3	ε_{W-H} x10^3
x=0	3.976	4.009	1.0086	63.39	43.479	66.0	3.19	1.6
X=5	4.001	4.029	1.0069	64.47	21.893	42.0	3.88	1.3
X=10	3.996	4.016	1.0050	64.14	32.065	40.8	4.32	1.6
X=15	4.032	4.024	0.9980	65.43	30.658	53.3	4.13	1.9
X=20	3.840	4.020	1.0469	59.28	27.291	51.3	4.12	1.4
X=30	4.052	4.026	0.9936	66.07	40.649	39.6	3.59	3.0

Table (2) Tolerance factor (t), bulk density (ρ_b), x-ray density (ρ_x), porosity (p), and average particle size of Y^{3+}-doped $BaTiO_3$ samples

$BaTiO_3$ sample	Tolerance factor (t)	Bulk density (ρ_b) (g/cm^3)	X-ray density (ρ_x) (g/cm^3)	Porosity p (%)	Average particle size (μm)
x=0%	0.992	3.480	6.110	43.0	0.199
x=5%	0.993	3.403	6.008	43.4	
x=10%	0.995	3.370	6.040	44.2	
x=15%	1.002	3.520	5.920	40.5	
x=20%	0.955	3.420	5.970	45.7	0.336
x=30%	1.007	3.090	5.860	47.3	0.361

Proceedings of 5th International Specialized Conference of Education College on Physics and Applied Sciences (5thICECAS24), 22-23 April 2024

Preparation of Silver Oxide Nanoparticles by *Salvia Rosmarinus* Extract for Biomedical Applications

Wedian K. Abad [1]
Hind K.K.S. Al-Whaili [2]
Ahmed N. Abd [3]

[1] *University of Technology-Iraq*
[2] *Department of Biology, College of Science, Mustansiriyah University, Baghdad, IRAQ*
[3] *Department of Physics, Faculty of Science, Mustansiriyah University, Baghdad, IRAQ*

In this study, silver oxide nanoparticles were prepared by Salvia rosmarinus extract and sliver nitrate as precursors. Result showed that silver oxide nanoparticles have polycrystalline structure and average crystallite size of 46.04nm. These nanoparticles have nearly spherical forms with varying diameters between 40 and 55nm. Spherical granules were revealed and other pyramidal-like shapes smaller than 20nm in size were also revealed. The absorption broad peak at 300-500nm confirms the formation of silver oxide nanoparticles and energy gap was 3.70eV. The vibration of Ag-O bond at 500–800 cm^{-1} was confirmed. Using the prepared silver oxide nanoparticles, from the well diffusion method (Agar well), it was found that the higher inhibition zone for Klebsiella bactrial was 28mm and for fungi was 23mm.

Keywords: Silver oxide; Nanoparticles; Antimicrobial effect; Salvia rosmarinus
Received: 19 January 2024; Revised: 4 March 2024; Accepted: 4 April 2024

1. Introduction

In an effort to develop inexpensive, environmentally benign nanostructured materials, a number of scientific, engineering, and biotechnology studies have been carried out throughout the last 20 years [1-3]. Nanostructured materials are used in many different industrial areas, such as the chemical, electrical, bio-medical, and automotive industries, due to their exceptional properties [4,5]. Their ability to interact with other molecules and catalyze processes is enhanced as a result [6,7]. Consequently, a number of metal oxide nanoparticles (MNPs) were generated. Among the many MNPs with particular uses and frequent usage are silver oxide nanoparticles have the larger band gap (2.5-3.1eV), where silver oxide is transparent in the infrared and visible regions. Despite their diminutive size, they have a large surface area [8,9]. Given how a material's physiochemical properties are impacted by its size, these nanoparticles are extremely important [10,11]. Today, the MNPs are well-known for their numerous industrial uses of applied nanotechnology, which are found in a broad variety of sectors such as textile, food, health, agriculture, and cosmetics. The global environmental pollution crisis has led to an increase in the use and prevalence of green chemistry and technology. Due to their distinctive nanostructures created using plant extracts, nanomaterials - especially atom clusters or molecules of metal and oxide - have garnered significant attention from scientific groups in recent years. Because green synthesis is simple to apply and environmentally benign, it is an improvement over physical and chemical approaches. High pressure, high temperature, high energy, and harmful chemicals are not required for this procedure. Three primary aspects of nanoparticle synthesis should be taken into account for the advancement of green chemistry: (i) solvent medium selection, (ii) environmentally friendly reducing agent selection, and (iii) nontoxic material selection for nanoparticle stabilization [12,13]. This makes using the green synthetic method for the creation of metal oxide nanoparticles more sensible. That antibacterial activity of nanoparticles relies on of size. The proper functioning of the cell membrane, including respiration and permeability, is severely disrupted by silver nanoparticles, primarily in the 1–10 nm range, adhered to its surface [14-19]. The biological synthesis of silver oxide nanoparticles using bacteria, fungi, and plants has been documented in a great deal of literature to date. These nanoparticles stabilized and reduced of metal compounds due to the reducing or antioxidant properties of the microorganisms. Plant-based materials appear to be the most promising and are appropriate for large-scale nanoparticle "Bio-synthesis". Plant components like leaves, stems, seeds, and roots are used to make silver oxide nanoparticles. Because it contains no harmful chemicals and offers natural capping agents to stabilize the nanoparticles, it is the perfect medium on which to create them. Several research works have produced silver oxide nanoparticles using various plant materials for various purposes. Silver oxide

nanoparticles (AgO NPs) were made using the Artocarpus heterophyllus (Jackfruit tree) for its antibacterial activity against dental pathogens; cubes to octapods were used to produce AgO NPs for their antibacterial application; and Callistemon lanceolatus (Myrtaceae) aqueous leaf extract was used to produce AgO NPs [20-22]. The waste part of mango peels was used to synthesize AgO NPs [23, 24]. Garcinia mangostana fruit extract was used to synthesize AgO NPs for antibacterial and antioxidant applications [22]. Carica papaya root extract was used to synthesize AgO NPs [22]; and Ficus benghalensis prop root extract (FBPRE) was used to synthesize AgO NPs in an environmentally friendly manner. Salvia rosmarinus was used in this study to produce AgO NPs. The mint family includes Rosmarinus officinalis L. (Family: Lamiaceae), which is usually known as rosemary. Numerous assertions have been made regarding the medicinal properties of rosemary, such as its antibacterial and antioxidant properties [22,23]. Its effectiveness as a chemopreventive drug and antimutagenic is well acknowledged [24]. The plant extract is a beneficial natural feed component since it has also been demonstrated to have anti-carcinogenic, cognitive-improving, and some glucose-lowering properties [24]. The aim of this study preparation of silver oxide using rosemary extract and evaluates the effectiveness against microbial.

2. Experimental Part

The rosemary was bought from the local market in November 2023. In the first step, about 20g of leaves was collected and thoroughly cleaned with distilled water to get rid of dust, then it was dried and grinded to prepare rosemary powder as shown in Fig. (1).

Fig. (1) Salvia rosmarinus raw and powder

In the second step, about 2 g of the powder was mixed with 100 ml of distilled water and put on a magnetic stirrer set to 60°C for 60 min. The solution was filtered three times using cotton to remove the insoluble components in order to produce the extract. To obtain the aqueous solution of silver nitrate, about 1.69 g of $AgNO_3$ was mixed with 100 ml of distilled water at room temperature and constantly stirring for 30 min. Finally, to form silver oxide nanoparticles, 5 ml of plant extract was combined with the aqueous solution of silver nitrate (concentration 0.1M) at 70°C with magnetically agitated for 1h. Figure (2) shows the extract (left), the aqueous solution of $AgNO_3$ (middle) and AgO (right).

3. Results and Discussion

The structural characteristics of the synthesized samples were studied by x-ray diffraction (XRD) as illustrated in Fig. (3). The data were compared to the JPCDS cards 01-1164, 01-1041, and 43-1038. The average crystallite size of the Ag nanoparticles was evaluated using Scherrer's formula to be 46.04 nm. Few peaks were also seen indicating that the silver nanoparticles' surface is where the bioorganic phase crystallizes [26-32].

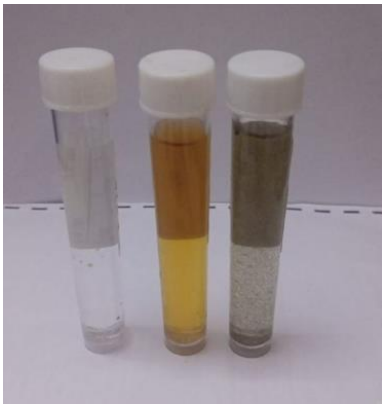

Fig. (2) Workflow steps: plant extract on the left, $AgNO_3$ solution in the middle, and AgO solution on the right

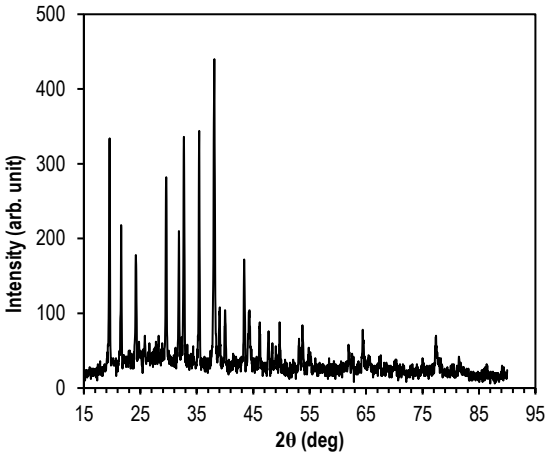

Fig. (3) XRD pattern of AgO NPs

Table (1) XRD results of Ag, AgO and Ag_2O NPs

Sample	2θ (deg)	hkl	FWHM (deg)	C.S. (nm)
Ag_2O	24.2	(220)	0.20	40.72
	38.1	(331)	0.23	36.62
	43.4	(422)	0.18	45.25
AgO	32.6	(200)	0.15	55.31
	32.7	(-111)	0.19	43.67
	35.5	(132)	0.16	52.25
	64.5	(022)	0.16	58.80
	77.4	(023)	0.26	39.19
Ag	19.5	(200)	0.19	42.53
	38.16	(111)		
	64.5	(220)		
	77.4	(311)		

The shape and particle size were determined using scanning electron microscopy (SEM), as shown in Fig. (4). The SEM image demonstrates the equal dispersion of fine grains in the material as well as approximately spherical morphologies of the AgO nanoparticles, which range in diameter from 40 to 55nm. The massive particles that are slightly larger than 100nm in size are combined to form this size because some of the particles are gathered with plant proteins.

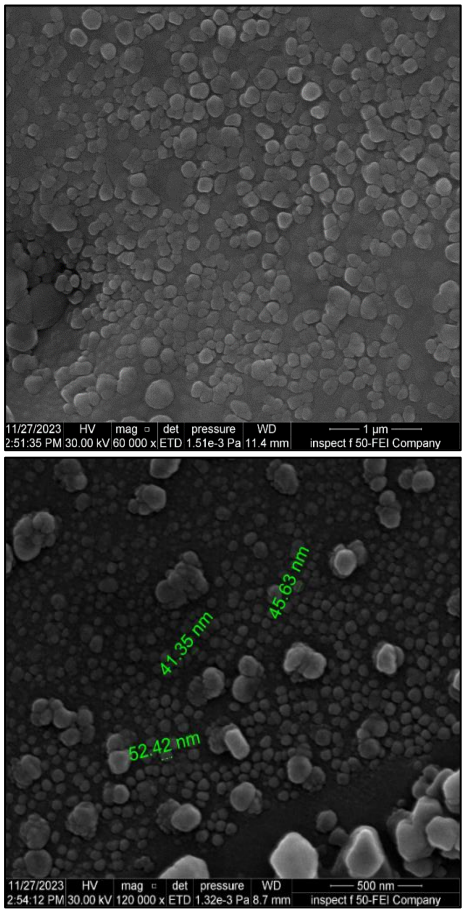

Fig. (4) SEM images of the synthesized AgO NPs

Figure (5) shows 3D imgae of the atomic force microscopy (AFM) as well as the histogram of size distribution at 80°C substrate temperatures. Different grain growth morphologies were observed in the micrographs as a result of s substrate temperature. These included grains with spherical shapes and others with less than 20nm in size that resembled pyramids. The maximum height (Sz) was 17.55nm, the mean roughness (Sa) was 1.56nm, and the root mean square (RMS) roughness (Sq) was 1.95nm.

UV-visible spectroscopy was used to determine the optical characteristics of the synthesized AgO NPs. The absorption spectrum show a peak at 300nm, as seen in Fig. (6).

The significant indication of nanoparticles' formation is the absorption in the 300-500nm range [33], where the peaks at 300, 362, and 484nm are attributed to Ag, AgO, and Ag_2O, respectively. This confirms the findings of XRD. Thus, the maximum absorption in the UV-visible spectrum, which was observed at 300nm, proved that nanoparticles have formed. The optical direct band gap of the produced nanoparticles is 3.70eV, as determined by a Tauc's plot, as shown in Fig. (7). A quantum containment effect is one reason for higher band gap value [34].

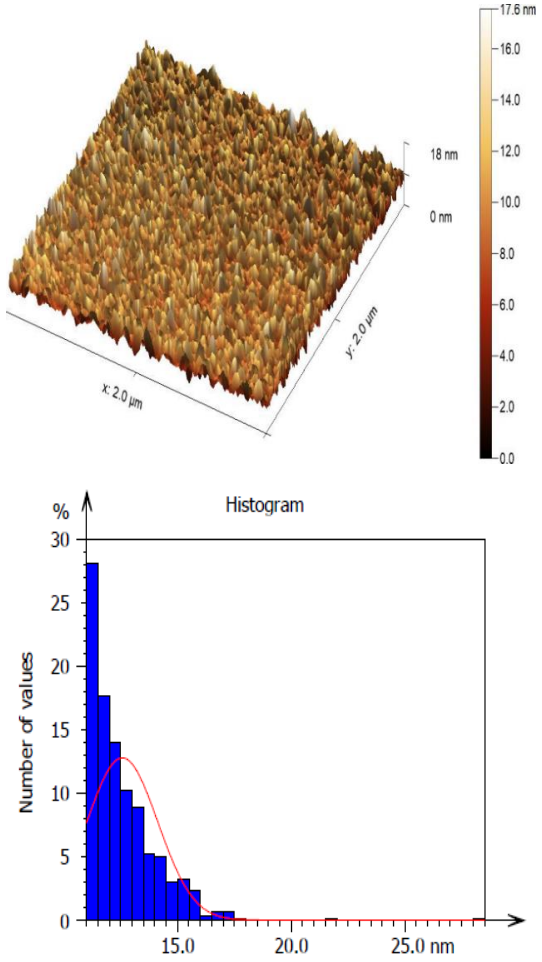

Fig. (5) 3D AFM image and size distribution of the synthesized AgO NPs

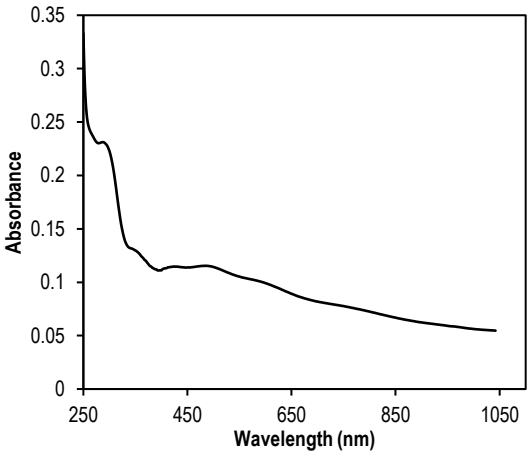

Fig. (6) Absorption spectrum of the synthesized AgO NPs

The well-diffusion technique (Agar well) was used to assess the antibacterial effectiveness of Ag/AgO NPs against Gram-positive (GP), Gram-negative (GN), and fungal (*Staphylococcus aureus, Staphylococcus epid., Klebsiella, Escherichia coli, and Candida albicans*) bacteria. Muller Hinton agar plates were seeded with 106 CFU/mL of cell density using sterilized swabs. Using a sterile gel borer, wells were cast on the agar. AgO NPs were introduced at a concentration of 100 µg/mL into the wells. Agar plates were kept in an incubator at 35°C for an entire day. The zone of inhibition that AgO NPs produced against the bacterial/fungal strains was measured in millimeters, as shown in figures (8) and (9).

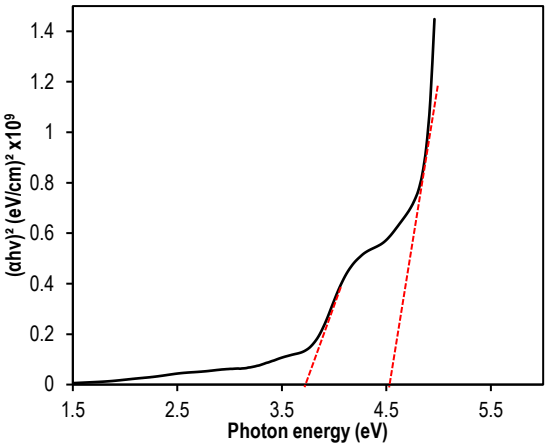

Fig. (7) Determination of energy band gap values

It is believed that once AgO NPs enter a bacterial cell, AgO and/or Ag^{+}, which have antibactericidal effects, are released. AgO NPs are also capable of producing O_2, which possesses inherent antibacterial qualities. The effects of nanoparticles are mediated via five mechanisms. The first technique includes attaching itself to the cell wall, directly damaging: cytoplasmic elements and the cell envelope [41-45]. Binding to protein SH-groups causes a functional impairment, which is the second pathway of harm. As a result, oxidative stress is generated, intracellular ROS production rises, ATP synthesis is inhibited, and the cells' energy balance is thrown off. Oxidative stress is the third pathway.

Table (2) Diameter values for different samples

Types	Inhibition zone (mm)
Staphylococcus aureus,	24
Staphylococcus epid,	25
Klebsiella	28
Escherichia coli	23
Candida albicans	23

When ROS generation rises, the cell walls and biofilms of both GPB and GNB are destroyed. The fourth mechanism by which AgO NPs exhibit antibacterial activity involves their interaction with phosphoric acid residues in DNA molecules and proteins when they penetrate a bacterial cell, and preventing cell division as a result. The photocatalysis process is the fifth mechanism. It is noteworthy that conjugating AgO NPs with specific drugs, like moxifloxacin, significantly increased their photocatalytic activity [46-50].

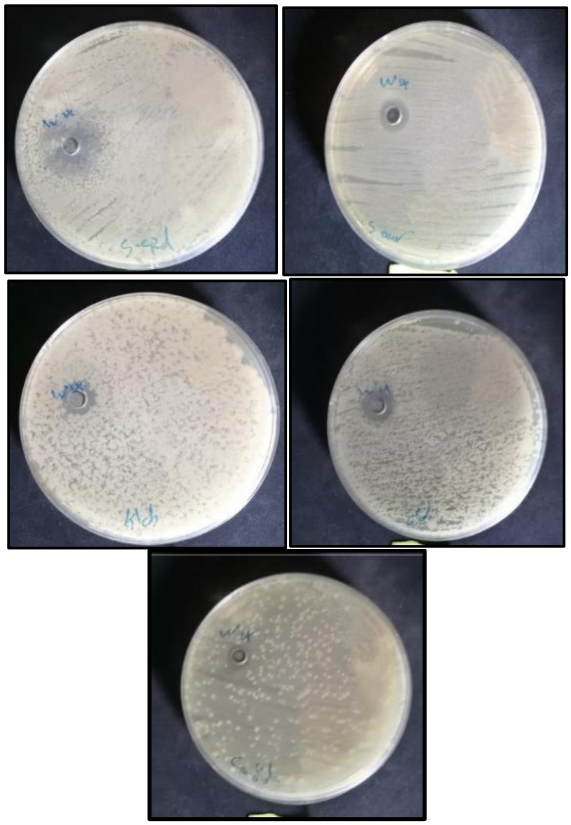

Fig. (8) Determination of growth-inhibition zone using the synthesized AgO NPs

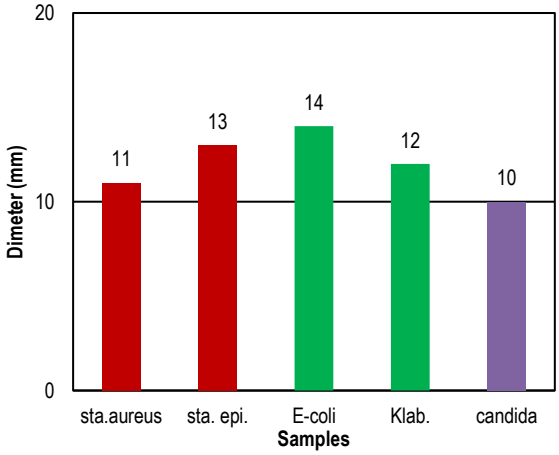

Fig. (9) Diameter of inhibition zone for different samples

4. Conclusion

The use of rosemary plant had an effective role in oxidation and reduction, because it contain high phenols, as we obtained silver oxide particles with size less than 100nm. This results is important role in inhibition bacterial and fungi. The results of our work opens the door to the development of

environmentally safe antibacterial materials and treatments.

References

[1] M. Ahmad et al., "Biosynthesized silver nano-particles using Polygonatum geminiflorum efficiently control fusarium wilt disease of tomato", *Front. Bioeng. Biotechnol.*, 10 (2022) 1-13.

[2] M. Khatami et al., "Super-paramagnetic iron oxide nano-particles (SPIONs): Greener synthesis using Stevia plant and evaluation of its antioxidant properties", *J. Clean. Prod.*, 208 (2019) 1171-1177.

[3] S. Hameed et al., "Precursor effects on the physical, biological, and catalytic properties of Fagonia indica Burm. f. mediated zinc oxide nano-particles", *Microscop. Res. Tech.*, 84 (2021) 3087–3103.

[4] E.A. Latief, A.T. Mohi and A.N. Abd, "Effect of Natural Dye on the Spectral Response of the Heterojunction Ag/ZnO/Ps/Si/Ag for Photodetector Application", *Int. J. Nanosci.*, 22(6) (2023) 2350048.

[5] L. Li et al., "Silver nanoparticles induce protective autophagy via Ca^{2+}/CaMKKβ/AMPK/ mTOR pathway in SH-SY5Y cells and rat brains", *Nanotoxicology*, 13 (2019) 369-391.

[6] M.S.S. Danish et al., "Green Synthesis of Silver Oxide Nano-particles for Photocatalytic Environmental Remediation and Bio-medical Applications", *Metals*, 12 (2022) 769.

[7] R. Li et al., "Bio-synthesis of silver oxide nanoparticles and their photocatalytic and Anti-microbial activity evaluation for wound healing applications in nursing care", *J. Photochem. Photobiol. B Biol.*, 199 (2022) 111593.

[8] B. Rashmi et al., "Facile green synthesis of silver oxide nanoparticles and their electrochemical, photocatalytic, and biological studies", *Inorg. Chem. Commun.*, 111 (2019) 107580.

[9] S. Ahmad et al., "Green nanotechnology: A review on green synthesis of silver nanoparticles - An eco-friendly approach", *Int. J. Nanomed.*, 14 (2019) 5087-5107.

[10] A.T. Khalil et al., "Single precursor-based synthesis of transition metal sulfide nanoparticles and evaluation of their anti-microbial, antioxidant and cytotoxic potentials", *Appl. Nanosci.*, 11 (2021) 2489-2502.

[11] S. Uddin et al., "Green synthesis of nickel oxide nanoparticles using leaf extract of Berberis balochistanica: Characterization, and diverse biological applications", *Microscop. Res. Tech.*, 84(9) (2021) 2004-2016.

[12] P. Sevilla, "Molecular characterization of drug's nanocarriers based on plasmon-enhanced spectroscopy: fluorescence (SEF) and Raman (SERS)", *Optica Pura Y Aplicada*, 46(2) (2013) 111-119.

[13] B.J. Alwan, A.N. Abd and N.H. Zaki, "Inhibitory effect of lithium oxide nanoparticle produced by green synthesis method", *AIP Conf. Proc.*, 2834 (2023) 090012.

[14] N.F. Habubi et al., "Improved photoresponse of porous silicon photodetectors by embedding CdS nanoparticles", *World Sci. News*, 53 (2015) 718-724.

[15] S. Honary et al., "Green synthesis of copper oxide nanoparticles using Penicillium aurantiogriseum, Penicillium citrinum and Penicillium waksmanii", *Dig. J. Nanomater. Bios.*, 7(3) (2012) 999-1005.

[16] J.E. Hutchison, "Greener nanoscience: a proactive approach to advancing applications and reducing implications of nanotechnology", *ACS Pub.*, 2(3) (2008) 395–402.

[17] M.A. Faraj, M.A. Jabbar and A.N. Abd, "Bismuth oxide aqueous colloidal NPS obtained by a green synthesis inhibit candida albicans", *AIP Conf. Proc.*, 2834 (2023) 090009.

[18] R.B. Malabadi et al., "Silver nanoparticles synthesized by in vitro derived plants and callus cultures of Clitoria ternatea; Evaluation of Anti-microbial activity", *Res Biotech.*, 3(5) (2012) 26-38.

[19] J.R. Morones et al., "The bactericidal effect of silver nanoparticles", *Nanotechnology*, 16(10) (2005) 2346.

[20] V. Manikandan, "Green synthesis of silver oxide nanoparticles and its antibacterial activity against dental pathogens", *Biotech.*, 7(1) (2017) 72.

[21] M.-J. Kim et al., "Morphological evolution of Silver Oxide microstructures from cubes to octapods and their antibacterial activities", *Bull. Korean Chem. Soc.*, 32(10) (2011) 3793-3795.

[22] M. Yadav, "Biological synthesis and antibacterial activity of silver oxide nanoparticle prepared from Carica papaya root extract", *Int. J. Pure Appl. Biosci.*, 6(2) (2018) 1632-1639.

[23] S. Rajakannu et al., "Bio-synthesis of silver nanoparticles using Garcinia mangostana fruit extract and their antibacterial, antioxidant activity", *Int. J. Curr. Microbiol. Appl. Sci.*, 4(1) (2015) 944-952.

[24] S. Ravichandran et al., "A novel approach for the Bio-synthesis of silver oxide nanoparticles using aqueous leaf extract of Callistemon lanceolatus (Myrtaceae) and their therapeutic potential", *J. Exp. Nanosci.*, 11(6) (2016) 445-458.

[25] M. Jalees, "Green synthesis of silver oxide nanoparticles prepared from waste part of mango peels", *Int. J. Pure Appl. Biosci.*, 6(3) (2018) 502- 508.

[26] M. Govarthanan et al., "Bio-synthesis and characterization of silver nanoparticles using panchakavya, an Indian traditional farming formulating agent", *Int. J. Nanomed.*, 4(9) (2014) 1593-1600.
[27] N.F. Habubi et al., "Fabrication and characterization of a p-AgO/PSi/n-Si heterojunction for solar cell applications", *Silicon*, 10 (2018) 371-376.
[28] N.R.C. Raju, K.J. Kumar, A. Subrahmanyam, "Physical properties of silver oxide thin films by pulsed laser deposition: effect of oxygen pressure during growth", *J. Phys. D Appl. Phys.*, 42 (2009) 135411.
[29] B. Gauril et al., "Synthesis and Characterization of Ag/AgO nanoparticles as alcohol sensor", *Res. J. Chem. Enviro*., 20(10) (2016) 1-6.
[30] R.I. Priyadharshini et al., "Microwave-mediated extracellular synthesis of metallic silver and zinc oxide nanoparticles using macro-algae (Gracilaria edulis) extracts and its anticancer activity against human PC3 cell lines", *Appl. Biochem. Biotechnol.*, 174 (2014) 2777-2790.
[31] K. Roy et al., "Green synthesis of silver nanoparticles using fruit extract of Malus domestica and study of its Anti-microbial activity", *Dig. J. Nanomater. Biostruct.*, 9 (2014) 1137–1147.
[32] M. Vanaja and G. Annadurai, "Coleus aromaticus leaf extract mediated synthesis of silver nanoparticles and its bactericidal activity", *Appl. Nanosci.*, 3 (2013) 217-223.
[33] A.J. Das et al., "Sunlight irradiation induced synthesis of silver nanoparticles using glycolipid bio-surfactant and exploring the antibacterial activity", *J. Bioeng. Biomed. Sci.*, 6 (2016) 1-5.
[34] N.Kh. Abdalameer, K.A. Khalaph and E.M. Ali, "Ag/AgO nanoparticles: Green synthesis and investigation of their bacterial inhibition effects", *Mater. Today: Proc.*, 45(6) (2021) 5788-5792.
[35] J.A. Tanna et al., "Histidine-Capped ZnO Nanoparticles: An Efficient Synthesis, Spectral Characterization and Effective Antibacterial Activity", Bionanosci., 5(3) (2015) 123.
[36] R.G. Chaudhary et al., "Synthesis of nickel nanoparticles: Microscopic investigation, an efficient catalyst and effective antibacterial activity", *Juneja, Adv. Mater. Lett.*, 6(11) (2015) 990-998.
[37] S.M. Meshram et al., "Green synthesis of silver nanoparticles using white sugar", *IET Nanobiotech.*, 7(1) (2013) 28-32.
[38] K. Paulkumar et al., "Green synthesis of silver nanoparticle and silver based chitosan bionanocomposite using stem extract of Saccharum officinarum and assessment of its antibacterial activity", *Adv. Nat. Sci.: Nanosci. Nanotech.*, 8 (2017) 035019
[39] A.M. Allahverdiyev, E.S. Abamor and M. Bagirova, "Antimicrobial effects of TiO_2 and Ag_2O nanoparticles against drug-resistant bacteria and leishmania parasites", *Future Microbiol.*, 6(8) (2011) 933-940.
[40] A. Rita et al., "Structural, optical and magnetic properties of silver oxide (AgO) nanoparticles at shocked conditions", *J. Nanostruct. Chem.*, 10 (2020) 309-316.
[41] Z. Lin, Y. Lu and J. Huang, "A hierarchical silver oxide nanoparticle/TiO_2 nanotube composite derived from natural cellulose substance with enhanced photocatalytic performance", *Cellulose*, 26 (2019) 6683–6700.
[42] S. Haq et al., "Fabrication of pure and moxifloxacin functionalized silver oxide nanoparticles for photocatalytic and Anti-microbial activity", *J. Photochem. Photobiol. B Biol.*, 186 (2018) 116-124.
[43] K. Harish and K. Manisha, "Synthesis and characterization of silver oxide nanoparticles by sol-gel method", *Int. J. Adv. Res. Sci. Eng.*, 7 (2018) 632-637.
[44] K.T. Sullivan et al., "Synthesis and reactivity of nano- Silver Oxide as an oxidizer for energetic systems yielding Anti-microbial products", *Combust. Flame*, 160 (2013) 438-446.
[45] C.M. Phan and H.M. Nguyen, "Role of Capping Agent in Wet Synthesis of Nanoparticles", *J. Phys. Chem. A*, 121 (2017) 3213-3219.
[46] V. Sergey et al., "Silver Oxide Nanoparticles as a Candidate for Anti-microbial Compounds of the New Generation", *Pharmaceut.*, 15 (2022) 968.
[47] O.F. Abdullah, S.M. Abulkarem and W.K. Abad, "Selenium Dioxide Nanoparticles from Hibiscus Sabdariffa Flower Extract Induce Apoptosis in Bacterium (Gram-negative, Gram-positive) and Fungi", *NeuroQuantology*, 20 (2022) 198-203.
[48] W.K. Abad, A.N. Abd and N.F. Habubi, "Synthesis of Silver Oxide Nanoparticles via Fresh Pomegranate Peel Extract for Bioapplications", *Nano Biomed. Eng.*, 15(4) (2023) 2150-5578.
[49] M.Y. Ali et al., "Rapid Synthesis of SeO_2 Nanoparticles and Their Activity against Clinica Isolates (Gram positive, Gram negative, and Fungi)", Nano World J., 9(3) (2023) 89-93.
[50] E.M. Ali et al., "Green Synthesis, Characterization and Antimicrobial activity of CuO nanoparticles (NPs) Derived from Hibiscus sabdariffa a plant and CuCl", *J. Phys.: Conf. Ser.*, 1963 (2021) 012092.

Proceedings of 5th International Specialized Conference of Education College on Physics and Applied Sciences (5thICECAS24), 22-23 April 2024

Muneer H.J. Alzubaidy [1]
Firas M.D. Al-Jaafari [1]
Wedian K. Abad [2]
Ahmed N. Abd [3]

[1] *Department of Physics, College of Science, Wasit University, Kut, IRAQ*
[2] *Applied Physics Branch, Department of Applied Science, University of Technology- Iraq*
[3] *Department of Physics, Faculty of Science, Mustansiriyah University, Baghdad, IRAQ*

Microbial and Chemical Synthesis of Cobalt Oxide Nanoparticles and Their Antimicrobial Activities

The production of cobalt oxide nanoparticles was chemistry. Two phases of cobalt oxide nanoparticles were identified. The cobalt oxide particles are widely distributed and spherical in shape. The band gaps of cobalt oxide nanoparticles are 3.7 and 4.6 eV. Functional groups of the prepared compounds were identified. The anti-bacterial activity of the produced cobalt oxide nanoparticles greatly inhibits the growth of a number of pathogenic microorganisms.

Keywords: Cobalt oxide; Antimicrobial activity; Chemical method; Agar disk
Received: 19 January 2024; Revised: 4 March 2024; Accepted: 4 April 2024

1. Introduction

The remarkable features of nanostructure materials have attracted a lot of interest recently. Of these, a great deal of study has been done on the basic properties and uses of transition-metal oxides [1-3]. Cobalt oxides are malleable materials that exhibit stability in the natural environment and are classified as transition-metal oxides [4-6]. The optical band gaps at 1.48 and 2.19 eV define cobalt oxide a significant p-type semiconductor [7-9]. Cobalt oxide nanostructures have received a lot of interest lately in terms of production and research because of their potential applications [10-12]. Since they are less expensive than noble metal nanoparticles and exhibit distinct electrical and magnetic properties, Co_3O_4 NPs have attracted a lot of attention lately [13-15]. Bio-medical researchers have looked at the possible use of cobalt nanoparticles as therapeutic agents to treat disorders, including microbial infections [16-18]. Cobalt nanoparticles are safe at low doses, have potent anti-bacterial and anti-fungal effects, and are less toxic to the body than anti-biotic [19,20]. Around the world, bacterial illnesses harm both human and animal populations. Different conventional antibiotics were found in the 20th century to treat a variety of ailments, and they are now seen to be the mainstay in the fight against a variety of bacterial infections that spread easily. These antibiotics have low molecular weights and are organic in nature. However, the misuse of antibiotics in the past several years has caused bacterial resistance to evolve through many processes, including evolution [1,2]. Anti-microbial resistance (AMR) to conventional antibiotics is one of the major problems confronting the world today, posing a severe danger to the survival of both humans and animals. Therefore, one possible answer to the AMR issue, at least partially, is to replace conventional antibiotics with alternative anti-microbial. Worldwide researchers are striving to develop new medications and tactics to fight resistant illnesses and stop bacterial resistance [3]. One of the most promising alternatives to conventional antibiotics is the use of materials at the nanoscale. The nanoparticles possess unique properties. They are thought to have unique bactericidal action routes and to be highly effective against a variety of diseases, making them a viable alternative to traditional antibiotic therapies. Compared to traditional antibiotics, nanoparticles are much smaller and more easily absorbed by cell membranes, allowing for faster and more effective delivery of the drug to various regions of the body. Metals and their oxides have garnered significant interest. According to studies, metal oxide nanoparticles have strong biocidal activity against both gram (negative and positive) bacteria, and nanoparticles can be employed as potential bactericidal materials [21].

In this research, cobalt oxide was prepared in a simple chemical way at low concentrations, its properties were studied, and the prepared particles were used as an antibacterial and antifungal within the specialty of medical physics.

2. Preparation of Samples

Co_3O_4 NPs were made via a chemical process. Cobalt (II) nitrate hexahydrate (2.9 g) was dissolved

in 100 mL of filtered water and well mixed. After that, the reaction mixture was heated to 50°C for 60 minutes, after a concentration of 1M from NaOH was added put on a stirrer for two hours at 50°C.The mixture's color changed from pink to light black. This shows that the reduction and reaction process had taken place. The spin coating technique was used to deposit thin films. By using the gravimetric method to measure the thickness of cobalt oxide thin films by 100 µL, or a maximum of 0.9 µm, the morphological and structural characteristics of the films were examined. Fig. (1): Spin coating technique for forming thin films and the procedures involved in preparing Co_3O_4 NPs.

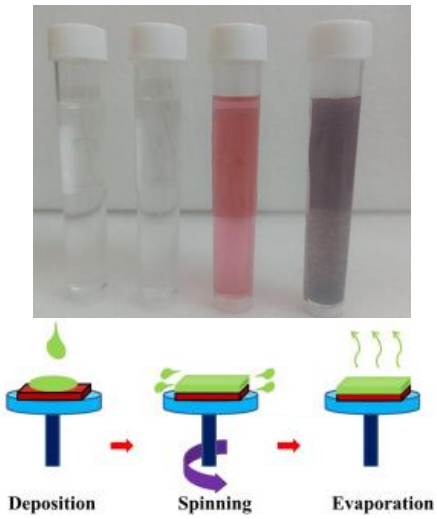

Fig. (1) Photograph and schematic of preparation steps of CoO NPs and the method of thin film formation by the spin-coating process

3. Results and Discussion

As can be seen from Fig. (2), the planes (220), (311), and (222) are associated to the characteristic peaks situated at 31.8°, 36.3°, and 39.0° in the XRD pattern. These peaks the cubic phase of cobalt oxide (JCPDS card 42–1467). Moreover, the peaks at 36.54° and 42.44°, which match the bulk XRD pattern (CoO, JCPDS card 78-0431) [22-26], corresponding to the (111) and (200) planes with shape of face-centered cubic (f.c.c.) CoO. The average size of the crystal was 53.3 nm. The results showed formation of morphology spherical Co_3O_4 NPs as shown in Fig. (2) and the average diameter was 25.78 nm with average particle size of 167.22 nm, mean roughness of 5.53 nm and root-mean-square (RMS) roughness of 6.85 nm.

Figure (4) displays the FT-IR spectrum of the Co_3O_4 NPs. The large peak seen between 500 and 698 cm^{-1} was attributed to the Co^{2+}, Co^{3+} with O stretching vibration modes. The peaks are caused by the spinel structure of the Co_3O_4 NPs at the tetrahedral and octahedral sites [27]. Two notable peaks were seen at 3455 and 1643 cm^{-1}, represented to the bending and stretching vibrations of the adsorbed water molecules [5]. Also, a small peak at 1378 cm^{-1} is seen, which is generated by the $Co(NO_3)_3$ residue and linked to the presence of NO_3^- [28-30].

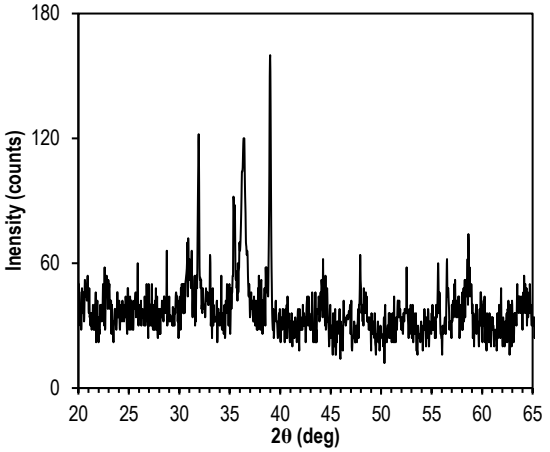

Fig. (2) XRD pattern of a cobalt oxide film sample

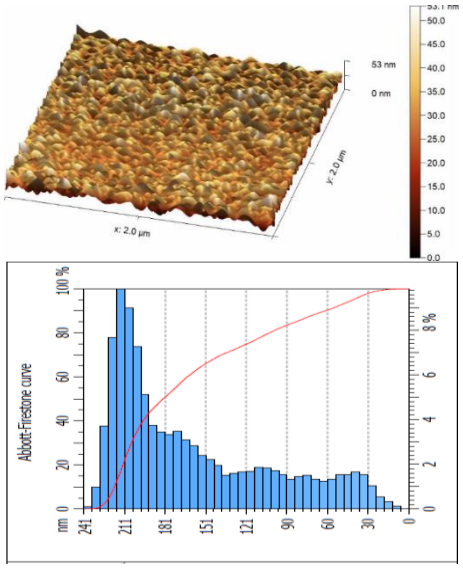

Fig. (3) AFM results of cobalt oxide film sample

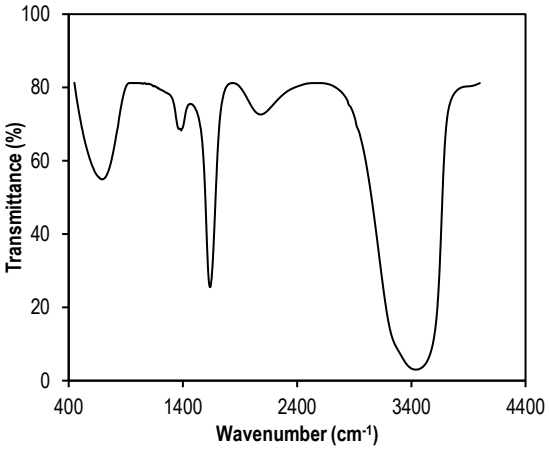

Fig. (4) FTIR spectrum of cobalt oxide colloidal sample

The optical characteristics of the Co_3O_4 NPs were examined using UV-visible spectroscopyas displayed in Fig. (5a). The results indicate two absorption bands in the wavelength ranges of 298–and 500–520 nm for the chemical production process. The $O_2^- \rightarrow Co^{2+}$ charge transfer mechanism can be linked to the first band, while the $O_2^- \rightarrow Co^{3+}$ charge transfer is associated with the second one. The production of nanoparticles is the cause of these absorption peaks. Weak resonance indicated that there was no agglomeration of nanoparticles. The absorption band gap may be found using the relationship $(\alpha hv)^2 = A(hv - E_g)$, where hv is the energy of photon (eV), A is a constant, α is the coefficient . By extending the linear part of the $(\alpha hv)^2$ versus hv plot, one may estimate the band gap. As seen in the inset of Fig. (5b), two absorption bands result in two E_g values for the product at 4.6 and 3.7eV. These values are blue-shifted in comparison to published values for the bulk sample data (1.77 and 3.37 eV, respectively). The small size impacts of nanoparticles may be connected to the rise in band gaps of Co_3O_4 NPs [31-33].

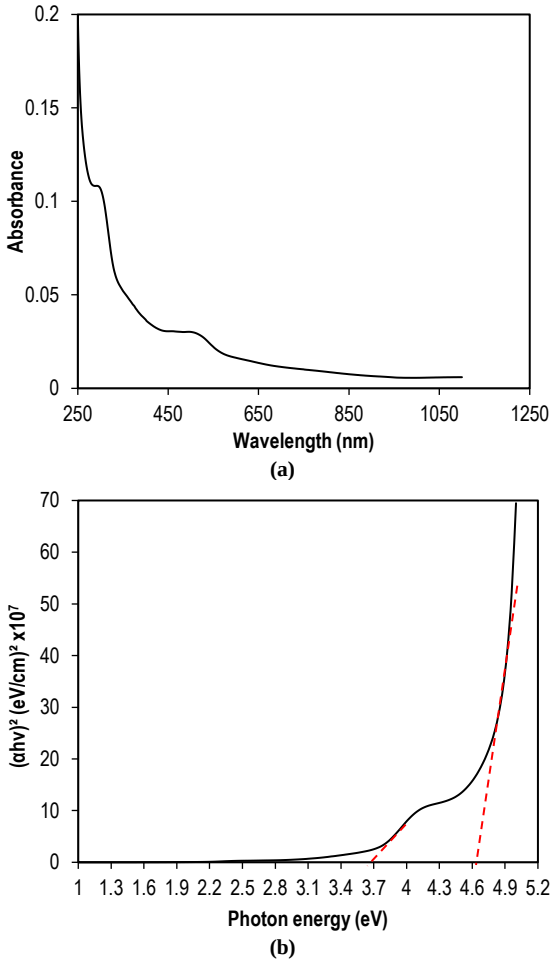

Fig. (5) UV-visible spectrum (a) and energy band gap (b) of cobalt oxide colloidal sample

To evaluate the antibacterial activity of the produced Co_3O_4 NPs against antimicrobials, the Agar diffusion well technique was employed. Figure (6) shows the antibacterial activity of Co_3O_4 NPs that were produced using straightforward chemical methods. The results showed that the produced Co_3O_4 NPs induced strong anti-fungal and anti-bacterial activities. It was discovered that Co_3O_4 NPs have good activity towards both bacterial and fungal. The variations in oxidative stress tolerance of distinct bacterial strains account for the variations in their susceptibility. The shape, and size of particle for Co_3O_4 NPs are the main parameters affecting their antibacterial capability. The antibacterial properties of metal oxide nanoparticles have several explanations. In aqueous solutions of Co_3O_4 NPs, reactive species such as super oxide radical anions and hydroxyl radicals develop. Through its interactions with radicals present in aqueous Co_3O_4 NPs, the negatively charged surface of the bacterium hinders vital biological processes such as cell division and respiration. Conversely, the thiol group of crucial bacterial enzymes interacts with cobalt ions from cobalt oxides, leading to deactivation and cell death. When absorbed O_2 combines with the surface of Co_3O_4 NPs, an excited electron is created. Hydrogen peroxide is created when this electron joins the O_2 ion to form the O_2 ion, which then interacts with the H_2O molecule. As a result, H_2O_2 penetrates the cell, impairing cytoplasmic processes and killing [34,35].

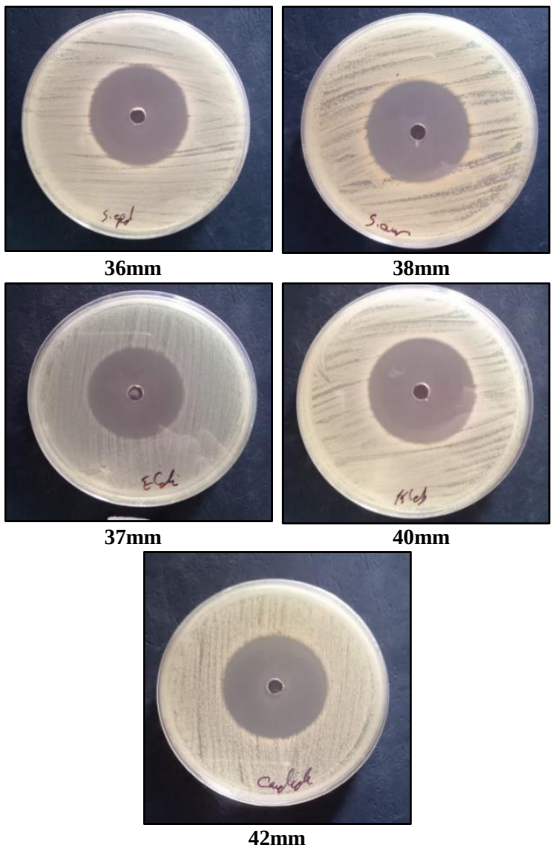

Fig. (6) Inhibition region determination using Co_3O_4 NPs

4. Conclusions

The results of the study showed that cobalt salts and sodium hydroxide may be reacted to create cobalt oxide particles in a straightforward chemical process, however this required at least an hour and certain concentrations. The obtained results suggest that the antibacterial activity of the synthesized Co_3O_4 NPs has a noteworthy inhibitory effect on the development of several harmful microorganisms. The present study may provide a novel and advantageous exploration for biomedical

References

[1] M. et al., "Overcoming challenges in treating autoimmuntity: Development of tolerogenic immune-modifying nanoparticles", *Nanomedicine,* 18 (2019) 282-291.

[2] M. Kiani et al., "High-gravity-assisted green synthesis of palladium nano-particles: The flowering of nanomedicine", *Nanomedicine,* 30 (2020) 102297.

[3] M.S. Niasari, N. Mir and F. Davar, "Synthesis and characterization of Co_3O_4 nanorods by thermal decomposition of cobalt oxalate", *J. Phys. Chem. Solids,* 70 (2009) 847-852.

[4] W.W. Wang and Y. Zhu, "Microwave-assisted synthesis of cobalt oxalate nanorods and their thermal conversion to Co_3O_4 rods", *J. Mater. Res. Bull.,* 40 (2005) 1929-1935.

[5] S.C. Petitto et al., "Cobalt oxide surface chemistry: The interaction of CoO(100), Co_3O_4(110) and Co_3O_4(111) with oxygen and water", *J. Mol. Catal. A Chem.,* 281 (2008) 49-58.

[6] O.A. Hammadi and N.E. Naji, "Fabrication and Characterization of Polycrystalline Nickel Cobaltite Nanostructures Prepared by Plasma Sputtering as Gas Sensor", *Phot. Sen.,* 8(1) (2018) 43-47.

[7] V. Patil et al., "Synthesis and Characterization of Co_3O_4 Thin Film", *Soft Nanosci. Lett.,* 2(1) (2012) 1-7.

[8] S.A. Hamdan and I.M. Ali, "Synthesized pure cobalt oxide nanostructure and doped with yttrium by hydrothermal method for photodetector applications", *Iraqi J. Phys.,* 17(40) (2019) 77-87.

[9] T. Ozkaya et al., "Synthesis of Co_3O_4 nanoparticles and its magnetic characterization", *J. Magn. Magn. Mater.,* 321 (2009) 2145-2149.

[10] L. Sun et al., "Synthesis of Co_3O_4 nanostructures using a solvothermal approach", *Solid State Sci.,* 11 (2009) 108-112.

[11] P. Torelli et al., "Nanostructuration of CoO film by misfit dislocations", *Surf. Sci.,* 601 (2007) 2651-2655.

[12] Z.A. Hrbe, M.H.J. Alzubaidy and A.N. Abd, "ZnO:CuO Nanocomposite Produced by Laser Ablation in Water for Anti-bacterial Activity", *J. Pharmaceut. Neg. Res.,* 13(3) (2022).

[13] J. Liu et al., "Metallic cobalt nanoparticles imbedded into ordered mesoporous carbon: A non-precious metal catalyst with excellent hydrogenation performance", *J. Colloid Interface Sci.,* 505 (2017) 789-795.

[14] Y.S.Y. Zhu et al., "Cobalt nanoparticles embedded in N-doped carbon as an efficient bifunctional electrocatalyst for oxygen reduction and evolution reactions", *Nanoscale,* 6 (2014) 15080-15089.

[15] N.A.H. Hashim and F.J. Kadhim, "Structural and Optical Characteristics of Co_3O_4 Nanostructures Prepared by DC Reactive Magnetron Sputtering", *Iraqi J. Appl. Phys.,* 18(4) (2022) 31-36.

[16] M. Azharuddin et al., "A repertoire of biomedical applications of noble metal nanoparticles", *Chem. Commun.,* 55 (2019) 6964-6996.

[17] A. Aseri et al., "Magnetic nanoparticles: Magnetic nanotechnology using biomedical applications and future prospects", *Int. J. Pharm. Sci. Rev. Res.,* 31 (2015) 119-131.

[18] N.A.H. Hashim, F.J. Kadhim and Z.S. Abdulsattar, "Characterization of Electrochromism and Photoelectrochromism of N-Doped TiO_2 and Co_3O_4 Thin Films Prepared by DC Reactive Magnetron Sputtering: Comparative Study", *Iraqi J. Appl. Phys.,* 19(1) (2023) 5-12.

[19] I. Liakos, A.M. Grumezescu and A.M. Holban, "Magnetite nanostructures as novel strategies for anti-infectious therapy", *Molecules,* 19 (2014) 12710-12726.

[20] N.E. Eleraky et al., "Nanomedicine fight against anti-bacterial resistance: An overview of the recent pharmaceutical innovations", *Pharmaceutics,* 12 (2020) 142.

[21] V. Gupta et al., "Comparative evaluation of anti-bacterial potentials of nano cobalt oxide with standard Anti-microbials", *J. Indian Chem. Soc.,* 99(7) (2022) 100533.

[22] R. Bhargava et al., "Investigation of Structural, Optical and Electrical Properties of Co_3O_4 Nanoparticles", *AIP Conf. Ser.,* 1953 (2018) 030034.

[23] K. Deori and S. Deka, "Morphology oriented surfactant dependent CoO and reaction time dependent Co_3O_4 nanocrystals from single synthesis method and their optical and magnetic properties", *Cryst. Eng. Comm.,* 15 (2013) 8465-8474.

[24] S. Faisal et al., "*Juglans regia L.* mediated synthesis of cobalt oxide and zinc‑doped cobalt oxide nanoparticles: characterization and evaluation for environmental, anti-bacterial and cytotoxic potential", *Nanotech. Enviro. Eng.,* 7 (2022) 675-689.

[25] S. Farhadi, K. Pourzare and S. Sadeghinejad, "Synthesis and characterization of Co_3O_4 nanoplates by simple thermolysis of the $[Co(NH_3)_6]_2$ $(C_2O_4)_3$ $4H_2O$ complex", *Polyhedron*, 67 (2014) 104-110.

[26] A.B. Vennela et al., "Structural and optical properties of Co_3O_4 nanoparticles prepared by sol-gel technique for photocatalytic application", *Int. J. Electrochem. Sci.*, 14(4) (2019) 3535–3552.

[27] M.A. Ghasemzadeh, M.H. Abdollahi-Basir and Z. Elyasi, "Synthesis of some Novel Imidazoles Catalyzed by Co_3O_4 Nanoparticles and Evaluation of their Anti-bacterial Activities", *Combinat. Chem. High Throu. Screen.*, 21 (2018) 1-10.

[28] R. Packiaraj et al., "Electrochemical investigations of magnetic Co_3O_4 nanoparticles as an active electrode for supercapacitor applications", *J. Supercond. Nov. Magn.*, 32 (2018) 2427.

[29] A. Diallo et al., "Green synthesis of Co_3O_4 nanoparticles via *Aspalathus linearis*: physical properties", *Green Chem. Lett. Rev.*, 8 (2015) 30-36.

[30] T. He et al., "Solubility-controlled synthesis of high-quality Co_3O_4 nanocrystals", *Chem. Mater.*, 17 (2005) 4023-4030.

[31] P. Gowthami et al., "Biosynthesis of Co_3O_4 nanomedicine by using *Mollugo oppositifolia* L. aqueous leaf extract and its Anti-microbial, mosquito larvicidal activities", *Sci. Rep.*, 13 (2023) 9002.

[32] V.S. Coker et al., "Harnessing the extracellular bacterial production of nanoscale cobalt ferrite with exploitable magnetic properties", *ACS Nano*, 3 (2009) 1922-1928.

[33] W.K. Abad, A.N. Abd and N.F. Habubi, "Synthesis of Silver Oxide Nanoparticles via Fresh Pomegranate Peel Extract for Bioapplications", *Nano Biomed. Eng.*, 15(4) (2023) 2150-5578.

[34] M.Y. Ali et al., "Rapid Synthesis of SeO_2 Nanoparticles and Their Activity against Clinica Isolates (Gram positive, Gram negative, and Fungi)", *Nano World J.*, 9(3) (2023) 89-93.

[35] E.M. Ali et al., "Green Synthesis, Characterization and Anti-microbial activity of CuO nanoparticles (NPs) Derived from Hibiscus sabdariffa a plant and CuCl", *J. Phys.: Conf. Ser.*, 1963 (2021) 012092.

Proceedings of 5th International Specialized Conference of Education College on Physics and Applied Sciences (5thICECAS24), 22-23 April 2024

Effect of Partial Replacement of Copper with Zinc on Dielectric Properties of $PbSr_2Ca_2Cu_3O$ Compound

Naba F. Hamady
Shatha H. Mahdi

Department of Physics, College of Education for Pure Science - Ibn Al-Haitham, University of Baghdad, Baghdad, IRAQ

The $PbSr_2Ca_2Cu_{3-Y}Zn_YO_{8+\delta}$ compound with different Zn concentrations (Y = 0, 0.06, and 0.12%) were prepared successfully via solid-state reaction methods. The structural properties were investigated and the electrical properties were studied throughout alternating electrical conductivity and they indicated that any change in zinc concentration causes a change in the dielectric constant and dielectric loss coefficient for all prepared samples.

Keywords: Zinc compounds; Pb compounds; X-ray diffraction; Electrical resistivity
Received: 19 January 2024; Revised: 4 March 2024; Accepted: 4 April 2024

1. Introduction

By studying replacement processes and related methodologies, we can have optimism and expand our understanding of the mechanisms underlying superconductivity in elements and compounds particularly those whose compositions rely on copper oxide (cuprates). In 1913, it was discovered that lead is a superconducting element with a critical temperature which is slightly higher than Mercury (7.2K) [1-5]. The discoveries continued until (2008), when electric superconducting materials appeared which contained an iron layer of lead antioxidant-anti layer Iron as a superconducting compound. In 2022, the critical temperature of the superconducting compound $(Bi,Pb)_2Sr_2Ca_2Cu_3O_x$ was found to be 106K .The BCS model of copper pairs formed from electron-phonon interactions that overpower Coulomb repulsion reactions gives these superconducting ceramic materials superconducting properties. However, many features of electron-phonon interactions in the confirmed theory of BCS in metals seem to be weak or absent in the infrared spectra of ceramics [6-11].

The electrical insulation and resistance to electric current vary for different materials and chemical components. The dielectric constant is particularly significant because it is determined by comparing the capacitance of the electric capacitor when the ceramic insulator is used as an insulating medium to its capacity when the air becomes only the insulating medium present. The movement of free electrons or ions and their presence determines the electrical conductivity of air as an electrical medium. These charged particles or strong bonds between atoms in insulating materials, which are mediated by strong covalent bonds, keep electrons in the material connected. For this reason, the electrons in insulating materials are highly concentrated within their atoms and cannot move freely, which results in a large energy gap and low electrical conductivity, conductivity varies between insulators [12-14].

The electric charge created by the voltage will stay stored in the electrical circuit when a voltage is applied to two conductive plates that are vacuum-separated from one another. The value of the charge stored between the two conductive plates is known as the capacitance [15,16]. It is anticipated that no electric current will flow. The value of stored charged (Q) and capacitance (C_0) can be determined using the following formula [17,18]:

$$Q = C\,V \quad (1)$$

$$C_0 = \varepsilon_o\,(A/d) \quad (2)$$

When two conductive plates store an electrical charge, the amount of charge is measured in C, the capacitance is measured in F, and the voltage is measured in V. The capacitance value depends on various factors, including the material used between the plates, its size, shape and distance between them. When there is a vacuum as the separator between the plates, the capacitance can be calculated using Eq. (2), where the vacuum permittivity, denoted as ε_0, has value of $8.85\text{x}10^{-12}$ F/m. The distance between two plates is represented by "d" and is measured in meters. The surface area of each plate is denoted by "A" and is measured in m^2. The capacity in the presence of a vacuum is represented by the C_0. When the surface is an insulating material between two conductive plates it allows polarization and storage of additional charges, increasing capacitance [19,20] as

$$C = \varepsilon\,(A/d) \quad (3)$$

The dielectric constant (έ) can be calculated from equation below:

$C/ C_o = \varepsilon / \varepsilon_0 = \acute{\varepsilon}$ (4)

So, the dielectric constant can be written in another formula as

$\varepsilon' = C\, d / \varepsilon_0 A$ (5)

An isolated loss (tan δ) is given by the following relation:

$\varepsilon'' = \tan\delta\, \varepsilon'$ (6)

To calculate alternating electrical conductivity, we use the following relationship:

$\sigma_{a.c.} = w\, \varepsilon_o\, \varepsilon''$ (7)

where w is the angular frequency which equals to 2πf

The research aims to know the impact of adding ZnO to the $PbSr_2Ca_2Cu_{3-Y}Zn_YO_{8+\delta}$ (Pb1223) compound on some of its properties, specifically its insulating properties. The study was conducted using percentages of 0%, 0.06%, and 0.12% of ZnO.

2. Experimental Part

For sample preparation, table (1) shows the use of high-quality raw materials of universal origin and pure oxides such as PbO, SrO, CaO, Cu_2O, and ZnO. The solid-state reaction method [21] was used to prepare the samples, which is the most commonly used method for preparing compounds and oxides this process was carried out in many steps, including calculating the weights of the oxides used according to the following chemical equation:

$PbO + 2SrO + 2CaO + (3\text{-}Y)\, CuO + (Y)\, ZnO \rightarrow PbSr_2Ca_2Cu_{3-Y}Zn_YO_{8+\delta}$

Table (1) Specifications of oxides used in the preparation process in this work

Oxide	Atomic Weight (g/mol)	Purity	Origin
PbO	223.1994	99%	JAPAN/Cicc
SrO	130.6194	99%	Germany/Merck
CaO	56.07740	95%	England /BDH
Cu_2O	143.0914	99%	England/M&B
ZnO	81.37940	99%	INDIA

The mixing and grinding process was carried out using a manual mortar made of agate material (Gate Mortar), as this process of grinding and mixing was carried out for a full hour, as this process aims to obtain fine powders with a high degree of homogeneity. The samples were formed in the form of cylindrical discs using a mold with a diameter of 1.5cm, with a thickness of 0.63cm, using a hydraulic press and under a pressure of 5.4MPa for two minutes, and using a two-way axial pressing mechanism to obtain the best and highest density value. Then the samples were sintered at a temperature of 850°C, for 24 hours under normal atmospheric pressure at a heating rate of 2 °C/min and cooled to room temperature at the same heating rate. The purpose of the sintering process is to obtain coherent samples and to ensure an optimal diffusion process between the atoms, sintering was done with an electric oven. Figure (1) shows the images of sintered samples.

Fig. (1) Photograph of the sintered samples

The x-ray diffraction (XRD) technique was used to determine the crystalline structure of all prepared samples. The obtained XRD patterns were compared with the information given in the references [22,23]. The atomic force microscopy (AFM) is one of the very high-resolution scanning probe microscopes, having an analysis capacity of up to fractions of a nanometer. With its help, it is possible to obtain three-dimensional topographic images of the studied sample. AFM uses two-dimensional and three-dimensional images with a size of 3000x3000nm and high resolution, drawing the topography of surfaces and surface specifications regarding grain size, the total number of grains in the sample and height. To measure the average diameter of the sample grain and surface appearances of the sample, where the amplitude of the capacitance and the isolation loss were measured by the LCR meter and by applying equations (5), (6), and (7), ε ′, ε and $\sigma_{a.c.}$ are calculated, respectively, within a frequency range of 50 to 1 MHz

3. Results and Discussion

Figure (2) shows the XRD patterns of $PbSr_2Ca_2Cu_{3-Y}Zn_YO_{8+\delta}$ samples where (Y=0, 0.06, and 0.12%). We can conclude from this figure that all samples have a polycrystalline nature with an orthorhombic phase configuration. The divergence of the scales was observed due to the diffraction pattern of different levels, which led to the appearance of mixed phases.

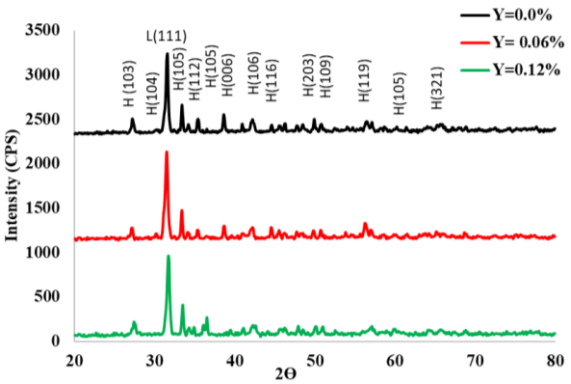

Fig. (2) XRD patterns of $PbSr_2Ca_2Cu_{3-Y}Zn_YO_{8+\delta}$ samples where (Y =0, 0.06, and 0.12%)

The $PbSr_2Ca_2Cu_3O_{8+\delta}$ sample was analyzed and it was found that it contains a high phase Pb-1223, a low

phase Pb-1212, and some small concentrations of unknown phases. This suggests that an increase in Zn concentration leads to a decrease in the formation of high-phase Pb-2223. This addition affects the high-phase compared to the base sample due to a lower replacement ratio than the effective ratio of the replacement process $\frac{1}{d^2}=\frac{h^2}{a^2}+\frac{k^2}{b^2}+\frac{l^2}{c^2}$ [23], which can be used to calculate the distance (d) between perpendicular planes of different planes based on Bragg's law ($n\lambda=2d\sin\theta$), where n is the order of reflection from the planes [24]. The calculations are performed using a computer program. The following table displays data for a, c, c/a, and the volume fraction of the high phase Pb-1223 and Pb-1212. It is evident from the table that $PbSr_2Ca_2Cu_3O_{8+\delta}$, $PbSr_2Ca_2Cu_{2.94}Zn_{0.06}O_{8+\delta}$, and $PbSr_2Ca_2Cu_{2.88}Zn_{0.12}O_{8+\delta}$ are compounds of the orthorhombic phase.

With an increase in the content of Zn up to 0.12%, the coefficient of lattice *"a"* is observed, while a decrease in the coefficient of lattice *"c"* is demonstrated. Table (2) shows the lattice coefficients and phase sizes for three compounds [$PbSr_2Ca_2Cu_3O_{8+\delta}$, $PbSr_2Ca_2Cu_{2.94}Zn_{0.06}O_{8+\delta}$, and $PbSr_2Ca_2Cu_{2.88}Zn_{0.12}O_{8+\delta}$].

AFM test was conducted to describe the surface topographies of the prepared samples. Figures (3), (4), and (5) display 2D images of the base samples with dimensions of 1819x1819nm and ratios of y=0%, 4511x4511nm when y=0.06%, and 1265nm-1265nm when y=0.12%. It was found that the average diameters of the ratios y=0%, 0.06% and 0.12% are 64.68nm, 141.2nm, and 20.68 nm, respectively. The results obtained from the AFM analysis show that the mean range values varied from 20.68 to 64.68nm with an increase in Zn content from 0 to 0.12%. The component of samples within ultrafine particles are described according to the standard [25].

The dielectric constant, loss factor, and electrical conductivity were calculated. Figure (6) shows the relation between dielectric constant and frequency at room temperature. From this figure, one can observe that the behavior of the dielectric constant is dependent on the mechanics of polarization. At frequencies lower than 10^5 Hz, the dielectric constant values are high due to the action of four polarization mechanisms, namely the vacuum. At frequencies higher than or equal to 10^5 Hz, the partial and electronic charge begins to decrease and then stabilize due to the inability of the space charge to change direction with the applied field [26]. This causes an increase in polarization. In general, the curves indicate that the ε values decrease with increasing applied frequency as shown in Eq. (6).

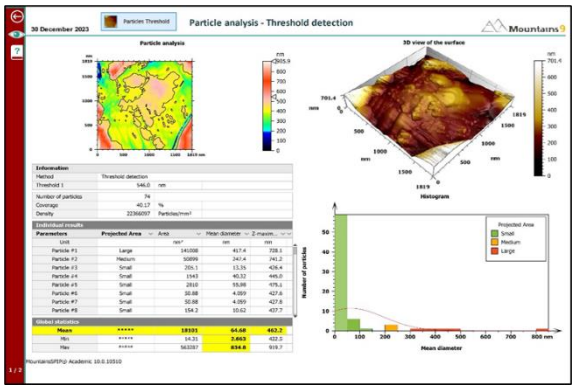

Fig. (3) AFM result for the prepared sample at Y=0%

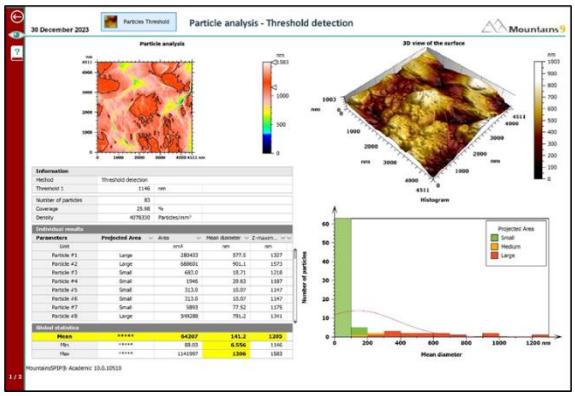

Fig. (4) AFM result for the prepared sample at Y =0.06%

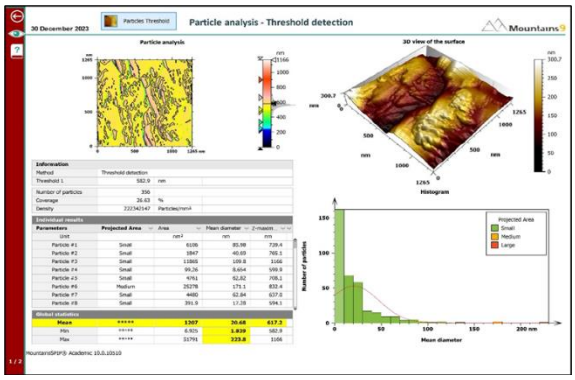

Fig. (5) AFM result for the prepared sample at Y = 0.12%

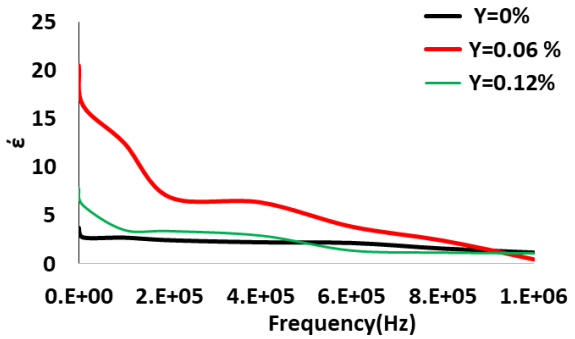

Fig. (6) Real dielectric constant with frequency at room temperature

Figure (7) shows the electrical insulation. However, the material limits phase convergence and

charge movement. A decrease in conductivity leads to a corresponding decrease in the dissipation factor. The tanδ of the samples is plotted as shown in Fig. (8). It was noticed that all samples had a low tanδ value (tanδ≥1) and the figures indicated maximum absorption at 1 MHz [20]. This shows a high value of ε" at this frequency, which reflects the direct relationship between the dielectric loss factor and the tangent loss (Eq. 6). Increasing the mobility of the cation leads to an increase in dielectric loss, and the layered effect, to the extent that it increases the conductivity of ceramics, it can also lead to significant increases in dielectric loss, and the crystal structure and can affect both W and tanδ. The measurement of alternating electrical conductivity ($\sigma_{a.c.}$) was conducted at room temperature for the samples. Which represents the form Fig. (9) with an increase in the applied frequency up to 1 MHz, The $\sigma_{a.c.}$ increases. Changes in the granular boundary composition and crystal structure directly affect and tanδ, therefore on the values of $\sigma_{a.c.}$.

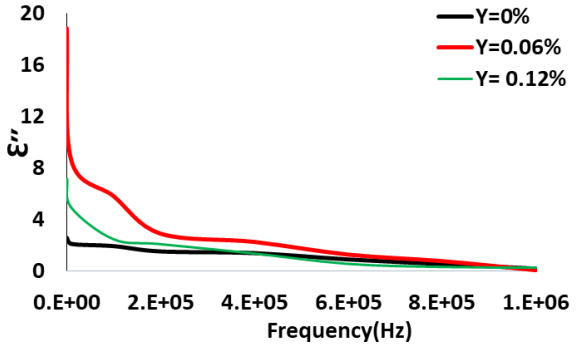

Fig. (7) Imaginary dielectric constant with frequency at room temperature

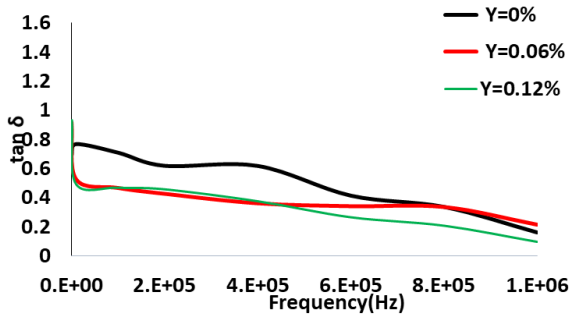

Fig. (8) Variation of tanδ with frequency at room temperature

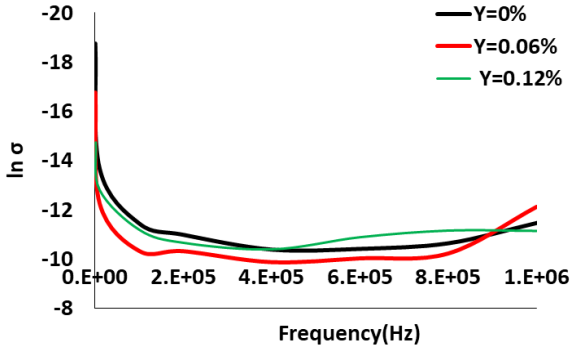

Fig. (9) Variation of σ_{ac} with frequency at room temperature

4. Conclusion

In concluding remarks, three samples of $PbSr_2Ca_2Cu_{3-Y}Zn_YO_{8+\delta}$ (Y=0.0, 0.06, 0.12%) were synthesized using the solid-state reaction method. All samples had a polycrystalline structure with four different phases and the formation of the Pb-2223 phase was difficult, especially when the zinc concentration increased. The average range values of lattice constants were decreased. The dielectric constant as well as dielectric loss factors change with any changing zinc content. In general, a decreased in the dielectric loss coefficient leads to an increased absorption of more electrical energy.

References

[1] L.A. Mohammed and K.A. Jasim, "Synthesis and Study the Structural and Electrical and Mechanical Properties of High Temperature Superconductor $Tl_{0.5}Pb_{0.5}Ba_2C_{an-1}Cu_{n-x}Ni_xO_{2n+3-\delta}$ Substituted with Nickel Oxidefor n=3", *Ibn Al-Haitham J. Pure Appl. Sci.*, 31(3) 2018.

[2] H. Sahi, "Preparation and Study the effective of addition (In and La) on $Bi_{2-x}In_xSr_2Ca_2Cu_{3-y}La_yO_{10+\delta}$) Superconductor Compound", Ph.D. thesis, University of Baghdad (2017).

[3] M.A.N. Thejeel et al., "Effect of Partial Substitution of Sr by Ba on the Structural Properties of $Tl_{0.8}Ni_{0.2}Sr_{2-x}Ba_xCa_2Cu_3O_{9-\delta}$ System", *Key Eng. Mater.*, 900 (????) 172-179.

[4] R.N. Fadhil et al., "Effect Partial Substitution of Calcium by Cadmium on Dielectrically Properties of $Li_{0.4}Cd_{0.6}Ba_2Ca_2Cu_3O_{10+\delta}$ System", *Mater. Sci. Forum*, 1050 (????) 35-40.

[5] S.H. Mahdi et al., "", *Dig. J. Nanomater. Biostruct.*, 18(2) (2023) 579-590.

[6] N.A. Ahmad, A.D. Ali and S.H. Mahdi, "Studying the effect partial Ni_2O_3 nanoparticles compensation on the properties of the compound $Bi_2Sr_{2-x}Y_xCa_2Cu_{3-y}Ni_yO_{10+\delta}$ superconductors", *J. Ovonic Res.*, 19(4) (2023) 463-469.

[7] A.D. Ahmad, A.D. Ali, S.H. Mahdi, "Effect of the laser CO_2 properties on the superconducting nanocomposite $Bi_2Sr_{2-x}Y_xCa_2Cu_{3-y}Ni_yO_{10+\delta}$ at high temperatures", *Dig. J. Nanomater. Biostruct.*, 18(3) (2023) 881-887.

[8] S.H. Mahdi et al., "Preparation and study the partial substitution of aluminum with copper on some physical properties of the compound $TlSr_2Ca_2Cu_3O_{8+\delta}$", *AIP Conf. Proc.*, 2769 (2023) 020041.

[9] S.H. Jobayr et al., "Effect of antimony on characteristics of $HgBa_2CaCu_{2-x}Sb_xO_{8+\delta}$ superconducting", *J. Ovonic Res.*, 18(3) (2022) 357-371.

[10] N.S. Abed et al., "Manufacturing and studying the effect of partial substitution on the properties of the compound $Bi_{2-x}Ag_xSr_{1.9}Ba_{0.1}Ca_2Cu_3O_{10+\delta}$ superconductors", *IOP J. Phys.: Conf. Ser.*, 1178 (2019) 012025.

[11] N.S. Abed et al., "Partial substitution of Zn effects on the structural and electrical properties of high-temperature HgAgBaCaCuO superconductors", *IOP J. Phys.: Conf. Ser.*, 1003(1) (2018) 012098.
[12] A.K. Saadon, "Studying the Effect of Zirconia on Some Physical Properties of Porcelain", *Ibn Al-Haitham J. Pure Appl. Sci*., 29(3) (2016).
[13] G.J. Ibraheem, "The Alternative Electrical Properties of (Al-$CdSe_{0.8}Te_{0.2}$-Al) Capacitor at Room Temperature", *Ibn Al- Haitham J. Pure Appl. Sci*., 22(4) (2009).
[14] H.M.J. Haider and K.A. Jasim, "Effect of Composition and Dielectric Properties for (YBCO) Superconductor Compound in Different Preparation Methods", *Ibn Al-Haitham J. Pure Appl. Sci.*, 33(1) (2020).
[15] A.K. Saadon, "Preparation and Study of Some Electrical Properties of Mn-$NiFe_2O_4$", *Ibn Al-Haitham J. Pure Appl. Sci.*, 26(3) (2013).
[16] A.K. Saadon, "The Effect of Silica SiO_2 on the Dielectric and Physical Properties of Mn–Ni Ferrite", *Ibn Al-Haitham J. Pure Appl. Sci.*, 25(3) (2012).
[17] G.A. Naeem, "Effect of Temperature and Nickel Concentration on the Electrical and Dielectric Properties of Polyethylene-Nickel Composites", *Ibn Al-Haitham J. Pure Appl. Sci.*, 29(1) (2016).
[18] K.A. Jasim, M.A.N. Thejeel and R.S. Al-Khafaji, "The Effect of Doping by Sr on the Structural, Mechanical and Electrical Characterization of $LaBa_{1-x}Sr_xCa_2Cu_4O_{8.5+\delta}$", *Ibn Al-Haitham J. Pure Appl. Sci*., 27(1) (2014).
[19] S.B.H. Farid, "Dielectric Properties of High Alumina Glass", *Ibn Al- Haitham J. Pure Appl. Sci*., 21(4) (2008).
[20] S.H. Mahdi et al., "Epoxy/Silicone Rubber Blends for Voltage Insulators and Capacitors Applications", *Ener. Proc.*, 119 (2017) 501-506.
[21] B.H. Hussein et al., "Synthesis and Study the Structure, electrical and optical properties of BiCdSrCaCuO thin film Superconductors", *Ener. Proc.*, 157 (2019) 100-110.
[22] X.J. Wu, International Superconductivity Technology Center, Japan, private communication (1999), PCPDFWIN (50-1838).
[23] R.H. Ghani, "Studying the Effect of Partial Substitution of Zinc Instead of Copper on the Structural and Electrical Properties of Some Superconducting Compounds", MSc thesis, University of Kufa, Iraq (2023).
[24] S.H. Mahdi et al., "Fabricated and investigated the structure and super conductivity properties of BiSrCaCuO compound", *AIP Conf. Proc.*, 1968 (2018) 030043.
[25] ASTME 2456-06 Standard Terminology Relating To Nanotechnology (2020), DOI:10.1520/2456-06R20
[26] K.A. Jassim et al., "Study characteristics of (epoxy-bentonite doped) composite materials", *Ener. Proc.*, 119 (2017) 670-679.

Table (2) Lattice parameters and phase sizes for three compounds $PbSr_2Ca_2Cu_{3-Y}Zn_YO_{8+\delta}$ samples where (Y =0.0.06 and 0.12%)

Ratio (Y%)	a(Å)	b(Å)	c(Å)	c/a	V(Å)^3	ρ_m (g/cm^3)	HTP (%)	LTP (%)
0	3.7968	3.6612	18.5669	4.8902	258.100	5.0255	55.10	44.90
0.06	3.8002	3.5483	18.7339	4.9297	252.612	5.1354	47.94	48.87
0.12	3.8238	3.5418	18.7269	4.8974	253.623	5.1156	51.13	47.72

Proceedings of 5th International Specialized Conference of Education College on Physics and Applied Sciences (5thICECAS24), 22-23 April 2024

Effect of Cold Plasma Jetting on Optical Properties and Surface Morphology of CuO Thin Films Prepared by RF Magnetron Sputtering

Basim A. Zachi [1]
Abdul H.A. Khadayeir [2]
Ziad M. Abood [1]

[1] *Department of Physics, College of Education, Mustansiriyah University, Baghdad, IRAQ*
[2] *Department of Physics, College of Education, Al-Qadisiyah University, Diwaniyah, IRAQ*

In this study, CuO films were prepared on glass substrates by RF magnetron sputtering plasma method. The roughness of the films was investigated and found to decrease with increasing AC voltage. Optical properties of the prepared films were also examined in the wavelength range 300-1000nm. For all prepared films, optical absorption and absorption coefficient were found to decrease with increasing wavelength. The optical energy gap increased from 2 to 2.24eV before and after exposure to the cold plasma jet.

Keywords: Cold plasma jet; Thin films; RF sputtering; Plasma deposition
Received: 19 January 2024; Revised: 4 March 2024; Accepted: 4 April 2024

1. Introduction

By carefully controlling the condensation of individual ionic species, atoms, molecules, and particles, thin films are defined as layers formed on top of solid materials, either physically through physical processes or indirectly chemically through chemical or electro chemical reactions [1]. Two types of copper oxides are known, the most common being cuprite (Cu_2O) and tenorite (CuO) [2,3]. Higher oxides of copper are copper (II) oxides, often known as copper oxides (CuO). CuO is called tenorite as a mineral, is a dark solid, its crystalline structure is an ionic, and it melts at temperatures above 1200°C, losing some oxygen. CuO is an attractive for many researchers because of its potential uses in solar cells, catalysis, and magnetic devices [4,5]. CuO has a wide range of applications, including photovoltaic materials, solar cells, chromium electroplating, gas sensors, catalytic cells, and super capacitors [6,7]. CuO has many advantages, including non-toxicity, availability of unrefined components, low production cost, small energy gap, and electrical and thermal properties [7-10]. Thermal oxidation, electrolytic deposition, RF magnetron sputtering, and induced physical vapor deposition methods have been used to prepare copper oxide films [7,9,11,12]. In this study, CuO films are prepared by RF magnetron sputtering followed by cold plasma jet treatment, and optical properties before and after cold plasma jet (CPJ) irradiation are compared.

2. Experimental Part

The thin films were prepared using the reactive RF method of magnetron sputtering. The deposition target was 99.99% pure Cu, in the form of a disc 5cm in diameter, and the surface was smoothed with coarse grits and paper. Experiments were performed using a Varian D S219 rotary pump with a mixing ratio of oxygen to argon (1:7) to obtain sufficient pressure to oxidize pure Cu to form CuO. The vacuum pressure during evaporation was approximately 2×10^{-2} torr. The boat was placed at a distance of 7 cm from the substrate. The substrate temperature reached 350°C. Thin films were deposited on commercial glass slides. Before deposition, the substrates were cleaned with detergent and gauze, rinsed repeatedly with distilled water, washed with detergent solution, washed with distilled water, and finally washed with ethanol solution. The glass substrates were cleaned with isopropyl alcohol using an ultrasonic cleaner, and the substrates were air dried. The Cu target was irradiated by RF magnetron sputtering, and the effect on the morphology and optical properties of the deposited films was investigated. The deposition time was 2 hours and the film thickness was 222.21 nm. Cold plasma jetting was then per formed with a frequency of 75 kHz, gas flow rate of 50 L/h, AC voltage of 10-20kV, and exposure time of 10 s.

3. Results and Discussion

The crystal structure of the copper oxide thin films was determined by x-ray diffraction (XRD). Figure (1) shows the XRD patterns of CuO thin films

deposited on glass substrates by RF magnetron sputtering. The XRD results show that the deposited films are polycrystalline and contain CuO and Cu_4O_3. Furthermore, the CuO films were found to have larger particles than the Cu_4O_3 films. The preferred orientation was 34.752°, which is consistent with [9], according to which the results agreed with the cards for CuO (48-1548) and (45-0937), Cu_4O_3 (49-1830) and Cu_2O (34-1354). Table (1) details the XRD results.

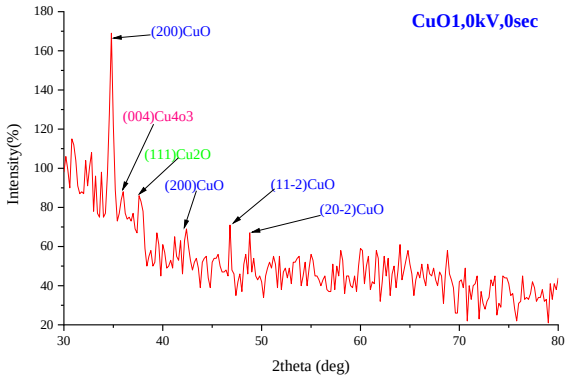

Fig. (1) XRD pattern of CuO thin film deposited onto a glass substrate at 350°C

The surface topography of the CuO thin film analyzed using atomic force microscopy (AFM) is shown in Fig. (2). The AFM image results show the effect of increasing the alternating voltage of the cold plasma jet on the surface roughness of the prepared thin films, and the surface roughness and root mean square roughness of the prepared CuO thin films decrease after the cold plasma jet treatment as shown in table (2).

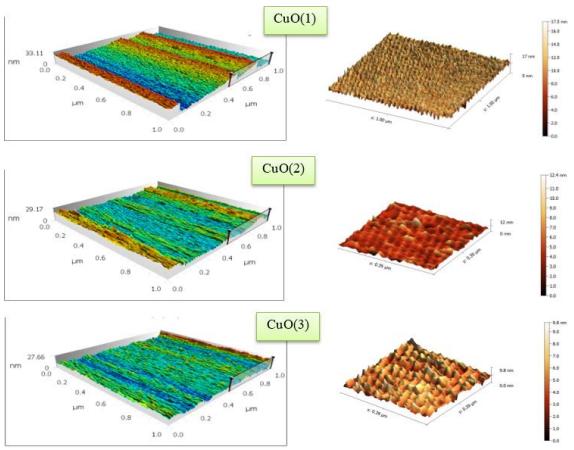

Fig. (2) AFM results of cupric oxide films deposited for (CuO (1) before, after CuO(2), and CuO(3)) treated with cold plasma jetting at, different AC voltages (10-20kV), respectively, with exposure time of 10s

The surface roughness decreased after treatment with cold plasma jet as shown in table (2). The AFM images showed that the prepared thin films were homogeneous and had good adhesion. The surface was tight and homogeneous, consistent with [13]. The surface of each CuO thin film is uniformly granular and smooth. Optoelectronic devices, gas sensors, and biosciences have all benefited greatly from these Nano structured films [14,15].

Table (2) Results of AFM analysis of CuO thin films

Type of system	Parameter's	CuO1	CuO2	CuO3
Mountains SPIP® Expert 8.2.9843	Roughness (Sa) (nm)	6.489	4.898	2.637
	Sms (Rq) height nm	9.047	5.979	3.295

Figure (3) illustrates the surface of the cuprous oxide films using FE-SEM images, from which it is clear that these films have a completely homogeneous nanostructure, which is well-defined, coarse, and has small pores without holes or exfoliation sat the macroscopic level. The obtained granules are almost homogeneous in shape, oval or spherical. These samples were deposited at substrate temperature 350°C-1D52 and their roughness and average roughness are shown in table (2), CPJ is an important source of hydroxyl radicals as well as oxygen, which leads to an increase in the surface energy of the electrode [13,16,17].

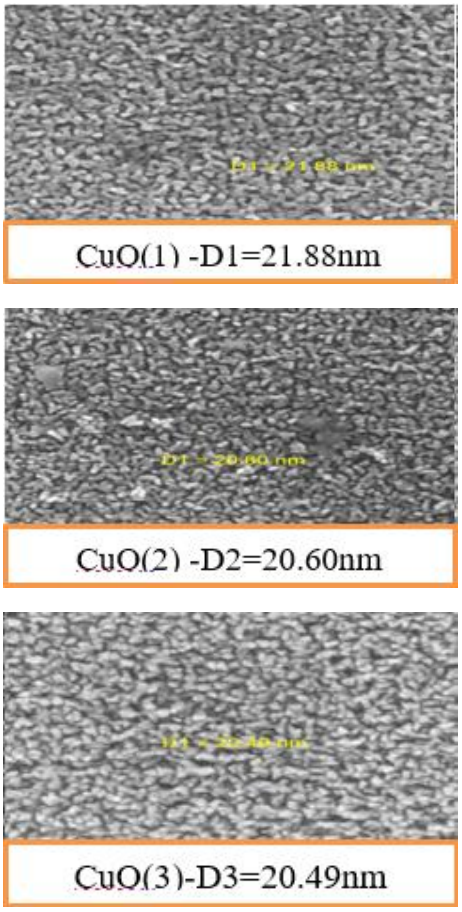

Fig. (3) The FE-SEM images of cupric oxide films deposited, for (CuO(1) before, after CuO(2), and CuO(3)) treated with cold plasma jetting at, different AC voltages (10-20kV), respectively, exposure time of 10s

Optical properties of copper oxide thin films were measured at room temperature in the wavelength range 200-1100nm using an Ocean Optics USB4000-UV-visible fiber optic spectrometer. From the optical absorption spectra in Fig. (4), it is observed that the optical absorption of the thin films prepared before exposure to the cold plasma jet decreases with increasing wavelength, whereas after exposure to the cold plasma jet, the optical absorption of the thin films increases with increasing AC voltage of the exposure to the cold plasma jet. Increasing the AC voltage can increase the grainsize of the thin film [12]. The reason for this is that photon shave higher energy at shorter wavelength sand are absorbed, resulting in higher absorbance, and the films have potential applications in solar cell fabrication [12,18], and reflection-free coatings [13].

The optical transmittance spectrum in Fig. (5) shows that the optical transmittance of the thin film fabricated before cold plasma jet irradiation increased with increasing wave length. However, after cold plasma jet irradiation, the optical transmittance decreased with increasing cold plasma jet irradiation voltage. It is thought that the increase in AC voltage increased the particle size of the copper oxide thin film, resulting in a decrease in transmittance. Photons are absorbed at lower wavelengths due to their high energy, resulting in lower transmittance [19,20]. The use of these films as detector windows allows for solar cell applications in the infrared region [21].

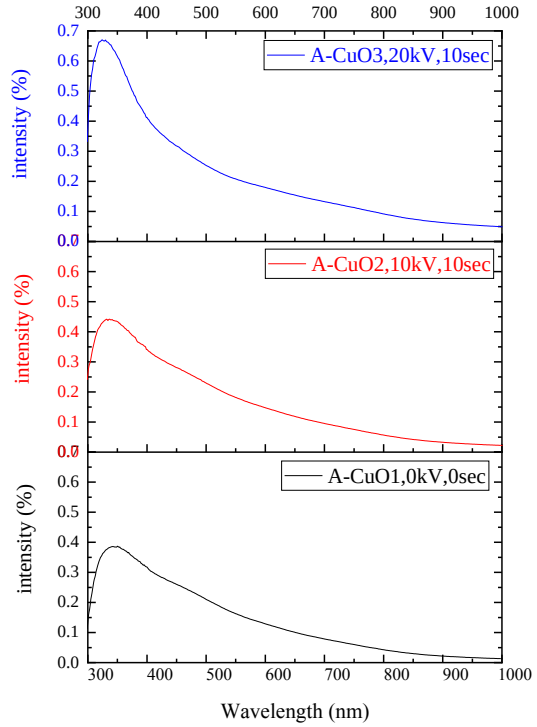

Fig. (4) The absorption spectra of (CuO) films, for (A1 before, after A2, and A3) treated with cold plasma jetting at, different AC voltages (10-20kV), respectively, exposure time of 10s

From the light transmittance spectral data, the absorption coefficient was determined by the following equation

$$\alpha = \frac{\ln\frac{1}{T}}{t} \quad (1)$$

Here, transmittance is T, film thickness is t, and cross-sectional are a is used for the measurement [22]. Figure (6) shows that the absorption coefficient (α) decreases with increasing wavelength. It is also shown that the optical absorption coefficient increases with increasing AC voltage and exposure to low-temperature plasma jets. This is because ($\alpha > 10^4 cm^{-1}$), it is within the high absorption region. This helps to increase the likelihood of direct transitions occurring [23,24].

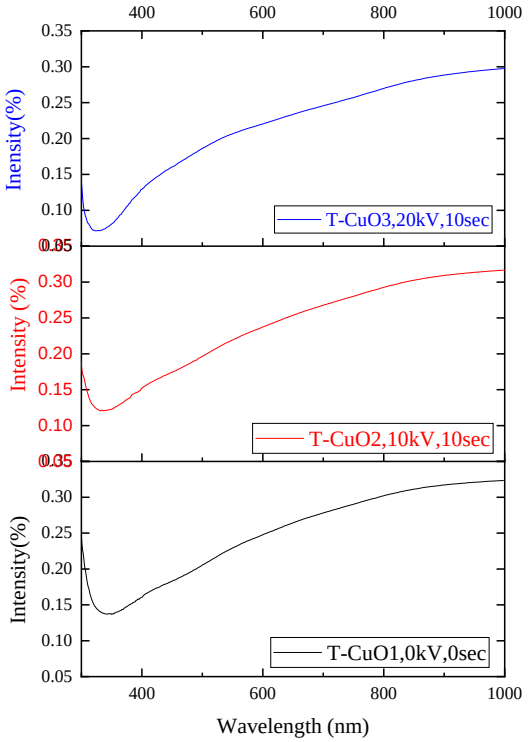

Fig. (5) The transmission spectra of cupric oxide films deposited, for (T1 before, after T2, and T3) treated with cold plasma jetting at, different AC voltages (10-20kV), respectively, exposure time of 10s

The relationship between the photon energy (hν) and the absorption coefficient (α) of the directly allowed transitions is given by the theory of optical absorption: according to Tuac's relation, the dependence of the absorption coefficient (α)of the photo-induced transitions on the photon energy (hν) is [25].

$$\alpha h\nu = k(h\nu - \mathrm{Eg})^n \quad (2)$$

The absorption coefficient is α, hν is the photon energy, the constant is k, E_g represents the optical energy gap, n is a number determined by the type of transition, direct transmission is allowed (n = 1/2) or prohibited (n = 3/2), indirect transmission is allowed (n = 2) or prohibited (n = 3) , and E_g was calculated for. Figure (7) shows a graph of $(\alpha h\nu)^2$ versus hν, and

E_g was calculated by extrapolating the straight part of the curve to zero absorption [26,27].

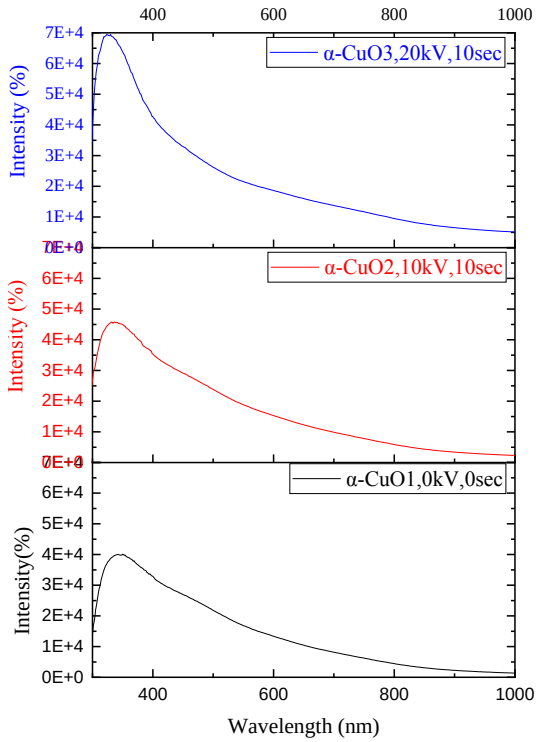

Fig. (6) The Absorption coefficient plot of cupric oxide films deposited, for (α1 before, after α2, and α3) treated with cold plasma jetting at, different AC voltages (10-20kV), respectively, exposure time of 10s

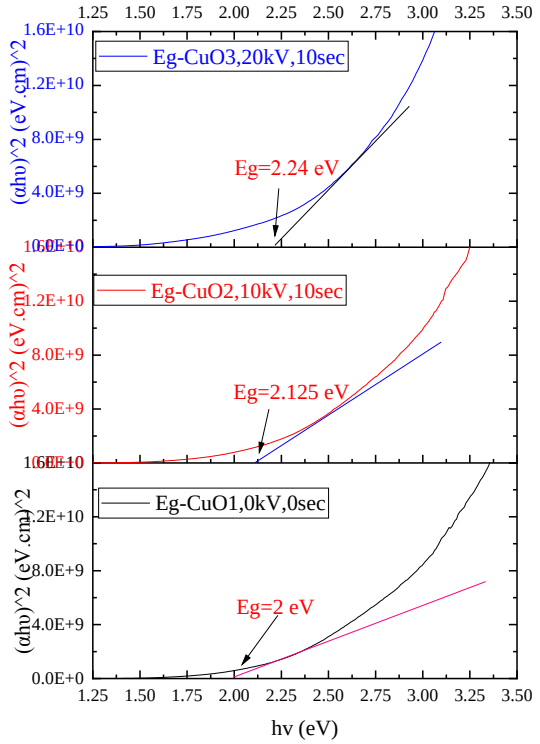

Fig. (7) The energy gap of cupric oxide films deposited, for (Eg1 before, after Eg2, and Eg3) treated with cold plasma jetting at, different AC voltages (10-20kV), respectively, exposure time of 10s

The results show that the optical energy gap (E_g) increases with exposure to low-temperature plasma. This energy gap is higher than the value of the energy gap of copper oxide thin films, which is consistent with [13,23,26,27]. It is possible that the energy gap is higher due to the removal of defects and disorder in the prepared films [17]. Quantum confinement effects are responsible for the shift of the direct energy gab higher than the bulk value (2.24eV). As a result, semiconductor devices such as fiber optic communication systems, image amplifiers, and modulators can utilize these nanoparticles [16].

4. Conclusion

After preparing CuO films using RF sputtering technique and exposing them to cold plasma jets, it caused a change in both the roughness and optical properties of the prepared films. We conclude that cold plasma jetting is an effective method to modify the properties of thin films.

Acknowledgments

The authors would like to acknowledge the support provided by Al-Qadisiyah University, Iraq and Mustansiriyah University.

References

[1] M. S. Cohen and K. L. Chopra, “Thin film phenomena.” McGraw-Hill, New York, 1969.

[2] A. Tamm, A. Tarre, V. Verchenko, H. Seemen, and R. Stern, “Atomic layer deposition of superconducting CuO thin films on three-dimensional substrates,” *Crystals*, vol. 10, no. 8, p. 650, 2020.

[3] O.A. Hammadi, “Production of Nanopowders from Physical Vapor Deposited Films on Nonmetallic Substrates by Conjunctional Freezing-Assisted Ultrasonic Extraction Method”, *Proc. IMechE, Part N, J. Nanomater. Nanoeng. Nanosys.*, 232(4) (2018) 135-140.

[4] W. A. A. Alhassan and I. A. Wadi, “Determination of optical energy gap for copper oxide at different temperatures,” *Int. J. Adv. Eng. Res. Sci.*, vol. 5, no. 3, p. 237422, 2018.

[5] M.A. Hameed, S.H. Faisal, R.H. Turki, “Characterization of Multilayer Highly-Pure Metal Oxide Structures Prepared by DC Reactive Magnetron Sputtering Technique”, *Iraqi J. Appl. Phys.*, 16(4) (2020) 25-30

[6] A. Dey *et al.*, “Ultrafast epitaxial growth of CuO nanowires using atmospheric pressure plasma with enhanced electrocatalytic and photocatalytic activities,” *Nano Sel.*, vol. 3, no. 3, pp. 627–642, 2022.

[7] W.-J. Lee and X.-J. Wang, “Structural, optical, and electrical properties of copper oxide films grown by the silar method with post-annealing,” *Coatings*, vol. 11, no. 7, p. 864, 2021.

[8] A. M. Selman, M. A. Mahdi, and Z. Hassan, “Fabrication of Cu2O nanocrystalline thin films

photosensor prepared by RF sputtering technique," *Phys. E Low-dimensional Syst. nanostructures*, vol. 94, pp. 132–138, 2017.
[9] G. Mahendra *et al.*, "RF sputter-deposited nanostructured CuO films for micro-supercapacitors," *Appl. Nano*, vol. 2, no. 1, pp. 46–66, 2021.
[10] J. Lee, T. S. Williams, and R. F. Hicks, "Atmospheric pressure plasma reduction of copper oxide to copper metal," *J. Vac. Sci. Technol. A*, vol. 39, no. 2, 2021.
[11] P. I. Kyesmen, N. Nombona, and M. Diale, "A promising three-step heat treatment process for preparing CuO films for photocatalytic hydrogen evolution from water," *ACS omega*, vol. 6, no. 49, pp. 33398–33408, 2021.
[12] A.M. Hameed and M.A. Hameed, "Highly-Pure Nanostructured Metal Oxide Multilayer Structure Prepared by DC Reactive Magnetron Sputtering Technique", *Iraqi J. Appl. Phys.*, 18(4) (2022) 9-14.
[13] O. Diachenko *et al.*, "Structural and optical properties of CuO thin films synthesized using spray pyrolysis method," *Coatings*, vol. 11, no. 11, p. 1392, 2021.
[14] R. A. Hammoodi, A. K. Abbas, and A. K. Elttayef, "Structural and optical properties of CuO thin films prepared via RF magnetron sputtering," *Int. J. Appl. or Innov. Eng. Manag.*, vol. 3, no. 7, 2014.
[15] S. Siol *et al.*, "Band alignment engineering at Cu2O/ZnO heterointerfaces," *ACS Appl. Mater. Interfaces*, vol. 8, no. 33, pp. 21824–21831, 2016.
[16] A. Dey *et al.*, "Atmospheric pressure plasma engineered superhydrophilic CuO surfaces with enhanced catalytic activities," *Appl. Surf. Sci.*, vol. 564, p. 150413, 2021.
[17] A. A. Radhakrishnan and B. B. Beena, "Structural and optical absorption analysis of CuO nanoparticles," *Indian J. Adv. Chem. Sci*, vol. 2, no. 2, pp. 158–161, 2014.
[18] S. Hussian, ", Optical characteristics of CuO thin film prepared by Chemical spray pyrolysis," *Int. J. Adv. Res.*, vol. 4, no. 6, pp. 428–434, 2016.
[19] M. G. Faraj, A. K. Kaka, and H. D. Omar, "Electrical and Structural properties of Copper Oxide (CuO) thin films on Plastic substrate deposited by spray pyrolysis technique," *ARO-The Sci. J. Koya Univ.*, vol. 7, no. 2, pp. 14–18, 2019.
[20] S. S. Roy, A. H. Bhuiyan, and J. Podder, "Optical and electrical properties of copper oxide thin films synthesized by spray pyrolysis technique," *Sensors & Transducers*, vol. 191, no. 8, p. 21, 2015.
[21] S. A. M. H. M. Ali and S. A. Makki, "The thickness effects characterization properties of copper oxide thin films prepared by thermal evaporation technique," *J. Multidiscip. Eng. Sci. Stud.*, vol. 2, pp. 532–535, 2016.
[22] M. Patel, M. Kumar, H.-S. Kim, W.-H. Park, E. H. Choi, and J. Kim, "Reactive sputtering growth of Co3O4 thin films for all metal oxide device: a semitransparent and self-powered ultraviolet photodetector," *Mater. Sci. Semicond. Process.*, vol. 74, pp. 74–79, 2018.
[23] B. K. H. Al-Maiyaly, I. H. Khudayer, and A. J. Ibraheim, "Effect ambient oxidation on structural and optical properties of copper oxide thin films," *Int. J. Innov. Res. Sci. Eng. Technol*, vol. 3, pp. 8695–8700, 2014.
[24] R. M. Obodo *et al.*, "Influence of pH and annealing on the optical and electrochemical properties of cobalt (III) oxide (Co3O4) thin films," *Surfaces and Interfaces*, vol. 16, pp. 114–119, 2019.
[25] M. Manickam, V. Ponnuswamy, C. Sankar, R. Mariappan, and R. Suresh, "Influence of substrate temperature on the properties of cobalt oxide thin films prepared by nebulizer spray pyrolysis (NSP) technique," *Silicon*, vol. 8, pp. 351–360, 2016.
[26] T. Ehara, R. Iizaka, M. Abe, K. Abe, and T. Sato, "Preparation of CuAlO2 thin films by radio frequency magnetron sputtering and the effect of sputtering on the target surface," *J. Ceram. Sci. Technol.*, vol. 8, no. 1, pp. 7–12, 2017.
[27] K. Yin *et al.*, "Unsupported single-atom-thick copper oxide monolayers," *2D Mater.*, vol. 4, no. 1, p. 11001, 2016.

Table (1) Results of the XRD analysis of CuO films

Type	2θ (deg)	d (nm)	β (deg)	XS_G (nm)	XS_C (nm)	(hkl)	Crystal System	Reference Card
CuO	34.752	0.25793	0.676	12	12.31	(002)	Monoclinic	48-1548
Cu_4O_3	36.116	0.2485	1.302	6	6.41	(004)	Tetragonal	49-1830
Cu_2O	37.843	0.23754	0.739	11	11.36	(111)	Cubic	34-1354
Cu_2O	42.489	0.2126	0.738	11	11.54	(200)	Monoclinic	34-1354
CuO	46.938	0.1934	0.483	18	17.93	(11-2)	Monoclinic	48-1548
CuO	48.807	0.1864	1.155	7	7.55	(-202)	Monoclinic	45-0937

Proceedings of 5th International Specialized Conference of Education College on Physics and Applied Sciences (5thICECAS24), 22-23 April 2024

Bashaer S. Faris
Ahmed N. Abd
Basaad H. Hamza

Department of Physics, College of Science, Mustansiriyah University, Baghdad, IRAQ

Synthesis of Tin Oxide Nanoparticles by Celery Leaves Extract for Antibacterial Activity

Tin oxide nanoparticles (SnO_2 NPs) were prepared by a biological method using plant extracts as reducing agents. Celery extract serves as both a reducing agent and a protective layer for the Sn ions. The prepared tin oxide nanoparticles were crystalline. Antimicrobial and antifungal properties of these nanoparticles were demonstrated. While it had an inhibition effect of about 16 mm on Candida, E. coli, and Klebsiella sp., the corresponding effects were 18 mm and 15 mm, respectively.

Keywords: Tin oxide; Nanostructures; Biosynthesis; Antifungal effects; Celery extract
Received: 19 January 2024; Revised: 4 March 2024; Accepted: 4 April 2024

1. Introduction

Despite developments in these fields, nanotechnology is still vital to the study of materials in general, and to the establishment of their basic properties in particular, in contexts where the microscopic scale is crucial. [1]. Therefore, nanoparticles are now very important in all areas of chemistry, as well as in business and health. In nanobiotechnology, the main focus is on integrating nanotechnology into different biological systems. This field is focused with the coupling of nanotechnology and biology. The creation of nanomaterials and nanoparticles that are biocompatible, environmentally safe, and biogenic is another application of nanobiotechnology [2-4].Materials, systems, and devices at the atomic and macromolecular levels are the focus of nanoscience, while nanotechnology encompasses a wide range of techniques for manipulating structures, materials, and devices at the nanoscale in design, synthesis, characterization, and application. It is common for the dimensions to be less than 100 nanometers (<100 nm) in scale. [5].An important n-type semiconductor with a 3.6 eV band gap, SnO2 has many uses in electronics, optics, sensors, and rechargeable batteries. The synthesis of SnO2 NPs has been accomplished using various methods, such as sol-gel, hydrothermal, co-precipitation, solve thermal, and chemical vapor deposition. Nevertheless, because of their low cost, ease of handling, and environmental acceptability, nanomaterials synthesized from plant resources are preferred. Utilizing XRD, SEM, AFM, FTIR, and UV-Vis data inside the biological approach, the surface and structural characteristics of the synthesized SnO2 NPs were investigated [6].Crucial are eco-friendly technologies and nanoparticles produced in a sustainable manner [7, 8]. "Biogenic synthesis" is an emerging field of nanotechnology that has the potential to create nanoparticles in an eco-friendly and cost-effective way [9–11]. In this research, we discuss the preparation of celery extract used to reduce tin salts to prepare tin oxide nanoparticles and use them for medical applications.

2. Experimental Part

Plant extract-mediated bio reduction is the usual procedure for producing nanoparticles at temperatures below 80°C. This involves mixing an aqueous plant extract with an aqueous solution of the metal salt and deionized water. Figure (1) demonstrates that the time required to complete this technique might range from thirty minutes to an hour or more, depending on how long it takes for the plant to dissolve. Consequently, in order to produce high-quality nanomaterials (artificial methods), a straightforward and easy biosynthesis of mineral nanoparticles is necessary. Natural occurrences in biological systems are a part of the biological pathway, which follows the laws of nature. The term "green nanotechnology" has recently gained a lot of traction. Due to its strict crop management restrictions and high sanitary requirements, microbial-mediated synthesis, a biological approach for generating NPs, is not now commercially practicable [12].

In Fig. (2), we can see a solution of celery extract with SnO_2 NP_s. The process of creating SnO_2 nanoparticles using celery extract yields these results. In order to make an aqueous solution, the celery plant is ground to a consistency of 150 mL in distilled water heated to 50 to 60 degrees Celsius. Then, 2 grams of the plant are added gradually and left at the same temperature for 30 minutes. The solution turns

yellow after a while. A gradual shift in color indicates the creation of tin oxide nanoparticles, represented by the symbol (B2). Once cooled in a beaker, the extract was filtered using filter paper. In a 100 mL beaker, dissolve 1.89g of SnCl2 at 60°C for one hour under standard atmospheric pressure. After being thoroughly mixed at 60°C, the extract (15 mL) was added.

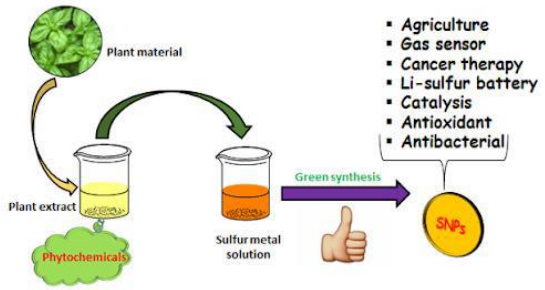

Fig. (1) Green synthesis method [13]

Fig. (2) Celery plant and (SnO_2) NP_s solution

A variety of characterization techniques were used to describe the production of SnO_2NP_s. These included x-ray diffraction (XRD), field-emission scanning electron microscopy (FE-SEM), atomic force microscopy (AFM), Fourier-transform infrared (FTIR) spectroscopy, and UV-visible spectroscopy. Determining the degree of a drug's influence on the environment and human health may require the detection or diagnosis of the substance.

3. Results and discussion

One helpful method for studying crystalline materials is X-ray diffraction. Sample orientation, lattice parameters, composition, and crystalline phase can all be ascertained using this method. Figure (3) displays the X-ray diffraction pattern (XRD) of a biosynthetic tin oxide nanostructured film that was cast on a glass substrate using a three-drop drop casting procedure [14]. The reflections of (110), (101), (211), and (301) are identical to the patterns of SnO_2 reference (JCPDS card 00-046-1088), as is readily apparent. The size of the biosynthesized SnO_2 nanocrystals was also determined using the Debye-Scherrer formula [15-17], as shown in table (1).

$$D = \frac{0.9\lambda}{\beta \cos\theta} \quad (1)$$

where D or C.S., λ, β or FWHM and θ are crystalline size, wavelength for x-ray which is equal to 1.5406Å, the full-width at half maximum, and a degree of the diffraction or the Bragg angle, respectively

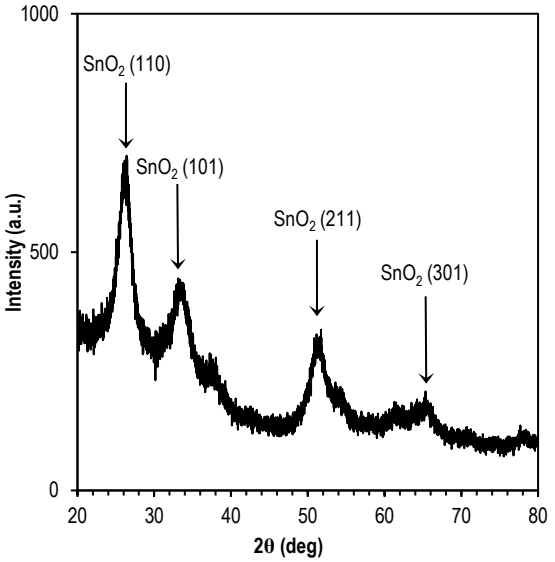

Fig. (3) XRD pattern of SnO_2 nanostructure, which precipitated on a glass

Table (1) Structural parameters of B2 nanostructure

Method	2θ (deg)	FWHM (deg)	D (nm)	η X 10^2	σ (LINE/m^2)
Biological	25.9	1.828	4.442	7.799	50.665
	32.8	2.303	3.583	9.670	77.885
	51.03	3.514	2.497	13.8750	160.347
	65.3	4.401	2.138	16.203	218.685

The heat treatment technique causes micro-strains and structural dislocations in the film. Equation (2) calculates the dislocation density [18]:

$$\sigma = \frac{1}{D^2} \quad (2)$$

Where **δ** is the dislocations density, where the micro-strain of the film was estimated using the equation [18]:

$$\eta = \frac{\beta \cos\theta}{4} \quad (3)$$

Tin oxide nanoparticles made using the green synthesis method were studied for size, shape, and morphology with the use of field-emission scanning electron microscopy (FE-SEM), which examines material's morphology at extremely high magnifications [19]. An examination was carried out using FE-SEM at 1.00kx and 120.00kx magnifications, with a resolution varying from 10μm to 500nm, as shown in Fig. (4). Tin oxide nanoparticles were produced using an environmentally friendly process, and their size, shape, and morphology were examined using FE-SEM technology. Drop casting was employed to biosynthesize and fabricate the B2 thin film on a glass

substrate. A value of about 72.20 nanometers was produced by the nanostructure.

Figure (5) displays the results of the surface topographic analysis, a method for identifying and mapping the topography of surfaces with micro and nano dimensions, conducted on films generated using the biosynthetic process and applied onto glass substrates at a temperature of 80°C. Such surfaces were photographed and studied using a high-powered atomic force microscope (AFM) [20]. The outcomes are shown in Fig. (5).

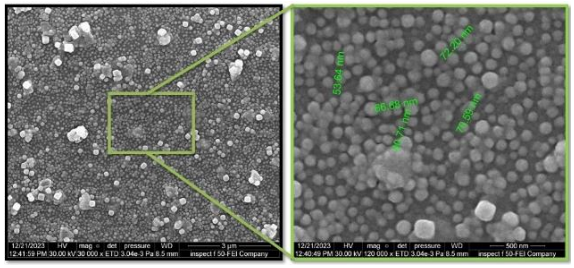

Fig. (4) FE-SEM images of green synthesized SnO_2 NPs deposited on a glass (scale bar = 3µm, 500nm)

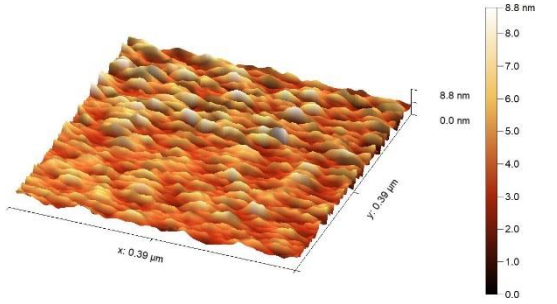

Fig. (5) 3D AFM image for SnO_2 NPs

One intriguing tool utilized in nanotechnology for gauging the pliability of micro and nanoparticles is the atomic force microscope. Scanning microscope probes (SPMs) include instruments like atomic force microscopes. Surface areas of insulators and conductors are the usual targets for its measurement capabilities. It also gives us precise data on the quantity and size of grains, the surface roughness, and the rate of surface roughness (RMS).

The functional groups discovered in the material being examined are depicted in Fig. (6) [21]. Using FTIR spectroscopy to look into the many vibration modes that the chemical bonds involved in SnO_2 NP_s biosynthesis could exhibit [22]. The functional groups were recorded within the range between 400-4000 cm^{-1}, and figure (6) clearly shows this. FTIR spectra of B2 NPs can be seen in it, and it shows strong peaks at 547, 1074, 1111, 2359, 2600, 2853 and 3371 cm^{-1}. Alcohols, phenols with hydroxyl O–H may be identified by the peak located at 3371cm^{-1}. CH and CH_2 stretching aliphatic group are responsible for the peak at 2853cm^{-1}, the alkynes groups' C≡C and C-O-C polysaccharide modes are responsible for the peak at 1111cm^{-1}, and C-O carbohydrate modes are responsible for the peak at 1074cm^{-1}. Finally, for CH out of plane aromatic band which is located at the peak 547cm^{-1}. Biosynthesis-produced nanoparticles have UV-visible absorption spectrum, which is explained in Fig. (7).

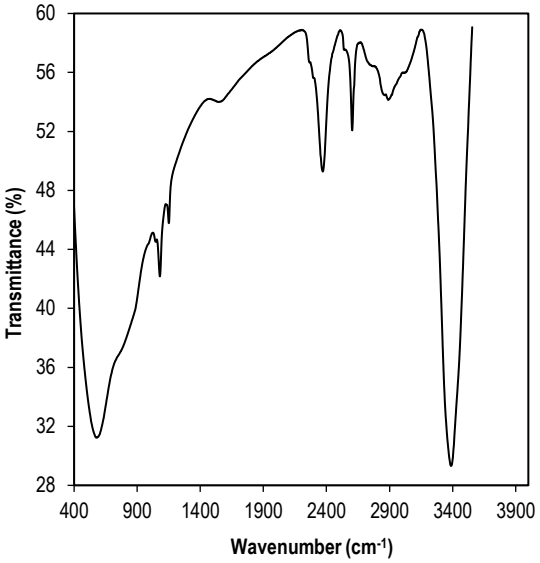

Fig. (6) FTIR spectrum for the transmittance of (SnO_2) NP_s synthesized method

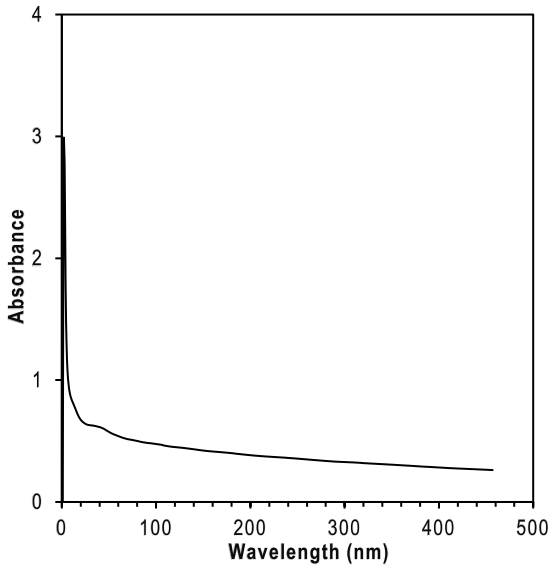

Fig. (7) UV-visible absorption spectrum of SnO_2 NP_s colloid

While most of the 10 million annual fatalities and numerous chronic illnesses caused by microbiological infections occur in tropical nations, the developed world is not immune either. Antibiotics have been utilized to treat bacterial illnesses due to their efficacy and affordability. While antibiotics have undoubtedly helped biobiotics, their abuse has led to bacterial resistance mechanisms and the subsequent rise of multidrug-resistant microbes [23]. The rise of drug-resistant bacteria has left doctors with little choice but to resort to extreme measures to treat their patients. Because antibiotics encourage the emergence and evolution of strains with varied genetic and phenotypic features, their

promise as therapeutic agents is diminished by their overuse. Bacteria can cover themselves with a biofilm and start multiplying. They become immune to antibiotics when they clump together and encase themselves in an extracellular matrix they create [24]. Antidrug resistance ranks high among the most pressing global public health concerns. Consequently, there has to be a change in approach to treating microbial diseases. Biological imaging, medication delivery, and antibacterial activity are just a few of the biological applications of nanoparticles due to their unique physical and chemical properties, which include a large surface area, optical qualities, antimicrobial activity, catalytic activity, electrical characteristics, and magnetic properties [25]. Even now, people are talking about it [26]. Nanoparticles' effects on bacteria and fungi are a matter of debate. Nanoparticles have the ability to bind to the cell wall of bacteria or fungi, which they can then penetrate to change the structure of the cell membrane, making it more permeable. This process leads to the death of the bacteria. Metal oxide nanoparticles have recently been recognized as an effective antimicrobial agent with the ability to target several locations within and outside of cells. One mechanism by which nanoparticles exert their antibacterial effects is through the ions they emit. Their high surface area to volume ratio and diminutive size allow them to bind tightly to tiny membranes, which enhances their activity even further. Based on the composition and structure of their cell walls, bacteria can be classified as either Gram-positive (+) or Gram-negative (-). When it comes to the impact of nanoparticles on bacteria, the makeup and chemistry of the cell walls of Gram-positive and Gram-negative bacteria are significantly different. Candida, a type of fungus that can cause skin infections, is one of the many types of fungi shown in Fig. (8), which also includes other types of fungi worldwide [27].

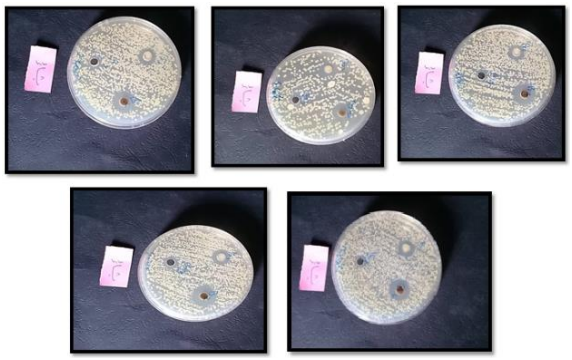

Fig. (8) Antibacterial activity of SnO_2 NPs

4. Conclusion

There are several ways to prepare tin oxide nanoparticles, but one of the most effective is the green synthesis method. This approach uses salts and plants instead of water, and it generates vast quantities of tin oxide nanoparticles of highly inexpensive quality. Additionally, it poses less of a threat than any of the alternatives. Thus, our research has laid down a quick method for creating SnO2 nano-structures utilizing celery extract in a biological approach to SnO2 manufacture or green synthesis. All of the outcomes were nanoscale, which proves that green synthesis is a viable method for making nanoparticles. Because it is a sustainable, nontoxic, environmentally friendly, and cost-effective process, green NPs production has garnered a lot of attention. Using various plant materials, microorganisms, and naturally existing proteins, several studies have shown that SnO_2 NPs can be synthesized in an ecologically friendly manner. Regardless of their origin, the literature review reveals that green substrates act as reducing agents, stabilizing agents, and caps.Because plant-mediated synthesis is less expensive, easier to handle, and less hazardous than utilizing microbes, it is one of the more environmentally acceptable methods of synthesizing SnO_2.

References

[1] E.A. Latief, A.T. Mohi and A.N. Abd, "Effect of Natural Dye on the Spectral Response of the Heterojunction Ag/ZnO/Ps/Si/Ag for Photodetector Application", *Int. J. Nanosci.*, 22(6) (2023) 2350048.

[2] D. Ananda et al. "Synthesis of gold and silver nanoparticles from fermented and non fermented betel leaf", *Int. J. Nanomater. Biostruct.*, 5 (2017) 20-23.

[3] Y. Wang and N. Herron, "Nanometer-sized semiconductor clusters: materials synthesis, quantum size effects, and photophysical properties", *J. Phys. Chem. A*, 95 (1991) 525-532.

[4] M.A. Faraj, M.A. Jabbar and A.N. Abd, "Bismuth oxide aqueous colloidal NPS obtained by a green synthesis inhibit candida albicans", *AIP Conf. Proc.*, 2834 (2023) 090009.

[5] H. Singh et al., "Ecofriendly synthesis of silver and gold nanoparticles by Euphrasia officinalis leaf extract and its biomedical applications", *Artif. Cells, Nanomed. Biotech.*, 46(6) (2018) 1163-1170.

[6] S. Haq et al., "Green synthesis and characterization of tin dioxide nanoparticles for photocatalytic and antimicrobial studies", *Incl. Pub. Trust. Sci. Exp.*, 7 (2020) 025012.

[7] B.J. Alwan, A.N. Abd and N.H. Zaki, "Inhibitory effect of lithium oxide nanoparticle produced by green synthesis method", *AIP Conf. Proc.*, 2834 (2023) 090012.

[8] K. Fleischer, E. Arca and I.V. Shvets, *Sol. Ener. Mater. Sol. Cells*, 101 (2012) 262-269.

[9] N.F. Habubi et al., "Improving the Photoresponse of Porous Silicon for Solar Cell Applications by Embedding of CdTe Nanoparticles", *Indian J. Pure Appl. Phys.*, 53 (2015) 718.

[10] M.K. Al Turkestani and K. Durose, *Sol. Ener. Mater. Sol. Cells*, 95 (2011) 491-496.
[11] S. Girish Kumar and K.S.R. Koteswara Rao, *Ener. Enviro. Sci.*, 7 (2014) 45-102.
[12] S. Iravani, "Green synthesis of metal nanoparticles using plants", *Green Chem.*, 13 (2011) 2638-2650.
[13] B.J. Alwan, A.N. Abd and N.H. Zaki, "Inhibitory effect of lithium oxide nanoparticle produced by green synthesis method", *AIP Conf. Proc.*, 2834 (2023) 090012 (2023).
[14] A.N. Abd, "Improved photoresponse of porous silicon photodetectors by embedding CdS nanoparticles", *World Sci. News*, 19 (2015) 32.
[15] K. Murali, P. Elango and K. Andavan, "Preparation of Ag nanoparticles films and their characteristics", *J. Mater. Sci.: Mater. Electron.*, 19(3) (2008) 289-293.
[16] S. Kotthaus, B. Hang and H. Schafer, "Study of isotropically conductive bondings filled with aggregates of nano-sited Ag-particles", *IEEE Trans. Compon. Packag. Technol.*, 20 (1997) 15-20.
[17] Y.N. Al-Jammal "Solid State Physics", Mosul University, Arabic version (1990).
[18] W. Zhang, "Research and development for antibacterial materials of silver nanoparticle", *New Chem. Mater.*, 31 (2003) 42-44.
[19] S.J.B. Reed, **"Electron microprobe analysis and scanning electron microscopy in geology"**, Cambridge University Press (2005).
[20] K.M. Lang et al., "Conducting atomic force microscopy for nanoscale tunnel barrier characterization", *Rev. Sci. Instrum.*, 75(8) (2004) 2726-2731.
[21] M.A. Mijares, UV-Visible Photodetector with Silicon Nanoparticles (2012).
[22] M.M. Silván, "HAP/TiO_2 and HAP/TiN Structures Surface Modifications for Enhanced Biocomptatibility", PhD thesis, Universidad Autónoma de Madrid (2001).
[23] I.E. Mba and E.I. Nweze, "Nanoparticles as therapeutic options for treating multidrug-resistant bacteria: Research progress, challenges, and prospects", *World J. Microbiol. Biotech.*, 37 (2021) 1-30.
[24] F. Amaro et al., "Metallic nanoparticles—friends or foes in the battle against antibiotic-resistant bacteria?", *Microorgan.*, 9(2) (2021) 364.
[25] T. Iqbal et al., "Plant-mediated green synthesis of zinc oxide nanoparticles for novel application to enhance the shelf life of tomatoes", *Appl. Nanosci.*, (2022) 1-13.
[26] S. Chauhan, D.N. Kumar and L.S. Upadhyay, "Facile synthesis of iron oxide nanoparticles using Lawsonia inermis extract and its application in decolorization of dye", *BioNanoScience*, 9 (2019) 789-798.
[27] A. Yoo, "Effect of zinc oxide and silver nanoparticles on intestinal bacteria", PhD thesis, University of Missouri, Columbia (2013).

Proceedings of 5th International Specialized Conference of Education College on Physics and Applied Sciences (5thICECAS24), 22-23 April 2024

Temperature Sensor Based on Photonic Crystal Fiber Fabry-Perot Interferometer

Namaa S. Rahim
Soudad S. Ahmed

Department of Physics, College of Science, University of Baghdad, Baghdad, IRAQ

Photonic crystal fiber (PCF) Fabry-Perot interferometer (FPI) based on surface plasmon resonance (SPR) is introduced in this work for sensing and measuring the temperature of the surrounding environment. An FPI was fabricated by straight splicing the PCF solid core with the multi-mode fiber (MMF) sensor end, followed by coating a 50nm gold nanofilm on the PCF solid core end. The suggested sensor contains an exact SPR result, according to the conclusions of investigations. Figures of Merit (FOM), Resolution (R), Signal-to-noise ratio (SNR), and Sensitivity (S) for PCF are evaluated as 0.0005, 0.2, 0.01, and 0.5, respectively.

Keywords: Photonic crystal fiber; Optical fiber; Temperature sensor; Interferometry
Received: 19 January 2024; Revised: 4 March 2024; Accepted: 4 April 2024

1. Introduction

The benefits of optical fiber-based sensing technology are becoming increasingly common due to its many advantages over conventional sensing technologies; optical fiber sensors have increased popularity in recent decades. These advantages include easy fabrication, consolidated size, flexibility, and greater stability. Furthermore, they are unsusceptible to electromagnetic interference, which makes them ideal for monitoring structural health in remote locations and difficult environments [1-3]. Constructed on the concept of 2D photonic crystals, photonic crystal fiber contains of a periodic shape of air gaps that extend alongside the entire fiber length [4-7]. It has an elastic structure that supplies a lot of benefits corresponding with traditional optical fiber, for instance, high confinement, single-mode propagation, low non-linearity, controllable birefringence, etc. [8-9]. At the metal-dielectric interface, the SPR appears [10-12]. Transformations in metal and dielectric permittivity, as well as structural changes, are particularly sensitive to it [13-15]. An SPR is a collective oscillation of free electrons on the edge between a metal and a dielectric. As the wavelengths of the incoming photons and electrons equal, resonance happens [16-19]. Excitations happen due to the oscillations of electrons between the dielectric and the metal is called a surface plasmon [20-22]. The surface plasmons can excite due to, optical components like a diffraction grating, refractive index prism, and optical fiber are utilized [23-25]. Fabry-Perot Interferometer (FPI) is commonly formed of two equivalent reflecting surfaces divided through a particular distance [26]. Infrequently it is called an etalon [27]. Interference appears as a result of the many super-positions of transmitted and reflected rays at similar surfaces [28]. In the case of fiber optic subjects, it can be simply formed through consciously constructing reflectors outside or inside of fibers. FPI instruments can be considered for two classes: intrinsic and extrinsic [29,30].

In this work photonic crystal fiber based on surface plasmon resonance (SPR) as Fabry-Perot interferometer as temperature environmental sensor when involved the fabrication and implementation of PCF (ESM-12) covered with a thin layer of gold (50nm) which represent the sensing element. This element is splicing with multimode optical fiber Based on SPR for sensing and estimating the temperature of the surrounding environment.

2. Performance Parameter

PCF-SPR sensors have performance parameters found in some parameters like signal to noise ratio, sensitivity, resolution, and figure of merit [20-22]: the sensitivity is the change in the resonance wavelength for the change of temperature [31,32]

$$S_\lambda = \frac{\Delta\lambda_{res}}{\Delta T} \quad \left[\frac{nm}{^\circ C}\right] \qquad (1)$$

where ΔT and $\Delta\lambda_{res}$ is the difference in the temperatures and the wavelength resonance peak, respectively

Another important parameter is the figure of merit (FOM), which is defined as the ratio of sensor sensitivity to spectral curve width. A good sensor has a high FOM value, which indicates that it has a sharp spectrum (narrow FWHM) and a good sensitivity. FOM is expressed as [31,32]

$$FOM = \frac{S(\frac{nm}{^\circ C})}{FWHM(nm)} \qquad (2)$$

where FWHM is the full-width at half maximum

The signal-to-noise ratio (SNR) measures the sensor performance and is represented by the equation [20-22]

$$SNR = \frac{\Delta\lambda_{res}}{FWHM(nm)} \quad (3)$$

The resolution (R) of the sensor indicates how much minor variation in the temperatures can be observed and may be calculated from the equation [20-22]

$$R[RIU] = \Delta T \times \frac{\Delta\lambda_{min}}{\Delta\lambda_{peak}} \quad (4)$$

where $\Delta\lambda_{peak}$ is the resonance wavelength difference between the two adjacent temperature resonance peaks and ΔT is the difference between the two adjacent temperatures

3. Fabrication of PCF Sensor

Utilizing a 4 cm long photonic crystal fiber (PCF) sensor of an external diameter of 125 µm and a diameter core of 12 µm and splicing with multi-mode fiber (MMF) on one side, MMF has a core diameter of 62.5 µm and a clad of 125µm, as shown in Fig. (1). The proposed MMF-PCF sensor was fabricated in four steps: first, the coating of a stub of PCF and MMF were removed by using a mechanical stripping (JIC-375 Tri-Hole). Then, the second step was cleaved the PCF and MMF, which was done by fiber cleaver (CT-30), and third step was cleaning the fibers. Then, the stub of PCF (SEM-12) was spliced to the MMF by a conventional splicing machine. Finally, an Au sensing layer with 50 nm thickness is deposited on the end face of PCF by using the Sputter Coater (Quorum Q150R ES, UK) which worked with a gold target bombarded using ions of argon gas . The coating process was achieved inside the chamber at a pressure of 3×10^{-3} Torr, sputter current of 20 mA and sputter time of 147 s. Figure (2) shows schematic diagram of MMF-PCF based on SPR.

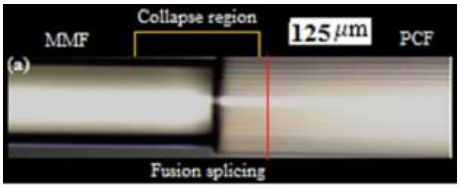

Fig. (1) Microscope image of the splicing MMF-PCF

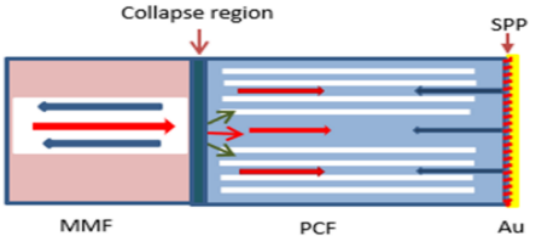

Fig. (2) The Schematic diagram of the MMF-PCF based on SPR sensor

4. Experimental Work

The experimental set up of the presented work is displayed in Fig. (3). It is essentially divided into six parts; a light beam produced by a laser diode with a wavelength of 652nm with power 0.05mW, Thermostat Water Bath HH-1 of KW-1000DC, TRUE RMS MULTIMETER from FLUKE 179, PCF (ESM-12) (THORLABS Co.), multi-mode fiber, couplers, and a computer-connected spectrophotometer (HR4000CG UV-NIR) with resolution of 0.1 nm . A light beam from a laser diode illuminates the PCF-SPR sensor. When the sensor was immersed in the water inside thermostat water bath the light in the sensing area was modified by external environmental solutions, the SPR curves with data values are displayed online on the computer screen and saved by and advanced software provided by THORLABS.

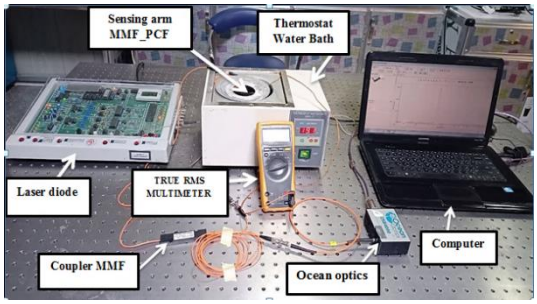

Fig. (3) Photo of Experimental work of the SPR -PCF sensor

5. Results and Discussion

In both the numerical calculations and the experimental study, the following values were used for the parameters: photonic crystal fiber numerical aperture (NA) = 0.09±0.02; photonic core diameter (D) =12.2±0.5 µm; sensing region (L) =4 cm; thickness of the metal layer (d) =50 nm; and various temperatures values (40, 42, 44, 46, 53, 54, 55, and 60°C) of water. The spectra are created by calculating the transition curves T for light using an optical cable, the transmission (T) is computed by dividing intensity (I) recorded with the effect of increasing temperature of water inside the thermostat water bath to the intensity without any effect of temperature, that is before placing the sensor inside the thermostat water bath (I), and (I_0) is the intensity of air.

The fabricated sensor was placed in a water bath and different temperatures were measured. Figure (4) shows plasmon resonance curves at different temperatures. These figures are presented in terms of normalized reflected power. The SPR curve, shown in Fig. (4), is determined as a percentage by dividing intensity (I) recorded with the effect of increasing temperature of water inside the thermostat water bath to the intensity without any effect of temperature, that is before placing the sensor inside the thermostat water bath (I_0).This normalized reflected is plotted as a function of the wavelength of the incident light. In these figures, the responses are simulated for a designed sensor illustrated in Fig. (3). The resonance occurs such as a dip as illustrated in the SPR curves, and at a certain wavelength known as the resonance wavelength λ_{res}, a sharp dip occurs in transmission due to incoming light energy transfer to metal electrons, reducing the intensity of reflected light.

The dip appears at a λ_{res} due to the transmission of the highest energy from the reflected power of light directed through the fiber to the surface plasmons (SPs). Increasing the temperature of water inside the water bath or increasing the resonance wavelength (λ_{res}) to longer wavelength (red shift), which may be explained by the resonance condition of surface plasmon waves. Figure (5) explains a linear relationship between resonant wavelength and various temperatures.

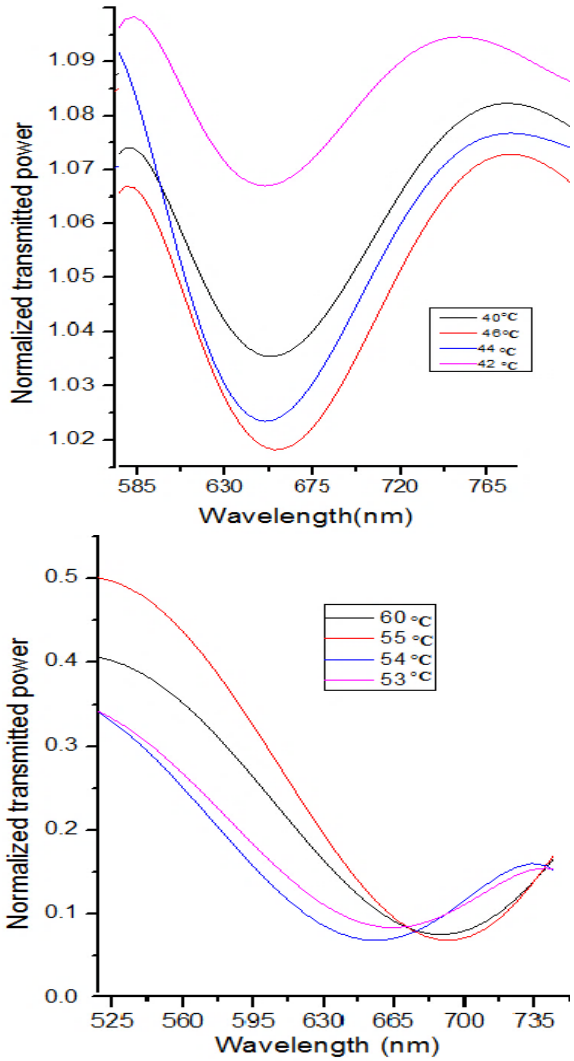

Fig. (4) SPR curves of the PCF with Au metal for various temperatures

Table (1) exhibits the performance parameters of a sensor covered by gold. The values of the sensitivity, figure of merit, signal-to-noise ratio, and resolution were calculated according to equations (1), (2), (3), and (4), respectively.

Table (1) Performance parameters of gold layer

Metal	Sensitivity (S_n) (nm/°C)	Signal to noise ratio (SNR)	Figure of merit (FOM) ($°C^{-1}$)	Resolution (°CU)
Gold	0.5	0.01	0.0005	0.2

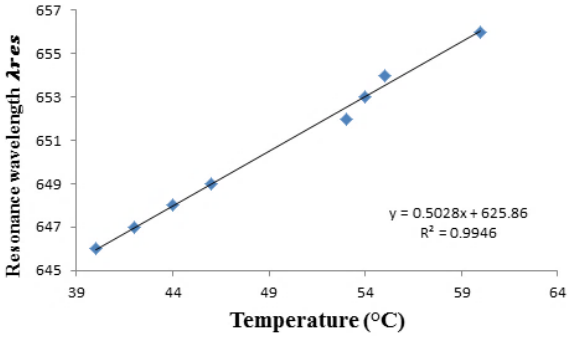

Fig. (5) Resonance wavelengths as a function of temperature for an Au-coated layer

Table (2) shows the temperatures of different resonance wavelengths. The values of the sensitivity, figure of merit, signal-to-noise ratio, and resolution were calculated according to equations (1), (2), (3), and (4), respectively.

Table (2) Temperatures values for various resonance wavelengths (nm)

Kind of fiber	Resonance wavelength λ_{res} (nm)	Temperatures (°C)
PCF	646	40
	647	42
	648	44
	649	46
	652	53
	653	54
	654	55
	656	60

6. Conclusion

A temperature sensor is constructed on ESM-12 photonic crystal fiber directly spliced with multimode fiber on one side. As the temperature of water rises inside the water bath, the resonance wavelength increases and shifts in the direction of longer wavelengths (redshift). Since the sensing medium's temperature is somewhat increased, the real part of the SP-wave is larger of the imaginary part. Therefore, the resonance principle is happened at high wavelengths.

References

[1] N.S. Rahim, S.S. Al-Bassam and M.F. Sultan, "Estimating Sugar Concentration in Human Blood Serum using Surface Plasmon Resonance (SPR) –Based Optical Fiber Sensor", *Iraqi J. Phys.*, 17(43) (2019) 41-48.

[2] S. S. Al–Bassam, "Tapered coated coreless optical fiber pollution sensor", *J. Phys.: Conf. Ser.*, 2114(1) (2021) 012054.

[3] K. Wang et al., "Advances in optical fiber sensors based on multimode interference (MMI): a review", *IEEE Sens. J.*, 21(1) (2020) 132-142.

[4] F.F. Abbas and S.S. Ahmed, "Photonic crystal fiber pollution sensor based on surface Plasmon resonance", *Iraqi J. Sci.*, 64(2) (2023) 658-667.

[5] N.F. Muhammed et al., "Simulation Design of Hollow Core Photonic Crystal fiber for Sensing Water Quality", *J. Phys.: Conf. Ser.*, 1530 (2020) 012134.
[6] H.J. Taher, "Low Loss in a Gas Filled Hollow Core Photonic crystal fiber", *Baghdad Sci. J.*, 7(1) (2010) 129-138.
[7] M.J.B.M. Leon and M.A. Kabir, "Design of a liquid sensing photonic crystal fiber with high sensitivity, bireferingence & low confinement loss", *Sens. Biosens. Res.*, 28 (2020) 100335.
[8] F.F. Abbas and S.S. Ahmed, "Photonic crystal fiber pollution sensor based on the surface Plasmon resonance technology", *Baghdad Sci. J.*, 20(2) (2023) 0452.
[9] X. Yan et al., "Photonic crystal fiber SPR liquid sensor based on elliptical detective channel", *Micromachines*, 12(4) (2021) 408.
[10] E. Khaddar and S.S. Al-Bassam, "Surface Plasmon Plastic Optical Fiber Resonance with Multi-Layer as Chemical Sensor", *Iraqi J. Sci.*, 19(50) (2021) 51-59.
[11] M.F. Sultan, A.A. Al-Zuky and S.A. Kadhim, "Surface plasmon resonance based fiber optic sensor: theoretical simulation and experimental realization", *Al-Nahrain J. Sci.*, 21(1) (2018) 65-70.
[12] H. Yang et al., "Highly sensitive graphene-Au coated Plasmon resonance PCF sensor", *Sensors*, 21(3) (2021) 818.
[13] Y. Zhang et al., "Design of diamond-shape photonic crystal fiber polarization filter based on surface plasma resonance effect", *Chinese Phys. B*, 29(3) (2020) 034208.
[14] C. Caucheteur, T. Guo and J. Albert, "Review of plasmonic fiber optic biochemical sensors: improving the limit of detection", *Anal. Bioanal. Chem.*, 407 (2015) 3883-3897.
[15] Z. Fan, "A tunable high-sensitivity refractive index of analyte biosensor based on metal-nanoscale covered photonic crystal fiber with surface plasmon resonance", *IEEE Photon. J.*, 11(3) (2019) 1-14.
[16] G.M. Jassam, S.S. Al-Bassam and M.F. Sultan, "Fabrication of a Chemical Sensor Based on Surface Plasmon Resonance via Plastic Optical Fiber", *Iraqi J. Sci.*, 61(4) (2020) 765-771.
[17] G.M. Jassam and S.S. Ahmed, "Estimating concentration of toxic ions Arsenic in water by using Photonic Crystal Fiber based on Surface Plasmon Resonance (SPR)", *Baghdad Sci. J.*, 21(2) (2024) 0445.
[18] Y. Yang et al., "High-sensitivity three-core photonic crystal fiber sensor based on surface Plasmon resonance with gold film coatings", *Japanese J. Appl. Phys.*, 60(12) (2021) 122002.
[19] M. Al Mahfuz et al., "Dual-core photonic crystal fiber-based plasmonic RI sensor in the visible to near-IR operating band", *IEEE Sens. J.*, 20(14) (2020) 7692-7700.
[20] G.M. Jassam and S.S. Ahmed, "D-Shaped Photonic Crystal Fiber Toxic Metal Ions (Arsenic) Sensor Based on Surface Plasmon Resonance", *Iraqi J. Phys.*, 21(2) (2023) 91-98.
[21] K.M. Rahman, M.S. Alam and M.A. Islam, "Highly sensitive gold-coated surface plasmon resonance photonic crystal fiber sensor in near-infrared region", *Results in Optics*, 7 (2022) 100223.
[22] M.H. Salman, H.K. Muhammad and H.A. Yasser, "Effects of holes radius on plasmonic photonic crystal fiber sensor with internal gold layer", *Periodic. Eng. Nat. Sci.*, 8(3) (2020) 1288-1296.
[23] N.S. Rahim, S.S. Ahmed and M.F. Sultan, "Optical fiber biomedical sensor based on surface plasmon resonance", *Iraqi J. Sci.*, 61(7) (2020) 1650-1656.
[24] Y. Chen and H. Ming, "Review of surface Plasmon resonance and localized surface Plasmon resonance sensor", *Phot. Sens.*, 2 (2012) 37-49.
[25] W.F.A. Shehab, "Performance analysis of optical fiber surface plasmon resonance sensor in single-mode operation region", *J. Electr. Eng.*, 71(5) (2020) 340-346.
[26] B.H. Lee et al., "Interferometric fiber optic sensors", *Sensors*, 12(3) (2012) 2467-2486.
[27] J.S. Sirkis et al., "In-line fiber etalon for strain measurement", *Opt. Lett.*, 18(22) (1993) 1973-1975.
[28] F.L. Pedrotti, L.S. Pedrottie and L.M. Pedrotti, "Introduction to Optics", Pearson International Edition (2007).
[29] W.H. Tsai and C.J. Lin, "A novel structure for the intrinsic Fabry-Perot fiber-optic temperature sensor", *J. Lightwave Technol.*, 19(5) (2001) 682-686.
[30] T.Y. Kim, J.E. Kim and K.S. Suh, "Erratum: On-line monitoring of transformer oil degradation based on fiber optic sensors", *Sens. Mater.*, 20(5) (2008) 201-209.
[31] Y. Lu et al., "Temperature sensing using photonic crystal fiber filled with silver nanowires and liquid", *IEEE Photon. J.*, 6(3) (2014) 1-7.
[32] N. Cennamo et al., "Low cost sensors based on SPR in a plastic optical fiber for biosensor implementation", *Sensors*, 11(12) (2011) 11752-11760.

Proceedings of 5th International Specialized Conference of Education College on Physics and Applied Sciences (5thICECAS24), 22-23 April 2024

Noor-Alhuda R. Ali
Majid H. Hassouni

Department of Physics, College of Education, Mustansiriyah University, Baghdad, IRAQ

Biosynthesis of Manganese Oxide Nanoparticles Prepared by Saffron Plant Extract

This investigation aimed to determine some properties of MnO-NPs by using the characterization methods of AFM, UV-Vis, XRD, and FTIR. MnO NPs were prepared by using the green synthesis method. The results demonstrated that the shape of MnO NPs was spherical, with a size of 0.154 nm. The average diameters of the AFM pictures were 14.09 nm.

Keywords: Manganese oxide; Nanoparticles; Biosynthesis; Saffron plant extract
Received: 19 January 2024; Revised: 4 March 2024; Accepted: 4 April 2024

1. Introduction

The most common definition of nanotechnology is a field of science that aims at the development, production, design, and characterization of 1–100 nanometer-sized matter by testing it at atomic and molecular levels [1]. In recent years, the interest of researchers in the nanotechnology field has developed rapidly due to their unique chemical and physical properties. Which vary from those of raw materials, including diffusion, electrical resistivity, conductivity, hardness and strength, chemical reactive characteristics, and a variety of beneficial biological activities [2, 3]. Metal oxide nanoparticles have sparked particular interest since they are frequently employed in medical applications, such as antimicrobials in disinfection, as well as fillers, opacifiers, catalysts, and semiconductors. They are also beneficial in the development of cosmetics and microelectronics [3-4]. Due to its low toxicity, manganese dioxide (MnO_2) is receiving attention from researchers in the field of nanotechnology [5]. Manganese oxides can be used in several applications because of their exceptional physicochemical properties, such as batteries, magnetic materials, water treatment, and imaging contrast agents [6, 7]. MnO NPs are a promising choice as a soil remediation agent due to their catalytic activity and comparatively large surface area (compared to bulk form). Successful decontamination was recorded, for instance, for species of lead, cadmium, thallium, arsenic, and selenium in the soil [8, 9]. The aim of this research is to prepare manganese oxide particles in a biological way using saffron extract with manganese salts at a very low concentration.

2. Materials and Method

The Saffron plant was gathered from local markets in the month of October 2022 and verified by the Ministry of Health's herbarium. It was washed to remove dust particles, then dried and ground into a fine powder using an electronic grinder. 4 g of *Saffron* powder were mixed with 400 milliliters of distilled water. The mixture was heated up for 15 minutes at 60 degrees Celsius with a hot plate stirrer. After filtration using filter paper (20-µm pore size), then extract was cooled and refrigerated at 4°C until ready for use [10].

In order to prepare 1M of manganese nanoparticles (Fig. 1), 1.258 g of manganese chloride $MnCl_2$ (molar mass = 125.5 g/mol) was dissolved in 100 ml of distilled water. The mixture was heated to 120 °C for 2 hours, during which time 10 ml of plant extract was gradually added to 100 ml of $MnCl_2$ solution and continuously mixed with a magnetic stirrer. When the color become golden brown, the mixture was allowed to cool to room temperature before centrifuging for 15-20 minutes at 3500 rpm. The process was performed twice, and the deposit was eliminated and dried at 130°C for 6 hours.

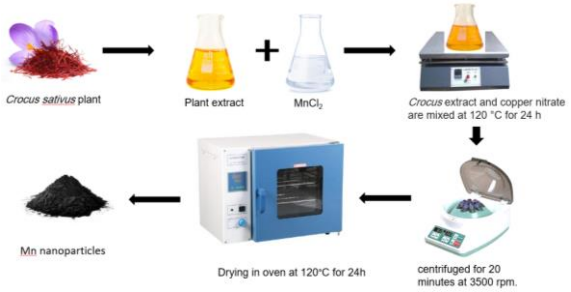

Fig. (1) Scheme of Green Synthesis of MnO Nanoparticles from *Crocus sativus* Plant Extract

A UV/visible spectrophotometer (UV-2610/UK) was employed to verify the synthesis of MnO nanoparticles; the UV-visible absorption spectra and

color change of the solution served as indications of synthesis. The absorbent capacity of the solution suspension was recorded across several time periods, and the maximum absorption was determined by scanning at 200-1100 nm.

Photoluminescence was used to examine the fluorescence features of a substance utilizing fluorescence spectrum, allowing one to determine the molecular composition of a substance.

XRD peaks appear as XRD peaks. Through the prevalence of atoms within the crystal lattice, the XRD density is determined where It represents the pattern and identity of matter for its periodic atomic structure Screening of nanoparticles was performed using an XRD machine[11] (XRD 6000- Shimadzu/-Japan) with Cu_K radiation at = 1.5406 for two values ranging from 20 to 80 degrees. The Debye-Scherer equation was used Calculate the average particle size (D) of the generated nanoparticles.

The atomic force microscope is described as a low-cost instrument. With the development of the scanning microscope, the microscope that relies on atomic force has also developed. The cam force is mechanically calculated, and in this procedure a flexible protrusion is used between the wall and the atomic point of the end of the metal tip. The electronic activity can be examined through a scanning tunneling microscope along the surface, and this is done by changing individual atoms. Through this method, it is possible to study chemical interactions with other forces, such as magnetic and electrical forces [12].

The analysis is widely and frequently used in chemicals, And analysis of biomedical samples. And detect active groups in Samples are under examination. FT-IR was analyzed using an instrument (FTIR 8400S/Shimadzu, Japan). The samples under study were examined at the University of Technology.

3. Results and Discussion

In this study, saffron extract was used as a catalyst in the green process of nano manganese oxide. Through this method and work, the color changes from light yellow to dark yellow within a few minutes, usually not more than a few minutes at most (note Fig. 2).

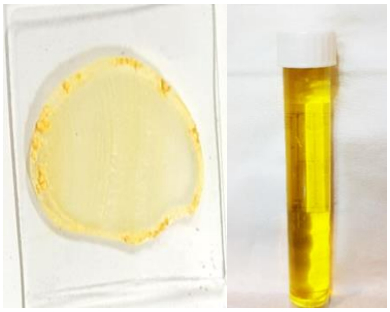

Fig. (2) MnO NPs after mixing with saffron extract and the color becomes pale green

The presence of nanoparticles of manganese oxide was confirmed using UV-visible spectroscopy. Figure (3a) indicates that the absorption spectrum was obtained using a spectrophotometer with a xenon lamp and a wavelength range of 190-990nm. The UV-Vis spectrum is essential because it provides information about the optical band. It was discovered that as particle size decreases, the optical absorption spectra move towards shorter wavelengths due to an increase in the optical energy band gap. Due to the quantum size effect, the surface plasmon resonance (SPR) brought about by the oscillation of electrons on the nanocomposite surface gave rise to the developed nanocomposite's brown hue. Theoretically, MnO NPs have an absorption peak that is between 350 and 410 nm in wavelength. The graph of $(hv)^2$ vs. photon energy (hv) in Fig. (3b) on the right shows that, according to Tauc's relation, MnO has a band gap of 2.6 eV. The band gap has increased to 3, which the quantum size effect may be responsible for. The quantum size effect, which results in a blue shift, affects the optical spectra of nanostructured objects. The quantum size effect causes the band gap of a bulk semiconductor to shift to a higher energy level [13].

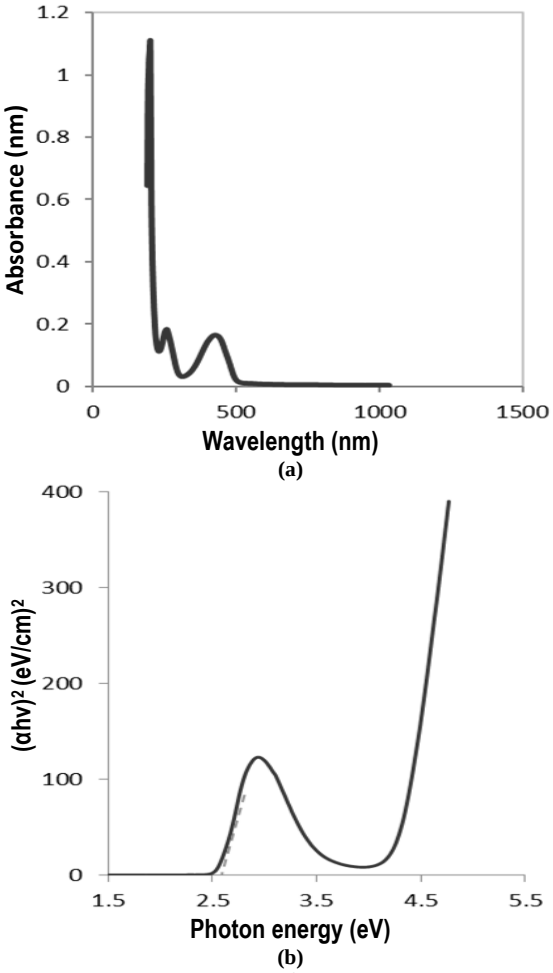

Fig. (3) (a) UV-visible spectra of MnO NPs sample prepared by Crocus plant extract and (b) $(\alpha hv)^2$ vs. hv for MnO NPs

In order to detect the fluorescence characteristics of the material, PL examination was used. The results shown in Fig. (4) indicate that when an energy gap of 2.6eV is present, the biosynthesized MnO nanomaterials glow. This is because phytochemicals are present in the MnO nanoparticles' attached crocus plant extract [14]. Claim that MnO nanoparticles created biologically have a greater PL intensity than those produced chemically.

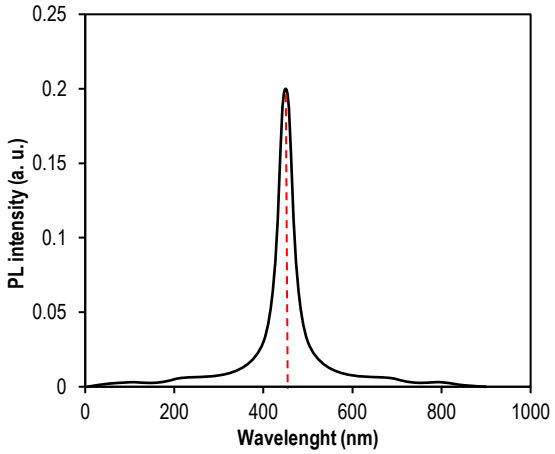

Fig. (4) Photoluminescence spectrum of MnO NPs

The form and size of MnO nanoparticles were identified using an atomic force microscope. Figure (5) shows a 3D image of a thin MnO layer generated at substrate temperature. The grains were evenly distributed, with each columnar grain extending high. According to the AFM analysis, the pore's average grain size was approximately 14.09 nm, with an RMS roughness of 3.06 nm and an average roughness of 14.11 nm, as shown in table (1).

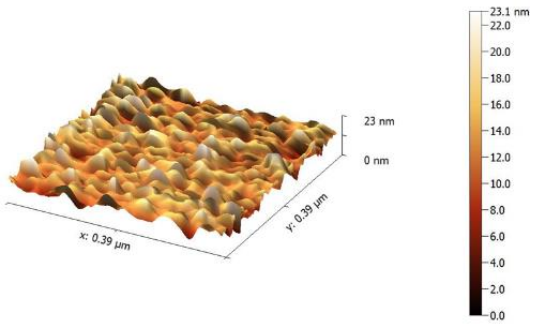

Fig. (5) 3D AFM image of the green synthesized material

Table (1) The parameters of manganese surface

Average value	14.09 nm
Minimum	0.00 nm
Maximum	29.53nm
Median	14.11 nm
Ra	2.34 nm
RMS roughness (grain-wise)	3.06 nm

X-ray diffraction can be utilized to confirm the shape and size of crystals as they form. The crystal structure of MnO NPs was determined using the peak positions of the XRD pattern. Manganese oxide nanoparticles exhibit strong diffraction lines, with eight unique peaks identified at 2θ values of 32.50, 36.99, 38.13, 41.02, 42.09, 49.01, 56.39, and 57.12o, respectively. The values of the Miller indices (220), (202), (400), (411), (420), (431), (332), and (333) are shown in Fig. (6). The crystallite size in the biosynthesized MnO nanostructure was calculated using the Debye-Scherrer formula [15].

$$D = k\lambda / \beta \cos\theta \quad (1)$$

where K is a constant equals to 0.94, D is the average crystallite size, λ is the x-ray radiation wavelength (0.154 nm), as shown in table (2)

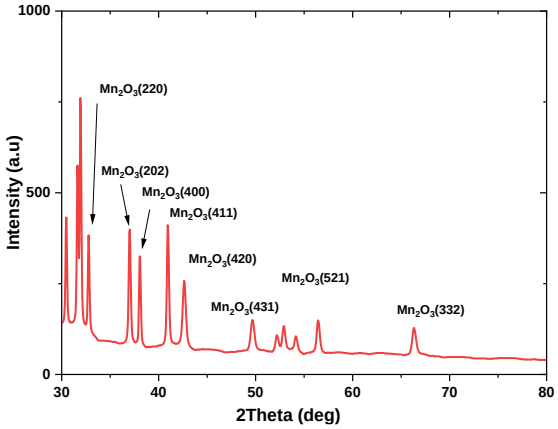

Fig. (6) XRD pattern of Mn NPs prepared from *Crocus Sativus* (Saffron) flower extract

Table (2) Structural parameters of MnO NPs

2θ (deg)	D (nm)	FWHM (deg)	Strain x10^{-4}	hkl
32.5	54.88	0.0026	6.31	(220)
36.99	55.56	0.0026	6.23	(202)
38.13	83.63	0.0017	4.14	(400)
41.02	52.75	0.0028	6.56	(411)
42.09	11.29	0.0013	30.67	(420)
49.01	10.72	0.014	32.29	(431)
56.39	30.42	0.0051	11.38	(332)
57.12	14.52	0.010	23.85	(333)

The FTIR analysis was employed to identify the bio-molecules and functional groups in the produced MnO nanoparticules. The results of the FTIR in Fig. (7) show that the surface of the NPs contains biocomponents, including alcohols and phenolic compounds with potent hydrogen bonds. The reaction between protein molecules and manganese salts that can reduce Mn ions and stabilize MnO NPs was studied using FTIR measurements. The FTIR study of the hydroxyl group (OH), C-O, MnO, and other vibrations revealed some surprising bands. This matches the surface-bound MnO-NPs and biocompounds [16,17]. The C=C group is said to be responsible for the distinct bands at 1639 cm^{-1}, which are most likely caused by the aromatic conjugates of the biomolecules found in the extract. The C-O stretching vibration is responsible for the connection at 1100 cm1. Strong hydrogen bonding in alcohols and phenolic chemicals was identified as the cause of the peaks at 3500 cm^{-1}. The produced MnO NPs have

residues like hydroxyl and carboxyl groups on their surface.

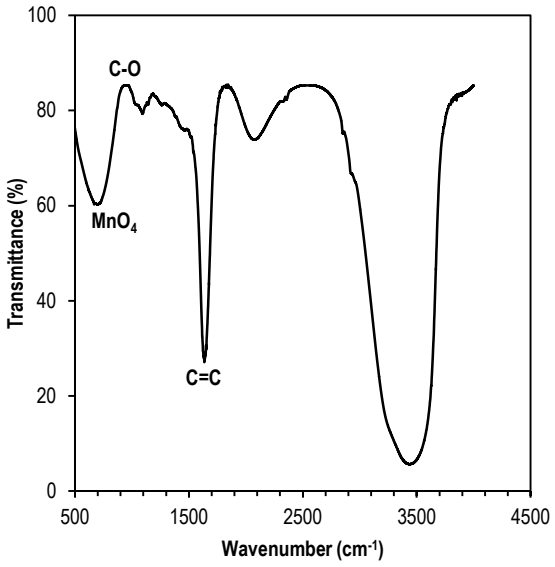

Fig. (7) FTIR spectrum of MnO produced using flower extract from *C. sativus* (saffron)

4. Conclusion

MnO4 NP was prepared using an aqueous extract of C. sativus as a reducing agent. UV-visible spectroscopy, atomic force microscopy, X ray diffraction analysis, and fourier transform infrared spectroscopy were employed to analyze the produced MnO4 nanoparticle. The results revealed that the produced MnO4 nanoparticles are 14.09 nm in size, spherical in form.

References

[1] A.M. Al-Ghareebawi, B.N. Al-Okaily and O.M.S. Ibrahim, "Characterization of zinc oxide nanoparticles synthesized by olea europaea leaves extract (part L)", *Int. J. Agricul. Sci.*, 52(3) (2021) 580-588.

[2] M. Sahooli, S. Sabbaghi and R. Saboori, "Synthesis and characterization of mono sized CuO nanoparticles", *Mater. Lett.*, 81 (2012) 169-172.

[3] K.S. Khashan, G.M. Sulaiman and F.A. Abdulameer, "Synthesis and antibacterial activity of CuO nanoparticles suspension induced by laser ablation in liquid", *Arab. J. Sci. Eng.*, 41 (2016) 301-310.

[4] R. Katwal et al., "Electrochemical synthesized copper oxide nanoparticles for enhanced photocatalytic and antimicrobial activity", *J. Indust. Eng. Chem.*, 31 (2015) 173-184.

[5] C. Burda et al., "Chemistry and properties of nanocrystals of different shapes", *Chem. Rev.*, 105(4) (2005) 1025-1102.

[6] R.N. Reddy and R.G. Reddy, "Synthesis and electrochemical characterization of amorphous MnO_2 electrochemical capacitor electrode material", *J. Power Sour.*, 132(1-2) (2004) 315-320.

[7] Y. Chen et al., "Preparation of single-crystal α-MnO_2 nanorods and nanoneedles from aqueous solution", *J. Alloys Comp.*, 397(1-2) (2005) 282-285.

[8] Z. Michálková et al., "Selected Fe and Mn (nano) oxides as perspective amendments for the stabilization of As in contaminated soils", *Euro. Sci. Pol. Res.*, 23 (2016) 10841-10854.

[9] X. Huangfu et al., "Significantly improving trace thallium removal from surface waters during coagulation enhanced by nanosized manganese dioxide", *Chem.*, 168 (2017) 264-271.

[10] G. Binnig, C.F. Quate and C. Gerber, "Atomic force microscope", *Phys. Rev. Lett.*, 56(9) (1986) 930.

[11] A.A. Bunaciu, E.G. UdriŞTioiu and H.Y. Aboul-Enein, "X-ray diffraction: instrumentation and applications", *Chem. Rev. Anal. Chem.*, 45(4) (2015) 289-299.

[12] R. Ishwarya et al., "Facile green synthesis of zinc oxide nanoparticles using Ulva lactuca seaweed extract and evaluation of their photocatalytic, antibiofilm and insecticidal activity", *J. Photochem. Photobiol. B: Biol.*, 178 (2018) 249-258.

[13] S. Sundar, G. Venkatachalam and S.J. Kwon, "Biosynthesis of copper oxide (CuO) nanowires and their use for the electrochemical sensing of dopamine", *Nano*, 8(10) (2018) 823.

[14] A. Muthuvel, M. Jothibas and C. Manoharan, "Synthesis of copper oxide nanoparticles by chemical and biogenic methods: photocatalytic degradation and in vitro antioxidant activity", *New Enviro. Eng.*, 5(2) (2020) 14.

[15] A.M. Majeed et al., "Fabrication and characterization of copper oxide nanoparticles/psi Heterodiode", *Int. Lett. Chem. Phys. Astro.*, 1 (2015) 57-25.

[16] E.M. Ali et al., "Green Synthesis, Characterization and Antimicrobial activity of CuO nanoparticles (NPs) Derived from Hibiscus sabdariffa a plant and CuCl", *IOP J. Phys.: Conf. Ser.*, 1963(1) (2021) 012092.

[17] A.K. Halder and M.N. Cordeiro, "Probing the environmental toxicity of deep eutectic solvents and their components: An in silico modeling approach", *ACS Sustain. Chem. Eng.*, 7(12) (2019) 10649-10660.

Proceedings of 5th International Specialized Conference of Education College on Physics and Applied Sciences (5thICECAS24), 22-23 April 2024

Antimicrobial Activity of Al_2O_3 Nanoparticles Prepared by Simple Chemical Method

Thaer A. Mezher [1]
Hameed H. Ahmed [2]
Adil H. Dhari [3]

[1] *Directorate General of Education in Diyala, Diyala, IRAQ*
[2] *Directorate General of Education of Salah Al-Din, Salah Al-Din, IRAQ*
[3] *Directorate General of Education Karkh/3, Baghdad, IRAQ*

Everyday, new nanoparticles are prepared, and their properties are evaluated according to their unique properties, which are completely different from their predecessors. Aluminum oxide nanoparticles have different shapes and properties. In this study, aluminum oxide nanoparticles were successfully prepared using a simple chemical method. The deposited films were analyzed using several techniques such as FTIR, XRD, AFM, and (UV-Vis) to study the optical properties.The antibacterial and antifungal activity of the prepared nanoparticles was studied against several pathogenic bacteria, including Gram-positive (+) bacteria (Staphylococcus aureus, Sta. epid.) and Gram-negative (-) bacteria (Klebsiella sp., E. coli) using well diffusion method. The results showed that the prepared particles have a good inhibitory effect against all types of bacteria under study.

Keywords: Aluminum oxide; Nanoparticles; Chemical method; Antibacterial activity
Received: 19 January 2024; Revised: 4 March 2024; Accepted: 4 April 2024

1. Introduction

With the aim to develop new nanoscale materials, nanotechnology is quickly developing in both science and technology. [1]. When compared to bulk kinds of same chemical composition, nanoparticles exhibit varied chemical properties [2]. When compared to organic molecules, metal oxide nanoparticles offer reduced toxicity, greater durability, higher stability, and selectivity [3]. Furthermore, these particles' basic physical and chemical characteristics alter depending on their size. These particles exhibits remarkable applications in diagnosis, catalysis, drug delivery, cosmetics, semiconductors, sensing and water treatment, [4,5]. Aluminum Oxide nanoparticles employed in a variety of industries [6], including the ceramics sector, absorbents in heterogeneous catalysis, as abrasives, biomaterials, and reinforcements for metal-matrix composites [7,8]. Recently, the appearance and spread of novel resistant bacterial strains have alarmed the global community. Therefore, it is urgently necessary to develop antimicrobial medicines that are effective against bacterial strains resistant to antibiotics while also preventing the establishment of resistance Additionally, a wide range of human infections can be brought on by Candida species [9-12].

In the current study, Al_2O_3 NPs are prepared using a simple chemical method, and study the structural, optical, and morphological properties. By different techniques and then evaluated antibacterial and antifungal activity of the NPs prepared on different types of pathogens

2. Experimental part

The basic chemical approach is a unique, quick, and low-cost procedure that does not require lengthy or sophisticated equipment. For each material made independently, 21.2g of aluminum nitrate $Al(NO_3)_3$ was mixed with 4g NaOH in 100 ml of distilled water (DW) solution. Whereas 100ml of aluminum nitrate was placed in a magnetic stirrer device for 30 minutes to form a homogenous solution, and around 15 ml of NaOH (1M) was rapidly added to the combination, a nanopowder suspension was formed as shown in Fig. (1).

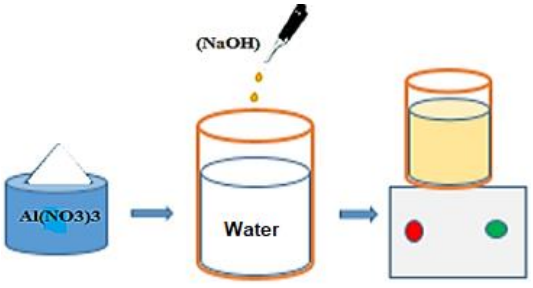

Fig. (1) Schematic diagram of simple chemical method

Because the substance is at the bottom of the device and there is a lot of salt in the water solution, the material is taken away from the device and kept for a period of time. To eliminate any

contaminations, the particles were centrifuged and rinsed with distilled water; this technique (washing the material) is done three or four times to remove as much salt as feasible. After the final solution formulation — a transparency substance called Al_2O_3 — is reached, the material that is needed can be extracted out of the top with a special syringe (YE3K061872:10-100ML). Apply the material using the drop casting technique to the glass substrate. The procedure starts with four drops applied to the glass sample using a syringe in a particular amount., followed by heating to dry for (20 min) to generate an Al_2O_3 thin layer (as shown in Fig. 2) ensure the material by X-Ray diffraction method checking.

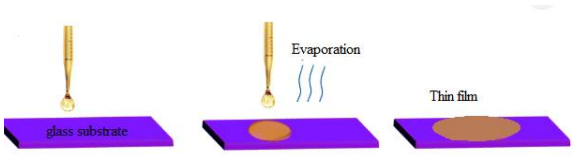

Fig. (2) Drop casting method

3. Results and Discussion

Figure (3) depicts an XRD pattern of Al_2O_3 produced by a simple chemical technique and coated by drop casting on a glass substrate (1.5x1.5cm^2) (4 drops). The broad peak in the Fig. indicates the formation of the nanostructure. The XRD patterns of the Al_2O_3 nanoparticles were compared to the JCPDS card no. 36-1457, which is the standard pattern. Use the width of a peak that emerges at angle 26.4° to get the crystalline size using Scherrer's formula, as in Eq. (1) [13,14]. The crystalline size was 11.45nm

$$C.S. = \frac{0.9\lambda}{\beta \cos\theta} \qquad (1)$$

where λ is the wavelength for x-ray (1.5406$\dot{A}$), β is the full-width at half maximum and θ is the diffraction angle

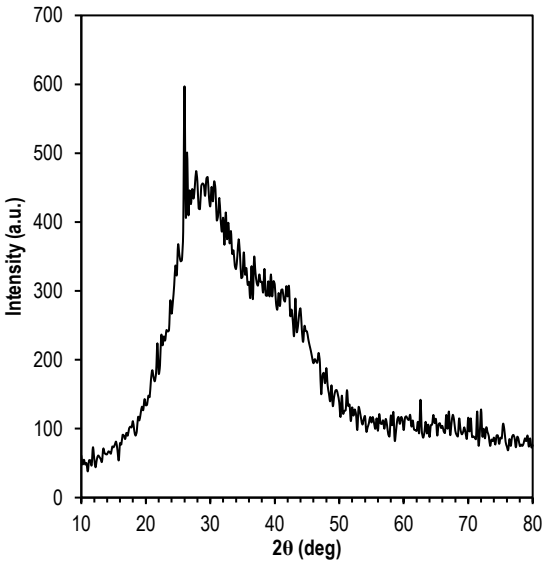

Fig. (3) XRD pattern of Al_2O_3 NPs

Figure (4) shows the AFM image of the Al_2O_3 nanocrystalline films that depo-sited on glass substrate by drop casting method. It is clear to observe from the image that the surface-free crack, high density and good attachment to the glass substrate. The Al_2O_3 nanostructures revealed pointed and broad hills shaped. From histogram of nanoparticles the dominant sizes of the particles are 80.63nm and Root-mean-square height 8.201nm.

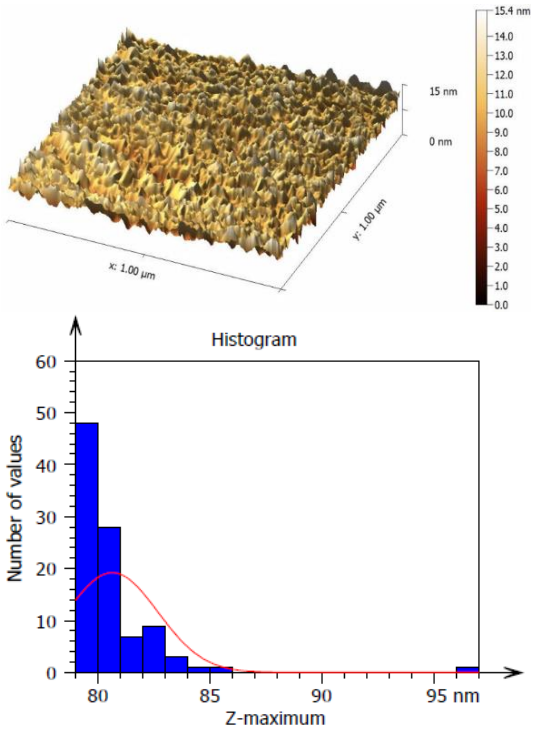

Fig. (4) AFM image and histogram of Al_2O_3 NPs

The optical characteristics studied in the range 200-1100 nm for Al_2O_3 NPS. The transmittance spectrum of Al_2O_3 as in Fig. (5a), the spectrum show the increase with increase wavelength. Maximum transmittance was observed at the wavelength region. (240- 1100) nm, where it recorded 93%, this indicates that the material has high transparency. For deposited Al_2O_3 thin films, figure (5b) illustrates the change of $(\alpha h\upsilon)^2$ as a function of photon energy ($h\upsilon$). The graph indicates an energy gap of 4.8 eV. Since the band gap of Al_2O_3 in bulk is 8.7 eV, a value of around 4.8 eV is anticipated for Al_2O_3 films. [15]. The lower values obtained in this investigation can be explained by the development of some defect levels in the band gap [23,24].

Figure (6) depicts the FTIR spectra for the various products produced. The synthesized materials' findings are consistent with those described in the literature. The FT-IR patterns show the presence of two bands: the band at 1638 cm^{-1}, which corresponds to physisorbed water, and the broad band at 3248-3600 cm^{-1}, which is associated to the -OH stretching vibration that is coupled to Al^{+3}. The formation is validated by the valley between 1000 and 435 cm^{-1}, whereas the bending

vibrations of the Al-O bond are associated with the valley at 700 cm^{-1}. In the gamma phase of alumina, an Al-O-Al bond generates the band at 670 cm^{-1}. These findings are compatible with the XRD study, which found the g-phase [16,17].

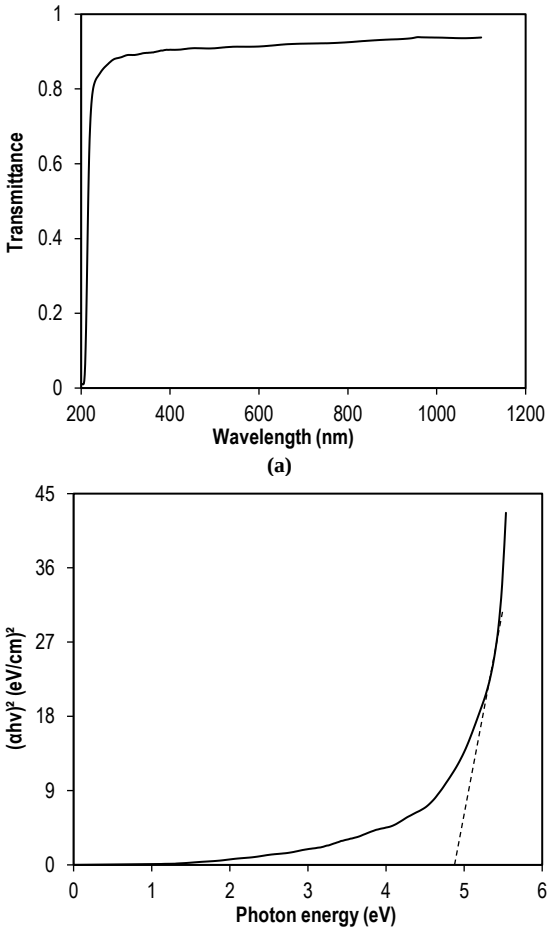

Fig. (5) (a) UV-visible transmission spectrum of Al_2O_3 NPs and (b) determination of energy band gap

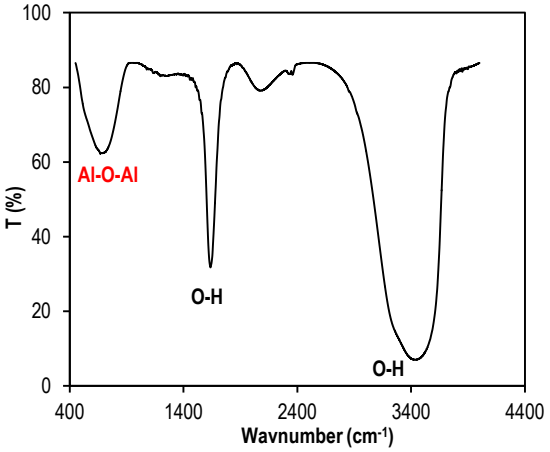

Fig. (6) FTIR spectrum of $A1_2O_3$ NPs

The anti-bacterial activity of the Aluminum oxide nanoparticle against bacterial strains Klebsiella Pneumonia was determined by zone of inhibition as shown in Fig. (7) by Agar well diffusion method. Aluminum oxide nanoparticles showed activity against all the tested bacteria in the concentration of 100µg.

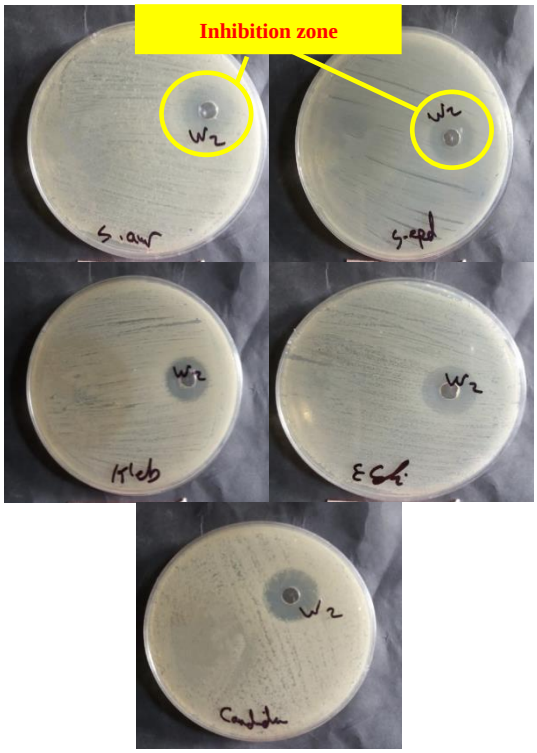

Fig. (7) Antibacterial and antifungal assay test using well diffusion method

Among the tested bacteria, E-coli, Sta. aureus and Sta. epid. Were found to be more sensitive to the Aluminum oxide nanoparticle as in Fig. (8). Direct contact between Al_2O_3 NPs nanoparticles and the exterior membrane surface might be one of the causes of the damage.

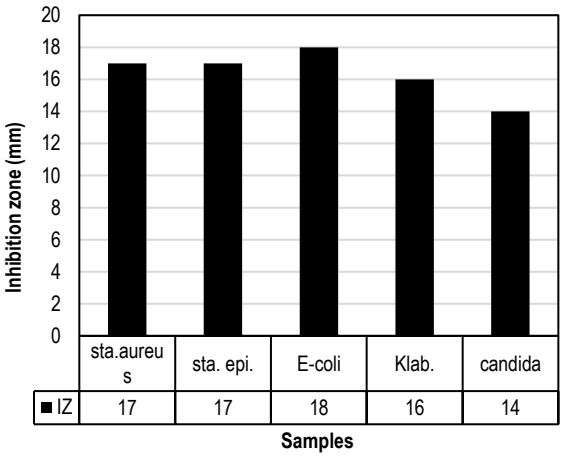

Fig. (8) Diameter of inhibition zone using Al_2O_3 NPs

More research is needed to corroborate these findings. It is still unclear if oxide nanoparticles may enter bacterial cells and how they interact with the cell wall. Al_2O_3 NPs bond to bacterial cells via electrostatic attraction forces since they are much

smaller than bacterial cells, neutralizing the bacterium's surface charge and forming large aggregations. Large NP/bacteria complex aggregates would soon develop in the suspension. This points to a phenomena where the size of the particles is important. By using electrostatic forces of attraction, small, negatively charged bacterial cells could easily ensnared NPs [18-20].

4. Conclusion

The simple chemical method is an effective way to prepare aluminum oxide nanoparticles. The results of the compositional diagnosis confirmed the formation of monocrystalline aluminum oxide nanostructures with an average crystal size of 11.45nm. The surface characteristics also showed that the shape of the grains is very similar, with sharp peaks and their distribution is very homogeneous. The peak of ultraviolet absorption indicates at 200 nm, which corresponds to the lowest transmittance of the prepared films. As for the results of antibacterial activity, the diameters of the inhibition zones for the types of bacteria and fungi studied were relatively high. This is evidence of the possibility of using aluminum oxide in the field of biomedicine and developing it in the future.

References

[1] D. Manyasree, P. Kiranmayi and R. Kumar, "Synthesis, characterization and antibacterial activity of aluminum oxide nanoparticles", *Int. J. Pharm. Pharm. Sci*, 10(1) (2018) 32-35.

[2] D.B. Warheit, "How meaningful are the results of nanotoxicity studies in the absence of adequate material characterization?" *Tox. Sci*., 101(2) (2008) 183-185.

[3] S. Stankic et al., "Pure and multi metal oxide nanoparticles: synthesis, antibacterial and cytotoxic properties", *J. Nanobiotech.*, 14(1) (2016) 1-20.

[4] S.A. Corr, "Metal oxide nanoparticles", *Nanosci.*, 1 (2013) 180-207.

[5] T.A. Mezher, A.M. Ali and A.N. Abd, "Iron oxide nanoparticle biosynthesis, characterization, and antimicrobial activity using *Nigella sativa* seeds extract", *Int. J. Nanosci.*, 22(4) (2023) 2350026.

[6] L.L. Hench, "Bioceramics: from concept to clinic", *J. Am. Cer. Soc.*, 74(7) (1991) 1487-1510.

[7] N. Travitzky et al., "Rapid synthesis of Al_2O_3 reinforced Fe–Cr–Ni composites", *Mater. Sci. Eng. A*, 344(1-2) (2003) 245-252.

[8] P. Ganguly and W.J. Poole, "*in situ* measurement of reinforcement stress in an aluminum–alumina metal matrix composite under compressive loading", *Mater. Sci. Eng. A*, 352(1-2) (2003) 46-54.

[9] J.S. Kim et al., "Antimicrobial effects of silver nanoparticles", *Nanomed. Nanotech. Biol. Med.*, 3(1) (2007) 95-101.

[10] A.R. Allafchian, S.S. Banifatemi and S.A. Jalali, "Synthesis and characterization of Ag/SiO_2 nanoparticles embedded in TPS and TEOS sol-gel matrix with excellent antibacterial activity", *Nanosci. Nanotech. Asia*, 8(1) (2018) 33-40.

[11] A. Gupta et al., "Combatting antibiotic-resistant bacteria using nanomaterials", *Chem. Soc. Rev.*, 48(2) (2019) 415-427.

[12] T.A. Mezher, A.M. Ali and A.N. Abd, "Using Nigella Sativa Seeds Extract for the Biosynthesis, Characterization and Antimicrobial Activity of CuO NPs", *Int. J. Nanosci.*, 22(4) (2023) 2350035.

[13] V.R. Santoyo et al., "Effect of aluminum precursor on physicochemical properties of Al_2O_3 by hydrolysis/precipitation method", *Nova scientia*, 10(20) (2019) 83-99.

[14] M. Maruthapandi et al., "Antimicrobial activities of Zn-doped CuO microparticles decorated on polydopamine against sensitive and antibiotic-resistant bacteria", *ACS Appl. Poly. Mater.*, 2(12) (2020) 5878-5888.

[15] M.A. Hameed et al., "Preparation and characterization of Al_2O_3 nanostructures by pulsed-laser deposition", *J. Optoelectron. Photon.*, 6(8) (2015) 43-46.

[16] B. Xu et al., "Synthesis and characterization of mesoporous Si-modified alumina with high thermal stability", *Micropor. Mesopor. Mater.*, 238 (2017) 84-89.

[17] M. Riad, "Influence of magnesium and chromium oxides on the physicochemical properties of γ-alumina", *Appl. Catal. A: Gen.*, 327(1) (2007) 13-21.

[18] M.A. Ansari et al., "Antibacterial potential of Al_2O_3 nanoparticles against multidrug resistance strains of Staphylococcus aureus isolated from skin exudates", *J. Nanopart. Res.*, 15 (2013) 1-12.

[19] P.A. Prashantha et al., "Synthesis, characterizations, antibacterial and photoluminescence studies of solution combustion-derived-Al_2O_3 nanoparticles", *J. Asian Cer. Soc.*, 3(3) (2015) 345-351.

[20] D. Wu et al., "Investigation into the antibacterial activity of monodisperse BSA-conjugated zinc oxide nanoparticles", *Curr. Appl. Phys.*, 14(11) (2014) 1470-1475.

Proceedings of 5th International Specialized Conference of Education College on Physics and Applied Sciences (5thICECAS24), 22-23 April 2024

Duha A. Abid
Maisam A. Abdul Resool
Batool Z. Fahim
Abdul H.A.Z. Raheim
Ihab A. Thabet
Muslim A. Abid
Wisam J. Aziz

Department of Physics, College of Science, Mustansiriyah University (MU), Baghdad, IRAQ

Synthesis of FeO/Cu Nanocrystalline Alloy by Combining $FeCl_3$ and Cu_2NO_3 Salts with Oats Extract for Methylene Blue Dye Degradation

FeO nanoparticles (NPs) and FeO/Cu NCs were made using a straightforward chemical process at 300 °C for two hours for degradation MB dye. The FCC structure of the crystallite size of FeO NPs ranged from 64 nm, but the crystallite size of the FeO/Cu NCs generated with *oats* extract exhibited an increase to 14 nm. FeO NPs synthesized without the use of *oats* extract, FE-SEM images revealed a nano-cubic like structure with particle size (56.02 to 156.6) nm. In addition, the morphology of FeO/Cu NCs revealed a nano-ball like structure with smaller particle size (45.21 to 50.32) nm. Energy gap value for FeO NPs was found to blue shift from 3.2 eV to 5 eV for the FeO/Cu NCs that used *oats* extract, according to UV-Vis tests.

Keywords: Oats extract; Iron oxide; Methylene Blue dye; Green synthesis
Received: 19 January 2024; Revised: 4 March 2024; Accepted: 4 April 2024

1. Introduction

Nanotechnology has grown in use in a variety of industries, including the fabrication of microelectronics, lithium batteries, nonlinear optics systems, transistors, diodes for sensors and solar cells, and in medicine as an essential cancer-fighting agent and antimicrobial and antibiotic agents. Its chemical, biological, and physical characteristics have all risen with time [1]. Because of their small band gap, chemical consistency, magnetic qualities, and other characteristics, (FeO) NPs and FeO/CuNCs have been described as remarkable materials for biomedical to environmental applications. As was previously mentioned, various chemical and physical methods were used to synthesize nanoparticles made of iron oxide. However, these methods require a highly toxic reaction to reduce materials like sodium hydrazine and the borohydride [2]. The environmentally friendly techniques that numerous researchers in the last decade have devised were dubbed "biosynthesis" or "green synthesis" [3]. In earlier research, Koli et al. [4] have produced metal oxide nanoparticles and used them to degrade dyes. Priya et al. [5] have produced nanoparticles and used them in waste water treatment processes. Iron ore was produced by Sheila et al. [6] for use in environmental treatments.

This investigation examined how the absorption mechanism might quickly and efficiently remove MB dye in a short amount of time when exposed to typical levels of visible light. For the first time, iron nitrate, and copper nitrate were combined with oats extract using a straightforward chemical process that was performed at 300°C for two hours to produce FeO nanoparticles and FeO/Cu NCs.

2. Experimental Part

The salts of iron (iii) and copper (iii) nitrate (Cu_2NO_3) (Sigma-Aldrich, India, purity 99.99%) were provided, and the oats was also supplied too. These plants are abundant in minerals, collagen, and protein. The methylene blue (MB) dye was used for degradation tests. The oats samples were broken into little pieces and thoroughly washed to remove contaminants. Then, using an electronic blender, the dried peels were crushed into a soft powder. A mixing of 5 g of oats powder and 100 ml of distilled water produced oats extract. The preparation of FeO nanoparticles involves mixing 100 ml of Fe_2NO_3 salt (1M) with 100 ml of distilled water. The solution combination was then stirred for 30 minutes at 70°C using a magnetic stirrer. In order to obtain a nanopowder, a ceramic eyelid was sealed with a 25 ml solution of FeO nanoparticles and baked for two hours at 300°C. In 100 ml of deionized water, 10 mg each of Fe_2NO_3 and Cu_2NO_3 salts were dissolved, and the mixture was magnetically agitated for 10 minutes.

The degradation of MB dye solution was used to measure the photocatalytic activity of FeO NPs and FeO/Cu NCs. A 1mg of MB (3×10^{-5}M) was mixed with 100 ml deionized water to produce a final concentration of 10 mg/L. Next, 3 mg of FeO NPs and FeO/Cu NCs powder were mixed together in a glass beaker. To keep the suspension of FeO NPs and FeO/Cu NCs in balance, the mixture was swirled for ten minutes in the dark using a magnetic stirrer. This was done after 10 min. Following a final

centrifugation of around 4 mL of the solution for 10 min at 10,000 rpm, the absorbance of the supernatant was determined using a Shimadzu UV-1800 UV–visible spectrophotometer by keeping an eye on the greatest absorption at λ=664nm. The MB dye removal efficiency ($\eta_{removal}$) was computed using the following formula

$$\eta_{removal}\ (\%) = C_{ini} - \frac{C_{fin}}{C_{ini}} \times 100\% \qquad (1)$$

The removal percentage of the MB dye using FeO NPs was determined via equation as follow:

$$Removal\ (\%) = \left[1 - \frac{C_{ini}}{C_{fin}}\right] \times 100\% \qquad (2)$$

where C_{ini} is the initial concentration of MB dye, C_{fin} is the final concentration of MB dye, t is irradiation time (min)

3. Results and Discussion

The XRD analysis of the FeO NP films deposited on glass substrates after 2 hours of evaporation at 300°C without oats extract is shown in Fig. (1a).

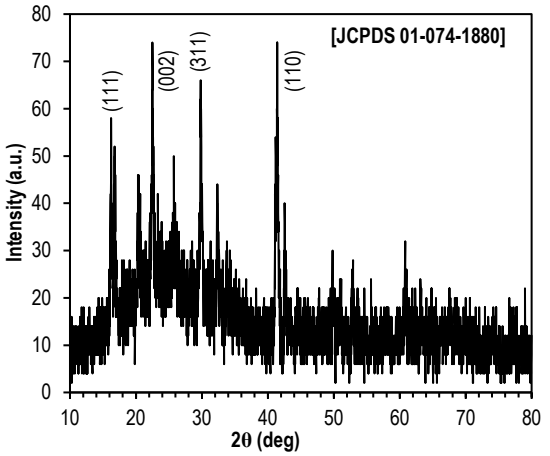

Fig. (1) XRD pattern of (a) FeO NPs, and b) FeO/Cu NCs

Figure (1b) displays the preferred orientation of FeO NPs produced by a chemical process at 300°C for two hours with oats extract. To get the crystalline size (D), the Scherrer's equation [7] was utilized as follows:

$$D = \frac{k.\lambda}{\beta cos\theta} \qquad (3)$$

where k is the form factor (0.9), λ is the x-ray wavelength (0.15418nm), β is the full-width at half maximum (FWHM), and θ is the diffraction angle

FE-SEM was carried out on the FeO NPs deposited on glass substrates without oats extract and the shape and average grain size were examined. As described in the literature [8], a micrograph of the face center cubic (f.c.c.) structures is shown in Fig. (2a,b). The average grain size was ranging from 56.02 to 156.6nm. Figure (2a,b) display FE-SEM images of FeO/CuNCs deposited on glass substrates using a chemical method with oats extract. The average particle size and shape with discernible nano-ball formations ranged from 45.21 to 50.32 nm. The FE-SEM images demonstrate the variations in grain size and nanostructure shape before to and following employing the oats extract.

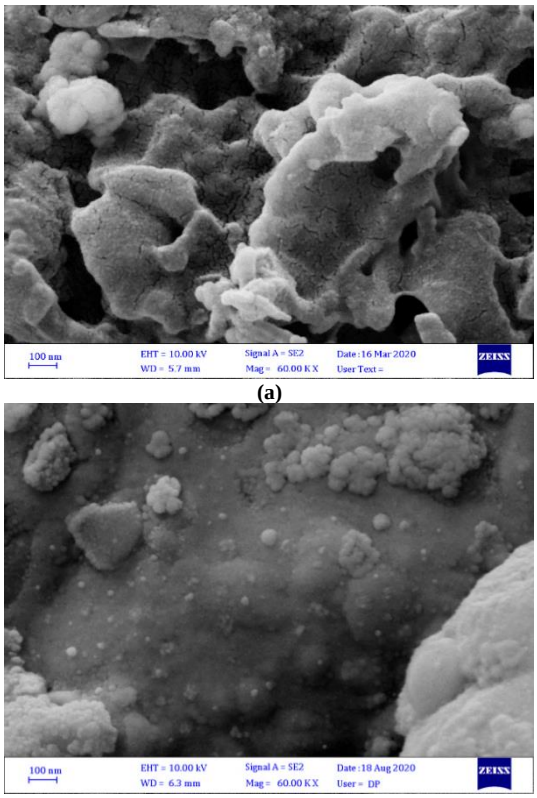

Fig. (2) FE-SEM images of (a) FeO NPs, and (b) FeO/Cu NCs

The UV-visible spectrum of the prepared FeO NPs deposited on glass substrate, was used to study the optical transmittance spectra of FeO NPs (Fig. 3a,b). Figure (3a) displays the transmission spectrum of the FeO NPs deposited on glass substrate, while figure (3b) displays the transmission spectrum of the FeO/Ag NCs.

Plotting $(\alpha h\nu)^2$ vs. photon energy ($h\nu$) yields the energy band gap of FeO NPs produced without oats extract (Fig. 4a). The straight line is extrapolated to $(\alpha h\nu)^2$, which gives the energy band gap. It was discovered that the optical band gap of FeO NPs

ranged from 3.0 to 3.2 eV. The utilization of oats extract resulted in an increase in the energy gap of the FeO/Cu NCs, as shown in Fig. (4b), which ranges from 4.9 to 5 eV. The energy band gap is computed using the equation [9]

$(\alpha h\nu)^n = A(h\nu - E_g)$ (4)

where A is constant, $h\nu$ is the energy of light, and n is a constant that varies depending on the type of the electron transfer

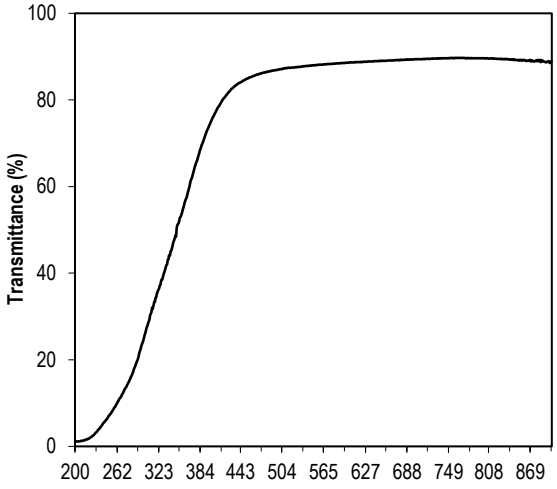

(a) FeO NPs

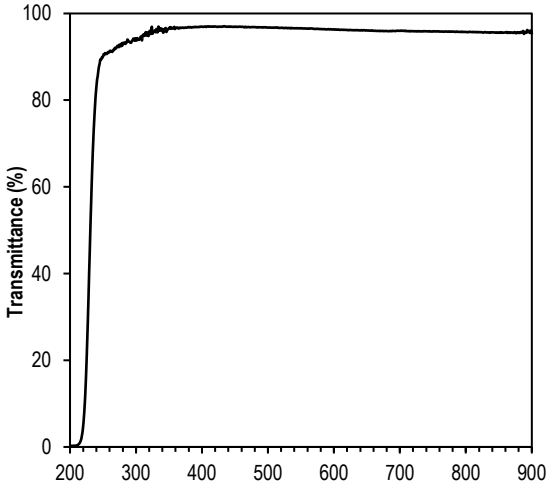

(b) FeO/Cu NCs

Fig. (3) UV-visible transmission spectra (a) FeO NPs, and (b) FeO/Cu NCs

The photocatalytic activity of chemically synthesized FeO NPs and FeO/Cu NCs, both with and without oats extract, was evaluated based on the degradation of the MB dye solution. Figure (5) illustrates how this enhanced the pace of chemical interaction between MB dye and FeO NPs and FeO/Cu NCs, enabling faster and more effective dye degradation at the absorption peak (664nm). The degradation efficiency (%) of MB dye at 10 g/L for FeO NPs generated without using oats extract is shown in Fig. (6a) after 120 minutes of normal room light irradiation (90%) and normal room temperature.

The use of FeO/Cu NCs significantly increases the MB dye's degradation efficiency (by 94%) after 60 minutes, as shown in Fig. (6b) [10].

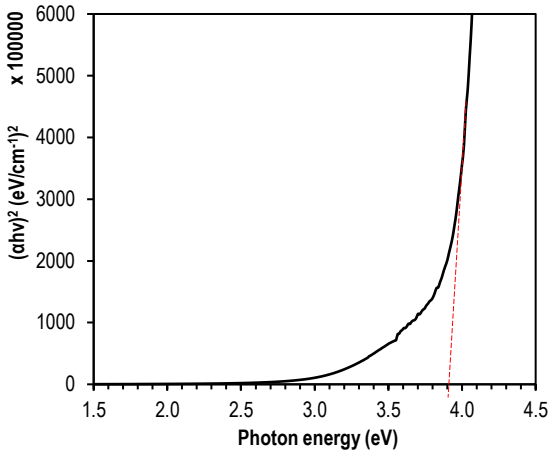

(a) FeO NPs

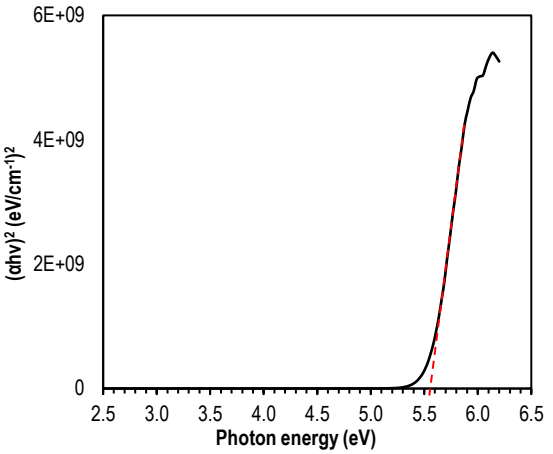

(b) FeO/Cu NCs

Fig. (4) Energy band gap of (a) FeO NPs, and b) FeO/Cu NCs

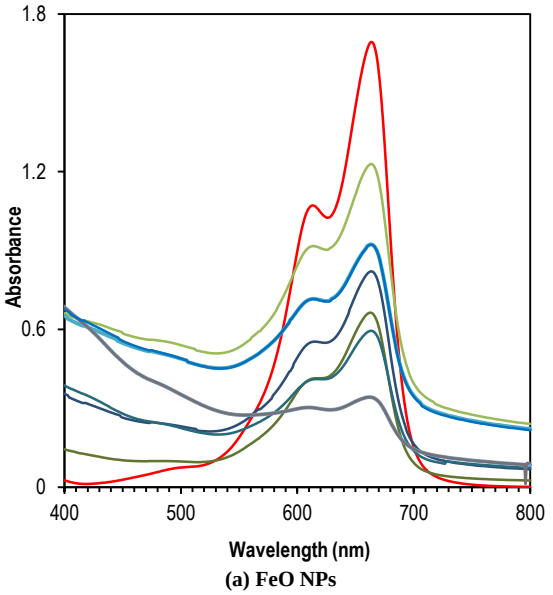

(a) FeO NPs

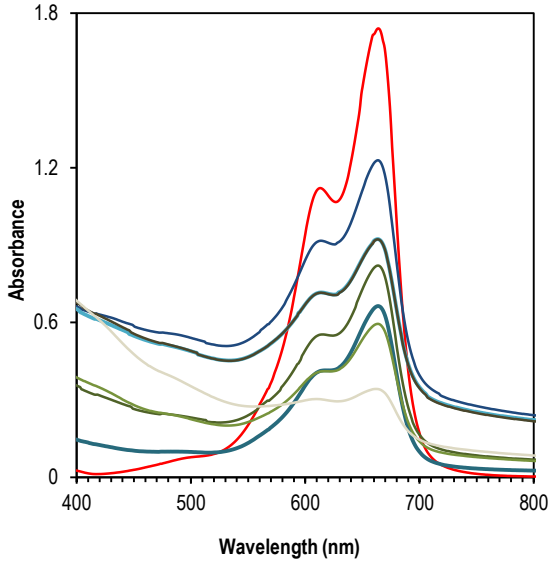

(b) FeO/Cu NCs

Fig. (5) UV-visible spectra showing the degradation of MB dye using (a) FeO, and (b) FeO/Cu NCs

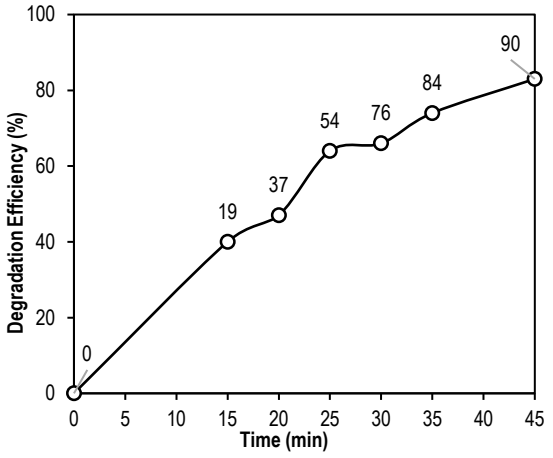

(a) FeO NPs

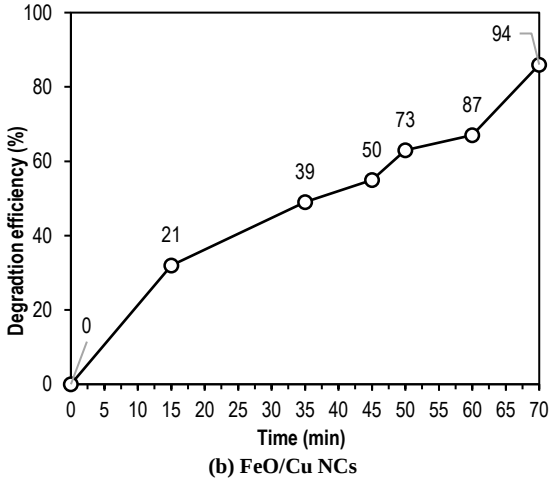

(b) FeO/Cu NCs

Fig. (6) Linear plot of MB dye degradation at 10 g/L under normal light irradiation in presence of (a) FeO NPs, and (b) FeO/Cu NCs

4. Conclusion

In this work, using the oats extract converts Fe_2NO_3 and Cu_2NO_3 salt to FeO, FeO/Cu NCs by acting as a reducing, stabilizing, and anti-caking agent. The crystallite size increased from 14 to 64 nm with a f.c.c. structure, whereas the crystallite size of FeO NPs ranged from 64 to 14 nm. A nano-cubic like structure with particle size 56.02-156.6nm of FeO NPs was revealed.

References

[1] A. Ali et al., "Synthesis, characterization, applications, and challenges of iron oxide nanoparticles", *Nanotech. Sci. Appl.*, 9 (2016) 49-67.

[2] M.A. Abid and D.A. Kadhim, "Novel comparison of iron oxide nanoparticle preparation by mixing iron chloride with henna leaf extract with and without applied pulsed laser ablation for methylene blue degradation", *J. Enviro. Chem. Eng.*, 8(5) (2020) 104138.

[3] T. Deng et al., "*in situ* formation of polymer-inorganic solid-electrolyte interphase for stable polymeric solid-state lithium-metal batteries", *Chem.*, 7(11) (2021) 3052-3068.

[4] S. Devasahayam, "A novel iron ore pelletization for increased strength under ambient conditions", *Sustain. Mater. Technol.*, 17 (2018) e00069.

[5] T.P. Almeida et al., "Process map for the hydrothermal synthesis of α-Fe_2O_3 nanorods", *J. Phys. Chem. C*, 113(43) (2009) 18689-18698.

[6] A. Lassoued et al., "Synthesis, structural, optical and morphological characterization of hematite through the precipitation method: Effect of varying the nature of the base", *J. Mol. Struct.*, 1141 (2017) 99-106.

[7] J. Singh et al., "Green synthesis of silver nanoparticles using sun dried tulsi leaves and its catalytic application for 4-Nitrophenol reduction", *J. Enviro. Chem. Eng.*, 6(1) (2018) 1468-1474.

[8] N. Beheshtkhoo et al., "Green synthesis of iron oxide nanoparticles by aqueous leaf extract of Daphne mezereum as a novel dye removing material", *Appl. Phys. A*, 124 (2018) 1-7.

[9] F.R. Hussain, "Synthesis and Characterization of Metal Oxide Decorated Nanocomposite for Photocatalytic Application", PhD dissert., University of Lahore (2021).

[10] A.K. Saim et al., "Review of catalytic activities of biosynthesized metallic nanoparticles in wastewater treatment", *Enviro. Technol. Rev.*, 10(1) (2021) 111-130.

Proceedings of 5th International Specialized Conference of Education College on Physics and Applied Sciences (5thICECAS24), 22-23 April 2024

Structural and Electrical Properties of Zintl Antimonite Compounds, YbA_2Sb_2 (A=Zn, Cd, Mn) Prepared by Solid State Microwave Technique

Abrahim M. Jasim
A. Hmood

Department of Physics, College of Science, University of Basrah, Basrah, IRAQ

This work provide that can be introduce a microwave-assisted solid state technique to synthesize Zintl antimonite compounds $YbZn_2Sb_2$, $YbCd_2Sb_2$, $YbMn_2Sb_2$ in short time 10 mins with a maximum power of 1000W by utilizing an active carbon as a susceptor material . The microwave irradiation acts to accelerate the reactions induced by fast heat surrounding susceptor of primary components and give large ternary ingots. The XRD analysis detects that prepared compounds have a hexagonal structure with pure phase of all compounds $YbCd_2Sb_2$, $YbMn_2Sb_2$ and $YbZn_2Sb_2$. Thermoelectric characterizations have been performed for three antimonite compounds $YbZn_2Sb_2$, $YbCd_2Sb_2$, $YbMn_2Sb_2$, the best is $YbCd_2Sb_2$ with the high value of power factor is 0.48 μW/cmK^2 at 523K.

Keywords: Zintl antimonite; Microwave-assisted synthesis; Thermoelectric characteristics
Received: 19 January 2024; Revised: 4 March 2024; Accepted: 4 April 2024

1. Introduction

Thermoelectric (TE) materials describe the direct conversion process between heat and electricity [1-4]. According to the current development in the industrial material fields, ingots have emerged associated with much attention due to their use in many thermal and electrical applications. Merit $ZT=(S^2\sigma/K)T$ refers to high thermoelectric figure, where S, σ, K, and T are Seebeck coefficient, electrical conductivity, thermal conductivity, and absolute temperature, respectively [5-8]. The power factor ($S^2\sigma$) is considered as a crucial part in the study of thermoelectric materials (TEMs). To reach the high value in the figure of merit (ZT), higher value of power factor and lower thermal conductivity are required. In recent reports, TEMs have focused on increasing the power factor value and reducing thermal conductivity [9]. The Zintl phase compounds are considered as efficient thermoelectric substances having low electrical resistance, low thermal conductivity, and a large Seebeck coefficient. Furthermore, they exhibit small band-gap semiconductors with a range of concentration 10^{19}-10^{21} cm^{-3}, thus they act efficiently than metals or insulators. In addition, heavy atoms, large unit cell, and complex structure ultimately proceed in perfect thermoelectricity (TE) [10,11].

Thermoelectric Zintl phase compounds have been prepared by direct solid state reactions technique and found taking a long time under heating for example: $YbCd_{2-x}Mg_xSb_2$ at 1273K for 72h [12], $Ca_{1-x}Yb_xZn_2Sb_2$ at 1273K for 48h [13], $YbZn_2Sb_2$ at 1323K for 30h [14], $SrZn_2Sb_2$ at 1073K for 5 days [15]. $Ca_{1-x}Eu_xZn_2Sb_2$ at 1273K for 3 days [16], $Yb_xEu_{1-x}Cd_2Sb_2$ at 1200°C for 24 h [17]. While in our work, the Zintl antimonite compounds $YbZn_2Sb_2$, $YbCd_2Sb_2$, $YbMn_2Sb_2$ is synthesized in short time (10min) under a microwave-assisted solid state. Microwave irradiation is an efficient method employed to prepare the thermoelectric materials in short time. Frequency of 2.45 GHz and heating reach to 1273 K are declared to be the optimized conditions for coupling metal powders under microwave fields without causing visible electric discharges compared with bulk samples [18]. The Zintl phase families like 1-2-2-family which includes $YbZn_2Sb_2$, $YbCd_2Sb_2$, $YbMn_2Sb_2$ are considered as important TEMs. These TEMs are prepared to have cation parts (Yb^{+2}) and anion parts $(A_2Sb_2)^{-2}$ when A=Zn, Cd, Mn in 2D and 3D polyatomic nets [19]. Zintl compounds exhibit a high carrier concentration in the order of 10^{19} cm^{-3} without chemical doping, due to high concentrations of cation vacancies [20,21]. Many articles have introduced using a microwave-assisted solid state as an efficient technique which is employed to prepare Zintl phase compounds $YbZn_2Sb_2$, $YbCd_2Sb_2$, $YbMn_2Sb_2$ with fascinating thermoelectric applications. Importantly, a microwave-assisted solid state provides high energy, easy work up and eco-friendly methodology than other traditional techniques [22].

In this work, a successful modification in the percentage of cations $YbZn_2Sb_2$, $YbCd_2Sb_2$, $YbMn_2Sb_2$ under a microwave-assisted solid state synthesis are reported. To the best our knowledge, antimony (Sb)-based Zintl compounds have been demonstrated to behave as an efficient thermoelectric material possessing electric crystal, and photonic glass nature. Their unique structural crystal emerges in low lattice thermal conductivity at high temperature [23].

2. Experimental Part

The rapid microwave synthesis was used to prepare the Zintl phase antimonite compounds (Yb, Zn, Cd, Mn, and Sb >99.99% 120 meshes) semiconductor compounds were weighted 2g according to the stoichiometric ratio. The powder was subjected into an agate mortar and pestle in order to make a homogenous mixture under a period 20 min. The batched weight was taken inside a clean sealed quartz ampoule under high vacuum reaches to 10^{-5} mbar. The ampoule was further irradiated with a maximum power of 1000W microwave oven (LG) (MS2147C 1000 W) at 2.45 GHz. An active carbon (susceptor) was surrounded the quartz ampoule to absorb microwave irradiation and initiate heating under a microwave-assisted solid state synthesis. The active carbon helps to raise reaction temperature to reach 1123 K for 10 min (2 on: 2 off) as shown in Fig. (1). Thermometer (S-CA-1168) was used to control the temperature of ampoule (223-1173K) under an infrared power. The fusing materials were further cooled to room temperature to obtain ingot.

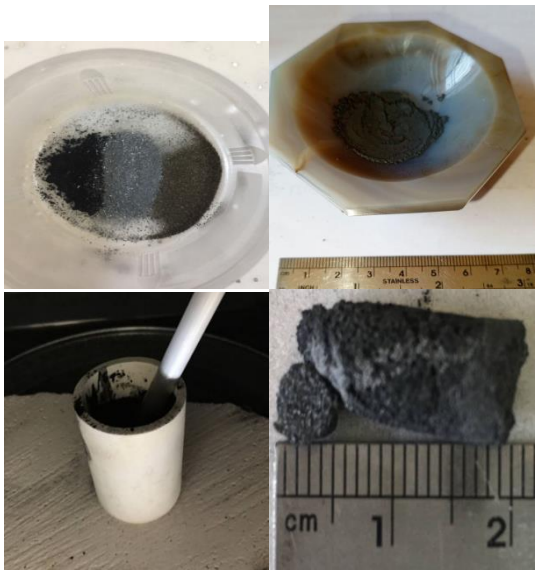

Fig. (1) Synthesis ingot of the compounds YbA_2Sb_2 (A=Zn, Cd, Mn)

The morphological, structural and thermoelectric characterizations were examined. Field-emission scanning electron microscopy (FE-SEM) (Leo-Supra 50VP, Carl Zeiss) was utilized to image the polycrystalline structures of the ingots. After grinding process, the powders were then conducted to identify their crystal structures using X-ray diffraction (XRD) (PANalytical X'Pert PRO MRD PW3040). The ingots $YbZn_2Sb_2$, $YbCd_2Sb_2$, $YbMn_2Sb_2$ were ground into fine powders were pressed into disk shapes with dimensions of 10x0.5mm were obtained using cold pressing at 10 tons. The determined slope of the linear relationship between the thermo-electromotive force and the varied temperatures between the two ends of each sample is used to calculate the Seebeck coefficient (S) of polished disks as referring in the reference [21]. The four-point probe method was employed to acquire the electrical conductivity (σ) under vacuum (10^{-3} mbar) with a range of temperature 298-523K. The carrier concentration (n) was determined at room temperature from the Hall voltage measurement with an applied magnetic field of 1 T using a PHYWE 6480 electromagnet.

3. Results and Discussion

XRD patterns of $YbZn_2Sb_2$, $YbCd_2Sb_2$, and $YbMn_2Sb_2$ are configured in Fig. (2). The dominant diffraction peaks of the prepared compounds were indexed as hexagonal structure type according to JCPDS co. (98-041-9689, 98-038-0375 and 01-083-1684). The data analysis indicated that the $YbZn_2Sb_2$, $YbCd_2Sb_2$, and $YbMn_2Sb_2$ have polycrystalline structure. Get the pure phase for all compounds $YbZn_2Sb_2$, $YbCd_2Sb_2$, and $YbMn_2Sb_2$ (Fig. 2).

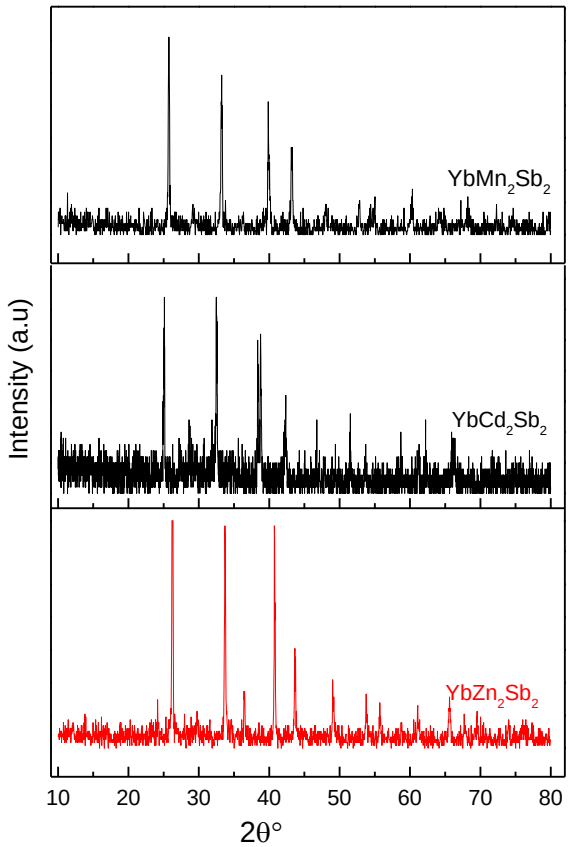

Fig. (2) XRD patterns of Zintl antimonite compounds, YbA_2Sb_2 (A=Zn, Cd, Mn)

Scanning electron microscopy (SEM) for the prepared compounds show that particles were emerged under irradiation process to form the nanoparticle structure on the surface of ingots as configured in Fig. (3). The nanoparticles were noticed as they appeared non-uniformly distributed over the surface. The electrical conductivity (σ) was measured for three prepare compounds YbA_2Sb_2 (A=Zn, Cd, Mn), the compounds $YbZn_2Sb_2$, $YbCd_2Sb_2$, and $YbMn_2Sb_2$ behavior as semiconducting materials,

whose electrical conductivity (σ) increased when the temperature was increased as shown in Fig. (4).

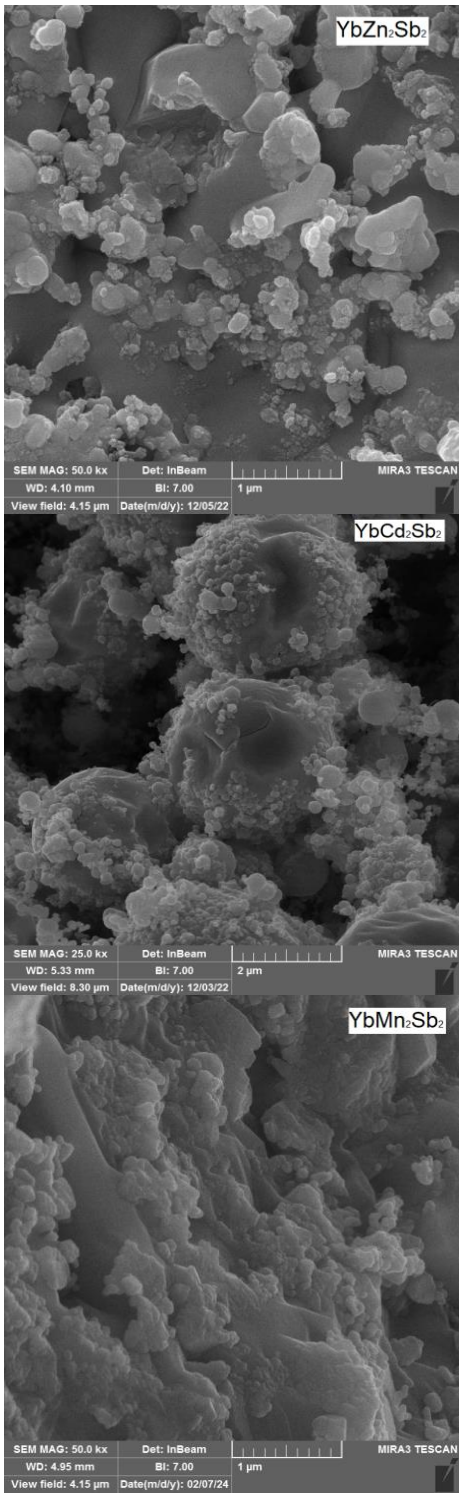

Fig. (3) SEM images for the prepared compounds YbA_2Sb_2 (A=Zn, Cd, Mn)

Figure (5) shows that the Seebeck coefficient of the prepared compounds YbA_2Sb_2 (A=Zn, Cd, Mn). The measurements appear the Seebeck coefficient of compound $YbZn_2Sb_2$ is positive that means the majority carriers for charge are holes and the highest value of the Seebeck coefficient is 32.15 µv/K at 523K, while for the two compounds $YbCd_2Sb_2$ and $YbMn_2Sb_2$, the Seebeck coefficient is negative that means the majority charge carriers are electrons and the highest values of Seebeck coefficient are -19.28 µV/K for $YbCd_2Sb_2$, and -47.09 µV/K for $YbMn_2Sb_2$ at 523K.

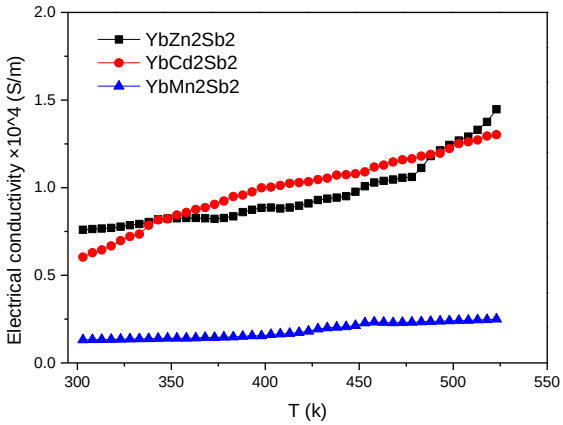

Fig. (4) Electrical conductivity (σ) of prepared compounds YbA_2Sb_2 (A=Zn, Cd, Mn)

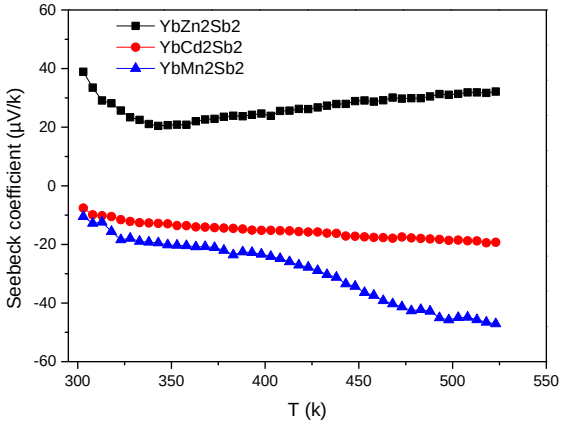

Fig. (5) Seebeck coefficient vs. temperature of three prepared compounds YbA_2Sb_2 (A=Zn, Cd, Mn)

The Seebeck coefficient of degenerate semiconductor is determined as [1,2]:

$$S = \frac{8\pi^2 k_B^2}{3eh^2} m^* T \left(\frac{\pi}{3p}\right)^{2/3} \quad (1)$$

where k_B is Boltzmann's constant, h is Planck's constant, and m^* is the effective mass

The above mentioned equation shows that Seebeck coefficient is highly dependent on electrical conductivity. Therefore, an increase in the Seebeck coefficient values could be attributed to an increasing of levels in acceptor state, as well as these values increased with the chosen Zintl compounds that have high values of m^*. Power factor ($S^2\sigma$) of the prepared compounds YbA_2Sb_2 (A=Zn, Cd, Mn) is shown in Fig. (6). We notice from comparison between the compounds that the optimum is $YbCd_2Sb_2$ with the highest value of the power factor is 0.48 µW/cm.K^2 at 523K.

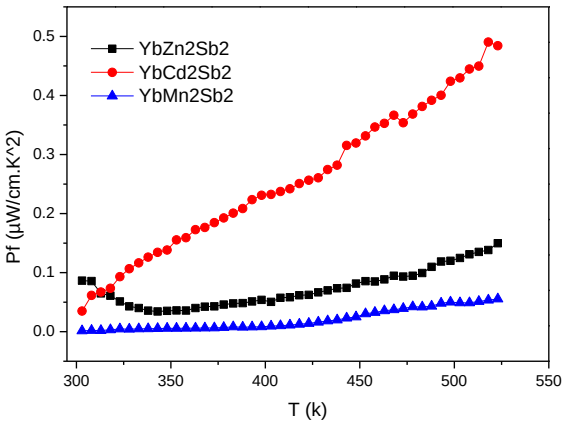

Fig. (6) Power factor ($S^2\sigma$) vs. temperature of the prepared compounds YbA_2Sb_2 (A= Zn, Cd, Mn)

4. Conclusions

Zintl compounds YbA_2Sb_2 (A=Zn, Cd, Mn) have been successfully produced in short time using microwave-assisted solid state method at 1123K for 10min. The prepared compounds have hexagonal structure, they are good as thermoelectric materials and the optimum is $YbCd_2Sb_2$ with high value of power factor (0.48 μW/cmK^2 at 523K).

Acknowledgements

The authors gratefully acknowledge support from the Department of Physics, College of Science, University of Basrah, Iraq.

References

[1] G.S. Nolas, J. Sharp and H.J. Goldsmid, **"Thermoelectrics Basic Principles and New Materials Developments"**, Springer-Verlag (Berlin, 2001), Ch. 3, p. 73.

[2] L. Chen, R. Liu and X. Shi, **"Thermoelectric Materials and Devices"**, Elsevier Inc. (2021), Ch. 1, p. 2.

[3] Y.X. Gan, **"Nanomaterials for Thermoelectric Devices"**, Pan Stanford Publishing Ltd. (2018), Ch. 1, p 3.

[4] W. He et al., "Recent development and application of thermoelectric generator and cooler", *J. Appl. Ener.*, 143 (2015) 1-25.

[5] X. Du et al., "Enhanced thermoelectric performance of n-type Bi_2S_3 with added ZnO for power generation", *RSC Adv.*, 5 (2015) 31004–31009.

[6] A. Kadhim, A. Hmood and H. Abu Hassan, "Electrical characterization of thermoelectric generators based on p-type $Bi_{0.4}Sb_{1.6}Se_{2.4}Te_{0.6}$ and n-type$Bi_2Se_{0.6}Te_{2.4}$ bulk thermoelectric materials", *J. Mater. Lett.*, 97 (2013) 24–26.

[7] M.W. Gaultois et al., "Data-Driven Review of Thermoelectric Materials: Performance and Resource Considerations", *J. Chem. Mater.*, 25 (2013) 2911−2920.

[8] A. Kadhim, A. Hmood and H. Abu Hassan, "Significant Influences of Selenium on the Electrical Properties of Bi2Te3 Compounds Synthesized Using Solid-State Microwave Irradiation", *J. Adv. Mater. Res.*, 501 (2012) 126-128.

[9] N. Ghazi and A. Kadhim, "Thermoelectric properties of solid state reaction-prepared ZnO based alloys with various CuO doping in $(CuO)_x(ZnO)_{1-x}$", *J. Solid State Commun.*, 361 (2023) 115058.

[10] D. Berettaa et al., "Thermoelectrics: From history, a window to the future", *Mater. Sci. Eng. R.*, (2018).

[11] I. Nandhakumar, N.M. White and S. Beeby, **"Thermoelectric Materials and Devices"**, The Royal Society of Chemistry, Printed by CPI Group (UK, 2017), Ch. 1, p. 4.

[12] Q. Cao et al., "Thermoelectric properties of $YbCd_2Sb_2$ doped by Mg", *J. Alloys Comp.*, 680 (2016) 278-282.

[13] F. Gascoin et al., "Zintl Phases as thermoelectric Materials Tuned transport properties of compounds $Ca_xYb_{1-x}Zn_2Sb_2$", *J. Adv. Func. Mater.*, 15 (2005) 1860–1864.

[14] X. Zhang et al., "Spontaneously promoted carrier mobility and strengthened phonon scattering in p-type $YbZn_2Sb_2$ via a Nano compositing approach", *J. Nano Ener.*, 43 (2018) 159-167.

[15] H. Zhang et al., "Thermoelectric Properties of Polycrystalline $SrZn_2Sb_2$ Prepared by Spark Plasma Sintering", *J. Electron. Mater.*, 39 (2010) 1772–1776.

[16] T.A. Wubieneh et al., "Thermoelectric properties of Zintl phase compounds of $Ca_{1-x}Eu_xZn_2Sb_2$ ($0 \leq x \leq 1$)", *J. Electron. Mater*, 45 (2016) 1942-1946.

[17] H. Zhang et al., "Thermoelectric properties of $Yb_xEu_{1-x}Cd_2Sb_2$", *J. Chem. Phys.*, 133 (2010) 194701.

[18] A.G. Whittakera and D.M.P. Mingos, "Microwave-assisted Solid-state Reactions involving Metal Powders", *J. Chem. Soc. Dalton Trans.*, (1995) 2073-2079.

[19] W. Zhao et al., "Enhanced thermoelectric performance via randomly arranged nanopores: Excellent transport properties of $YbZn_2Sb_2$ nanoporous materials", *J. Act. Mater.*, 60 (2012) 1741-1746.

[20] A. Zevalkink et al., "Nonstoichiometry in the Zintl Phase $Yb_{1-\delta}Zn_2Sb_2$ as a Route to Thermoelectric Optimization", *J. Chem. Mater.*, 26 (2014) 5710-5717.

[21] G.S. Pomrehn et al., "Defect-Controlled Electronic Properties in AZn_2Sb_2 Zintl Phases", *J. Ang. Chem.*, 126 (2014) 3490-3494.

[22] A. Kadhim, A. Hmood and H. Abu Hassan, "Physical properties of $Bi_2(Te,Se)_3$ and $Bi_2Se_{1.2}Te_{1.8}$ prepared using solid-state microwave synthesis", *J. Mater. Lett.*, 65 (2011) 3105–3108.

[23] Y. Takagiwa et al., "Thermoelectric properties of $EuZn_2Sb_2$ Zintl compounds: ZT enhancement through Yb substitution for Eu", *J. Alloys Comp.*, 703 (2017) 73-79.

Proceedings of 5th International Specialized Conference of Education College on Physics and Applied Sciences (5thICECAS24), 22-23 April 2024

Milad A.R. ALhammashi [1]
Fadhil K. Farhan [2]
Hashim A. Yusr [1]

[1] *Department of Physics, College of Science, University of Wasit, Kut, IRAQ*
[2] *Department of Medical Physics, College of Science, Al-Karkh University of Science, Baghdad, IRAQ*

Evaluation of Thermal and Mechanical Performance of β-Tri-Calcium Phosphate

The study evaluates the performance of bio ceramics, particularly tri-calcium phosphate from bovine bone waste and calcined calcium carbonate. Nano composites were prepared via wet chemical precipitation. Sintered samples, treated at temperatures from 1000°C to 1250°C, were tested for hardness, wear, friction, and compressive strength, with one group immersed in a simulated body fluid for 30 days. Results exhibited improved properties in the immersed group, confirmed by tests including differential thermal analysis up to 600°C.

Keywords: Bioceramics; $Ca_3O_8P_2$; Bovine bone; Simulated body suit
Received: 19 January 2024; Revised: 4 March 2024; Accepted: 4 April 2024

1. Introduction

In recent years, there has been remarkable progress in the field of biological materials, renowned for their ability to bond with bone tissue, notably calcium phosphate, extensively used in dentistry and orthopedics since 1926 [1]. Studies employing x-ray diffraction have highlighted the structural similarity between bone minerals and calcium phosphate minerals [2], such as apatite. Synthetic calcium phosphate-based bioceramic implants were pioneered in the early 20th century, demonstrating a stimulatory effect on osteogenesis. By the late 20th century, calcium phosphate materials found applications in various endodontic surgeries [3,4], including the implantation of hydroxyapatite cylinders as dental root substitutes [3,5]. Notably, by 1980, the clinical use of calcium phosphate witnessed significant advancements [3]. Due to their excellent biocompatibility, biodegradability, and potential biological activity, calcium phosphates constitute a distinct class of biomaterials. Biomaterials are categorized based on their intended applications, irrespective of their natural or synthetic origin, being moldable, inexpensive, and exhibiting no deficiency or deterioration in their physical and mechanical properties. They are utilized in the production of medical devices, such as implantable hearing aids and artificial hip joints, aiming to interact directly with living tissues and fluids [6]. The Chester (UK) Conference of the European Society for Biomaterials in 1991 provided a simplified definition [7,8], asserting that biological materials are non-living materials adapted for specific medical needs, compatible with the organism's biological system. These materials encompass metals, plastics, carbon compounds, and ceramic materials, taking diverse forms according to their intended functions. Biomaterials can be classified into two categories:
(A) Biopassive: Inert materials, such as Co-Cr alloys utilized in total joint replacements, are those that won't interact with the biological system that they are being employed in [9].
(B) Bioactive: relates to substances that will interact with a physical system, for as different polymers that break down inside the body [9]. Other Biomaterials Classification Biodegradable: The weather, soil, bacteria, plants, and animals are examples of natural effectors that can chemically breakdown or decompose it [10]. Previous studies [11] made a 3D-printed MgO biocomposite structure to study how a 3D Mg-rich environment affects CSD repair. The hybrid was made with a biodegradable polymer called polycaprolactone (PCL) as the matrix and MgO as the dispersion phase. Drevet et al. [12,13] have carried out a reaction that made it possible to make a bioactive layer. Electrode position happens in three steps that happen one after the other. These steps are electrochemical processes, changing the pH, and a calcium phosphate coating forming. During deposition, though, the process makes undesirable hydrogen bubbles because it reduces water, which is the electrolyte solution's solvent.

2. Experimental Part

To prepare beta-tricalcium phosphate from bovine bone waste, 500 g of cow bones were collected, cleaned, and sterilized. They were boiled in water for two hours, then dried and broken into small 5 cm

diameter pieces. Subsequently, they were burnt at 500°C to be brittle, crushed, and ground using an industrial electric mill. The resulting powder was then burnt at 800°C for 5 hours to obtain calcium oxide, confirmed via x-ray diffraction (XRD). It was then mixed with 85% phosphoric acid using the same method to obtain beta-tricalcium phosphate, diagnosed using XRD.

For the assessment of hardness, compressibility, wear, and density at 900°C, five samples were prepared and sintered at different temperatures (900, 1000, 1100, 1150, 1200, and 1250°C) for 2 hours. Particulate hardness was measured using a micro hardness device, while compressibility was examined using a universal machine with models of 2 cm diameter and 1.5 cm height. Wear resistance tests were conducted using a PIN-ON-DISC device under specific conditions, with samples of 1 cm diameter and 2 cm length, both with and without immersion in simulated body fluid (SBF), for comparison purposes.

3. Results and Discussion

The DTA curves in Fig. (1) illustrate the behavior of calcium carbonate at 600°C. An endothermic peak at approximately 830°C signifies the thermal decomposition of calcium carbonate, releasing carbon dioxide gas and leaving calcium oxide behind. DTA analysis measures the temperature difference between a sample and a reference material, reflecting thermal phenomena such as phase transitions.

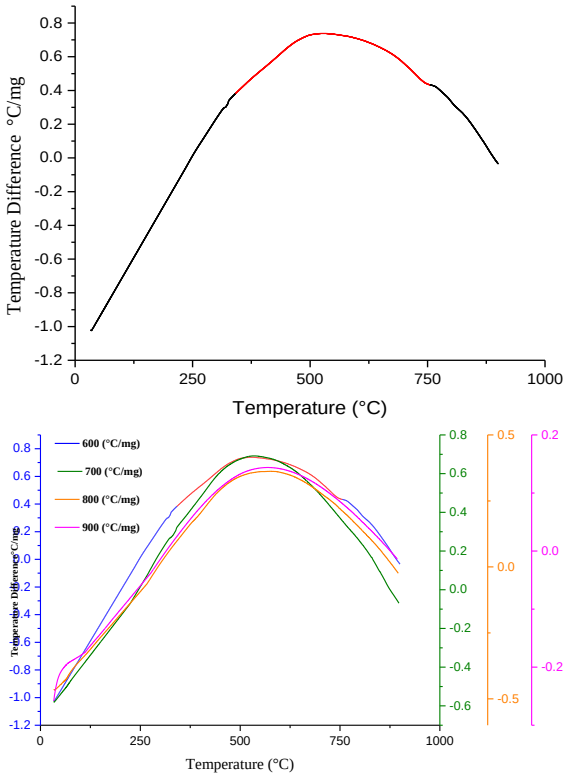

Fig. (1) Differential thermal analysis (DTA) of calcium carbonate in air atmosphere

Discussing hypothetical DTA results for calcium carbonate at 600°C, 700°C, 800°C, and 900°C reveals varying degrees of calcination. At 600°C, partial calcination yields a relatively low-intensity endothermic peak, while at 700°C and 800°C, the process intensifies, resulting in sharper peaks. Near completion at 900°C, the intensity of the endothermic peak may decrease, accompanied by a more pronounced exothermic peak.

Optimizing calcination temperature is crucial for specific applications, ensuring efficiency in the process.

(1) At 600°C, partial calcination of calcium carbonate might occur, potentially leading to the appearance of an endothermic peak on the DTA curve. This peak arises from the decomposition of a small fraction of calcium carbonate into calcium oxide and carbon dioxide. Its intensity will be relatively low since the reaction is not yet complete [14].

(2) At 700°C, the calcination process becomes more prominent, resulting in a sharper and more intense endothermic peak on the DTA curve. This indicates a higher degree of decomposition of calcium carbonate to calcium oxide and carbon dioxide [15].

(3) At 800°C, the calcination of calcium carbonate is near completion, and the DTA curve will exhibit a well-defined and intense endothermic peak, reflecting the significant decomposition of calcium carbonate. Additionally, there might be a small exothermic peak due to the formation of calcium oxide [16].

(4) At 900°C, calcination is almost complete. The DTA curve will still show an endothermic peak, but the intensity may start to decrease as most of the calcium carbonate has already decomposed. The exothermic peak corresponding to the formation of calcium oxide might become more pronounced [17].

In conclusion, analyzing the DTA curves of calcium carbonate calcined at different temperatures (600°C, 700°C, 800°C, and 900°C) can determine the extent of calcination and better understand the thermal events that take place during the process. It is essential to optimize the calcination temperature for specific applications and to maximize the efficiency of the process.

The density was determined for all CaPO compound samples annealed at various temperatures, as detailed in table (1).

Table (1) Density results of CaPO composite samples in the presence and absence of SBF

Sample code	Density without SBF (g/cm³)	Density with SBF (g/cm³)
CaPO 1000	2.45	2.56
CaPO 1100	2.56	2.76
CaPO 1150	2.87	2.98
CaPO 1200	2.97	3.1
CaPO 1250	3.13	3.54

Figure (2) illustrates that the density of all samples increases with both the addition of SBF and higher annealing temperatures. Sample CaPO-1250

exhibited the highest density without SBF (3.13 g/cm^3), which further increased with SBF addition to 3.54 g/cm^3. This enhancement in density with SBF addition is attributed to the presence of hydroxyapatite in SBF, resembling bone substance, thus augmenting density [18].

The mechanical properties of all CaPO samples were evaluated by analyzing wear and friction, as depicted in table (2). Figures (3) and (4) present the wear curves of CaPO samples with and without SBF. Samples without SBF exhibit higher wear values, ranging from 4.5x10^{-6} for CaPO-1000 to 3x10^{-7} for CaPO-1250. Addition of SBF decreases wear values, reaching a minimum of 1.5x10^{-7} for CaPO-1250. The discrepancy in wear values between samples with and without SBF diminishes with increasing annealing temperature, notably minimized for CaPO-1250.

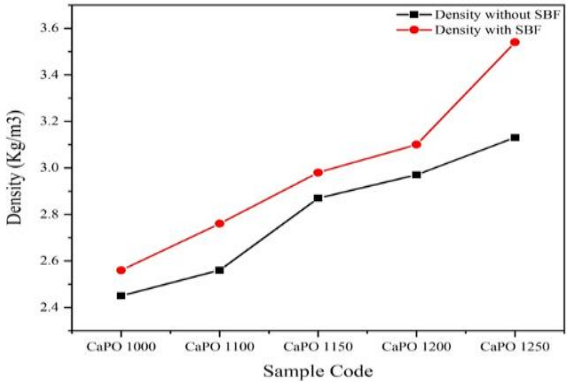

Fig. (2) Density curves of CaPO composite samples in presence and absence of SBF

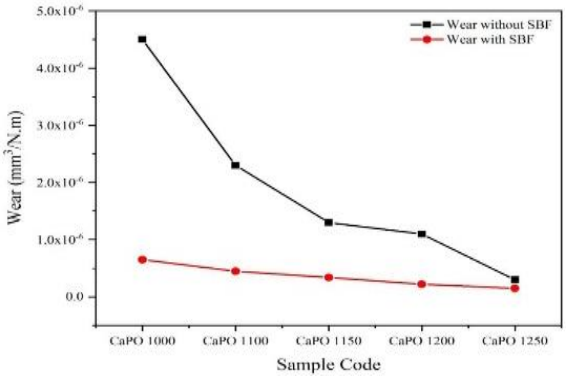

Fig. (3) Wear curves of Ca/PO composite samples in presence and absence of SBF

Figure (5) illustrates that the friction coefficient for all CaPO samples decreases with SBF addition, reaching a minimum of 0.09 for CaPO-1250. These reduced wear values and friction coefficients enhance the mechanical properties of the compound, mitigating adverse effects and promoting its suitability for various applications, particularly medical ones. This improvement is attributed to SBF presence during testing, reducing friction and enhancing wear resistance with increasing body fluid content [19].

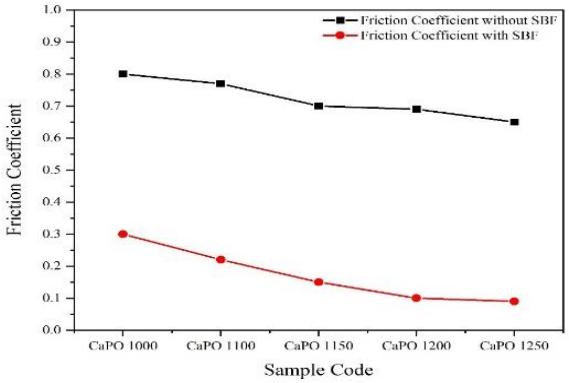

Fig. (4) Friction curves of CaPO composite samples in presence and absence of SBF

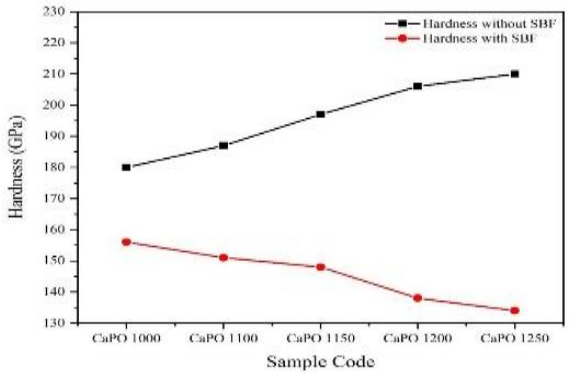

Fig. (5) Hardness curves of CaPO composite samples in presence and absence of SBF

Hardness and compressibility are crucial physical properties, reflecting a material's resistance to deformation and its ability to be compressed under pressure, respectively. These properties depend on the compound's chemical bonds and density. Table (3) illustrates the hardness and compressibility values for all compound samples, both before and after SBF addition. Figure (5) displays the hardness curve of CaPO samples with and without SBF. Hardness increases with annealing temperature, reaching a peak of 210 GPa for CaPO 1250 before decreasing to 134 GPa after SBF addition. Similarly, figure (6) demonstrates that compressibility follows a similar trend, with the lowest value of 173 Pa-1 observed for CaPO 1250 after SBF addition. Lower hardness facilitates material manipulation but may increase susceptibility to wear, while lower compressibility indicates greater stiffness and resistance to deformation, making it suitable for stability-critical applications [20,21].

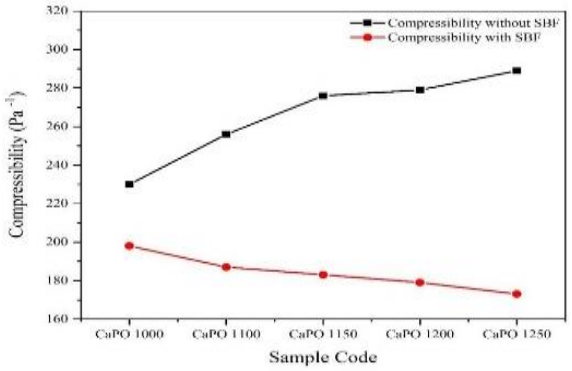

Fig. (6) Compressibility curves of CaPO composite samples in presence and absence of SBF

4. Conclusions

From the results, we can conclude that increasing sintering temperature leads to a notable enhancement in density, hardness, and compressive strength, accompanied by a reduction in wear rate and friction coefficient. The use of simulated body suit (SBF) results in decreased wear resistance and friction coefficient, along with a relative increase in density and compressive strength values. Samples calcined at 600-900°C exhibit consistent temperature absorption until the inflection point at 600°C, indicating uniform behavior across all calcination degrees.

References

[1] W.F. De Jong, "La substance minerale dans les os", *Rec. Trav. Chim. Pays-Bas*, 45(6) (1926) 445-448.

[2] M.P.d.M.A. Ferraz, "Bioactive ceramic coatings: Studies physiological conditions", PhD thesis, Universidade do Porto (Portugal, 2002).

[3] M. Vallet-Regí, "Biomimetics", Ch. 2, in **"Bio-Ceramics with Clinical Applications"**, Wiley (2014), pp. 17-22.

[4] E. Nery et al., "Bioceramic implants in surgically produced infrabony defects", *J. Periodontol.*, 46(6) (1975) 328-347.

[5] H.W. Denissen and K. de Groot, "Immediate dental root implants from synthetic dense calcium hydroxylapatite", *J. Prosthet. Dent.*, 42(5) (1979) 551-556.

[6] T. Crouzier, "Films multicouches à base de polysaccharides: étude de la composition interne et délivrance du facteur de croissance BMP-2", PhD thesis, Montpellier 2 (France, 2010).

[7] H. Ohgushi et al., "Porous ceramics for intra-articular depression fracture", Biomaterials and bioengineering handbook, Marcel Dekker (NY, 2000), 397-405.

[8] D.F. Williams, "The Language of Biomaterials-Based Technologies", *Regen. Eng. Transl. Med.*, 5 (2019) 53-60.

[9] R.W. Rice, "Introduction to Grain and Particle Effects on Ceramic and Ceramic Composite Properties", Ch. 1, in "Mechanical Properties of Ceramics and Composites: Grain and Particle Effects", CRC Press (2000) pp. 1-42.

[10] H.H. Al-Kayiem, S.C. Lin and A. Lukmon, "Review on nanomaterials for thermal energy storage technologies", *Nanosci. Nanotech. Asia*, 3(1) (2013) 60-71.

[11] B. Chen et al., "Enhancement of critical-sized bone defect regeneration by magnesium oxide-reinforced 3D scaffold with improved osteogenic and angiogenic properties", *J. Mater. Sci. Technol.*, 135 (2023) 186-198.

[12] R. Drevet and H. Benhayoune, "Electrodeposition of calcium phosphate coatings on metallic substrates for bone implant applications: a review", *Coatings*, 12(4) (2022) 539.

[13] S. Comini et al., "Novel silver-functionalized poly (ε-caprolactone)/biphasic calcium phosphate scaffolds designed to counteract post-surgical infections in orthopedic applications", *Int. J. Mol. Sci.*, 22(18) (2021) 10176.

[14] F. Ramos and J. Pedro, "Effect of Calcium Oxide Microstructure on the Diffusion of Isotopes", *CERN Aveiro*, (2012) 101.

[15] R.H.P. Devamani, N. Deepa, and J. Gayathri, "Morphology and thermal studies of calcium carbonate nanoparticles", *Int. J. Innov. Sci. Eng. Technol.*, 3 (2016) 87.

[16] D.-x. Li et al., "Study on the thermal decomposition kinetics of nano-sized calcium carbonate", *J. Zhejiang Univ. Sci.*, 4(3) (2003) 363-368.

[17] K. Habersberger and V. Balek, "Investigation of the thermal decomposition of calcium carbonate by simultaneous emanation thermal analysis, differential thermal analysis and evolved gas detection", *Thermochimica Acta.*, 4(6) (1972) 457-460.

[18] A. Pinna et al., "Effects of the Parent Alloy Microstructure on the Thermal Stability of Nanoporous Au", *materials*, 15(19) (2022) 6621.

[19] J. Dai et al., "Friction and wear behaviors of biodegradable Mg-6Gd-0.5 Zn-0.4 Zr alloy under simulated body fluid condition", *J. Magnesium Alloys*, 5(4) (2017) 448-453.

[20] W. Yang, R.G. Parr and L. Uytterhoeven, "New relation between hardness and compressibility of minerals", *Phys. Chem. Miner.*, 15(2) (1987) 191-195.

[21] V.A. Mukhanov, O.O. Kurakevych and V.L. Solozhenko, "The interrelation between hardness and compressibility of substances and their structure and thermodynamic properties", *J. Superhard Mater.*, 30 (2008) 368-378.

Table (2) Wear and friction results of CaPO composite samples in the presence and absence of SBF

Sample Code	Wear without SBF (mm^3/Nm)	Wear with SBF (mm^3/Nm)	Fraction without SBF	Fraction with SBF
CaPO 1000	0.0000045	0.00000065	0.8	0.3
CaPO 1100	0.0000023	0.00000045	0.77	0.22
CaPO 1150	0.0000013	0.00000034	0.7	0.15
CaPO 1200	0.0000011	0.00000022	0.69	0.1
CaPO 1250	0.0000003	0.00000015	0.65	0.09

Table (3) Hardness and Compressibility results of Ca/PO composite samples in the presence and absence of SBF

Sample Code	Hardness without SBF (GPa)	Hardness with SBF (GPa)	Compressibility without SBF (Pa^{-1})	Compressibility with SBF (Pa^{-1})
CaPO 1000	180	156	230	198
CaPO 1100	187	151	256	187
CaPO 1150	197	148	276	183
CaPO 1200	206	138	279	179
CaPO 1250	210	134	289	173

Proceedings of 5th International Specialized Conference of Education College on Physics and Applied Sciences (5thICECAS24), 22-23 April 2024

Ahmed K. Al-Kadumi
M. Al-Baghdadi

Department of Physics, College of Education for Pure Science, University of Karbala, Karbala, IRAQ

Effect of Temperature and Time on Etching to Form Porous Silicon

In this paper, a mathematical model is proposed to study the charge motion and the parameters affecting the reaction between any electrolyte acid and bulk silicon to produce porous silicon. The temperature is one of the parameters that affect the charge motion then the wave function can consist from the time and position of the charges. This position can be a function of temperature, then it can be easily determined the energy of the electron by using Schrödinger equation, and then some parameters which affect the current density of the reaction of bulk silicon with HF acid by using different etching times (10, 20, 30, 40, 50, and 60min), and different ratios of HF acid concentration (40%, 50%, 60%, 70%, 80%). These results were obtained by using MATLAB software.

Keywords: Porous silicon; Nanocrystalline silicon; Etching; Charge transfer
Received: 19 January 2024; Revised: 4 March 2024; Accepted: 4 April 2024

1. Introduction

Nanoscience is very important in many applications because the nano-sized matter shows new properties, which make it useful for a wide range of applications in different fields [1]. The porous silicon represents one of these fields, which make use of some properties of the nano-sized silicon those not found in bulk silicon. Experimentally, porous silicon can be produced by two methods; wet etching and dry etching. Wet etching can be divided into photoelectrochemical (PEC) etching, electrochemical etching, and stain etching [2]. All of these methods are based on electron transition between bulk silicon and adjustable acid which make appropriate etch in some preparation conditions in light of the application. Quantum mechanics can be used as a mathematical method to study the microscopic world. This method can be used to determine all properties of any microscopic system using a mathematical function called wavefunction, which contains all characteristics of the system [3]. This is an easy way to imagine the system having certain physical properties by mathematical steps giving theoretical results with assist of the operators. The etching process of bulk silicon to produce porous silicon is an example for such microscopic systems [4].

In this work, a theoretical treatment is proposed to describe the production of porous silicon from the reaction between hydrofluoric (HF) acid and bulk silicon. In this reaction, the electron transition between HF acid and bulk silicon can be represented by quantum mechanics using position- and time-dependent wavefunction to find the energy by the total energy operator or Schrödinger equation. Accordingly, the current density used to produce porous silico from the reaction can be determined and some effective parameters on this process can be studied. This work may assist to make a simulation for the mechanism of silicon etching to produce porous silicon.

2. Theoretical Treatment

According to the de Broglie principle, any particle moving with mass (m) and velocity (v) has a wavefunction (λ) given by [5]:

$$\lambda = \frac{h}{mv} \quad (1)$$

where h is the Planck's constant

The electron motion in the reaction between bulk silicon and HF acid to form porous silicon can be represented by the following wavefunction:

$$\Psi(x,t) = 3e^{(5x+7t)} \quad (2)$$

where t is the etching time, and x is the position of the electron, which can be represented by:

$$x = 10 - T \quad (3)$$

where T is the temperature

By using the total energy operator [6]:

$$\hat{E} = i\hbar\frac{\partial}{\partial t} \quad (4)$$

where $\hat{E}$ is the energy operator of the electron, $\hbar$ is the reduced Planck's constant, i is $\sqrt{-1}$

From that, the eigenvalue of the energy become:

$$E = 7i\hbar\left(3e^{(5x+7t)}\right) \quad (5)$$

From the momentum operator:

$$\hat{p} = -i\hbar\frac{\partial}{\partial x} \quad (6)$$

By that, the momentum of the electron becomes:

$$p = -5i\hbar\left(3e^{(5x+7t)}\right) \quad (7)$$

When the reaction between HF acid and bulk silicon begins, there are electrons most be transition between silicon and acid to make a new bond between them, and from that, the current density for porous silicon can be determined as [2]

$$J_{pSi} = Bc^{\frac{3}{2}}\exp\left(-\frac{E_{pSi}}{k_B T}\right) \quad (8)$$

Here, J_{pSi} is the current density of porous silicon, B is a constant equal to 3300 mA/wt.%, c is the

concentration in electrolyte, E_{pSi} is the activation energy equal, k_B is Boltzmann constant, and T is the temperature

By using equations (2), (4), and (5), one can find the current density as:

$$J_{psi} = Bc^{\frac{3}{2}} \exp\left(-\frac{7i\hbar}{k_B T}\right) \quad (9)$$

3. Results and Discussion

In recent years, the research works were mostly focusing on the applications of nanostructures and nanomaterials. This may be attributed to the important properties of these materials and their direct effects on these applications [7-9]. The current density of the reaction between the bulk silicon and HF acid depends on the concentration of the acid because increasing the acid concentration provides more charge carriers to the reaction and this causes to increase the current density of reaction, as can be shown in Fig. (1), which shows the highest value of the density when the acid ratio is 80%.

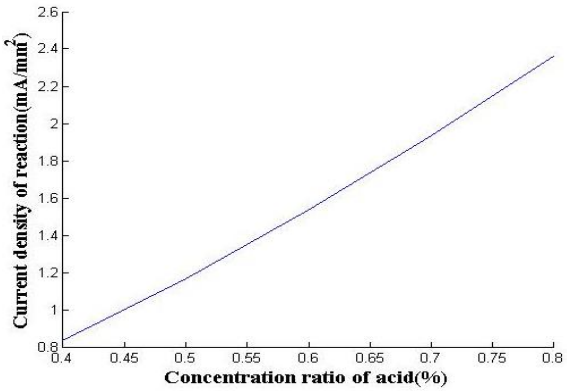

Fig. (1) The relation between the current density of reaction and the percentage concentration of acid

The current density as a function of etching time with different acid concentrations can be shown in Fig. (2). From this figure, one can show the stability of the current density until the point of 20 minute etching time, after that the current begin decreases to reach zero value at etching time of 30 minute. This is attributed to the depletion of the charge carriers along reaction time which breaks the original bonds and make new bonds between fluoride ion and the silicon, (which is called dangling bonds) before start to make a dip and then porous silicon [10,11].

The increase in the concentration rate makes the increase in the current density with same behavior at temperature of 30°C. Figure (2) confirms that etching time did not depend on the acid concentration then all values make the reaction vanished after 30 minutes. Figure (3) shows the relation between the current density of the reaction and the temperature for different values of acid concentration. In general, one can see the steady value of the current density with increasing temperature, then there is no change for the current density of reaction value for the same acid concentration value because the temperature does not produce new charge carriers in this case, then the temperature has no effect on the current and makes the same behavior for all acid ratios.

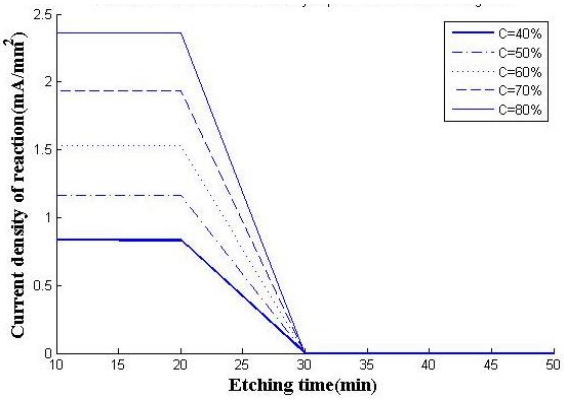

Fig. (2) The relation between the current density of reaction and etching time with different concentration ratios

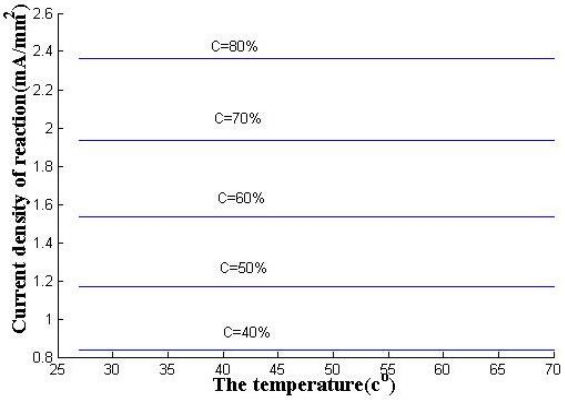

Fig. (3) The relation between the current density of the reaction and the temperature with different concentration ratios

Figure (4) represents the current density of reaction as a function of etching time for different temperatures. By this figure, the current density and reaction continue for limited etching time but this etching time becomes longer with increased temperature.

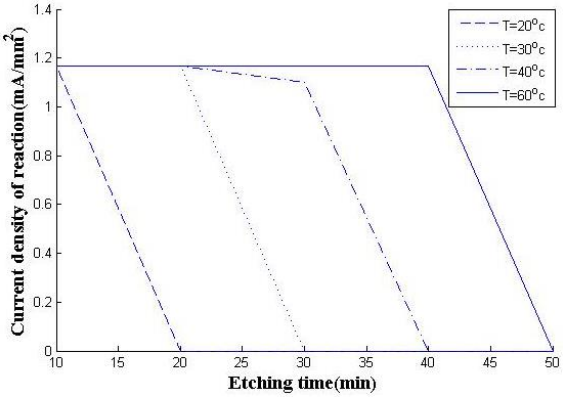

Fig. (4) The relation between the current density of reaction and the etching time with different temperatures

Then the temperature is the parameter controlling the stability between the current density and the end of reaction, as the optimization parameter for the etching process. This result can be compared with many works those experimentally carried out the reaction of etching process [12-14].

4. Conclusion

From this work, a simulation of the silicon etching process can be presented by predicting the wavefunction for electron reaction between hydrofluoric acid and the bulk silicon by using quantum systems and the Schrödinger equation to find the energy of the system. From that, the correlation between the current density of reaction, which represents the electron motion and time etching, acid concentration rate and temperature can be found. The wavefunction describing the quantum system can be imposed to determine the physical observable quantity by some quantum operators to find the parameters related to produce porous silicon. By that, the current density made from electrons can be deduced and the effects of acid concentration, etching time and temperature on this reaction can be introduced to theoretically describe the mechanism of etching silicon.

References

[1] A.H. Ali et al., "Effect of nanomaterial addition on the thermophysical properties of Iraqi paraffin wax", *Case Stud. Therm. Eng.*, 15 (2019) 100537.

[2] L. Canham, **"Handbook of Porous Silicon"**, Springer International Publishing (Berlin, 2014).

[3] A.C. Phillips, **"Introduction to Quantum Mechanics"**, John Wiley & Sons (2013).

[4] A.A. Khadom et al., "Theoretical evaluation of Citrus Aurantium leaf extract as green inhibitor for chemical and biological corrosion of mild steel in acidic solution: Statistical, molecular dynamics, docking, and quantum mechanic's study", *J. Mol. Liquids*, 343 (2021) 116978.

[5] J. Güémez, M. Fiolhais and L.A. Fernández, "The principle of relativity and the de Broglie relation", *Am. J. Phys.*, 84(6) (2016) 443-447.

[6] A. Hamoudi, "Statistical Fluctuations of Energy Spectrum, Electromagnetic Transitions and Electromagnetic Moments in ^{136}Xe Nucleus Using the Framework of Nuclear Shell Model", *Iraqi J. Phys.*, 8(11) (2010) 67-76.

[7] E.T. Salim, M.J. AbdulRazzaq and M.H. Wahid, "Effect of Different Parameters on Raman Scattering Released from Nb_2O_5 Nanostructures Prepared via PLD Technique", *Eng. Technol. J.*, 40(10) (2022) 1-9.

[8] S. Chupradit et al., "Morphological control: Properties and applications of metal nanostructures", *Adv. Mater. Sci. Eng.*, 2022 (2022).

[9] S.F.A. Albaayit, R. Abdullah and M.H.M. Noor, "Zerumbone-Loaded Nanostructured Lipid Carrier Gel Enhances Wound Healing in Diabetic Rats", *BioMed Res. Int.*, 2022 (2022).

[10] Q. Lei et al., "Sol–gel- based advanced porous silica materials for biomedical applications", *Adv. Funct. Mater.*, 30(1) (2020) 1909539.

[11] N.M. Al-Rahime, H.I. Salman and A.K. Al-Kadumi, "The effect of the acid concentration on morphology of nanocrystalline silicon", *Mater. Today: Proc.*, 2021.

[12] N.H. Harb and F.A.-H. Mutlak, "Effect of etching current density on spectroscopic, structural and electrical properties of porous silicon photodetector", *Optik*, 249 (2022) 168298.

[13] A.S. Alber and F.A.-H. Mutlak, "The role of various etching time in Si nanostructures for ultra-high sensitivity photodetector", *Optik*, 265 (2022) 169427.

[14] G. Zeb and X.T. Le, "Effect of surfactant and etching time on p-type porous silicon formation through potentiostatic anodization", *Adv. Nat. Sci.: Nanosci. Nanotech.*, 13(3) (2022) 035015.

Proceedings of 5th International Specialized Conference of Education College on Physics and Applied Sciences (5thICECAS24), 22-23 April 2024

Effect of Temperature Substrate on Structural, Optical, and Electrical Properties of Zinc Sulfide Thin Films Prepared by Thermal Chemical Spray

Sabah S. Hamdi [1]
Huda S. Ali [2]

[1] *Department of Physics, College of Education for Pure Sciences, University of Tikrit, Tikrit, IRAQ*
[2] *Department of Renewable Energy, College of Energy and Environmental Sciences, Al-Karkh University of Science, Baghdad, IRAQ*

In this research, thin films of zinc sulfide ZnS were prepared at a glass substrate with different temperatures (100-150 °C). X-ray diffraction results showed that the ZnS thin films have a polycrystalline nature of the cubic type and the preferred direction of growth (111). Optical properties proved the direct optical energy gap for ZnS-100C thin film, which equals 3.32eV. At the same time, at (150 C) it was 3.00eV. The thickness of the ZnS-100C film was equal to (100 nm) in comparison; at 150 C, it was equal to 120 nm and was measured by a simulation program (Hebal Optic), which was used on the computer to determine approximate values. The continuous conductivity measurements showed that the electrical resistance of all thin films changes inversely with increasing temperature and that the prepared thin films have two activation energies.

Keywords: Zinc sulfide; Theoria; Substrate temperature; Activation energy
Received: 19 January 2024; Revised: 4 March; Accepted: 4 April 2024

1. Introduction

Zinc sulfide (ZnS) is a mineral sulfide compound, defined by the term "sphalerite", a Greek word that hints at the lack of common similarity with other minerals. It is transparent or semi-transparent and yellow [1] and does not dissolve as long as its sublimation is low, dissolves in acids, does not dissolve in water, and is also of low toxicity. Zinc sulfide (ZnS) is excellent illumination due to its wide energy gap, which can be obtained in the almost visible range with suitable grafts [2]. Zinc sulfide (ZnS) is characterized by two compositions: one is the cubic phase (zincblende) and is the most stable composition at room temperature, which can move to the hexagonal phase (wurtzite) after being heated to a temperature of 1293K at atmospheric pressure, the other is the hexagonal phase (wurtzite) of the zinc sulfide compound (ZnS), which is the most desirable phase due to its preferred optical properties over the cubic phase and sulfide can be used. ZnS is used in lasers, blue light emitting diode industry, and anti-reflective and anti-corrosion coatings. It can also be used in the manufacture of television screens and x-ray screens [3].

2. Experimental Part

For the preparation of solutions used in the preparation of ZnS films, aqueous zinc nitrate ($Zn(NO_3)_2.6H_2O$), which is a powder material of rapid water soluble white masses, molecular weight of 297.384 g/mol and purity of 99.9%, and Theoria $CS.(NH_2)_2$, a substance in the form of a white powder rapidly soluble in water with molecular weight of 76.614 g/mol and purity of 98%. The first solution was prepared at room temperature and concentration of 0.05M by dissolving 1.486 g of $Zn(NO_3)_2.6H_2O$ in 100 ml of distilled water. The second solution was prepared at a concentration of 0.1M. The second solution was prepared at room temperature and a concentration of 0.01M by dissolving 0.076g of thiourea in 100 ml of distilled water as well. The solutions were mixed, and a magnetic stirrer was used to ensure the complete dissolution of the solutions. The solutions are left for 10min on the magnetic stirrer until homogeneous solutions are obtained and free of any plankton. Then, an equal volumetric ratio (1:1) is taken from both solutions and mixed. The solution is placed on the magnetic mixer for another 10 min to ensure complete dissolution and obtain a homogeneous solution. After the solution is deposited on a glass substrate and by chemical decomposition, we get thin ZnS films.

The thermal chemical spraying method has been used because it is suitable for the preparation of oxides and sulfate materials, economical due to the low cost of the manufactured devices used in the preparation of these membranes, and thin film can be prepared from the combination of two or more materials with different melting points, the thin films are prepared under normal conditions. The ZnS solution is deposited on a glass substrate with a temperature of 100-150°C. The distance between the spray device (nozzle) and the silicon substrate is

28cm because more than that causes the material to evaporate before it reaches the substrate.

Thin films were deposited on a glass substrate with a thickness of 0.1 cm. The glass substrate was cleaned well before spraying to remove impurities, as the presence of impurities affects the properties of the prepared thin films. The substrate was cleaned after cutting them into small squares of size 2.5x2.5cm^2, where the bases were washed first with water to get rid of plankton. Then, the substrate was placed in a glass flask containing acetone with a purity of 99.99% for a period of 10 min. Then, the substrate was placed in another peach containing ethanol with 99% purity for a period of 10 min. Finally, the substrate was placed in a flask containing only distilled water and left for 15 min to remove acetone and ethanol residues. Finally, the glass substrate was dried with a cloth to clean the glass lenses. ZnS thin film was deposited on the glass substrate at a substrate temperature of 100-150°C.

3. Results and Discussion

The results of XRD for ZnS thin film at a different substrate temperature 100-150°C annealed at 300°C for half an hour, the cubic system in the preferred growth direction (111) and figure (1) shows the XRD patterns of the thin films. Peak positions at 2θ=28.2° and 48.05° corresponding to (111) and (220) planes, respectively [4,5].

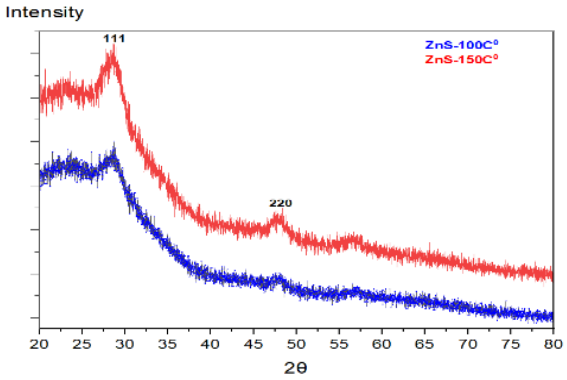

Fig. (1) XRD for ZnS thin films at different substrates temperatures

Table (1) Structural parameters of ZnS thin films at different substrate temperatures

Sample	2θ (deg)	(hkl)	d_{hkl} (Å)	FWHM (rad)	D (nm)
ZnS-100°C	28.20	(111)	3.1619	0.8656	9.89
	48.05	(220)	1.8330	0.6336	14.34
ZnS-150°C	28.60	(111)	3.1026	0.3876	22.10
	48.30	(220)	1.8980	0.4224	21.54

When comparing the locations of the peaks with the standard ICDD card (00-080-0020) for zinc sulfide, table (1) shows the structural parameters for standard peaks. We also note that the intensity of the ZnS peaks increases, as well as the decrease in the FWHM with increasing substrate's temperature. This confirms that the crystallization rate has increased because the increase in the height of the peaks is evidence of increased crystallization and reduced crystalline defects [6]. The average granular size was calculated using Eq. (1) [7], and it was found that the measured grain size values lie within the range 9.89-22.10 nm

$$D_{ave} = 0.9\lambda/\beta cos\theta \quad (1)$$

where λ=1.5406 Å is the x-ray wavelength (Kα -line), θ is the Bragg's diffraction angle, β is the full-width at half-maximum (FWHM) (in radians)

Throughout the study of surface morphology using field-emission scanning electron microscopy (FE-SEM) of the prepared thin films, as was shown in figures (2) and (3) that the thin film structure ZnS-100°C. In the form of nano-mounted sheets with increasing temperature (ZnS-150°C), these forms have become more aligned and arranged on top of each other and more coherent among them, and this is because the high temperature led to an increase in granular growth and the collection of granules in this way, and this is consistent [4-6]. A simulation program (Hebal Optic) was used to determine the thickness of the thin film. This program can determine approximate thickness values based on transmittance values and the thickness of ZnS-100°C equals 100nm and of ZnS-150°C equals 120nm.

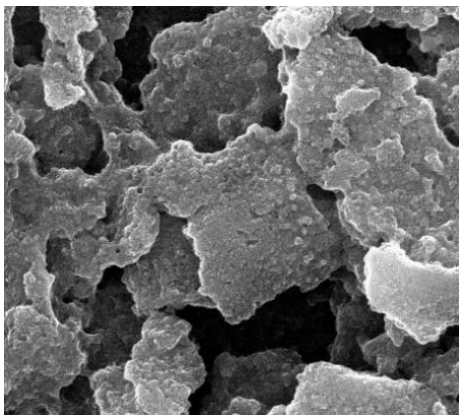

Fig. (2) FE-SEM image for ZnS-100°C thin film

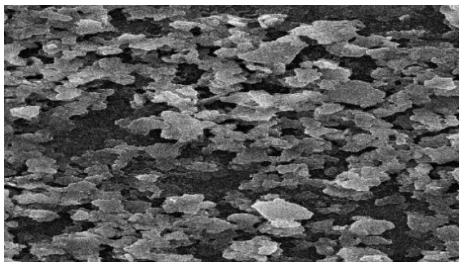

Fig. (3) FE-SEM image for ZnS-150°C thin film

The absorption coefficient of the prepared films was calculated by Eq. (2), and figure (4) shows the absorption spectrum as a function of wavelength. The results showed that the absorbance increases with increasing substrate's temperature. Figure (5) shows the absorption coefficient change as a function of the incident photon energy. The results showed that the

absorption coefficient increases with photon energy, as the most significant values of the absorption coefficient are at high photon energies (4-4.3eV), and this indicates the occurrence of the absorption process in this range (which includes the optical absorption edge). The probability of electronic transitions between the valence and conduction bands is consistent with the results of studies [8-10], and the energy gap value was calculated to estimate the difference between the valence band and the conduction band, which can help determine the electrical, thermal and electronic properties of materials. The Tauc's formula shown in Eq. (3) is used to determine the direct energy gap [11].

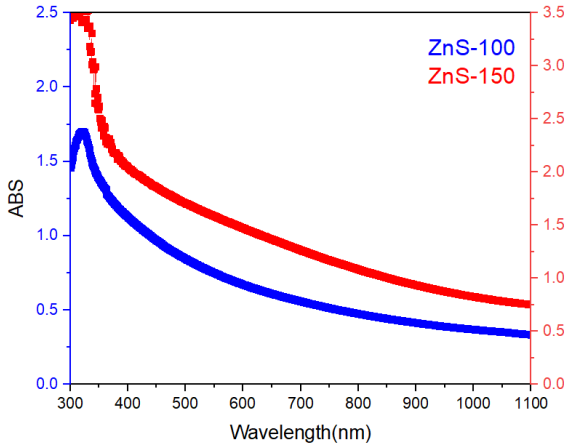

Fig. (4) Absorption spectra of ZnS-100°C and ZnS-150°C samples

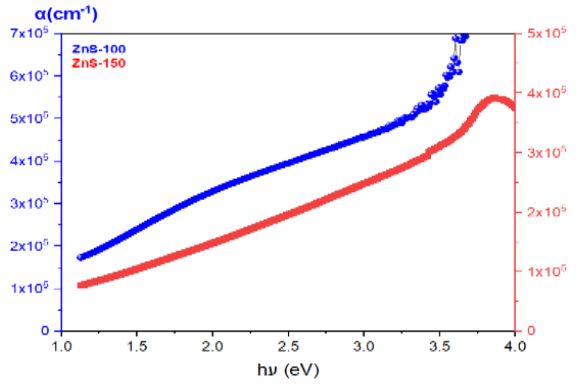

Fig. (5) Absorption coefficient of ZnS-100°C and ZnS-150°C samples as a function of photon energy

Since the transitions are of the direct type allowed, i.e., the value of the constant r=1/2, plotting the relationship between $(\alpha hv)^2$ and the energy of the incident photon (hv), and by extending the straight part of the curve to determine the point of intersection with the x-axis of the photon energy where $(\alpha hv)^2=0$, which represents the value of the optical energy gap and as shown in Fig. (6). It was found that the value of the optical energy gap of the ZnS-100°C thin film is 3.23eV and for the ZnS-150°C thin film is 3.00 eV, and this is approximately consistent with the results of [12,13]

$$\alpha = 2.303\frac{A}{t} \quad (2)$$

where A is the absorbance, t is the film thickness

$$\alpha hv = \beta(hv - E_g)^r \quad (3)$$

where β is a constant, α is the absorption coefficient, hv is the energy of an incident photon, E_g is the optical bandgap, and r=1/2 is for allowed direct transition

The dc electrical conductivity (σ_{dc}) of the prepared thin films was calculated using Eq. (4) [14]. By studying the change in electrical resistivity (ρ) as a function of temperature (T) within the thermal range 313-453K. Adopting Eq. (5) and as shown in Fig. (7) [15], we notice from that the electrical resistivity of all prepared thin films changes inversely with increasing temperature per sample, and this is one of the characteristics of semiconductors, as they are characterized by having a resistivity with a negative thermal coefficient unlike the characteristics of conductors, that is, the continuous electrical conductivity increases with increasing temperature and for all thin films.

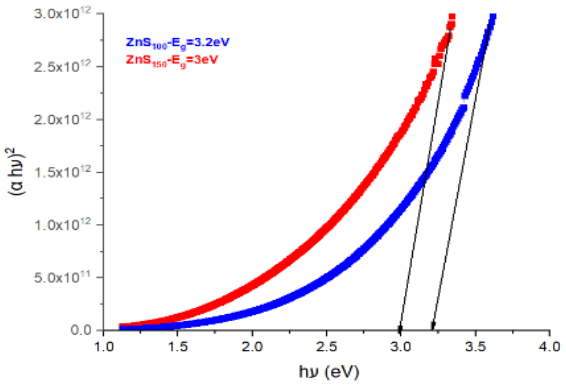

Fig. (6) Tauc's plots for ZnS-100°C and ZnS-150°C samples

Table (2) The activation energy and optical energy gap of the prepared samples

Sample	E_{a1} (eV) (303-343K)	E_{a2} (eV) (343-383)	E_g (eV)
ZnS-100°C	3.32	1.748	0.869
ZnS-150°C	3.00	1.323	0.811

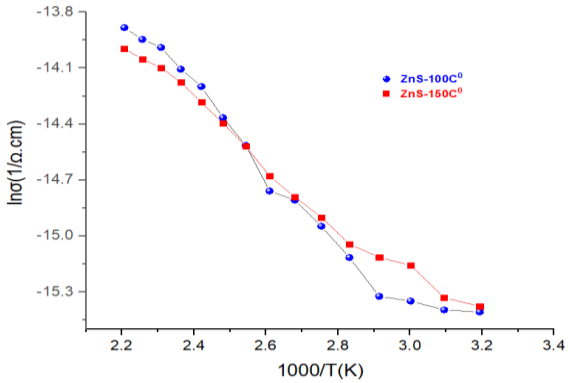

Fig. (7) Activation energy of ZnS-100°C and ZnS-150°C samples

Figure (7) shows the linear relationship between lnσ and 1000/T, which is used to calculate the activation energy (E_a). The change in the conduction mechanism is caused by the presence of two connected regions. For ZnS-100°C and ZnS -150°C, the first zone is at a low temperature (313-343K) and the second zone is at a higher temperature (343-453K), showing the two activation energy increases with increasing substrate's temperature and activation energy

$$\sigma = J/E = e(n\mu_e + p\mu_h) \quad (4)$$

where J is the electric current density, E is the applied electric field strength, e is the electron charge, μ_e is the electron mobility, μ_h is the hole mobility, n and p are electron and hole concentrations, respectively

$$\rho = R\frac{A}{L} \; where \; \{A = b.t\} \quad (5)$$

Where ρ is the resistivity, R is the electrical resistance of the thin film measured in Ω, L is the distance between the two poles of aluminum (cm), A is the cross-sectional area of the electron motion through the thin film, b is the electrode width (cm), and t is the film thickness

5. Conclusion

In this paper, ZnS thin films were prepared by thermal chemical spray and the effect of different substrate's temperatures on the properties of ZnS thin films was studied. All ZnS films show cubic structures with preferred (111) orientation. As the substrate's temperature is increased, the crystallinity of the films became better and particle sizes became larger, ranging from 9.89 to 22.10nm. The film thickness increased with increasing substrate's temperature. The optical band gap decreased from 3.23 to 3.00eV with increasing substrate's temperature, making this material suitable for solar cell devices. The electrical resistivity of all prepared thin films changes inversely with increasing temperature and the dc electrical conductivity increases due to the increase in crystallinity, resulting from reduced defects during the thermal process. The activation energies increase with increasing substrate's temperature.

References

[1] N. Imam and M.B. Mohamed, "Optical properties of diluted magnetic semiconductor Cu: ZnS quantum dots", *Superlat. Microstruct.*, 73 (2014) 203-213.

[2] W.K. Bae et al., "Highly efficient green-light-emitting diodes based on CdSe@ ZnS quantum dots with a chemical-composition gradient", *Adv. Mater.*, 21(17) (2009) 1690-1694.

[3] S.M. Sze, **"Semiconductors Devises Physics and Technology"**, Wiley (1990).

[4] W. Daranfed et al., "Substrate Temperature Influence on ZnS Thin Films Prepared by Ultrasonic Spray", *Thin Solid Films*, 518 (2009) 1082-1084.

[5] L.Q. Li et al., "Effect of [Zn]/[S] ratios on The Properties of Chemical Bath Deposited Zinc Sulfide Thin films", *Appl. Surf. Sci.*, 257 (2010) 122-126.

[6] A. Ates et al., "Annealing and Light Effect on Optical and Electrical Properties of ZnS Thin Films grown with the SILAR Method", *Mater. Sci. Semicond. Process.*, 10 (2007) 281-286.

[7] M. Caglar, S. ILcan and Y. Caglar, "Influence of Substrate Temperature on Structural and Electrical Properties of ZnO Films", *J. Sci*, 7(2) (2006) 153-159.

[8] R. Sahraei, G.M. Aval and A. Goudarzi, "Compositional, Structural and Optical Study of Nanocrystalline ZnS Thin Films Prepared by Anew Chemical Bath Deposition Route", *J. Alloys Comp*., 466 (2008) 488-492.

[9] N.P. Huse et al., "An Experimental and Theoretical Study on Soft Chemically Grown CuS Thin Films for Photosensor Application", *Mater. Sci. Semicond. Proc*ess., 67 (2017) 62-68.

[10] K. Priya et al., "A Comparative Study of Structural, Optical and Electrical Properties of ZnS Thin Films Obtained by Thermal Evaporation and SILAR Techniques", *Ceram. Int*., 43 (2014) 10487-10493.

[11] M. Lopez et al., "Growth of ZnS thin films obtained by chemical spray pyrolysis: The influence of precursors", *J. Cryst. Growth*, 285(1) (2005) 66-75.

[12] S. Mondal, S. Bhattacharyya and P. Mitra, "Effect of Al doping on the microstructure and optical band gap of ZnO thin film synthesized by successive ion layer adsorption and reaction", *Pramana*, 80(2) (2013) 315-326.

[13] C. Niedik et al., "Investigation on the electrical characterization of silicone rubber using D.C. conductivity measurement", in 2016 IEEE Int. Conf. Dielectr. (ICD), vol. 2, 1114-1118.

[14] D.S. McLachlan and G. Sauti, "The A.C. and DC conductivity of nanocomposites", *J. Nanomater.*, (2007).

[15] S.A. Garde, "LPG and NH3 Sensing Properties of SnO_2 Thick Film Resistors Prepared by Screen Printing Technique", *Sens. Transduc. J.*, 122(11) (2010) 128-142.

[16] P.-C. Tsai, I. Pai and H. Shieh, "Two-stage chemical bath deposition for well-covered and stoichiometric ZnS thin films", *Photovoltaic Specialists Conference* (PVSC), (2012).

Synthesis, Characterization and Spectroscopic Diagnostic of Copper Prepared by Plasma Technique

Abdulrhman H. Shaker
Kadhim A. Aadim

Department of Physics, College of Science, University of Baghdad, Baghdad, IRAQ

A cold Ar plasma system operated under atmospheric pressure was used in this study. Copper nanoparticles were prepared at a gas flow rate of 2.5 ltr/min and time of 4 min. For CuO nanoparticles prepared using AC plasma, it was found that the energy band gap was 3.93eV, crystallite size was 54.32nm, nanoparticle size was 35-65nm. For CuO nanoparticles prepared using DC plasma, the energy band gap was 3.11eV, crystallite size was 31.16nm, nanoparticle size was 30-65nm. The CuO nanoparticles prepared using DC were better than those prepared using AC plasma. At high voltage of 13kV and frequency of 50kHz, the plasma properties were measured for both AC and DC plasmas and the electron temperature and electron density were 1.20-2.29eV, (1.16-8.12)x10^{18} cm^{-3} and 1.19-2.18eV, (1.38-9.56)x10^{18} cm^{-3}, respectively. The results showed that AC plasma had a greater effect on the plasma properties than DC plasma.

Keywords: Non-thermal plasma; Copper plasma; Optical emission spectroscopy
Received: 15 August 2023; Revised: 07 September; Accepted: 14 September 2023

1. Introduction

The plasma jet is considered one of the most important modern sciences that has been studied and developed recently, as it is an advanced means of generating physical plasma. They are widely used in industrial and medical applications [1,2]. Plasma Jet produces non-thermal (cold) atmospheric pressure plasma, as the universe contains two types of plasma: very hot, which is the result of the total ionization of its particles, and cold, in which the particles are partially ionized [3-6]. Helium and argon are the most common gases used in the generation of non-thermal plasma jet as inert gases, but sometimes nitrogen and oxygen gases are used, but they are chemically active gases [7-10]. At a certain temperature limit, particles or atoms of matter form cold plasma. This transformation period makes the gas a gas with a highly interactive state composed of free radicals, electrons, and ions with electric fields [11-13]. Cold plasma jet is effective in industrial, medical, and biological use due to its ability to interact with cells, tissues, and various applications industrially in an easy way and without any significant effects [14].

The production of nanoparticles by plasma jet is widely investigated because of their very small atomic and molecular structures, which give them an important advantage from their bulk materials [15]. The potential of nanoparticles has a larger output because of the high area-to-volume ratio that gives different and variable properties [16].

In plasma physics, each type of plasma has its characteristics, which are considered as the fingerprint and through which its application destination, medically, industrially, or biologically, can be determined [17,18]. Certainly, the free electron temperature is the most important dynamic parameter and is the key to the plasma, in addition to the density. These two parameters enable us to predict the distribution of speeds and relative energy levels of molecules [19]. To measure plasma parameters, optical emission spectroscopy (OES) is adopted [20], as it represents a specific method that takes more than one sample of plasma without causing a defect in its structure, condition, or shape [21]. Its principal work depends on calculating the radiated optical emission from the produced plasma, representing its characteristics in an environment of chemical, ionic, and molecular radiation [22,23].

The temperature of the plasma in local thermal equilibrium can be calculated from the following equation [24]:

$$T_e = \frac{(E_2 - E_1)}{k \ln\frac{(I_1\lambda_1 A_2 g_2)}{(I_2\lambda_2 A_1 g_1)}} \quad \text{in eV} \qquad (1)$$

where A_1g_1 and A_1g_2 are the transition strength of the first and second wavelengths, respectively, and k is Boltzmann's constant, I_1 and I_2 are the peak intensities of the first and second wavelength of the plasma spectrum, and E_1 is the peak energy of the first wavelength and E_2 is the peak energy of the second wavelength in the resulting plasma spectrum. A is the transition probability that an atom in an upper-level state emits in an average direction in a de-excited state to a lower level and g is the static weight of the upper level [24]

From the Saha-Boltzmann equation, which depends on spectral lines, the plasma electron density can be calculated as [24]:

$$n_e = 6.04 \times 10^{21} \frac{I_1}{I_2^*}(T)^{\frac{3}{2}} e^{\frac{(E_1 - E_2 - X_Z)}{kT}} \qquad (2)$$

where

$$I_2^* = \frac{I_2\lambda_2}{g_2 A_2} \qquad (3)$$

X_z represents the amount of ionization energy

As for the plasma frequency parameter, which is considered basic and depends on the plasma density, it can be calculated from equation [25]:

$$f_P \approx 8.98\sqrt{n_e}, \quad \text{in Hz} \qquad (4)$$

Debye length, or Debye shielding that surrounds the plasma, is a parameter that gives the plasma the property of near-neutrality and makes it deal with external electric fields. It can be calculated through the equation [25]:

$$\lambda_D = \left(\frac{\varepsilon_o k T_e}{n_e e^2}\right)^{1/2} = 7430\left(\frac{kT}{n_e}\right)^{1/2} \qquad (5)$$

Debye number (N_D) can be calculated by the following [25]:

$$N_D = \frac{4\pi}{3} n_e \lambda_D^3 \qquad (6)$$

This work aims to characterize the nanoparticles produced by the copper oxide plasma jet system at a constant flow of 2 ltr/min of Ar gas and period of 4 min. The parameters of copper plasma are determined when using 0.5-2 ltr/min of Ar gas flow, and a high voltage of 13 kV using AC and DC power supplies, using a spectroscopic diagnostic method.

2. Experimental Work

Non-thermal atmospheric pressure plasma was produced using Ar gas at different flow rates using the plasma jet technique. This technology is formed as follows:

- Argon gas is used to create cold plasma
- The gas flow measuring device measures 0.5-2.5 ltr/min the amount of gas flowing through a tube connected at one end to a gas meter and connected at the other end to a hollow metal needle with a diameter of 3 mm, and connected to a wire tied to the negative pole of the power supply. Gas flows through the needle
- The metal plate used in this research (copper) with a surface area of 6x1cm^2, of which 4cm^2 was immersed in a beaker containing deionized water, was connected to the positive electrode of the power supply
- 13kV output from a high voltage AC or DC power supply to produce cold atmospheric pressure plasma, the frequency of AC power supply is 50 kHz

Figure (1) shows the method of setting up the cold plasma jetting system. The conductive end of the cathode electrode (the needle) is placed (1) cm from the surface of the deionized water in which the copper metal is immersed. The gas cylinder valve is opened, and the gas begins to flow at a rate of 2.5 ltr/min, and the duration of the gas flow toward the water surface is 4 minutes. An alternating current was used, and the second time direct current was used. After a short period, impurities began to increase inside the beaker, and the color of the water began to gradually change to brown, as shown in Fig. (2).

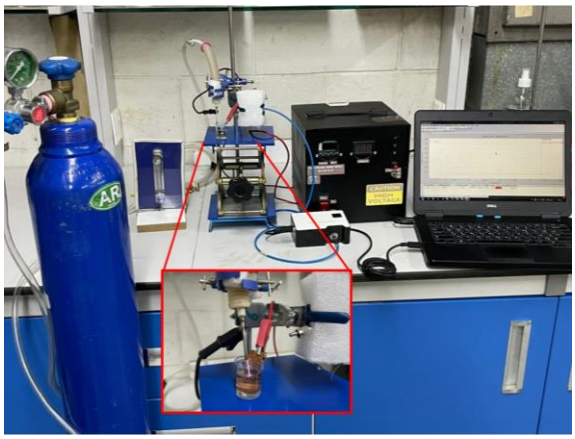

Fig. (1) Configuration of non-thermal plasma jets system, spectrometer, and electronic controller

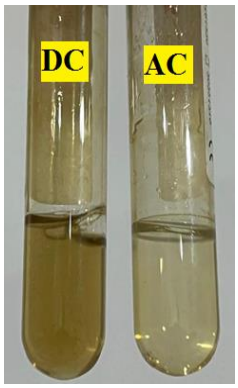

Fig. (2) Image of liquid samples of Cu nanoparticles manufactured by atmospheric plasma jet at flow of 2.5 ltr/min, high voltage of 13 kV with a duration of 4 min

The product's characteristics are highly affected by the arrangement of nanoparticles and their chemical composition, as well as the size of the solid in one, two, or three dimensions [26]. Therefore, three important variables are examined to characterize the metallic Cu nanoparticles: size, distribution, and shape. The produced nano-liquid was used in UV-visible light analysis; while the liquid was dripped onto glass slides and under a temperature of 100°C, we obtained a thin film to be analyzed by x-ray diffraction (XRD), field-emission scanning electron microscopy (FE-SEM), and energy-dispersive x-ray spectroscopy (EDX). Spectroscopic diagnosis was performed with a UV 3000 spectrophotometerin the range of 190-1100nm as the plasma was produced by changing the gas flow rate (0.5, 1, 1.5, 2, and 2.5 lt/min) at constant applied voltage (13kV) for both types (AC and DC) of power supply. The results of spectrophotometry were obtained and then compared with the US spectroscopic database (NIST) [26].

3. Results and Discussion

The absorption coefficient and optical energy gap were determined for the prepared copper nanoparticles. The absorption coefficient (α) can be determined from the highest absorption area near the fundamental absorption edge as [27]:

$$\alpha = 2.303 \frac{A}{t} \quad (7)$$

where A is the absorbance and t is the sample thickness

Figures (3) and (4) display the absorption spectra of the nanoparticles solutions prepared using AC and DC plasma jet [22].

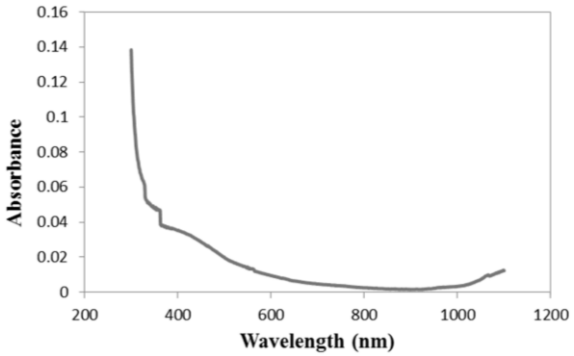

Fig. (3) Absorption spectrum of CuO NPs produced by the AC plasma jet

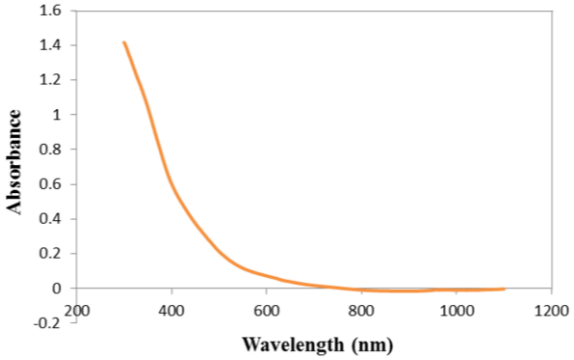

Fig. (4) Absorption spectrum of CuO NPs produced by the DC plasma jet

To identify the type of optical transition, the relation between $(\alpha h\nu)^{1/r}$ and the photon energy $(h\nu)$ for different values of (r) was examined [28]:

$$(\alpha h\nu) = B(h\nu - E_g)^r \quad (2)$$

It appeared that the energy gap was 3.39 eV, as shown in Fig. (5). The results show that the theoretical and experimental values of the energy gap were close to each other for the sample prepared usng AC source. When using DC source, it appeared that the energy gap was 3.11 eV, as shown in Fig. (6). It was also close to the theoretical value.

The CuO NPs thin films (obtained by deposition of the CuO NPs as thin film on glass slide) were subjected to XRD analysis using Phillips X-Pert PANalytical instrument. It was found that the XRD pattern, shown in Fig. (7), of CuO NPs produced using AC source, is matched to JCPDS card 71-4610 [29]. Two distinct diffraction peaks are found at 12.828° and 25.830°, which means that CuO NPs produced using AC power supply were crystalline. Scherrer's equation [30] was used to calculate the average crystallite size to be 54.32nm [31]. The XRD pattern, shown in Fig. 8, of CuO NPs produced using DC power supply was found to match JCPDS card 71-4610 [29]. As well, two distinct diffraction peaks are found at 12.835° and 25.809°. The CuO NPs produced using DC power supply were crystalline too and the average crystallite size was 31.16 nm [30,31].

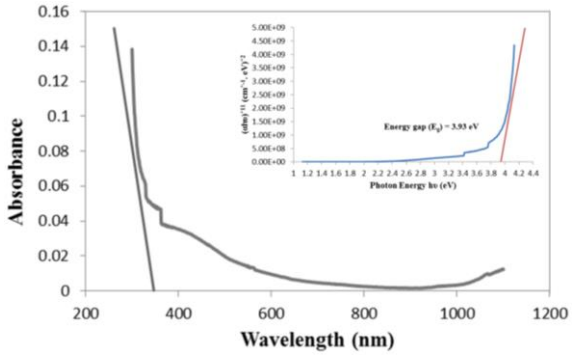

Fig. (5) Determination of E_g from the plot of $(\alpha h\upsilon)^2$ vs. $h\upsilon$ for CuO NPs prepared using AC cold plasma

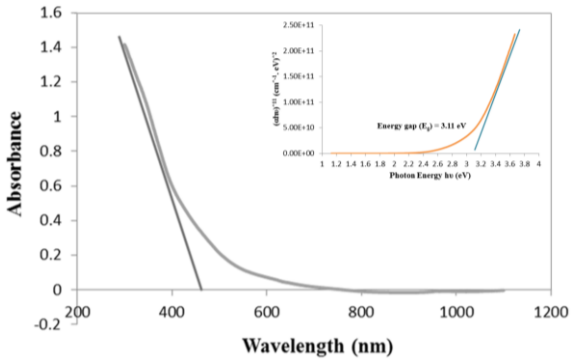

Fig. (6) Determination of E_g from the plot of $(\alpha h\upsilon)^2$ vs. $h\upsilon$ for CuO NPs prepared using DC cold plasma

Due to several factors (mainly, argon gas flowing through the plasma needle, water, immersed metal (Cu), free electrons on the surface of the metal, and oxygen) involved in the formation of the nanoparticles in the ionic water, the interactions increase and – as a result – the color of the liquid changes to copper color. The effect of time causes the nanoparticles to be extracted and formed with smaller sizes [32].

According to the results of FE-SEM carried out on thin film samples, when AC source was used, clusters were observed in the form of a mat of bubbles connected, as shown in Fig. (9). With higher magnification power, the shape of the prepared CuO NPs became clear so that each inclined spherical particle was connected, as in Fig. (10). The shape is almost close to the pictures of FE-SEM in reference [33]. It was observed that CuO NPs have diameters ranging between 35 and 65nm. For CuO NPs prepared using DC source, the non-thermal plasma jet worked on the synthesis of the CuO NPs in the form of interconnected ramifications. Figures (11) and (12) show spheres aggregated and connected to form a homogenized viscous gel of nanoparticles. The images were almost identical to what FE-SEM images showed in reference [34]. It was observed that the prepared CuO NPs have diameters ranging

between 30 and 65nm. The variation in the diameter of the particles and thus their sizes can be explained by the effect of the time parameter of the plasma on the surface of the liquid in which the metal piece of copper is immersed. The longest time was 4 min.

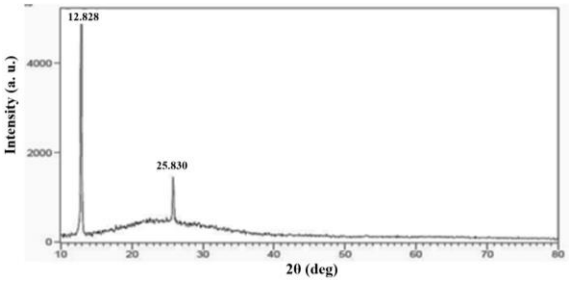

Fig. (7) XRD pattern of CuO NPs prepared after 4 min with applied voltage of 13 kV using AC cold plasma

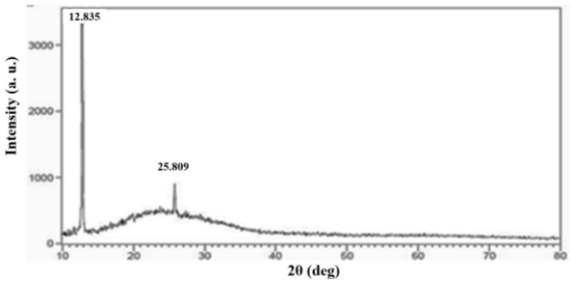

Fig. (8) XRD pattern of CuO NPs prepared after 4 min with applied voltage of 13 kV using DC cold plasma

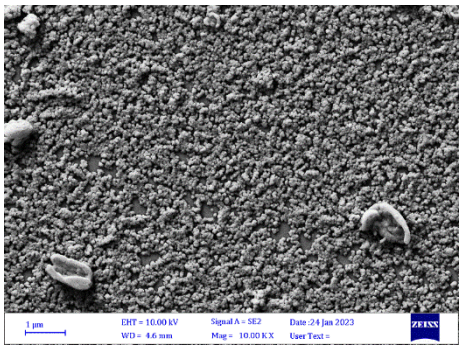

Fig. (9) FE-SEM image of CuO NPs prepared by AC cold plasma jet at 1µm scale

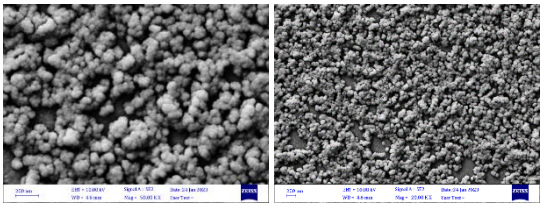

Fig. (10) FE-SEM image of CuO NPs prepared by AC cold plasma jet at 200nm scale

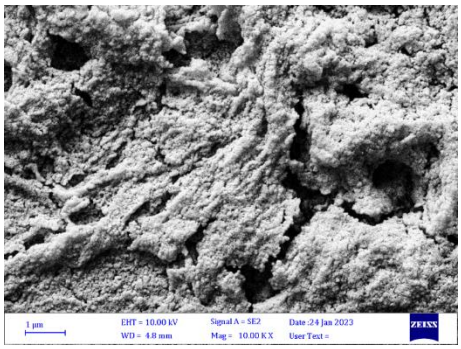

Fig. (11) FE-SEM image of CuO NPs prepared by DC cold plasma jet at 1µm scale

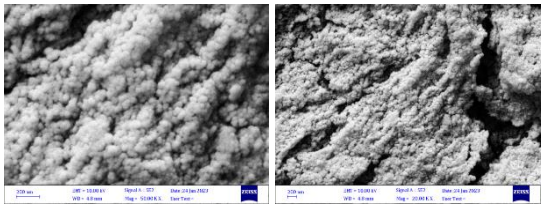

Fig. (10) FE-SEM image of CuO NPs prepared by DC cold plasma jet at 200nm scale

Figure (13) shows optical emission spectra (OES) for the Ar gas, N_2 gas, and Cu metal. Argon had an impact on the intensity of the emission line. Spectrum depicts the emergence of several peaks, including 6 for Ar gas, 3 for Cu metal, and multiple peaks for N_2 gas. These peaks are seen at 346.74nm for N_2, at 389.58, 427.21, and 666.57nm for Cu, and at 708.37, 762.35, 774.86, 821.77, 851.38, 919.92nm for Ar gas, as shown in Fig. (13). The atomic peak at 389.58nm and the ionic peak at 427.21nm of the spectrum were compared with those in NIST [35].

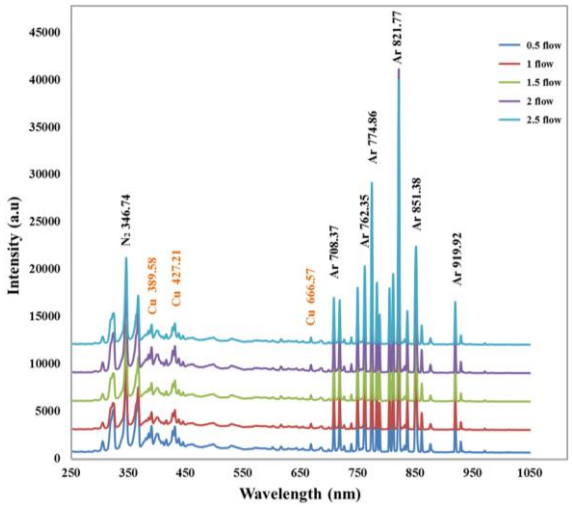

Fig. (13) Ar plasma spectrum using copper at 0.5-2.5 l/min flow rates using an AC power supply at high voltage of 13 kV

In Fig. (14), the resulting plasma was characterized using DC source. The spectrum shows several peaks, including 6 for Ar gas, 3 for the Cu metal, and numerous peaks for N_2 gas. These peaks are seen at 346.74nm for N_2 gas, at 367.26, 427.48,

678.74nm for Cu metal and at 708.37, 762.12, 774.86, 821.77, 851.38, 919.92nm for Ar gas. The ionic peak at 367.26nm and the atomic peak at 427.48nm for Cu were compared with those in NIST [35].

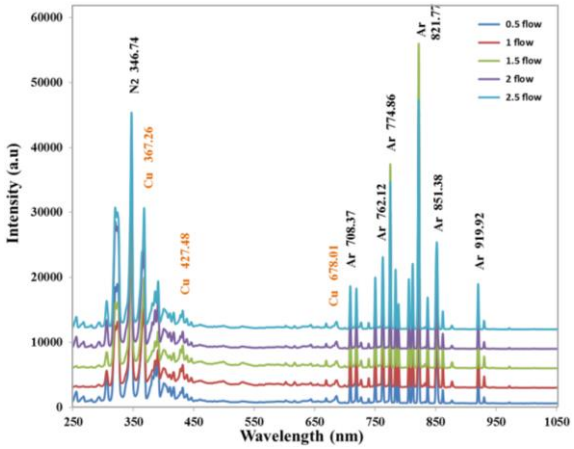

Fig. (14) Ar plasma spectrum using copper at 0.5-2.5 l/min flow rates using a DC power supply at high voltage of 13 kV

The properties of Cu NPs produced using AC power supply with high voltage of 13kV and frequency of 50kHz have been determined from their spectral lines shown in table (1). These properties include electron temperature (T_e), electron density (n_e), plasma frequency (f_p), Debye length (λ_D) and Debye number (N_D) for various flow rates (0.5-2.5 ltr/min) of Ar gas. Increasing flow rate leads to increase electron temperature and electron density to 1.20-2.29eV and $1.16x10^{18}$-$8.12x10^{18}$ cm^{-3}, respectively. The behavior of plasma frequency likewise increases as the flow rate is increased to $(1.153\text{-}8.095)x10^{13}$Hz, while the Debye length moves in the opposite direction to $(0.059\text{-}0.012)x10^{-5}$cm. Regarding N_D, it likewise exhibits the same behavior as the Debye length (14.15-5.31m), which decreased with increasing argon gas flow rate [36].

For Cu NPs produced using DC source, plasma parameters are shown in table (2), which shows how increasing flow rate leads to increase electron temperature and electron density to 1.19-2.18eV and $(1.38\text{-}9.56)x10^{18}cm^{-3}$, respectively. The plasma frequency increases with increasing gas flow rate to $(1.760\text{-}11.238)x10^{13}$Hz, while the Debye length decreased with increasing gas flow rate from $0.385x10^{-5}$ to $0.082x10^{-5}$cm. N_D likewise exhibits the same behavior as the Debye length (from 9.19 to 3.55) [36].

Table (1) Copper plasma parameter using an AC power supply and variable Ar gas flow at high voltage of 13kV

Gas flow rate (ltr/min)	T_e (eV)	n_e (cm^{-3}) $x10^{18}$	f_p (Hz) $x10^{13}$	λ_D (cm) $x10^{-5}$	N_D
0.5	1.20	1.16	1.153	0.059	14.15
1	1.51	2.21	2.558	0.030	8.97
1.5	1.89	3.09	4.997	0.017	6.46
2	2.03	4.47	6.004	0.015	5.97
2.5	2.29	8.12	8.095	0.012	5.31

Table (2) Copper plasma parameter using a DC power supply and a variable Ar gas flow at high voltage of 13kV

Gas flow rate (ltr/min)	T_e (eV)	n_e (cm^{-3}) $x10^{18}$	f_p (Hz) $x10^{13}$	λ_D (cm) $x10^{-5}$	N_D
0.5	1.19	1.38	1.760	0.385	9.19
1	1.38	3.08	2.964	0.246	6.77
1.5	1.86	5.78	7.398	0.114	4.24
2	1.92	8.19	8.127	0.106	4.06
2.5	2.18	9.56	11.238	0.082	3.55

4. Conclusion

A cold Ar plasma system operated under atmospheric pressure was used in this study. Copper nanoparticles were prepared at a gas flow rate of 2.5 ltr/min and time of 4 min. The CuO nanoparticles prepared using DC were better than those prepared using AC plasma. The results showed that AC plasma had a greater effect on the plasma properties than DC plasma.

5. Acknowledgment

We would like to express our gratitude and thanks to the plasma laboratory at the Department of Physics, College of Science, University of Baghdad.

References

[1] E.H. Choi, H.S. Uhm and N.K. Kaushik, "Plasma bioscience and its application to medicine", *AAPPS Bull.*, 31 (2021) 10.

[2] D. Braný et al., "Cold Atmospheric Plasma: A Powerful Tool for Modern Medicine", *Int. J. Mol. Sci.*, 21(8) (2020) 2932.

[3] M.A. Khalaf, B.A. Ahmed and K.A. Aadim, "Spectroscopic analysis of CdO_{1-X}:Sn_X plasma produced by Nd:YAG laser", *Iraqi J. Sci.*, 61(7) (2020) 1665-1671.

[4] H. Qassim and S.J. Kadhem, "Study the Effect of Dielectric Barrier Discharge (DBD) Plasma on the Decomposition of Volatile Organic Compounds", *Iraqi J. Phy.*, 20(4) (2022) 45-53.

[5] H.H. Marza and T.H. Khalaf, "The Effect of Power on Inductively Coupled Plasma Parameters", *Iraqi J. Phys.*, 20(3) (2022) 98-108.

[6] L. Moravský, M. Klas and Š. Matejčík. "Bioapplication of Plasma Jet Fed by Argon and Argon/O_2 Gas Mixture", *WDS'13 Proc. Contrib. Papers*, Part II (2013) 149-153.

[7] R.S. Mohammed, K.A. Aadim and K.A. Ahmed, "Estimation of in vivo toxicity of MgO/ZnO core/shell nanoparticles synthesized by eco‐friendly non‐thermal plasma technology", *Appl. Nanosci.*, 12 (2022) 3783-3795.

[8] P. Lamichhane et al., "Non-thermal argon plasma jets of various lengths for selective reactive oxygen and nitrogen species production", *J. Enviro. Chem. Eng.*, 10(3) (2022).

[9] O.A. Hammadi, "Analysis of Secondary Electron Emission in Gas Glow Discharges Used for Thin Film Deposition Processes", *Iraqi J. Appl. Phys.*, 16(1) (2020) 15-20.

[10] R.S. Mohammed, K.A. Aadim and K.A. Ahmed, "Synthesis of CuO/ZnO and MgO/ZnO Core/Shell Nanoparticles with Plasma Jets and Study of their Structural and Optical Properties", *Karbala Int. J. Mod. Sci.*, 8(2) (2022) Article 9.
[11] H.D. Stryczewska and O. Boiko, "Applications of Plasma Produced with Electrical Discharges in Gases for Agriculture and Biomedicine", *Appl. Sci.*, 12(9) (2022) 4405.
[12] A.F. Ahmed, K.A. Aadim and A.A. Yousef, "Spectroscopic study of Al nitrogen plasma produced by DC glow discharge", *Iraqi J. Sci.*, 59(1C) (2018) 494-501.
[13] H.M. Masroor and S.A. El-Dardir, "Characteristics of Langmuir Probe Diagnostics of Low-Pressure Ar:N2 Glow Discharge Plasma", *Iraqi J. Mater.*, 1(4) (2022) 145-156.
[13] K.A. Aadim, "Detection of laser-produced tin plasma emission lines in atmospheric environment by optical emission spectroscopy technique", *Phot. Sen.*, 7(4) (2017) 289-293.
[14] A. Afkhami and R. Norooz-Asl, "Removal, preconcentration and determination of Mo (VI) from water and wastewater samples using maghemite nanoparticles", *Coll. Surf. A Physicochem. Eng. Asp.*, 346(1-3) (2009) 52-57.
[15] R.K. Jamal et al., "Hydrogen Gas Sensors Based on Electrostatically Spray Deposited Nickel Oxide Thin Film Structures", *Phot. Sen.*, 5(3) (2015) 235-240.
[16] D. Wang and T. Namihira, "Nanosecond pulsed streamer discharges: II. Physics, discharge characterization and plasma processing", *Plasma Sour. Sci. Technol.*, 29 (2020) 023001.
[17] I.K. Abbas and K.A. Aadim, "Spectroscopic Diagnosis of Cobalt Plasma Produced by OES Technique and Influence of Applied Voltage on Plasma Parameters", *Iraqi J. Sci.*, 64(5) (2023) 2271-2281.
[18] M. Selçan and U. Demraluğlu, "Electrical Characteristics of Argon Discharge PlasmainDual-Magnetron Configuration", Iraqi J. Mater., 2(3) (2023) 135-142.
[19] J. Li, "Energy exchange modulation for selective control of gas temperature and electron number density in cold atmospheric plasmas", *Plasma Sour. Sci. Technol.*, 31 (2022) 055015.
[20] H. Akatsuka, "Optical Emission Spectroscopic (OES) analysis for diagnostics of electron density and temperature in non-equilibrium argon plasma based on collisional-radiative model", *Adv. Phys. X*, 4(1) (2019).
[21] A. Qusnudin, K. Kusumandari and T.E. Saraswati, "OH Radical Intensity of Dielectric Barrier Discharge (DBD) Plasma Measured by Optical Emission Spectroscopy (OES)", *J. Phys.: Conf. Ser.*, 1825 (2021) 012072.
[22] F.L. Tabares and I. Junkar, "Cold Plasma Systems and Their Application in Surface Treatments for Medicine", *molecules*, 26 (2021) 1903.
[23] K. Pardnsar, "Secondary Electron Emission in Glow DischargePlasmas", *Iraqi J. Mater.*, 2(4) (2023) 167-174.
[24] M.C. Chen and E.C. Chen, **"Introduction to Plasma Physics and Controlled Fusion"**, vol. 1, Academic Press (LA, 1983).
[25] M.L. Huber et al., "The NIST REFPROP Database for Highly Accurate Properties of Industrially Important Fluids", *Ind. Eng. Chem. Res.*, 61 (2022) 15449-15472.
[26] A.M. El Sherbini and A.A.S. AlAamer, "Measurement of Plasma Parameters in Laser-Induced Breakdown Spectroscopy Using Si-Lines", *World J. Nano Sci. Eng.*, (2012) 206-212.
[27] S.N. Rashid, K.A. Aadim and A.S. Jasim, "Silver Nanoparticles Synthesized by Nd:YAG Laser Ablation Technique: Characterization and Antibacterial Activity", *Karbala Int. J. Mod. Sci.*, 8(1) (2022) 71-82.
[28] M. Nasrollahzadeh, Z. Issaabadi and S.M. Sajadi, "Green synthesis of Cu/Al_2O_3 nanoparticles as efficient and recyclable catalyst for reduction of 2,4-dinitrophenylhydrazine, Methylene blue and Congo red", *Composites B: Eng.*, (2019) 112-119.
[29] M.A. Nawaz et al., "Microstructural Study of as Grown and 650°C Annealed ZnO Nanorods: X-ray Peak Profile Analysis", *Dig. J. Nanomater. Biostruct.*, 11(2) (2016) 537-546.
[30] V.V. Thekkae Padil and M. Cernik, "Green synthesis of copper oxide nanoparticles using gum karaya as a biotemplate and their antibacterial application", *Int. J. Nanomed.*, 8 (2013) 889-898.
[31] Ch. Ashok, K. Venkateswara Rao, Ch. Shilpa Chakra, "Structural analysis of CuO nanomaterials prepared by novel microwave assisted method", *J. Atoms Mol.*, 4(5) (2014) 803-806.
[32] C. Parvathiraja and S. Shailajha, "Bioproduction of CuO and Ag/CuO heterogeneous photocatalysis-photocatalytic dye degradation and biological activities", *Appl. Nanosci.*, (2021) 1411-1425.
[33] N.K. Abdaalameer, S.N. Mazhir and K.A. Aadim, "Diagnostics of zinc selenite plasma produced by FHG of a Q-switched Nd:YAG laser", *Chalcog. Lett.*, 18(7) (2021) 405-411.
[34] V.S. Johnson et al., "A cold atmospheric-pressure helium plasma generated in flexible tubing", *IEEE Trans Plasma Sci.*, 39(11) (2011) 2360-2361.
[35] J.-W. Lackmann and J.E. Bandow, "Inactivation of microbes and macromolecules by atmospheric-pressure plasma jets", *Appl. Microbiol. Biotechnol.*, 98 (2014) 6205-6213.

Najlaa L. Tubena
Majid R. Al-Bahrani

Nanomaterials Laboratory, Department of Physics, Faculty of Science, University of Thi-Qar, Thi-Qar, IRAQ

Enhancement of Power Conversion Efficiency for Perovskite Solar Cells Using ZnO-G-Ge as Electron Transport Layer

The current study utilized a hydrothermal method to create a nanocomposite (ZnONR/Ge-G). The electron carrier layer consisted of two refined constituents (ZnO NP and ZnO NR). TEM, SEM, and XRD investigations were conducted on ZnO nanoparticles (ZnO NP) and ZnO nanorods (ZnO NR). Long ZnO nanorods were efficiently synthesized using a low-temperature chemical immersion deposition approach. This method was used to create solar cells that included the FTO/ZnO nanorod structure. The results suggested that an energy conversion efficiency of 14.3055% was achieved. The synthesis of the ZnO NR-Ge-G QD nanocomposite was conducted, and subsequent investigation focused on its structural features. The fourth cell demonstrated enhanced electrical conductivity compared to other cells due to the deposition of germanium dot-dotted with graphene on ZnO NR. Thus, the surface area of the material increased, leading to improved rates of electron absorption and transmission that were more efficient compared to other options.

Keywords: Zinc white; Perovskites; Solar cells; Hydrothermal process
Received: 31 March 2024; **Revised:** 15 May 2024; **Accepted:** 22 May 2024

1. Introduction

Zinc oxide is a semiconductor with a high exciton binding energy (60 meV) and a wide direct bandgap energy (3.37 eV). It has been the subject of extensive research in recent decades due to its unique electrical, piezoelectric, catalytic, and other properties. These characteristics find applications in a variety of nanoscale devices, including Li-ion batteries, gas sensors, photodetectors, and photoelectrochemical cells [1-3]. Mahdi Sharif sol-gel method was used to incorporate zinc nanoparticles into an electron transfer layer by grafting porous titanium ETL with 2 mol.% zinc, which increased the PSC efficiency of the cell from 9.74% to 13.76%. [4]. Naresh Muthu have prepared ZnO nanoparticles using the doctor blade method, which resulted in a competent PCE of 3.7447%. [5]. Bandari et al. have used spin coating to produce thin films of ZnO nanoparticles [6]. Abd El-Lateef et al. have prepared ZnO nanoparticles (ZnO/C) composites and obtained efficiency of 19.6% [7]. Abdel Ali et al. have used several nanomaterials and hydrothermal technology resulting in a 9.45% conversion efficiency of PCE [8] . Abdulmohsin et al. have used of $CH_3NH_3PbI_3$ for perovskite solar cells of 22.26% conversion efficiency of PCE [9]. Zheng et al. have used a two-step spin coating deposition method to synthesize $CH_3NH_3PbI_3$ QDs with improved energy gap as an excellent option for perovskite solar cells [10]. The low-temperature chemical bath deposition method was effectively used to fabricate ZnO nanorods of controllable length, which are then used to fabricate solar cells using an FTO/ZnO structure for a high energy conversion efficiency of 12.85% [11]. Huang et al. have used a hydrothermal process to alter the natural properties of ZnO nanorods (obtaining an efficiency of 10.45%, which is 23% higher than non-doped zinc oxide) [12]. ZnO nanorods (NRs) have been made using hydrothermal method to improve the efficiency of perovskite solar cells, increasing the power conversion efficiency (PCE) from 10.33% to 15.06% [13].

In this research, we examine two forms of ZnO, nanoparticles and nanorods, to determine which is much more efficient. Nanoparticles exhibit entirely new or enhanced properties, including molecule form, size, distribution, and others. Applications for nanoparticles are quickly developing in several fields [14]. The aims of this study are to synthesize nanocomposites (ZnO NP/Ge-G and ZnO NR/Ge-G) using ZnO nanomaterials, nanoparticles, nanorods, graphene, and carbon using the hydrothermal method, and then deposit this compound (ZnONP/Ge-G) and (ZnO NR/Ge-G) on a film using the doctor blade and spin coating methods to form an electron transport layer (ETL) that will be used in the manufacturing of a perovskite cell (FTO/ZnO NP/Ge-G). These materials have been used to achieve high efficiencies. The most efficient composite material (ZnO NR/Ge-G) performed significantly better.

2. Experimental Part

Zinc oxide nanoparticles (ZnO NPs, 7.99%) and nanorods (ZnO NR, 9.9%) were synthesized by mixing germanium (Ge) with graphene (G) and acetic acid ($C_6H_8O_7$) (99%). The substance is ethyl cellulose ($C_{20}H_{38}O_{11}$), which makes up 99.7% of the composition. The ethox solution used in each investigation had a concentration of 99.9% and was acquired from Sigma-Aldrich.

A magnetic stirrer is used to mix together 2 g of ZnO NR, 1 g of $C_{20}H_{38}O_{11}$ with a purity of 99.7%, 16 µL of refined ethanol (C_2H_5OH) with a purity of 99.9%, and 400 µL of acetic acid ($C_6H_8O_7$) with a purity of 99% in a glass beaker. The blending process is sustained for a duration of 36 hours. The 1 cm^2 surface area is highly efficient due to the use of pristine FTO glass. The film's thickness and the dimensions of the heated region can be modified by applying additional layers of adhesive foil. Following a desiccation period of ten minutes, the substance underwent exposure to different temperatures and durations within a convection oven. The temperatures used in creating this image were as follows: The temperature sequence is as follows: The temperature sequence was as follows: 40°C for a duration of 10 minutes, followed by 80°C for 10 minutes, then 120°C for 15 minutes, 250°C for 30 minutes, and finally 375°C and 450°C [15].

A glass beaker with a magnetic stirrer is used to mix a solution containing the following components: 16 µL of pure ethanol with a 99.9% purity, 2 g of ZnO nanoparticles (ZnO NPs), 1 g of $C_{20}H_{38}O_{11}$ with a 99.7% purity, and 400 µL of $C_6H_8O_7$ with a 99% purity. The agitation method is carried out for a duration of 36 hours. When used as a spray, it creates a surface area of 1 cm^2, which is enough to thoroughly disinfect FTO glass. By applying a series of adhesive coatings, one can adjust the thickness of the film and expand the heated areas. After being dehydrated for 10 minutes, the substance was subjected to different temperatures and durations in a convection oven. The following temperatures were utilized to create this film: 40°C for a duration of 10 minutes, 80°C for a duration of 10 minutes, 120°C for 15 minutes, 250°C for 30 minutes, and finally 375°C and 450°C [16].

A mixture is formed by combining 1 g of ZnO nanorods with 1 g of Ge-Ga. After stirring, the mixture was kept at a temperature of 160°C for 72 hours in a non-thermal device, with the addition of 5 mL of deionized water.

An apparatus is used to mix 0.5 g of the chemical being studied with 0.5 g of ethyl cellulose ($C_{20}H_{38}O_{11}$) (99.7%), 200 µL of acetic acid ($C_6H_8O_7$) (99%), and 200 µL of pure ethanol (99.9%). The mixture is homogenized in a glass container using a magnetic stirrer for a period of 36 hours [17]. The glass beaker is constructed entirely from pristine FTO glass and possesses a surface area of 1 cm. By applying numerous layers of adhesive covers, it is possible to modify the thickness and dimensions of the heated region. After a 10-min dehydration period, we placed it in a convection oven that had a timer and temperature control.

The film was processed using temperatures of 375°C, 450°C, and 40°C for 10 minutes each, followed by 80°C for 10 minutes, 120°C for 15 minutes, and finally 250°C for 30 minutes [18].

3. Results and Discussion

Scanning electron microscopy (SEM) was employed for the analysis. Figure (1) displays the findings of a study on the morphology of ZnO NPs coatings that were applied to FTO glass. The ZnO NPs sample displayed consistent size and shape, with a spherical structure. The ZnO nanoparticles demonstrate attributes of being compact, uniform, and strongly attached to the glass substrate coated with FTO. Thin ZnO films with a ring-like structure were fabricated.

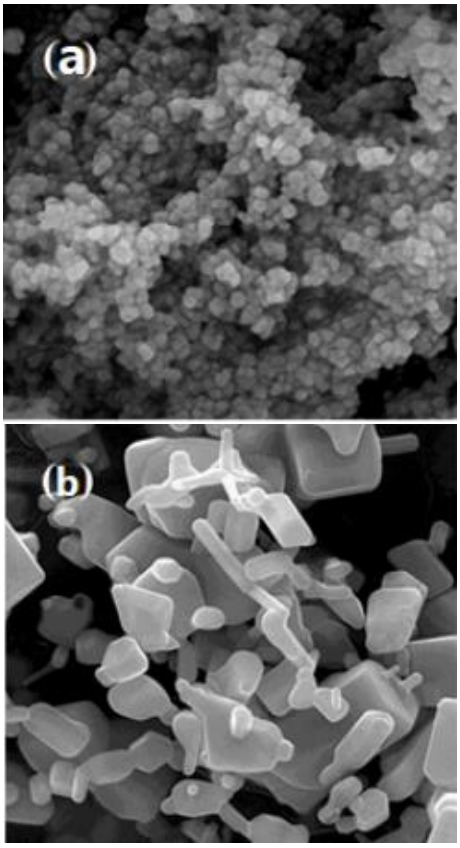

Fig. (1) SEM (a) ZnONP(b) ZnONR

The temperature was raised to 450°C, resulting in an increase in the size of the ZnO particles. Figure (2a) displays the XRD patterns of the crystalline phases in the ZnO NPs powder-mediated. A conspicuous and strong peak in the patterns verified the synthesis of nanosized crystalline ZnO material. The hkl planes (010), (002), (011), (012), (110), (013), (112), and (021) correspond to the observed XRD peaks at 2θ of 31.8475°, 34.4407°, 36.3168°, 47.764°, 56.5864°, 62.9141°, 67.9874°, and 69.111°, as indicated in table (1), which verified the hexagonal wurtzite phase of the crystalline zinc oxide nanoparticles. The XRD pattern's agreement with the ZnO NPs standard pattern in JCPDS card no. 98-0155780 indicates high-phase purity and crystallinity. The XRD results of ZnO NPs reveal peaks because of the material's purity; no phase related to any other material or phase was found,

demonstrating the composite sample's high level of purity.

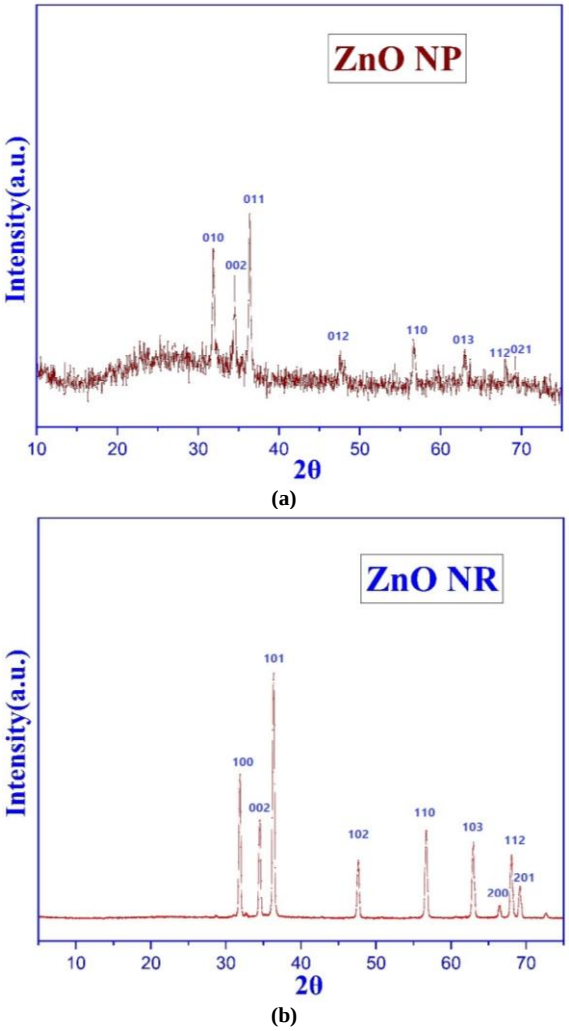

Fig. (2) Shows: (a) XRD ZnONP, and (b) XRD ZnONR

An analysis of the XRD lines provides valuable information about the characteristics of the nanoparticles in the sample. The presence of well-defined peaks suggests that the ZnO nanoparticles have a high degree of crystallinity, indicating that the material put into the FTO is of good quality. The crystallite size of the generated particles was calculated using the Debye-Scherrer's formula. Expanding the XRD line, Bragg's law is used to compute the d-space, or inter-planar separation, between atoms [19]

$$D = 0.9\lambda/\beta cos\theta \quad (1)$$

$$2d\ sin = n\lambda \quad (2)$$

where n is the order of diffraction (n=2), λ=1.540Å is the wavelength of x-rays, θ is the diffraction angle, β is the full-width at half maximum (FWHM), and d is the d-spacing, and D is the crystallite size of the particle. The crystal's lattice parameters, a = 3.77483 Å and c = 9.46318 Å, are found using the relation [20]. The Miller indices of the dominating peaks are represented by (hkl)

SEM images of ZnONR show (Fig. 3) that the rods have a hexagonal shape, which can be seen between the assembled nanotubes. These regions are necessary for improved perovskite penetration, which increases light absorption. Upon closely examining. The length of ZnO nanorods is not uniform. Additionally, the diameters are displayed in a variety of forms, such as the square, cubic, and hexagonal bases typical of zinc oxide nanoelectrodes. Figure (2b) displays the diffraction peaks that can be seen in these patterns at different theta levels. The nine peaks at 31.8241, 34.4744, 36.3047, 47.583, 56.631, 62.89, 66.408, 67.981, and 69.119 can be classified as (100), (002), (101), (102), (110), (103) (200), (112), and (201). These observed levels support the figure showing the powder diffraction file number 00-036-1451, which was previously reported, matches well with the wurtzite-organized NRs, where the XRD result reveals a very dominant orientation in the c-axis direction (i.e., perpendicular to the plane of the reactant). The crystallite size value for each sample (D) is determined by applying the Scherer equation (Eq. (1)) to the dominant growth peak (101). Where the x-ray wavelength is denoted by λ (0.1540 nm), k (0.9) is a constant, and β is the full width at half maximum (FWHM), the crystal size change can be observed as in Table (2).

Scanning electron microscopy (SEM) was initially used to examine the surface morphology of nanomaterials from the graphene family used in this work. Figure (3a) shows that graphene samples taken from nanoscale graphene powder show a typical wrinkle-like morphology. It also formed a thin, smooth, multilayer graphene layer on the surface of Ge. The surface morphology of the Ge NPs film is clearly visible in the SEM images shown in Figure (3b). The findings demonstrate that the Ge NPs film is made up of a large number of spherical nanoscale particles. The uniform and continuous thin film is formed by these particles coming into close contact with one another. Figure (3c) from SEM analysis shows the development of the ZnO NR/Ge-G nanocomposite, which displayed a shape typical of hexagonal nanorods by a layer of Ge-G nan sheet mixed with ZnONR. The absorbance properties are high because of the strong bond between them. Figure (3d) shows TEM pictures of ZnO NRs. The black shadow in the TEM image of ZnO NRs-G-Ge represents the shape of graphene around the germanium and ZnO NRs. For these functional groups to exist, a ZnO NRs-G-Ge complex needs to be formed. Figure (3e) shows an image of the resulting film taken using a scanning electron microscope. It is clear that the mixture of graphene and germanium is homogeneous, as seen by the SEM image in Figure (3f). Because Ge-G is present, these particles potentially offer a significant surface area for enhanced adsorption. When compared to the original ZnO NP, the form gets coarser, indicating that the compound is well mixed. Investigations

utilizing transmission electron microscopy revealed that Ge-G doping is responsible for the gray-black hue of ZnO nanoparticle powder, and TEM was used to monitor the formation of ZnO-NPs. They are widely dispersed, have a spherical shape, and vary in size, as figure (3g) illustrates.

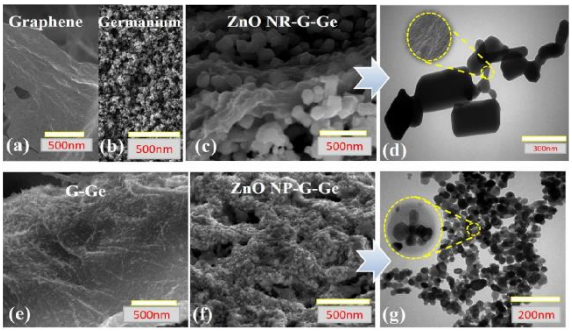

Fig. (3) SEM and TEM images: (4.a) Graphene, (4.b) Germanium, (4.c) ZnO NR-Ge-G, (4.e) Ge-G, (4.f) ZnO NP-Ge-G, TEM (4.d) ZnO NR-Ge-G, (4.g) ZnO NP-Ge-G

The Table (3) provides a sequential presentation of the photovoltaic performance of the solar cells, including variables such as photocurrent (ISC), open-circuit voltage (VOC), fill factor (FF), and power conversion efficiency (PCE). Furthermore, the table demonstrates the specific region of the cell that is actively engaged, measuring 1 cm^2, under varying levels of illumination. On the string, 4 cells (FTO/ZnO NP-G/Pre/HTL/M, FTO/ZnO NP-Ge-G/Pre/HTL/M, FTO/ZnO NR-G/Pre/HTL/M, and FTO/ZnO NR-Ge-G/Pre/HTL/M) were produced in order to test the photovoltaic function. The voltage in the open circuit, or VOC, is the cell's potential difference. ISC stands for open circuit current, or the current that results from the absence of an external load. VOCs dictate the absorbent material's energy bandgap in solar cells, whereas the incident solar count (ISC) represents the quantity of photons striking the cell. The fill factor (FF), which is also referred to as the proportion of our maximum power (P max) obtained from the solar cell, is greater than the power gap. The device parameter values for FTO/ZnONP-G/Pre/HTL/M, FTO/ZnONP-Ge-G/Pre/HTL/M, FTO/ZnONR-G/Pre/HTL/M, and FTO/ZnONR-Ge-G/Pre/HTL/M are displayed in the table. The ISC of the fourth gadget is greater than the initial, second, and third. As such, it implies that ZnO NR developed on the better and more conductivity-rich Ge-G substrate. Furthermore, because of the enhanced FTO/ZnO NR Ge-G bonding, the FF FTO/ZnO NR-G/Pre/HTL/M is superior to the FF of the third, second, and first cells. In addition, the increased electrical stimulation of FTO/ZnO NR-Ge-G/Pre/HTL/M results in a notable improvement in the PCE, as shown in Fig. (4).

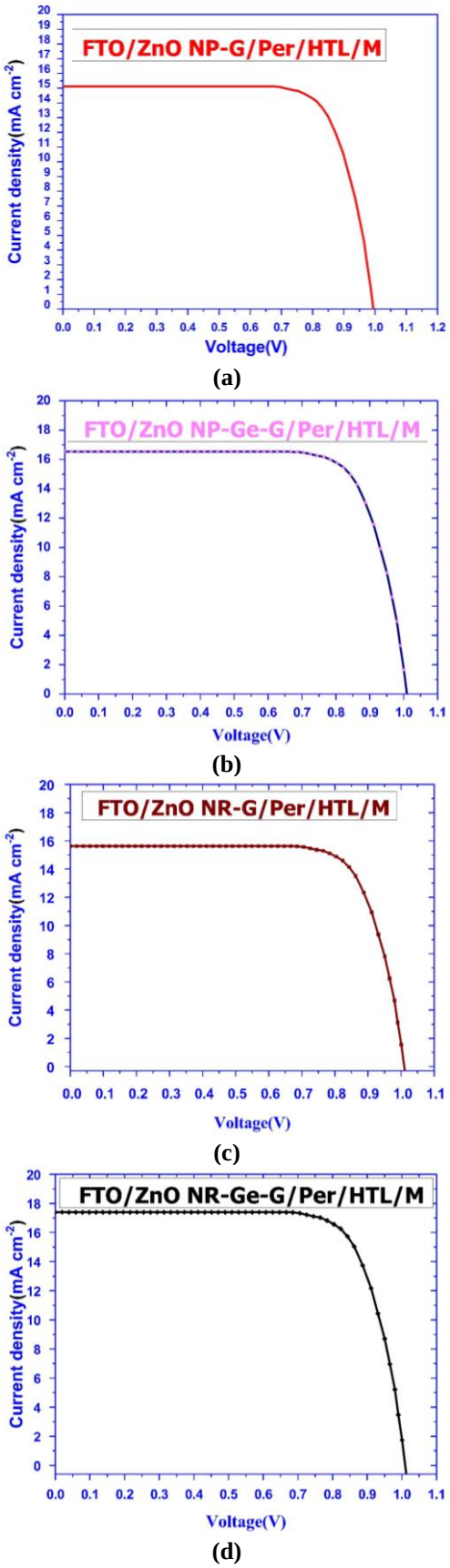

Fig. (4) Photocurrent density voltage characteristics of nanocomposites (a) FTO/ZnO NP-G/Pre/HTL/M. (b) FTO/ZnO NP-Ge-G/Pre/HTL/M. (c) FTO/ZnO NR-G/Pre/HTL/M, (d) FTO/ZnO NR-Ge-G/Pre/HTL/M

The remarkable performance and notable rise in PCE can be attributed to the higher surface area for interaction provided by the FTO/ZnO NR-Ge-G/Pre/HTL/M structure, which holds considerable potential for enhancing the demonstration of SCS cells. The inclusion of Ge-G in photoelectrocatalysis boosts the electrical conductivity and reduces the time needed for electron-hole pair reconnection, hence enhancing the PCE of FTO/ZnO NR-Ge-G/Pre/HTL/M. The power conversion efficiency (PCE) of perovskite solar cells was determined by extracting the photovoltaic (PV), fill factor (FF), short circuit current density (Jsc), and open circuit voltage (Voc) parameters from the current. Graph depicting the relationship between density and voltage (JV). PV was calculated using these relationships [21]:

$$PCE = \frac{P\,max}{Pin} x100\% = \frac{JSC.VOC.FF}{Pin} x100\% \quad (3)$$

where the solar power t incidenon a unit area is represented by Pin: input power (Pin = 100 mWcm-2), and the FF was determined using the relationship below [22]:

$$FF = \frac{Jm.vm}{JSC.VOC} \quad (4)$$

4. Conclusions

In this work, graphene (G) nanosheet fabrication and fusion with semiconducting germanium Ge, ZnO NR activation, and ZnO NR\Ge-G characterization by means of a hydrothermal approach. There was an enhanced surface area volume in the ZnO NR\Ge-G nanoparticles. Additionally, it has been demonstrated that the morphology and characteristics of the films were altered by the addition of germanium impregnated with graphene. The ZnO NR\Ge-G nanocomposite shows a high absorption light intensity, suggesting that it could enhance photocatalytic activity. ZnO NR grafted with Ge-G results in a decrease in the band gap, which accelerates electron transmission and increases conductivity, according to the band gap calculation. Perovskite solar cells are one example of an area where ZnO NR Ge-G is more connected and efficient than ZnO NP.

References

[1] V. Gurylev and T. P. Perng, "Defect engineering of ZnO: Review on oxygen and zinc vacancies", *J. Eur. Ceram. Soc.*, 41(10) (2021) 4977–4996. doi: 10.1016/j.jeurceramsoc.2021.03.031.

[2] V. Parihar, M. Raja, and R. Paulose, "A brief review of structural, electrical and electrochemical properties of zinc oxide nanoparticles", *Rev. Adv. Mater. Sci.*, 53(2) (2018) 119–130. doi: 10.1515/rams-2018-0009.

[3] X. Huang, H. Yu, S. Shi, and C. Huang, "Improving the performance of inverted polymer solar cells by the efficiently doping and modification of electron transport layer-ZnO", *Org. Electron.*, (65) (2019) 311–320. doi: 10.1016/j.orgel.2018.11.030.

[4] M. Sharafi and H. Oveisi, "A high-performance perovskite solar cell with a designed nanoarchitecture and modified mesoporous titania electron transport layer by zinc nanoparticles impurity", *Mater. Sci. Eng. B*, 296 (2023) 116608.

[5] R. N. Muthu, "Synthesis of Zinc Oxide Nanoparticles by Citrus Limon as an Effective Photoanode for Dye-Sensitized Solar Cells", Phys. Chem. Res., 12(2) (2024) 383-392. DOI: 10.22036/pcr.2023.407583.2378.

[6] K. P. Bhandari, D. R. Sapkota, M. K. Jamarkattel, Q. Stillion, and R. W. Collins, "Zinc Oxide Nanoparticles—Solution-Based Synthesis and Characterizations", *Nanomaterials*, 13(11) (2023) 1–15. doi: 10.3390/nano13111795.

[7] H. M. Abd El-Lateef, M. M. Khalaf, F. E. Heakal, M. F. Abou Taleb, and M. Gouda, "Electron transport materials based on ZnO@ carbon derived metal-organic framework for high-performance perovskite solar cell", *Sol. Energy*, 253(2023) 453–461.

[8] M. R. Al-bahrani, R. A. Abd Ali, and I. Shakir Mutashar, "Design and Fabrication of TiO2 NP/NM Nanocomposite as Photoanode for Solar Cells", *J. Nanostructures*, 12(2) (2022) 366–374.

[9] Z. Abdulsada, Z. Ali, B. Sally, M. Samir, and S. Hayder, "High Efficiency (22.46) of Solar Cells Based on Perovskites", *University of Thi-Qar J Science (UTJsci)* E-ISSN:2709-0256, P-ISSN: 1991-8690, 10(2) (2023).

[10] F. Zheng, L. Z. Tan, S. Liu, and A. M. Rappe, "Rashba spin-orbit coupling enhanced carrier lifetime in $CH_3 NH_3 PbI_3$", *Nano Lett.*, 15(12) (2015) 7794–7800. doi: 10.1021/acs.nanolett.5b01854.

[11] M. Makenali, I. Kazeminezhad, F. A. Roghabadi, and V. Ahmadi, "Efficiency improvement of perovskite solar cells by charge transport balancing using length tunable ZnO nanorods and optimized perovskite morphology", *Sol. Energy Mater. Sol. Cells*, 230 (2021) 111206. doi: 10.1016/j.solmat.2021.111206.

[12] Z. L. Huang, C. M. Chen, Z. K. Lin, and S. H. Yang, "Efficiency enhancement of regular-type perovskite solar cells based on Al-doped ZnO nanorods as electron transporting layers", *Superlattices Microstruct.*, 102 (2017) 94–102. doi: 10.1016/j.spmi.2016.12.012.

[13] S. Li, P. Zhang, Y. Wang, H. Sarvari, D. Liu, J. Wu, Y. Yang, Z. Wang, and Z. D. Chen,"Interface engineering of high efficiency perovskite solar cells based on ZnO nanorods using atomic layer deposition", *Nano Res.* 10 (2017) 1092–1103 (2017). https://doi.org/10.1007/s12274-016-1407-0

[14] S. Kaviya, J. Santhanalakshmi, and B. Viswanathan, "Green synthesis of silver nanoparticles using Polyalthia longifolia leaf extract

along with D-sorbitol: study of antibacterial activit", *J. Nanotechnol.*, 2011(2011) 1687-9503.
[15] S. K. Hussian and M. R. Al-bahrani, "Influence of SiO_2 nanoparticles on the structural, morphology, and optical properties of $CsPbBr_3$ Quantum Dots", *Materials Today: Proceedings*, 3(2) (2023) 62–69, 2023.
[16] H. H. Ali, "Multi-Wall Carbon Nanotubes with NiO and pt as Counter Electrodes for DSSC applications",*University of Thi-Qar J Science(UTJsci)*, E-ISSN:2709-0256,P-ISSN: 1991-8690, 10(2) (2023).
[17] N. Palladino, M. Occelli, G. Wallez, Y. Coquinot, Q. Lemasson, L. Pichon, S. Stankic, V. Etgens, and J. Salvant,"An analytical survey of zinc white historical and modern artists' materials", *Herit. Sci.*, 12(1) (2024). doi: 10.1186/s40494-023-01082-4.
[18] A. Alhadi, S. Abd, and M. R. Al-bahrani, "The effect of ZnO / Ge-G QD photo anode on photovoltaic properties of DSSCs", *Neuro Quant ology*. 20(10) (2022) 3201–3209. doi: 10.14704/nq.2022.20.10. NQ55319.
[19] C. Li, Z. Zhou, K. Liu, X. Sun, J. Tao, J. Wang, Z. Zou, G. Liao, F. Li, F. Ni, and J. Zhang, "Germanium nanoparticles film as a room-temperature electron transport layer for organic solar cells", *Sol. Energy*, 226 (2021) 421–426. doi: 10.1016/j.solener.2021.08.063.
[20] D. L. Dorset, "X-ray Diffraction: A Practical Approach" *Microsc Microanal.*, 4(5) (1998) 513-5. doi: 10.1017/S143192769800049X.
[21] I. M. Khan, and M. A. Mazumder, "**Perovskite based Materials for Energy Storage Devices**", *Materials Research Foundations*,151 (2023). ISSN 2471-8890 (pint), ISSN 2471-8904 (online). DOI: https://doi.org/10.21741/9781644902738.
[22] L. Ledwani, and J. S. Sangwai, "**Nanotechnology for Energy and Environmental Engineering**", *Green Energy and Technology*, Springer; 1st ed. 2020 edition (March 13, 2021). ISSN 1865-3529, ISSN1865-3537(electronic).

Table (1) Results of Debye-Scherer formula calculation of ZnO NPs

NO	Exp. Pos.[°2Th.]	Exp. D spacing [Å]	FWHM Left [°2Th.]	hkl	Reference code
1	31.8475	2.80764	0.3000	010	ICDS 98-0155780
2	34.4407	2.60195	0.3600	002	ICDS 98-015-5780
3	36.3168	2.47172	0.3000	011	ICDS 98-015-5780
4	47.7640	1.90266	0.9600	012	ICDS 98-015-4487
5	56.5864	1.62516	0.2680	110	ICDS 98-015-5780
6	62.9141	1.47607	0.4800	013	ICDS 98-015-5780
7	67.9874	1.37774	0.1800	112	ICDS 98-015-5780
8	69.1110	1.35806	0.2478	021	ICDS98-015-5780

Table (2) Results of Debye-Scherer formula calculation of ZnO NR

No.	2 Theta (deg)	(hkl)	FWHM *deg)	Crystallite size (nm)	d-spacing observed (Å)	Reference and JCDPS card No.
1	31.8241	100	0.258	32.03337	2.810288	00-036-1451
2	34.4744	002	0.256	32.50674	2.599730	00-036-1451
3	36.3047	101	0.264	31.67992	2.472556	00-036-1451
4	47.5830	102	0.271	32.04953	1.909519	00-036-1451
5	56.6310	110	0.274	32.94849	1.624078	00-036-1451
6	62.8900	103	0.276	33.75264	1.476802	00-036-1451
7	66.4080	200	0.270	35.17898	1.406684	00-036-1451
8	67.9810	112	0.257	37.29724	1.377996	00-036-1451
9	69.1190	201	0.276	34.96585	1.358075	00-036-1451

Table (3) Electrochemical properties and photovoltaic parameters

Solar Cells (configurations)	V_{oc} (V)	J_{sc} (mA/cm^2)	FF	PCE (%)
FTO/ZnONP-G/Pre/HTL/M	0.98	15.12	0.71	10.520496
FTO/ZnO NP-Ge-G/Pre/HTL/M	1.06	16.51	0.74	12.950444
FTO/ZnO NR-G/Pre/HTL/M,	1.02	15.69	0.73	11.682774
FTO/ZnO NR-Ge-G/Pre/HTL/M.	1.10	17.34	0.75	14.305500

Marwan S. Abdul Hamid
Isam M. Ibrahim

Department of Physics, College of Science, University of Baghdad, Baghdad, IRAQ

Ag-PVP nanofiber for UV Photodetector Produced by Electrospinning Technique

This work aims to produce UV detector from Ag-PVP nanofibers by using the electrospinning method. Polyvinylpyrrolidone (PVP) nanofibers and a Ag-PVP nanofiber composite with 1%, 2% and 3% Ag were effectively produced by the electrospinning method. The material's morphology, structural and optical characteristics are studied. The structure of the obtained nanofiber was amorphous. Ag-PVP film fibers are beaded produced with increasing Ag concentration increases. The optical energy gap for three concentrations of Ag-PVP nanofibers ranged between 1.52 and 3.94 eV, where the energy gap decreased with increasing silver concentration, the sensitivity for Ag-PVP nanofiber were obtained for UV detector at the wavelength of 360 nm, the sensitivity values were 8.4, 7.95, and 17.7 for doping with Ag 1%, 2%, and 3%, respectively.

Keywords: Polyvinylpyrrolidone; Nanofibers; Electrospinning; Flexible defector
Received: 02 April 2024; **Revised:** 30 May 2024; **Accepted:** 06 June 2024

1. Introduction

The study of nanocomposites dispersed inside a polymer matrix has gained momentum in the realm of materials research due to its great potential for industrialization customizable materials. Based on their quantity, dimensions, and form. There is evidence that these nanoparticles display a wide range of optical, thermal, electrical, and electrochemical characteristic depending on their quantity, size, and form. The polymer's composition and the arrangement of the nanoparticles inside the polymer matrix have been found to affect many of these features. Therefore, the electrical and optical properties of nanocomposites may encourage to use them in many applications such as sensors [1-6], microelectronics, wear-resistant coatings, biological implants, and optical coatings [7,8]. Polyvinylpyrrolidone (PVP)is biocompatible, nontoxic, and water-soluble polymer [9] pH-stable, non-ionic, colorless, temperature-resistant, and chemically inert [10,11], It may be used as a matrix to produce polymer nanocomposites that have intriguing properties different from PVP. lowering and stabilizing agent In the same procedure, Ag nanoparticles are synthesized using PVP. Thus, it is safe to assert the special qualities of PVP and Ag nanoparticles as well as the possible functional characteristics of the Ag-PVP nanocomposite. Today's materials science is mostly concerned with nanocomposites. Because the nano-fillers can change and enhance the properties of polymers, some novel products have been developed. Using electrospinning, composite nanofibers may be created directly from inorganic nanoparticle dispersions in polymer solutions. Electrospinning is a simple, flexible, robust, and useful technique for creating ultra-fine fibers with diameters ranging from a few nanometers to several micrometers. It can be used to create infinite, continuous nanofibers and has been used to electro spun a variety of polymers. Their massive ratio of surface area to volume, extended length, constant diameter and a sizable surface area makes them suitable for use as templates [12]. Because of their numerous applications and greater surface area to volume ratios, electro spun fibers with nanosized porous features have piqued the curiosity of many researchers. [13], Because of its amazing properties, using nanoparticles to change physiologically active compounds into potentially releasable molecules has become more popular in recent years. [14], Using electrospinning, inorganic nanoparticle dispersions in polymer solutions may be immediately converted into items composite nanofibers. PVP films' excellent optical quality makes them suitable for usage in optical sensors and systems. Polymeric nanofiber membranes have numerous applications, such as filter and battery materials. There is evidence that PVP nanocomposites have potential applications in many different scientific and technological fields. The focus of research is shifting from empirical engineering to advanced industrial applications. Investigating the fundamental issues related to the composed of polymer nanocomposites is of special interest to recent researchers. One of the main challenges facing current synthetic techniques is tailoring the physicochemical properties of polymer nanocomposites. Having a solid understanding of the pertinent situational factors and controlling the experimental conditions according to protocol could help to overcome the challenges. Concerning PVP nanocomposites [15], In this work, an ultra-high sensitivity photodetector PVP and Ag-PVP nanofibers is synthesize by electrospinning. Investigations have been done on the structural, optical, and sensing properties.

This paper examined the effects of Ag on fiber diameter, morphology, and optical characteristics, and from all above properties we aim to study the properties of flexible photodetector.

2. Experimental Part

The initial stage in making the electrospinning PVP solution was to dissolve (1g of the 90000 g/mol polyvinylpyrrolidone PVP polymer in 11.4 ml of alcohol) Then, using a magnetic stirrer, the liquid was stirred for six hours at room temperature.

Three solutions were prepared with three different concentrations of silver, (silver was prepared by pulsed laser ablation with energy of 200mJ and 200 pulses), (1%, 2%, 3%) Ag incorporated into the previously prepared polymer solution and set on a magnetic stirrer for 30 minutes at room temperature. The Ag-PVP composite solution changes to yellow. The solution was placed into a syringe needle a 27G, To be ready to prepare fibers with electric spinning system. Three essential parts make up the electric spinning system: a needle pump, a dc high voltage power source, and a conductive collector, such aluminum. Horizontal and vertical electrospinning installations are the two main varieties. For this experiment, the syringe pump was adjusted to the horizontal position, as shown in Fig. (1). A high-voltage power supply with an adjustable control range of 0-50 kV set at 20 kV DC, a syringe pump with a flow control range set at 0.5 mL/h, and a syringe with a metal needle were connected to the positive power source in order to charge the polymer solution with a positive charge. There are 11 centimeters separating the collection and needle.

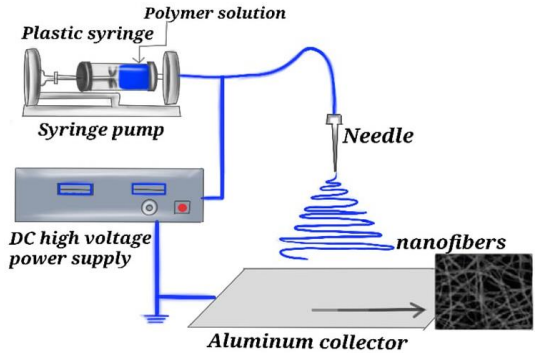

Fig. (1) The electrospinning device's assembly schematic

Table (1) Direct energy band gap for all samples at applied voltages of 20kV

Sample	E_g (eV)
Pure	4.20
PVP/1%Ag	3.94
PVP/2%Ag	3.912
PVP/3%Ag	1.52

The plastic syringe is filled with an Ag-PVP composite solution, which is then propelled by the injection pump. This process results in three steps for the solution's deposit on silicon and glass. The plastic syringe was filled with an electric field that was expelled into the Taylor cone at a specified flow rate because the Aluminum collecting plate and syringe needle combined to create the electric field using high voltage [16]. layer upon layer of nanofibers is formed as the solvent evaporates on route to the collecting plate. Optimal electrospinning settings and operating circumstances were determined by considering the effect on the nanofibers' structural morphology [17]. The FE-SEM was employed to investigate the produced nanofibers' structural morphologies. To verify the final structure, the x-ray diffraction is performed. Utilizing a Sp-8001 model UV-VIS spectrophotometer, the deposited nanofibers' optical absorption spectra were investigated as a function of wavelength (300–1100 nm). Using the Sensitive Fluke 8846A digital electrometers, the photosensitivity current-voltage (I-V) characteristic curves for Ag-PVP were investigated.

3. Results and discussion

X-ray diffraction were conducted, For the PVP nanofiber that were prepared with different concentrations. Figure (2) shows the XRD patterns for (pure PVP, PVP-1% Ag, PVP -2%Ag and PVP-3%Ag). the XRD pattern of PVP reveal that there are no directivity peaks which means the material is Amorphous, and this is a characteristic of many polymeric materials.

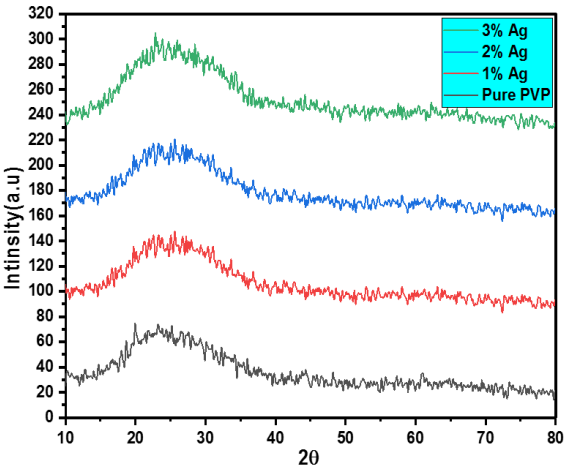

Fig. (2) X-ray diffraction at different concentrations

Examinations were conducted for the three mixtures that were prepared at different concentrations, and the results were as shown in Fig. (3). display the PVP nanofiber mat morphology that was acquired utilizing a 1µm SEM magnification. Smooth polymer nanofibers and various composite nanofibers might be produced using the electrospinning settings. SEM pictures showed that PVP (1%Ag) generated fibers containing beads. By increasing the concentration of silver (2%Ag) and (3%Ag), we will notice a significant increase in the beads. The presence of silver in the spinning solutions led to obtain nanofibers having diameter values much

lower than those of pure polymer nanofibers. This is due to the inclusion of an appropriate proportion of Ag. The observed change in the composite nanofibers' diameter values is caused by the increased solutions' conductivity when a high voltage is applied. The correlation between the solution's viscoelasticity and the composed of beads has been demonstrated [18]. Viscoelastic force enables the jet to elongate smoothly and continuously into fibers throughout the electrospinning process [19]. As the fiber moves toward the collector, it thins during the elongation process. In a low viscosity fluid, fiber thinning causes fiber break-up and bead production because polymer chain entanglement is reduced [20]. Increased incorporation of highly extensible chemicals (polymers) into the precursor solution might result in a high viscoelastic feature [18].

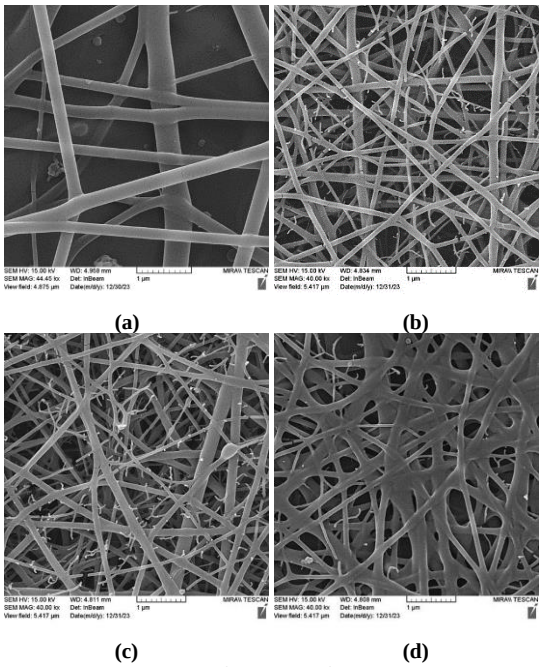

Fig. (3) FE-SEM images of PVP nanofiber mats, pure PVP and Ag-PVP at different concentrations (a) pure PVP (b) PVP+1% Ag (c) PVP+2% Ag (d) PVP+3% Ag

Figure (4) shows the PVP and Ag-PVP nanofibers' absorption, which shows that the rises with the addition of Ag. Consequently, It would make more sense to draw the conclusion that the nanocomposite exhibits significant UV visible absorption.

This kind of material has a wide range of potential applications, especially in optics, as shown by the observed increase in electromagnetic radiation absorption and broadening of the absorption spectra from 320 nm to 1100 nm wavelengths, which is attributed to the presence of silver in the polymer matrix [21]. With the use of equation (1), it is simple to determine the absorption coefficient at the frequency linked to the high absorption area from the absorbance (A) and the film thickness (t) [22]:

$$\alpha = 2.303\, A/t \qquad (1)$$

One of the most significant characteristics of the absorption spectra of crystalline and amorphous materials is the basic absorption edge. Understanding the transition from valence to conduction band is essential for calculating the material band gap. A calculation of the energy band gap (E_g) was made using equation (2) [22].

$$\alpha h\upsilon = B\,(h\upsilon - E_g)^r \qquad (2)$$

where E_g is the optical energy gap, B is a structure-dependent constant, and r is an index that describes the optical absorption process; the index values can be 1/2 depending on the kind of electronic transition that initiates the absorption [12,13]

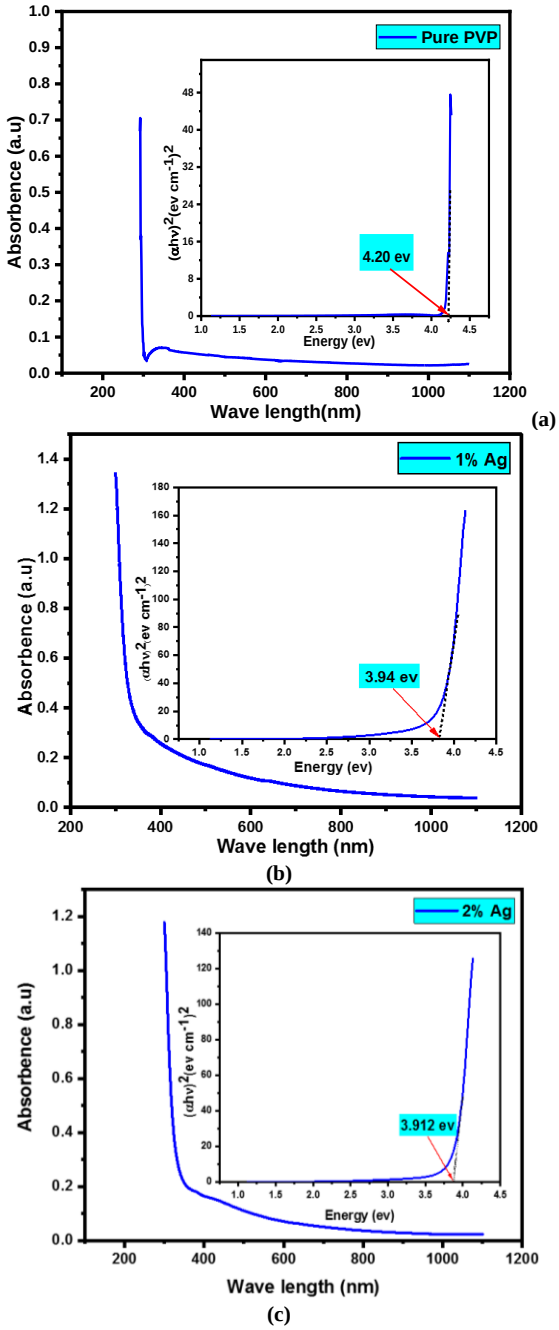

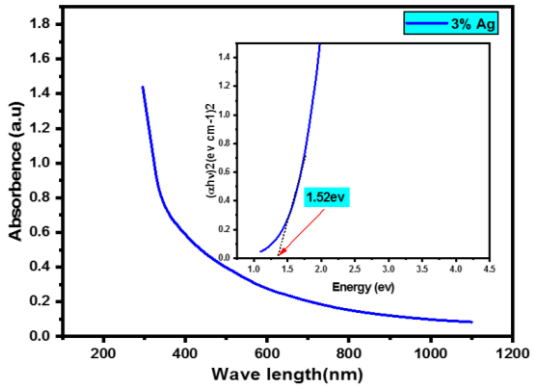

(d)

Fig. (4) Absorption spectra and the magnitude of the energy gap (a) pure PVP (b) PVP+1% Ag (c) PVP+2% Ag (d) PVP+3% Ag

The values of the absorption coefficient for each electromagnetic radiation wavelength were determined using UV-visible spectra. By use plots of $(\alpha h\nu)^2$ in the high absorbance area to project the linear sections of the plots to zero absorbance, the value of E_g is obtained.

Figure (4) displays Also the generated dependencies $(\alpha h\nu)^2$ in the radiative energy function with the x-intercept, which correspond to the energy gap width of the examined nanofibers.The energy gap of pure PVP polymer nanofibers was 4.20 eV, which is in line with earlier findings [23]. PVP-Ag composite nanofibers' direct energy gap values decreased when Ag nanoparticles were added to the polymer solution at concentrations (1%, 2%, and 3%) Ag in comparison to pure PVP nanofibers. The production of localized states (an increase in the number of traps) between the highest occupied molecular orbital and the lowest unoccupied molecular orbital energy bands may be explained.

The functional groups were identified by infrared absorption spectra (FTIR) analysis as part of the description of pure PVP nanofiber and composite Ag-PVP nanofiber generated by the electrospinning technique. From Fig. (5) the FTIR measurement explain the bonds of PVP structure where, revealed a large peak at wave number 3444 cm^{-1}, which is connected with the O-H bond, which stands for the hydroxyl group. At wave number 2935 cm^{-1}, there is an asymmetric stretching related to the C-H bond. The PVP's distinctive peaks may be seen at wave number 1665 cm^{-1}, which is associated with the stretch of the C=O (carbonyl group). As it can be seen from this figure the C=O bond affected significantly by adding Ag nanoparticles which may be due to the deformation in PVP chain, Asymmetric stretching is linked to the C-H vibration beam and happens at the peak of 1511 cm^{-1} pertains to the pure and 1414 cm^{-1} for the doping with silver. At the 1285 cm^{-1} absorption peak, there is a curvature towards the C-N vibration bond. At the absorption peaks (1014 cm^{-1} and 833 cm^{-1}), the C-C bond bends, these findings align with other studies [2,3] FTIR measurements have shown that the addition of Ag to PVP leads to a change in the intensity of the absorbing peaks of the oscillations.

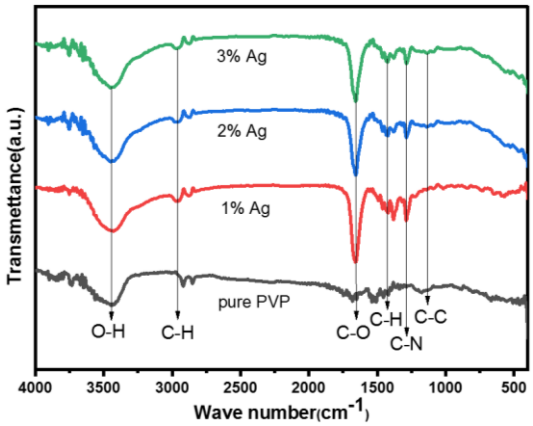

Fig. (5) Infrared spectra of pure PVP fibers and FTIR spectra of PVP-Ag

The photodetector's rapid fall times and reaction times are its most important features. Ag-PVP films were coated on an n-Si substrate at varying concentrations, and the photosensitivity of the detector was assessed for each film. In Fig. (6), the time-dependent optical currents of pure PVP organic polymer and doped with varying ratios of (1%, 2%, and 3%) Ag are displayed. Time-current properties (I-t) were measured, and two excitation wavelengths (360 nm and 465 nm) were used. from this figure, The relation was used to determine the sensitivity values of PVP that was pure and doped with silver nanoparticles. [24]:

$$S = \frac{I_{ph} - I_d}{I_d} \times 100\% \qquad (3)$$

where I_{ph} is Lighting current and I_d is darkness current

The results demonstrated high sensitivity and tracked the region close to the UV region, which is consistent with the previously mentioned optical properties that point to a high absorption in that area. It was discovered that when the doping rate increased, the photocurrent rose noticeably. The rise in current in a sample under light is measured by sensitivity (S). When a light is switched on, conductivity rises, and when the light is shut out, current returns to its initial level.

It is evident that the rise and fall timings for each state of the lights turning on and off throughout this procedure are less than twenty seconds. This process is done several times Additionally, The findings demonstrated that increasing the doping greatly increased the produced films' surface area, which in turn increased the absorption ratio and the production of charge carriers, thus improving the photodetector's sensitivity. The likelihood that the electron will be stimulated into the conduction band increases as a result. The photocurrent's pulse shape shows an improvement over the pure PVP pulse form, indicating a faster reaction to these light wavelengths. The results of the examination showed that the

concentration of 3%Ag had higher photosensitivity than the other concentrations.

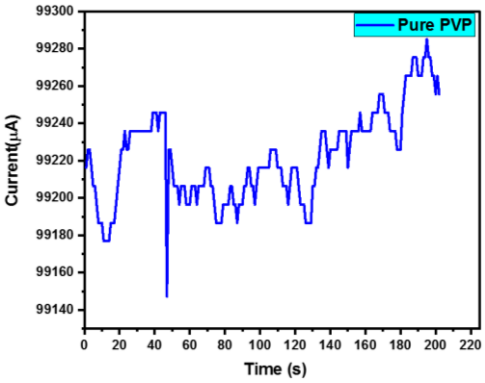

(a)

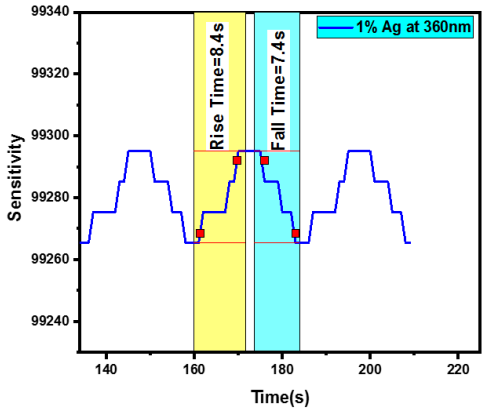

(b)

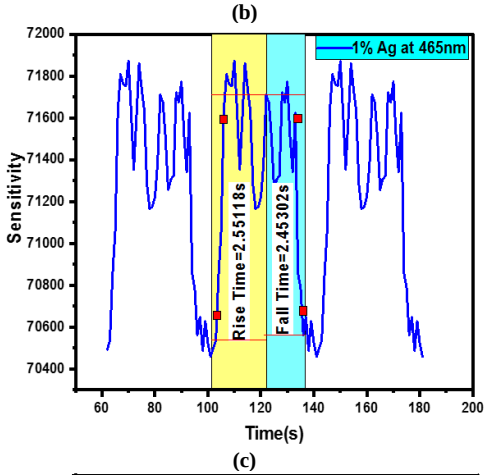

(c)

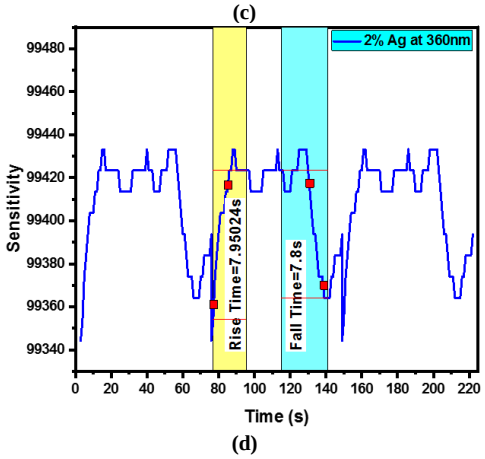

(d)

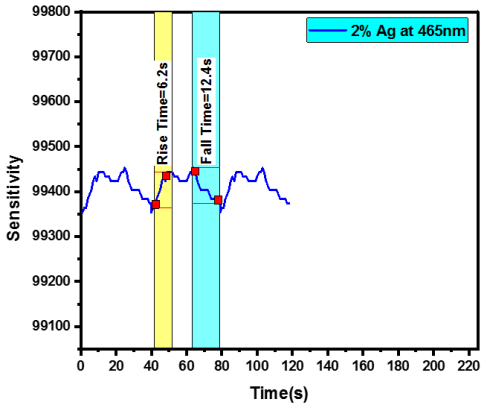

(e)

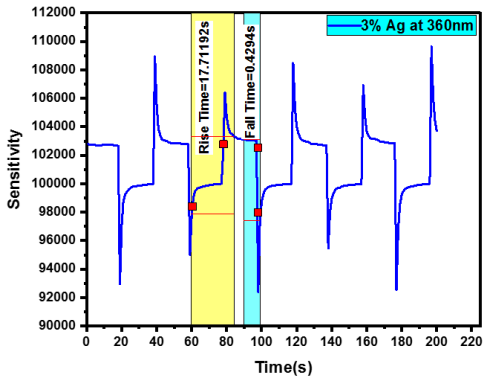

(f)

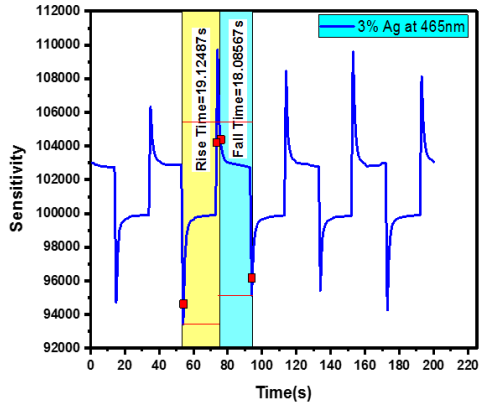

(g)

Fig. (6) Time-dependent photocurrent of the PVP and PVP-Ag (a) pure PVP (b) 1%Ag at 360nm (c) 1%Ag at 465nm (d) 2%Ag at 360nm (e) 2%Ag at 465nm (f)3%Ag at 360nm (g) 3%Ag at 465nm

5. Conclusions

In this work, PVP and Ag-PVP nanofibers were produced by electrospinning successfully. As demonstrated by the XRD results, homogenous structures, smooth surfaces, and a reduction in fiber diameter with the addition of Ag. The Ag-PVP nanocomposite exhibits an increased absorption spectrum and a shifted optical energy gap, moving from 4.20 eV to 1.52 eV, The good synthesis of UV detector was obtained, where the high sensitivity of Ag-PVP nanofiber reach to 1700% for the prepared sample at 3% Ag.

References

[1] O.G. Abdullah and S.A. Saleem, "Effect of Copper Sulfide Nanoparticles on the Optical and Electrical Behavior of Poly (vinyl alcohol) Films", *J. Electron. Mater.*, 45(11) (2016) 5910-5920.

[2] C. Virginia et al., "Electrospinning and characterization nanofibers and nanoparticle of Polyvinylpyrrolidone", *IOP Conf. Ser. Mater. Sci.*, 850(1) (2020).

[3] D. Andjani, I. Sriyanti and A. Fauzi, "Rotary Forcespun Polyvinylpyrrolidone (PVP) Fibers as a Mangosteen Pericarp Extracts Carrier", *ScieDirect.*, 170 (2017) 14-18.

[4] S.R. Mohammed et al., "Electrochemical Performance of $Co_{1-x}Mn_xFe_2O_4$ Decorated Nanofiber Polyaniline Composites", *J. Electrochem. Eng.*, 21(3) (2024).

[5] R.A. Ahmed, N.K. Hassan and I.M. Ibrahim, "The structural and figure of merit photodetector of PVP-doped with lanthanum", *Dig. J. Nanomater. Biostruct.*, 17(3) (2022) 759-770.

[6] D. Jwied, U. Nayef and F. Mutlak, "Improvement of responsivity of C:Se nanoparticles ablated on porous silicon", *Optik*, 241 (2021) 167222.

[7] A. Heilmann, **"Polymer Films with Embedded Metal Nanoparticles"**, Springer-Verlag, (2003) vol. 52.

[8] A. Slistan-Grijalva et al., "Classical theoretical characterization of the surface plasmon absorption band for silver spherical nanoparticles suspended in water and ethylene glycol", ??????, 27(1-2) (2005) 104.

[9] B.T. Raimi-Abraham, S. Mahalingam and S. Edirisinghe, "Generation of poly(N-vinylpyrrolidone) nanofibres using pressurized gyration", *Mater. Sci. Eng.*, 39 (2014) 168-176.

[10] B.H. Folttmann and A. Quadir, "Excipients in pharmaceuticals: An overview", *Drug Deliv.*, 8 (2008) 22-27.

[11] K. Halake et al., "Recent application developments of water-soluble synthetic polymers", *J. Ind. Eng. Chem.*, 20(1-6) (2014) 1843.

[12] H. Hou et al., "Poly-l-Lactide Nanofibers by Electrospinning - Influence of Solution Viscosity and Electrical Conductivity on Fiber Diameter and Fiber Morphology", *ResearchGate*, 10(35) (2003) 2429.

[13] G. Ma, D. Yang and J. Nie, "Preparation of porous ultrafine polyacrylonitrile (PAN) fibers by electrospinning", *Polym. Adv.*, 20(2) (2009) 147-150.

[14] S. Hasan, "A review on nanoparticles: their synthesis and types", *Res. J. Recent Sci.*, ??? (2015) 2502.

[15] M. Aslam, M.A. Kalyar and Z.A. Raza, "Polyvinyl alcohol: a review of research status and use of polyvinyl alcohol-based nanocomposites", *Polym. Eng. Sci.*, 58(12) (2018) 2119–2132.

[16] Z. Li and C. Wang, **"One-dimensional Nanostructures: Electrospinning Technique and Unique Nanofibers"**, Springer (2013), pp. 15-29.

[17] G.I. Taylor, "Electrically driven jets", *Proc. R. Soc.*, 313(1515) (1969) 453-475.

[18] P.P. Bhat et al., "Formation of beads-on-a-string structures during break-up of viscoelastic filaments", *Nature Phys.*, 6 (2010) 625-631.

[19] H. Fong, I. Chun and D. H. Reneker, "Beaded nanofibers formed during electrospinning", *Polymer*, 40 (1999) 4585-4592.

[20] S. Ramakrishna et al., "An Introduction to Electrospinning and Nanofibers", *World Scientific*, (2005).

[21] M. Afzali, A. Mostafavi and T. Shamspur, "Electrospun composite nanofibers of poly vinyl pyrrolidone and zinc oxide nanoparticles modified carbon paste electrode for electrochemical detection of curcumin", *Mater. Sci. Eng. C*, 68 (2016) 789–797.

[22] E.A. Davis and N.F. Mott, "Conduction in non-crystalline systems V. Conductivity, optical absorption and photoconductivity in amorphous semiconductors", *Philos. Mag.*, 22(179) (1970) 903-922.

[23] G.S. Ahmed, "Structural and Optical properties of Polymers (PVA/PVP) doped with V2O5 composites films", *Ibn Al-Haitham J. Pure Appl. Sci.*, 30(2) (2017).

[24] W. Matysiak, T. Tański and M. Zaborowska, "Manufacturing process and characterization of electrospun PVP/ZnO NPs nanofibers", *Bull. Polish Acad. Sci.*, 67(2) (2019) 193–200.

[25] S.M. Omran, E.T. Abdullah and O.A. Al-Zuhairi, "Polyvinylpyrrolidone/Multi-walled Carbon Nanotubes/Graphene Nanocomposite as Gas Sensor", *Iraqi J. Sci.*, 63(9) (2022).

[26] J.M. Lui, **"Photonic Devices"**, Cambridge University Press (2005), ISNB 0521551951.

Table (2) Absorption peaks of PVP mixed with Ag with different mixing ratios and DC voltage values using a direct current (DC) voltage (20 kV)

Samples	O-H Stretch Vibration	C-H Stretch Vibration	C=O Stretch Vibration	C- H Stretch Vibration	C-N bending Vibration	C-C bending Vibration
Pure PVP	3444	2935	1665	1511	1408	1126
1%Ag	3444	2935	1665	1414	1267	1088
2%Ag	3444	2935	1665	1414	1267	1088
3%Ag	3444	2935	1665	1414	1267	1088

Table (3) The sensitivity, response time and recovery time for PVP doped with different Ag doping ratios at high voltage (20 kV)

Sample	Sensitivity % at 360nm	Sensitivity (%) @465nm	Response Time (s) @360nm	Recovery Time (s) @360nm	Response Time (s) @465nm	Recovery Time (s) @465nm
1% Ag	8.4	2.55	8.4	7.4	2.55	2.45
2% Ag	7.95	6.2	7.95	7.8	6.2	12.4
3% Ag	17.7	19	17.7	0.42	19	18

Abdualkhalq H. Mohammed
Hanaa E. Jasim

Department of Physics,
College of Science,
Tikrit University,
Salah addin, IRAQ

Investigation into the Corrosion Behavior of Medical Grade Titanium Ti6Al4V Samples

In this study, plasma nitriding (using nitrogen gas) was utilized to treat the surface of a titanium alloy (Ti6Al4V) for varying durations (5, 10, 15, and 20 hours). The measurements revealed that nitrogen was deposited on the alloy, with the highest rate of deposition observed after a 20-hour treatment. Corrosion measurements demonstrated a substantial enhancement in the sample's corrosion resistance, with the corrosion rate for the untreated sample being 2.497×10^{-2} mm/year, gradually decreasing with longer nitriding treatment. It decreased to 1.350×10^{-4} mm/year for the sample treated for 20 hours, indicating a remarkable 184.96 fold improvement after the 20-hour treatment. Furthermore, the protection efficiency increased with the treatment duration. In the untreated sample, the protection was 0%, gradually rising to 99.45% for the sample treated for 20 hours. Additionally, the open circuit potential (OCP) shifted in the positive direction, from -0.439 V for the untreated sample to -0.050 V for the 20-hour treated sample. The results highlighted a significant improvement in the alloy's corrosion resistance after immersion in a simulated body fluid.

Keywords: Titanium; Processing period; Plasma nitriding; Corrosion rate
Received: 02 April 2024; **Revised:** 17 May 2024; **Accepted:** 23 May 2024

1. Introduction

Biomedical alloys are any synthetic material used to replace or restore the function of body tissues and are in continuous or intermittent contact with body fluids. This definition is somewhat restrictive as it excludes materials used in devices such as surgical instruments or dental tools. Typically, exposure to body fluids means that the biomaterial is placed inside the body to improve the recipient's health or save lives. However, no human-made structure is perfect. All manufactured devices have a failure rate. Additionally, all humans differ in genetics, gender, body chemistry, living environment, and levels of physical activity. Moreover, doctors implant or use these devices to varying degrees [1,2]. Studies in the field of biomaterials focus on two things:

- Developing new metallic materials with mechanical properties similar to human bone
- Surface modification techniques that enable achieving optimal biological compatibility closely linked to corrosion behavior in biological environments.

The properties of alloys used as biomaterials for bone surgery include high specific [3]. Biological material is a synthetic material used to replace a part of a living system or to work closely with living tissues. The ultimate goal of using biological materials is to improve human health by restoring the function of living tissues and organs in the body [4]. Corrosion resistance of surgically implanted alloys is one of the key properties, as metallic alloys come into contact with highly aggressive media such as body fluids due to the presence of chloride ions and proteins. In the corrosion process, the metallic components of the alloy are oxidized to their ionic forms and oxygen is reduced to hydroxide ions. The corrosion properties of alloys are greatly influenced by the thin film formed on the surface of the alloy and the presence of alloying elements. The corrosion rate can be determined from the following equation [5]

$$Corrosion\ rate(mmpy) = \frac{3.27\times10^{-3} i_{corr.(Eq.wt)}}{d} \quad (1)$$

2. Experimental Part

Samples are placed in the plasma chamber on the cathode, and the cathode is connected to a continuous power source while the room is grounded anode. As for the plasma discharge nitriding process, it is carried out under the following conditions: current of 24 mA, voltage of 600 V, distance of 4 cm, and pressure of 1.5×10^{-1} mbar. The plasma chamber is evacuated to a vacuum pressure of 1 mbar to ensure the removal of heavy gases such as hydrocarbons. Upon reaching the vacuum pressure, nitrogen gas is introduced into the chamber through the needle valve at a pressure of 1.5×10^{-1} mbar. The voltage of the continuous power source is increased until the plasma is generated, and after the specified treatment time (5 hrs), the system is turned off and left until the chamber temperature reaches room temperature. The valve at the top of the chamber is opened to equalize the pressure, samples are removed and placed in plastic containers, and the process is repeated for the remaining samples under the same conditions except the time, which changes to 20, 15, and 10 hours. After the completion of these treatment periods, it is observed that all samples have changed in color from silver to golden.

Corrosion behavior was measured using an advanced electrochemical system (model CHI 604e). Before starting the corrosion measurements, the samples were soaked for 60 min in a simulated body fluid (SBF) solution to achieve equilibrium state.

3. Results and Discussion

From Fig. (1) and table (1), it is evident that the corrosion of the samples decreased with an increase in the deposition period. The corrosion rate for the uncoated sample was 2.497×10^{-2} mmpy compared to the coated sample (h20) which was 1.350×10^{-4} mmpy. This means that the corrosion decreased by 184.962 compared to the base sample, and the corrosion rate for the other samples also decreased with an increase in the treatment period. From Fig. (2), it is evident that the open-circuit voltage of the uncoated sample (-0.439 V) has increased towards the positive direction compared to the coated sample (h20) which became -0.050 V. This means that the impedance has increased due to the increase in the thickness of the coating obtained as a result of the increase in the deposition period on the sample. Table (1) shows the open-circuit voltage of the samples. It is noted that all samples have gradually increased in impedance with the increase in the deposition period.

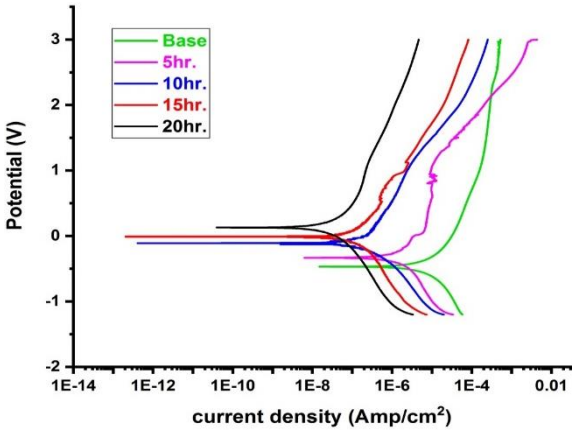

Fig. (1) Variation of potential with current density for different processing periods

Table (1) Corrosion measurements

It.	$E_{corr.}$ (V)	$I_{corr.}$ (A) x10^{-8}	Corr. Rate (mmpy) x10^{-4}	Bc	Ba	OCP (V)
Base	-0.471	286.9	249.7	0.205	0.200	-0.439
5hr	-0.331	78.44	68.27	0.212	0.254	-0.218
10hr	-0.113	18.22	15.85	0.150	0.161	-0.111
15hr	-0.004	6.612	5.754	0.232	0.252	-0.087
20hr	0.125	1.552	1.350	0.200	0.198	-0.050

The protection efficiency can be calculated from the following equation [6]

$$PE\% = \frac{I^{\circ}corr - I^{c}corr}{I^{\circ}corr} \times 100 \qquad (2)$$

From table (2), we notice that the calculated protection efficiency from Eq. (2) has increased with the increase in processing time, where for the coated sample for 20 hours it was 99.45%, which means that the coating for 20 hours has served the purpose by providing high protection for the sample.

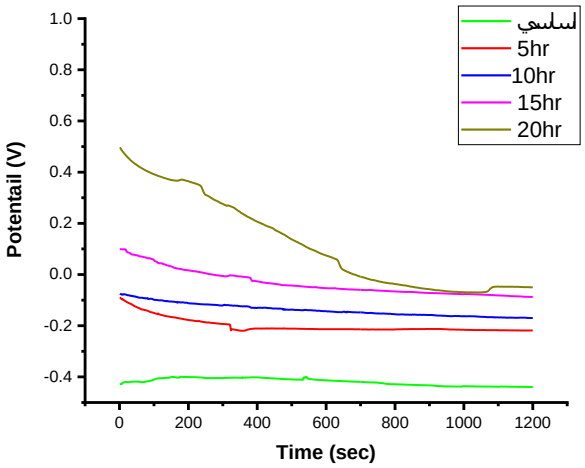

Fig. (2) Variation of potential with time for the uncoated sample

Table (2) protection efficiency

Processing period (h)	Protection efficiency (%)
Base	0
5	72.91
10	93.7
15	97.71
20	99.45

Resistance of Polarization can be calculated from the following equation [7]

$$R_P = \frac{\beta_a \beta_c}{2.303 I^{\circ}_{corr}(\beta_a + \beta_c)} \qquad (3)$$

Table (3) Resistance of Polarization

Processing period (h)	Resistance of Polarization (kΩ)
Base	15.321
5	63.966
10	1334.5
15	27852.998
20	2783.725

4. Conclusion

The electrochemical analysis of the (Ti6Al4V) alloy soaked in a simulated body fluid (SBF) reveals that the alloy maintains its oxidized state for over a minute under different treatments. Altering the chemical composition in the layer significantly enhances the corrosion resistance of the samples. Specifically, the sample treated for 20 hours displays exceptional corrosion resistance attributed to the elimination of selective corrosion observed in earlier treatment stages. These findings highlight the potential for developing a high-spec medical alloy suitable for bone grafting and enhancement by researchers.

References

[1] B.D. Ratner, **"Biomaterial science"**, 2nd ed., Elsevier (2004).

[2] M.E. Engelbrecht et al., "Functional performance and machinability of titanium alloys for medical implants: a review", SAIIE 25 Proc. Stellenbosch, South Africa (11 July 2013).

[3] Y.M. Salman, "A study of electrophoretic deposition of alumina and hydroxyapatite on tapered Ti-6Al-7Nb dental implants: mechanical and histological evaluation", PhD thesis, University of Baghdad (2011).
[4] N. Patel and P. Gohil, "A review on biomaterials: scope, applications & human anatomy significance", *Int. J. Emerg. Technol. Adv. Eng.*, 2(4) (2012) 91-101.
[5] J. Park and R.S. Lakes, **"Biomaterials"**, Springer Science & Business Media (2007), pp. 1-3.
[6] S.M. Yılmaz and G. Atun, "Corrosion protection efficiency of the electrochemically synthesized polypyrrole-azo dye composite coating on stainless steel", *Prog. Org. Coat.*, 169 (2022) 106942.
[7] M. Kouřil, P. Novak and M. Bojko, "Limitations of the linear polarization method to determine stainless steel corrosion rate in concrete environment", *Cement Concr. Comp.*, 28(3) (2006) 220-225.

Murad M. Kadhim
Qusay A. Abbas

Department of Physics, College of Science, University of Baghdad, Baghdad, IRAQ

Plasma Instability Effect in Magnetron Sputtering Discharges Using Bohm Diffusion Analysis

In this paper, we address the issue of plasma instability and its effect on Bohm diffusion, the key factor determining the particle flow in plasma and focusing on the Langmuir probe diagnostics. More precisely, we utilize Langmuir probe measurements to study the influence of two plasma instabilities, specifically, turbulence and orbital ionization fluctuations. With the help of these two experiments, we find and analyze complex relationships between instability and Bohm diffusion, demonstrating how these two factors interact. The study's findings obtained, help to understand that in the plasma instability and plasma parameters are changing and thus, the mobility of charge carriers is unstable and, as a result, the Bohm diffusion process is changing. Langmuir probe diagnostics makes it possible to turn into practically valuable information about the behavior of plasma systems, which in turn can be used to manage and optimize plasma technologies.

Keywords: Magnetron Sputtering; Langmuir probe; Bohm diffusion; Plasma Turbulence
Received: 09 April 2024; **Revised:** 15 May 2024; **Accepted:** 22 May 2024

1. Introduction

A magnetron sputtering device is a type of physical vapor deposition (PVD) tool used in thin film deposition processes [1,2]. Plasma instability arises when there are gradients or variations in the plasma parameters (e.g., density, temperature, magnetic field) along the direction of a particle's drift [3-5]. These gradients can create a situation where particles experience different forces as they drift, leading to a net accumulation of particles in certain regions. This particle accumulation can disrupt the equilibrium of the plasma, leading to the development of instability [6-10]. The I-V characteristics of a probe typically refer to the relationship between the current (I) passing through the probe and the voltage (V) applied across it, as presented in Fig. (1). Electron retardation region is characterized by a gradual increase in current with voltage. For Maxwellian distribution, the electron current is given by:

$$I_e = I_{es}\, exp\left[\frac{e(V_B - V_p)}{k_B T_e}\right] \qquad (1)$$

By taking ln of Eq. (1), one can get:

$$\frac{d \ln I_e}{dV} = \frac{e}{k_B T_e} \qquad (2)$$

Equation (2) above demonstrates that the slope of the curve for (lnI_e-V) is precisely 1/T_e(eV), which serves as an accurate indicator of the electron temperature [5], where I_e, I_{es}, e, V_B, V_p, k_B, and T_e are electron current, electron saturation current, electron charge, bias voltage, plasma potential, Boltzmann constant, and electron temperature, respectively

Thus, the electron density (n_e) is determined as:

$$n_e = \frac{4 I_{es}}{e\, A_p}\sqrt{\frac{\pi m_e}{8 k_B T_e}} \qquad (3)$$

where A_p and m_e, are probe surface area and electron mass, respectively

Plasma instabilities, for example, electron density fluctuations, temperature oscillations, or electric field dynamics, also have a considerable influence on Bohm diffusion in planar magnetron sputtering systems [11-17]. Bohm diffusion is the diffusion of plasma across a magnetic field with a diffusion coefficient equal to:

$$D_{Bohm} = \frac{1}{16}\frac{k_B T}{eB} \qquad (4)$$

where B is the magnetic field strength, and T is the temperature

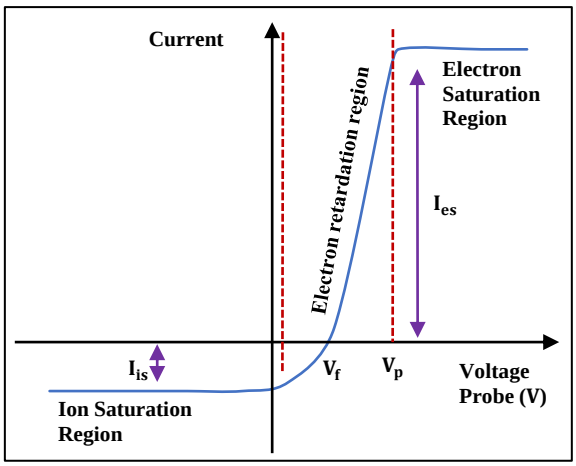

Fig. (1) Typical current-voltage characteristics of Langmuir probe in plasma

Particle flux (Γ) per unit area per unit time is equal to the product of particle density (n) and the mean velocity of the particles (<v>). The diffusion coefficient (D) which is related to particle flux caused by a density gradient (∇n), defined throughout [18,22]:

$$\Gamma = n < v > = n\frac{E}{B} = -D\,\nabla n \qquad (5)$$

This equation is called Fick's law.

Plasma turbulence refers to the chaotic, irregular behavior observed in plasmas, which are ionized

gases consisting of positively charged ions and negatively charged electrons. In this work, we will apply the concept of modified Bohm diffusion on two cases [23-26]: Strong turbulence, the diffusion coefficient (D_{st}) can be calculated from:

$$D_{st} = \frac{\gamma}{K_{\perp}^2} \quad (6)$$

The instability factor (C_{st}) will become equal to:

$$C_{st} = \frac{\gamma}{K_{\perp}^2} \frac{eB}{k_B T} \quad (7)$$

Weak turbulence, the diffusion coefficient (D_{wt}) can be calculated from:

$$D_{wt} = \frac{\gamma^2}{\omega K_{\perp}^2} \quad (8)$$

The instability factor (C_{wt}) will become equal to:

$$C_{wt} = \frac{\gamma^2}{\omega K_{\perp}^2} \frac{eB}{k_B T} \quad (9)$$

2. Experimental Part

The vacuum chamber, DC power supply, magnetic field settings, and Langmuir probe design were all included in the design of the planar magnetron sputtering apparatus used in this study. A schematic of the system is shown in Fig. (2). A 37cm long by 30cm diameter cylindrical piece of Pyrex glass is used to build the vacuum chamber. Two miniature pipes were joined at the mid-top and bottom of the vessel. One of these conduits was connected to the pumping mechanisms, while the other was utilized for the delivery of Argon gas. The two planar electrodes are constructed from aluminum and have an inner diameter of 6cm and an inner length of 3cm. Both electrodes are secured with Teflon to ensure no contact with the chamber walls, and the separation between the two electrodes is 10cm. The diagram of this chamber is presented in Fig. (2). This work involves the creation of a set of cylindrical probes that are used to research the plasma properties along the cathode in accordance with the single probe configuration. This group is made up of tungsten wires with a 0.3 mm diameter that are all coated in sleeve wire to provide insulation, with the exception of a brief exposed tip length. The tip has a length of 3 mm. These probes are inserted into a 4 mm diameter glass tube.

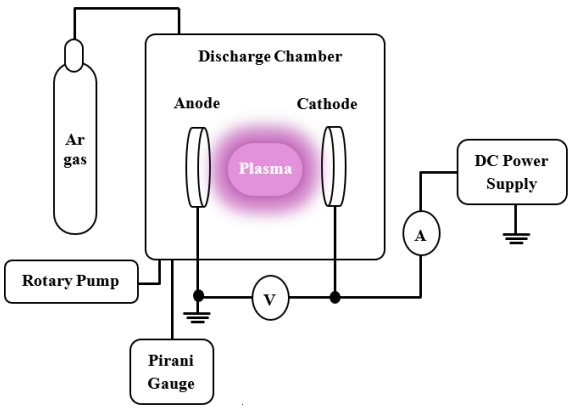

Fig. (2) Schematic of the DC planar magnetron sputtering system

3. Results and Discussion

The slope of the probe characteristics' lnI_e-V curve was used to compute the electron temperature, according to Eq. (2). The effect of gas pressure on the behavior of electron temperature at different places is seen in Fig. (3). In all radial places (cathode diameter), the results showed a decrease in electron temperature as the gas pressure rose from 0.04 to 0.4 Torr. This behavior might be brought on by a change in gas pressure, which would alter the gas discharge. Moreover, since electron energy is transferred to the gas atoms by inelastic collisions, the electron temperature decreases as the gas pressure rises. As a result, the temperature of the gas increases while the temperature of the electrons and their average kinetic energy fall. Important information about the properties of the plasma, including the electron number density, may be gleaned by examining the relationship between the applied voltage and the measured current.

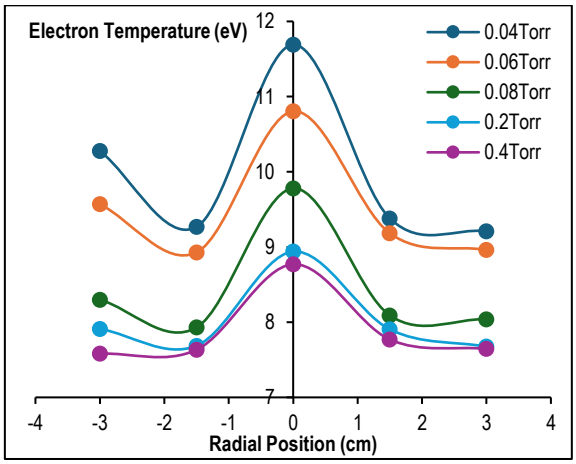

Fig. (3) Variation of electron temperature in plasma with different gas pressures at the cathode diameter (radial position)

Equation (3) may be used to calculate the electron number density. The effect of gas pressure on electron density at different sites is seen in Fig. (4). It is evident that when the gas pressure increases in all radial places (cathode diameter), the electron density increases. This is due to the fact that higher electron gas pressure causes more inelastic collisions between electrons and Ar atoms, which raise electron number density. Drift velocity can be calculated by using Eq. (5). The effect of gas pressure on the drift velocity at different places is shown in Fig. (5). According to the statistics, the drift velocity decreased as gas pressure rose in all radial locations. The mean free path of ions in the plasma is determined by gas pressure, which explains this pattern. Due to the increased likelihood of ions colliding with gas particles over shorter distances, the mean free path reduces with higher pressures. As a consequence of the decreased travel lengths between impacts, the drift velocity of ions may decrease with increased pressure. Furthermore, the drift velocity radial profile showed that the drift

velocity value rises toward the cathode ends and decreases in the center of the cathode. This trend is explained by the distribution of the magnetic field, which is greatest in the center and decreases toward the cathode ends.

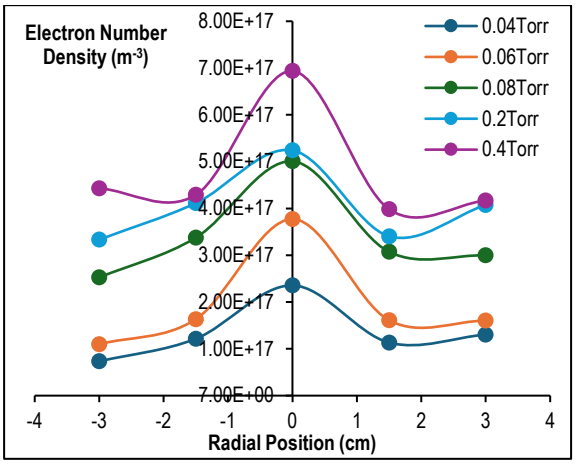

Fig. (4) Variation of electron number density in plasma with different gas pressures at the electrode diameter (radial position)

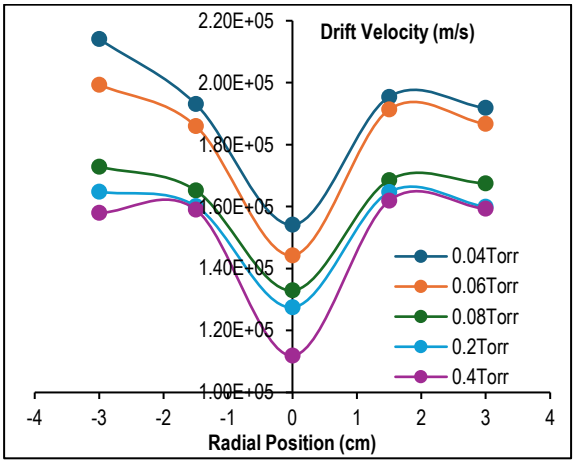

Fig. (5) Demonstrates drift velocity versus radial position

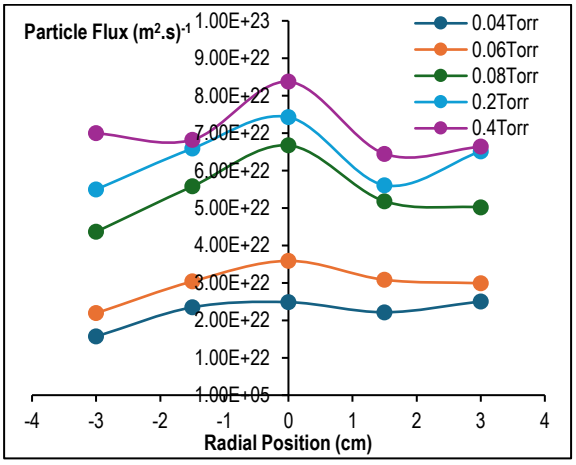

Fig. (6) The particle flux of drift wave instability as a function of radial position

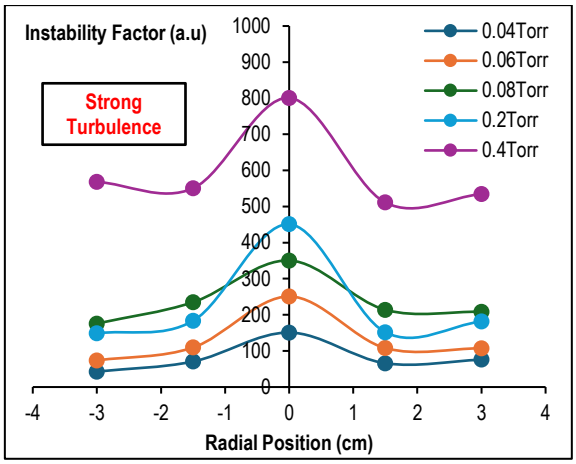

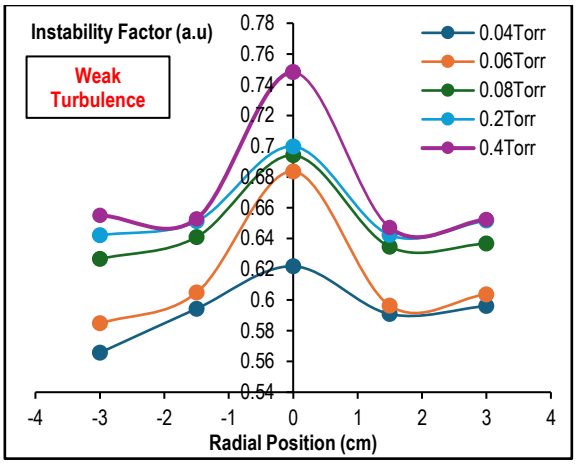

Fig. (7) The variation of instability factor (C-factor) with radial position

Equation (5) may be used to compute particle flux. The effect of gas pressure on the behavior of particle flux at different places is shown in Fig. (8). In every cases under investigation, it is possible to see that particle flow increases as gas pressure rises (radial positions). This indicates that there is a general relationship between greater gas pressure and higher rates of particle collisions in the plasma. The particles disperse more evenly in the radial direction as a result of the enhanced diffusion processes brought about by the higher collision frequency. However, by using equations (7) and (9), we are able to calculate the experimental values of strong turbulence instability factor (C_{st}) and weak turbulence instability factor (C_{wt}) as a function of radial position and plotted in Fig. (7). It is clear from this figure; the instability factor increases with increases of gas pressure in all-radial positions (with a higher rate in the strong turbulence compares with weak turbulence). This means that, gas pressure affects the plasma density profile. As well as, the stability factor has high values in the stable region (near from center of plasma column) and has small values in the unstable region, i.e., the instability factor has indirect proportional plasma density (because of the instability factor has similar behaviour to the plasma density).

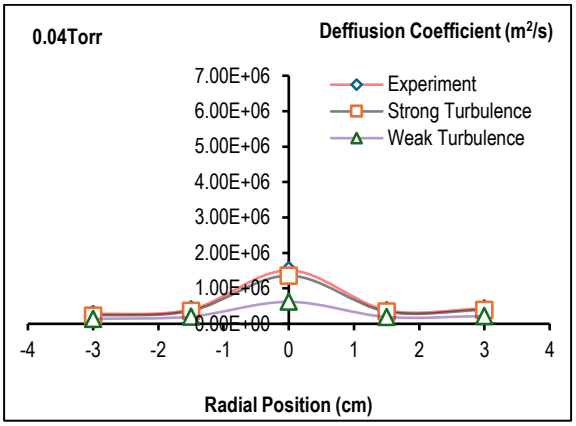

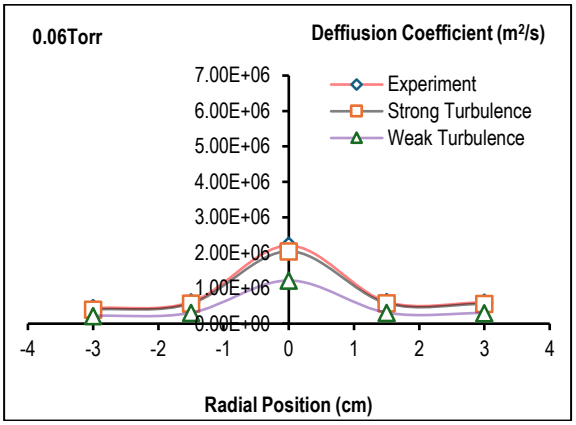

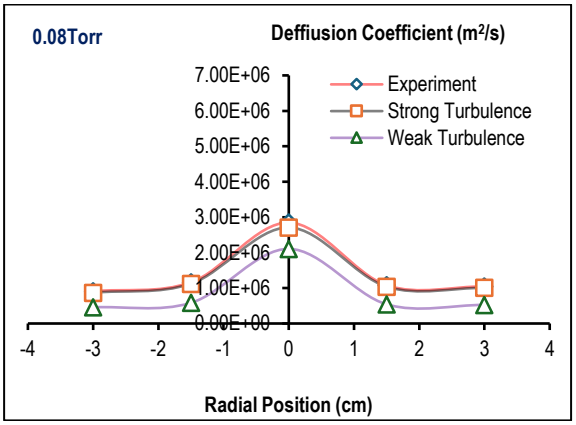

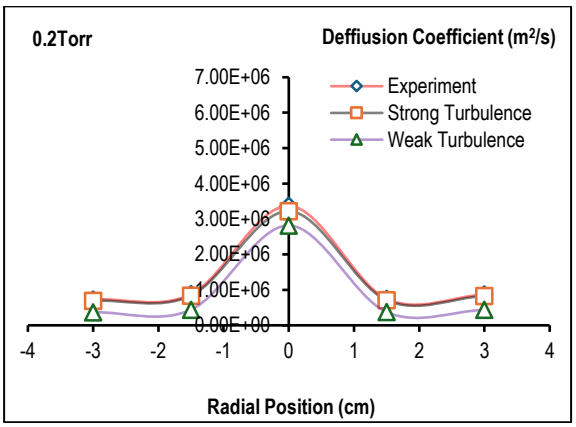

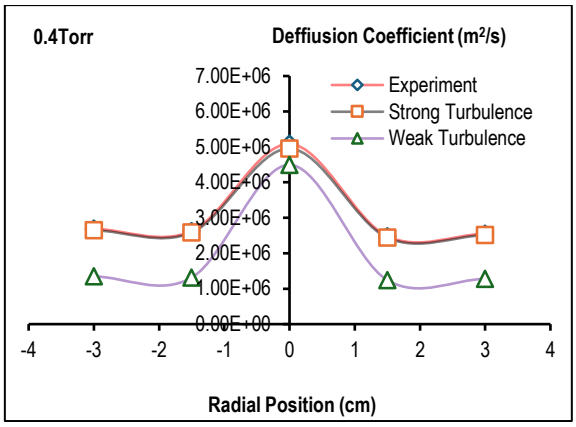

Fig. (8) The variation of diffusion coefficient with radial position

In Fig. (8), we have plotted the experimental values of D_{exp} (using Eq. 4), D_{st} (using Eq. 6), and D_{wt} (using Eq. 8) as a function of radial position. In addition to the fitting which is shown between D_{exp} and D_{wt}, we pointed out too, the D_{st} was approach from D_{exp} in the region near from center and edge of plasma. One can observe that the diffusion coefficient increasing with the increase of gas pressure in the all-radial positions (cathode diameter). This behavior can be explained as; Gas pressure affects the collisional of the plasma. At higher pressures, collisions between particles are more frequent, leading to enhanced particle diffusion. Radial position in the plasma can drastically affect the conduct of go with the flow waves and, therefore, the diffusion coefficient.

4. Conclusion

In this work, the effect of instability on Bohm diffusion has been demonstrated. The current findings show that, at all radial places (cathode diameter), the electron temperature declined as gas pressure increased from 0.04 to 0.4 Torr, whereas the electron number density increased as gas pressure increased. Furthermore, when gas pressure rises in all radial locations, the instability factor and diffusion coefficient both rise (with a higher rate in the strong turbulence compares with weak turbulence). The modified Bohm diffusion equation's instability factor and diffusion coefficient agree better with the unstable region than with the stable region, where the Bohm diffusion model's description of enhanced particle diffusion is influenced by instabilities in plasma behavior.

References

[1] P.J. Kelly and R.D. Arnell, "Magnetron sputtering: a review of recent developments and applications", *Vacuum*, 56(3) (2000) 159-172.

[2] F.F. Chen, "Langmuir Probe Diagnostics", University of California, Los Angeles, (2003).

[3] F.F. Chen, "Use of Electrostatic Probes in Plasma Physics", Plasma Physics Laboratory, Princeton University, Princeton, 4(2) (1961) 150-154.

[4] R.H. Huddleston and S.L. Leonard, **"Plasma Diagnostic Techniques"**, Academic Press, Inc. (NY, (1965).
[5] R.L. Merlino, "Understanding Langmuir Probe Current-Voltage Characteristics", University of Iowa, Iowa City, Iowa, 75(12) (2007) 1078-1085.
[6] M.M. Kadhim and Q.A. Abbas, "The Influence of the Magnetic Field on the Plasma Characteristics in Hollow Electrodes Discharge System", *Iraqi J. Sci.*, 63(10) (2022) 4254-4266.
[7] A.K. Bard and Q.A. Abbas, "Influence of cylindrical electrode configuration on plasma parameters in a sputtering system", *Iraqi J. Sci.*, 63(8) (2022) 3412-3423.
[8] Z.M. Hasan and Q.A. Abbas, "Influence of AC Frequency on Hollow Magnetron Sputtering Discharge Parameters", *Iraqi J. Phys.*, 22(1) (2024) 31-41.
[9] K.A. Aadim, "Control the deposition uniformity using ring cathode by DC discharge technique," *Iraqi J. Phys.*, 15(32) (2017) 57–67.
[10] Q.A. Abbas and R.T. Ahmed, "Diagnostics of dusty plasma properties in planar magnetron sputtering device", *Iraqi J. Phys.*, 13(26) (2015) 64-75.
[11] F.F. Chen, **"Introduction to plasma physics and controlled fusion"**, Plenum Press (NY, 1984).
[12] K. Lee, "Analysis of Bohm diffusions based on the ion-neutral collisions", *IEEE Trans. Plasma Sci.*, 43(2) (2014) 494-500.
[13] L. Spitzer Jr., "Particle diffusion across a magnetic field", *Phys. Fluids*, (1960).
[14] B.J. Eastlund, "Diffusion Measurements in a Fully Ionized Cesium Plasma", *Phys. Fluids*, 9(3) (1966) 594-602.
[15] P. Saikia, B. Kakati and B.K. Saikia, "Study on the effect of target on plasma parameters of magnetron sputtering discharge plasma", *Phys. Plasmas*, 20(10) (2013) 1-9.
[16] H.V. Boening, **"Plasma Science and Technology"**, Cornell University Press (UK, 1982).
[17] H. Kakati et al., "Sheath and potential characteristics in rf magnetron sputtering plasma", *J. Appl. Phys.*, 100(8) (2006).
[18] H.W. Hendel and T.K. Chu, "Collisional Drift Instabilities", *Meth. Exp. Phys.*, 9(9) (1971) 345-394.
[19] H.A. Aebischer and Y.S. Sayasov, "Drift waves and magnetic field oscillations in cylindrical plasmas", *J. Plasma Phys.*, 40(2) (1988) 319-336.
[20] M. Porkolabm and G.S. Kino, "Turbulent Diffusion Experiments in a Thermal Plasma", *Phys. Fluids*, 11(2) (1968) 346-353.
[21] A. Hecimovic and A. Keudell, "Spokes in high power impulse magnetron sputtering plasmas", *J. Phys. D: Appl. Phys.*, 51(45) (2018) 1-32.
[22] V.N. Tsytovich, **"Theory of turbulent plasma",** Consultants Bureau (NY, 1977).
[23] F.F. Chen, "Resistive Overstabilities and Anomalous Diffusion", *Phys. Fluids*, 8(5) (1965) 912-919.
[24] M.I. Sanduk, A.M. Al-Janabi and T.A. Shemala, "Bohm diffusion equation in quadrupole", *Indian J. Phys*., 73(3), (1999) 509-514.
[25] B. Fischer and M. Kramer, "Experimental study of drift wave turbulence and anomalous transport", *Plasma Phys. Control. Fusion*, 31(3) (1989) 453-470.
[26] O.A. Hamadi, "The Fundamentals of Plasma-Assisted CVD Technique Employed in Thin Films Production", *Iraqi J. Appl. Phys. Lett.*, 1(2) (2008) 3-8.

Bashar M. Salih
Asmiet Ramizy

Department of Physics, College of Science, University of Anbar, Anbar, IRAQ

Experimental and Simulation Investigation of AlGaN/CdS/p-Si Solar Cell Performance

In this study, a layer of CdS was deposited on a silicon substrate using vacuum deposition system, and a layer of AlGaN was deposited on a silicon substrate (30% AlN with 70% GaN) by using a pulsed-laser deposition (PLD) technique. The electrical properties of the prepared films of AlGaN and CdS were studied. The results of the photoluminescence test showed a bandgap of 2.62 eV for AlGaN film and 3.62 eV for CdS film. The measurement results (Hall effect) showed that composite films of AlGaN and CdS are of type N; the electrical conductivity values are 0.043 $(\Omega.cm)^{-1}$ and 0.127 $(\Omega.cm)^{-1}$ for AlGaN and CdS films, respectively, and the carrier density values are $-3.97x10^{15}$ cm^{-3} and $-1.59x10^{15}$ cm^{-3} for AlGaN and CdS films, respectively. The results of the experimental study in the computer simulation were used to study the effect of the thickness of $Al_{0.3}Ga_{0.7}N$ layer on the performance of solar cell $Al_{0.3}Ga_{0.7}N$/CdS/P-Si. The results of the simulation showed the increase of $Al_{0.3}Ga_{0.7}N$ thickness has a reverse effect on the efficiency of the solar cell, and the efficiency decreased from 2.69% at 0.1 µm thickness to 1.69 µm at 5 µm thickness due to the increased blocking of the solar spectrum by this layer from the main layer of absorption, the silicon, which led to a decreased contribution to the generation of the electron gap pair.

Keywords: Solar Cells; AlGaN; Aluminium nitrite; Gallium nitride; SCAPS; Simulation
Received: 01 May 2024; **Revised:** 03 June 2024; **Accepted:** 10 June 2024

1. Introduction

Semiconductors receive the most attention in the field of electronic industries from researchers, semiconductor materials are often subject to studies that aim to improve their electrical and optical properties, and most studies focus on the use of nanotechnology to control the properties of semiconductor materials. In addition to nanotechnology, another way can be used to control the electrical and optical properties, namely, mixing the semiconductor materials together in specific ratios to make semiconductor alloys with unique properties.

Group III nitride is considered a promising material in electronic optical appliances. GaN is considered the most popular material after silicon in making semiconductor materials and has a direct bandgap of 3.4 eV. Its electron mobility may be compared with silicon, but its bandgap is three times larger than that of silicon; hence, it is an excellent choice for high-power applications [1].

Aluminium nitride (AIN), a member of group III-N, is also widely used in many engineering and optical applications because of its wide direct transmission bandgap (6.2 V) and stability in high temperatures [2-4].

AlGaN alloy of unique properties is produced through mixing a precise amount of AIN with GaN to control the energy gap. Photovoltaic detectors that consist of AlxGa(1-x)N (where x determines the substituted part of aluminium) are important due to their resistance to temperature and radiation changes [5]. These alloys are used in making solar cells, where the ultraviolet part from solar spectrum can be used to increase the efficiency of solar cells. These materials are also characterised by adjustable absorbing edge [6,7]. When the Al ratio in the alloy is changed from 0 to 100, the band edge moves from 365 nm (3.4 eV) to 200 nm (6.15 eV) [8,9], which makes the appliance either transparent or opaque to the sun.

In this project, a formation of AlGaN was made according to the equation of energy gap provided by Bougrov et al. [10].

$$E_g^{Al_xGa_{(1-x)}N}(x) = E_g^{GaN}(1-x) + E_g^{AlN}x - bx(1-x) \quad (1)$$

Equation (1) consists of a linear part (Vegard's law) and a nonlinear part containing the factor b, where b is the direct gap bowing parameter. Eg^{GaN} and Eg^{AlN} are 3.45 and 6.13 eV at room temperature, respectively. In Fig. 3, the alloy band gap is shown as a function of the chemical composition. The downward bowing is evident and can be fitted with b=1.3 eV. The experimental error is estimated to be ±0.2 eV [11].

1.1. I–V Curve

To study curve I -V of prepared AlGaN films, metal electrodes being deposited on AlGaN films to obtain ohmic contact, also the measures of the I – V Curve being used to determine the transmission mechanism and electrical parameters of the sample, such as Ideality Factor (n), Barrier Height (Φ_B), Series Resistance (R) and Electron Affinity as follows. The equation describe the diode current:

$$I = I_s \exp[\frac{q(V-IR)}{nk_BT}] \quad (2)$$

where q is the electronic charge, V the voltage applied across the diode, k_B the Boltzmann constant, T the absolute temperature in K, and I_s is the saturation current derived from the straight-line intercept of ln$I$ at zero bias voltage. This equation can be rewritten in terms of current density:

$V = R\,A_{eff}\,J + n\,\Phi_B + (n/\beta)\ln(J/A^*\,T^2)$ (3)

where A_{eff} is the effective area of the diode, A^* is the effective Richardson constant that depends on the effective mass of carriers (120 A/cm^2.K^2 for free electron) [15,16]

Differentiating Eq. (3) with respect to J and rearranging terms, we obtain The relation between d(*V*)/d(ln*J*) with J as:

$$\frac{dV}{d(ln\,J)} = R\,A_{eff}J + \frac{n}{\beta} \quad (4)$$

This relation was employed to determine the ideality factor (*n*) from its y-intersection (where $\beta=q/k_BT$=38.63 C/J), while series resistance calculated from its slope, as shown in Fig. (5).

Another function of $H=V-(n/\beta)\ln(J/A^*T^2)$ was employed to determine the Φ_B according the relation

$$H = R\,A_{eff}\,J + n\,\Phi_B \quad (5)$$

So, Φ_B is determined from the liner relation between *H* and *J* from y-intersection. Electron affinity (χ) is calculated from the relation [17]:

$$\chi = (\Phi_M - \Phi_B) \quad (6)$$

where Φ_M represents the metal work function

1.2. SCAPS – 1D

SCAPS is a 1D solar cell capacitance simulation programme developed by Alex Niemegeers et al. to simulate the electrical properties of thin-film solar cells and heterojunction by solving the equations of essential semiconductors devices at equilibrium [18].

SCAPS solves the basic semiconductor equations, namely, the Poisson's equations for electrons and holes (1); the equations of continuity for electrons and holes (2) and the carrier transport equations for electrons and holes (3) to obtain the J-V performance of each simulated solar cell architecture [19].

Poisson's Equations:

$$\frac{d^2\varphi(x)}{dx^2} = \frac{e}{\varepsilon_0\varepsilon_r}\left[p(x) + n(x) + N_D^+ - N_A^- + \rho_p + \rho_n\right] \quad (7)$$

where φ, e, ε_0, ε_r, N_D^+, N_A^-, ρ_p, and ρ_n are the electrostatic potential, electrical charge, vacuum permittivity, relative permittivity, charged impurities of donor, charged impurities of acceptor, hole distribution and electron distribution, respectively

Continuity Equations:

$$J_n(x) = D_n\frac{dn}{dx} = \mu_n n\,d\emptyset/dx \quad (8)$$

$$J_p(x) = D_p\frac{dp}{dx} = \mu_p p\,d\emptyset/dx \quad (9)$$

Where J_n and J_p are the electron and hole current densities, respectively, μ_p and μ_n are the probability of the electron and gap moving through the cell, respectively [19]

Carrier Transport Equations

Semiconductor devices have two types of key transport mechanisms: drift and diffusion. This movement of charge carriers generates a current in the device. The density of total electron current J_n in drift and diffusion is expressed as follows [19]:

$J_n = J_{n,drift} + J_{n,diff}$

$$J_n = q(n\mu_n E + D_n\frac{dn}{dx}) \quad (10)$$

and same applies to holes:

$J_p = J_{p,drift} + J_{p,diff}$

$$J_p = q(p\mu_p E - D_p\frac{dn}{dx}) \quad (11)$$

2. Experimental Part

First Layer of CdS: Films of CdS were deposited by using a PVD system B on a substrate of p-type silicon and quartz, where a coating unit was used under high pressure of around 10^{-6} mbar. Thermal evaporation was performed by resistant heating using high-current energy sources, and the metal mass needed for evaporation was calculated to achieve the required thickness by using the following equation:

$$m = \rho_m t\,2\pi\,d^2 \quad (12)$$

where ρ_m is the mass density, *t* is the desired film thickness and *d* is the hight of the substrates above the evaporation boat

A thin film was obtained from nano CdS with a thickness of 100nm. Figure (1) illustrates the microscopic examination of the atomic force and cross-section inspection of the prepared films of CdS.

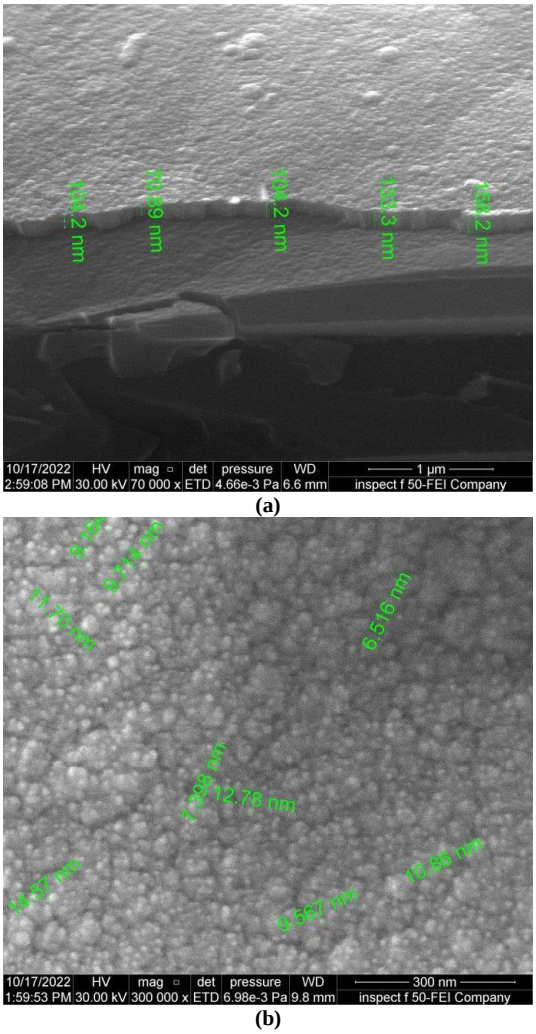

Fig. (1) FESEM morphological image of CDS film (a) Surface morphology (b) Cross-sectional view

Second Layer of AlGaN: Thin film of AlGaN was prepared by using pulsed-laser deposition (PLD)

technique. GaN and AlN target were prepared from 0.9g of AlN powder with a purity of 99.99% and 2.1g of GaN powder with purity of 99.99% were supplied from Sigma-Aldrich company. The main parameters of laser were selected as follows:

Nd:YAG laser (HuafeiTongda Technology-Diamond-288 pattern EPLS), wavelength of 532 nm, pulse duration of 10 ns, repetition frequency of 6 Hz and power supply of 220 V.

AlGaN was deposited on p-type silicon and quartz substrates. Film deposition was performed inside a 0.1 Torr evacuated vacuum chamber that contained the substrate holders and target. Laser beam with energy of 180 mJ was focused on the $Al_xGa_{(1-x)}N$ target. The sample was prepared using 300 laser pulses and a mixture of 30% AlN and 70% GaN. Figure (2) illustrates the microscopic examination of the atomic force and cross-section inspection of the prepared films of AlGaN.

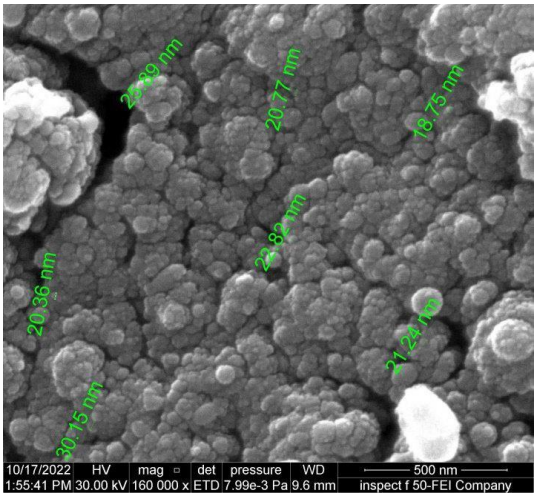

(a)

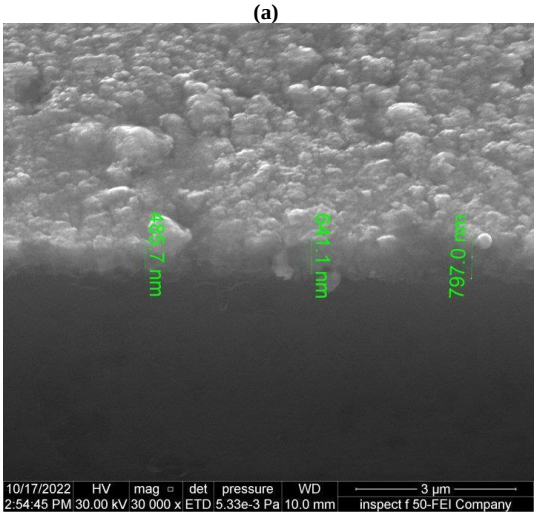

(b)

Fig. (2) FESEM morphological images of AlGaN (a) Surface morphology (b) Cross-sectional view

3. Results and Discussion

Photoluminescence (PL) spectrum was recorded for the prepared films, and a bandgap of 2.62 eV of CdS film was obtained, as shown in Fig. (3). Such increase in the bandgap from the common value (2.24eV) is attributed to the quantum confinement of energy levels for materials at nanoscale [20].

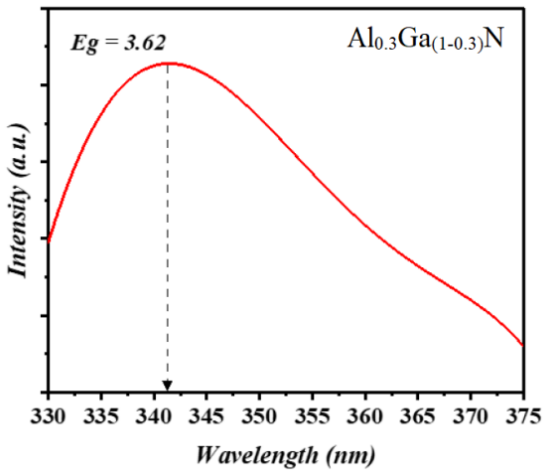

Fig. (3) PL emission spectrum of the $Al_{0.3}Ga_{0.7}N$ sample

The results for AlGaN film showed a bandgap value of 3.62 eV, and this value was determined through the ratios of each AlN and GaN in the film, as shown in Fig. (4).

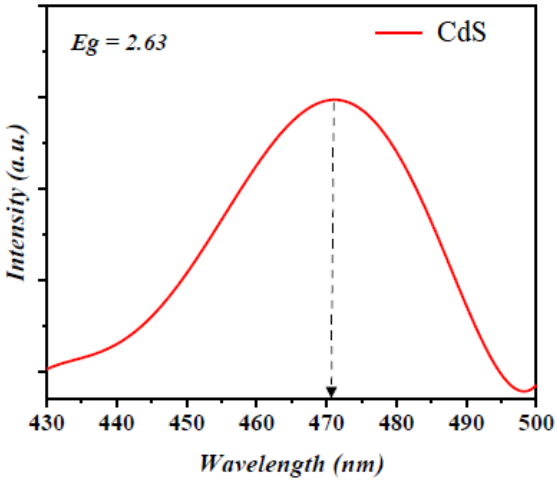

Fig. (4): PL emission spectrum of the CdS sample

The Hall effect on the prepared films was tested to study the electrical properties of AlGaN. The results of the Hall effect measure showed that AlGaN composite films are of n-type, which corresponds to the data reported [21]. Moreover, the test results reflected conductive values and density of prepared films carriers, as shown in table (1).

To study the I-V curve of the prepared AlGaN films, Au electrodes were deposited on AlGaN films by using PVD system to obtain a diode. The measures of the I-V curve were used to determine the transmission mechanism and electrical parameters of the sample, such as ideality factor, barrier height, resistance and electron affinity of diode through equations (2–6) and Fig. (5a).

Figure (5b) demonstrates the semilogarithmic relationship of forward bias properties of I–V of heterogeneous connection structure, which indicates that the current increases greatly for applied voltage of less than 1.1V. This exponential behaviour in low-voltage area may lead to compose depletion zone between metal and AlGaN [2]. In Fig. (5b), the Schottky barrier disappears when applied voltage is higher than 1.1V. Saturation current values, ideality factor, barrier height and electron affinity were calculated are shown in table (2). Value n equals 1 for ideal diode. However, n usually has a value higher than unit. Deviation of ideality factor from 1 is always attributed to the effects of facade cases, recombination of charges and existence of other elements.

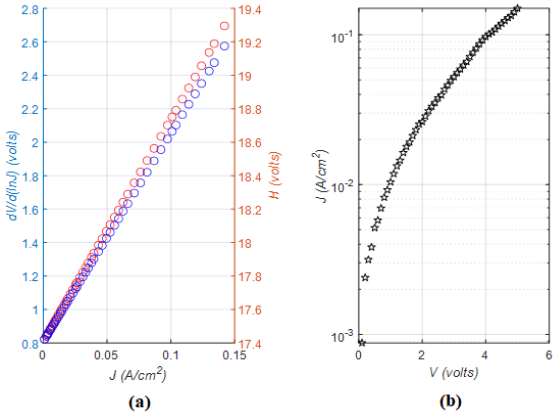

Fig. (5) As-deposited Au/AlGaN Schottky diode (a) Plots of dv/d(lnJ) vs J and H(J) vs J. (b) Experimental and calculated In J vs V plots

In this part of the study, SCAPS-1D was used to stimulate solar cell that contains of three layers AlGaN/CdS/p-Si, Figure (6) illustrates cell composition in this work.

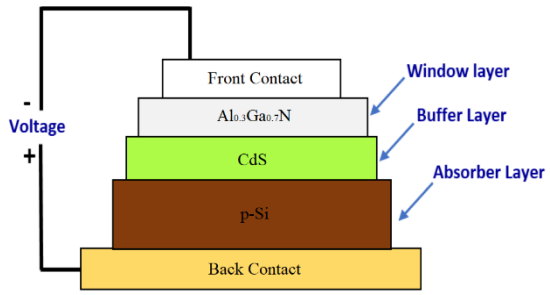

Fig. (6) Solar cell model diagram

The effect of thickness of AlGaN layer on the electrical properties of the designed cell, open-circuit voltage (V_{OC}), short-circuit current (J_{SC}), fill factor (F.F.) and quantum efficiency (η) were studied. Figures (7-11) illustrate the results revealed a clear decrease in the values of short-circuit current with an increase in thickness due to the increase in the electric resistance of the layer, which negatively affects the filling factor that is directly proportional to open circuit current leading to a decrease in the efficiency of the solar cell. The increase in the thickness of the layer causes the increase of the block of solar spectrum from the main absorbing layer, which is silicon. Hence, the contribution to the generation of electron gap pair decreases, and the increase in the thickness of this layer increases the undesirable recombination because of major diffusion.

The results of studying the effect of the thickness of the AlGaN permeation layer indicated that increasing the thickness reduces the efficiency of the solar cell slightly. The efficiency value remains approximately constant at 2.6% up to a thickness of 2.5 µm because this layer absorbs only ultraviolet rays from the solar spectrum and is permeable to the remaining part of the spectrum used. After that, the decrease in cell efficiency from 2.6% at a thickness of 2.6 µm accelerates to approximately 2% at a thickness of 5 µm because this layer blocks the electromagnetic spectrum from the rest of the cell parts, which means a decrease in the contribution to the affinity of the electron–gap pair. The results of the current curve showed that the value of the voltage remains almost constant, whereas the value of the current decreases with increasing thickness, and this is due to the increase in the electrical resistance of the cell.

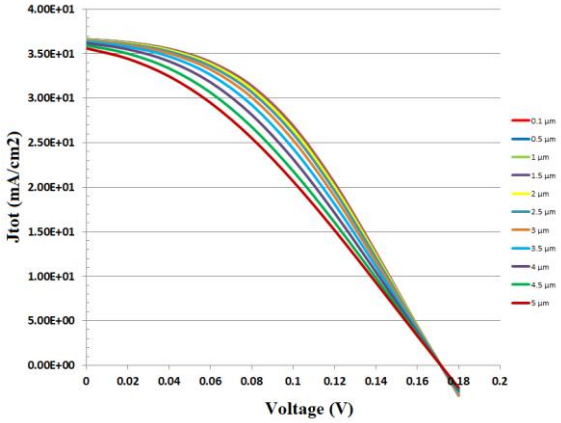

Fig. (7) Effect of thickness of AlGaN layer on I-V properties of cell AlGaN/CdS/p-Si

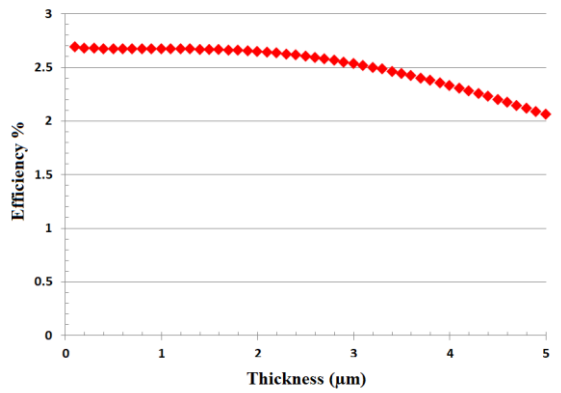

Fig. (8) Effect of the thickness of AlGaN layer on efficiency of cell AlGaN/CdS/p-Si

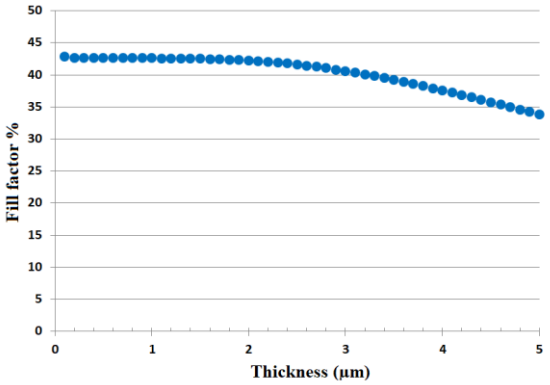

Fig. (9) Effect of the thickness of AlGaN layer on fill factor of cell AlGaN/CdS/p-Si

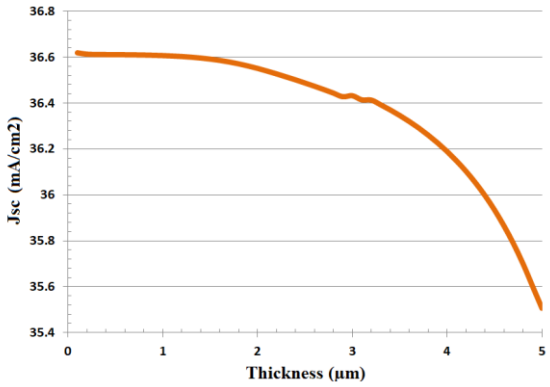

Fig. (10) Effect of the thickness of AlGaN layer on the short circuit current of cell AlGaN/CdS/p-Si

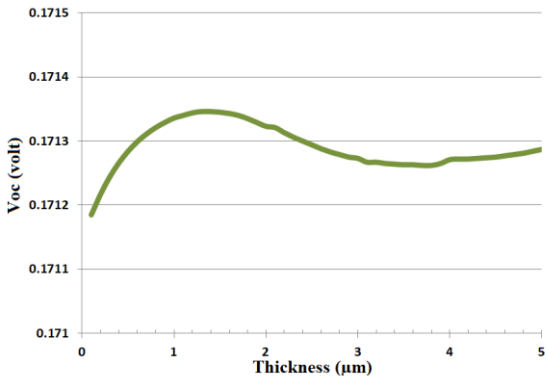

Fig. (11) Effect of the thickness of AlGaN layer the open circuit voltage for cell AlGaN/CdS/p-Si

4. Conclusion

The presence of a distinct absorption peak in CdS sample was confirmed in the visible region, whereas the characteristic absorption peak of the AlGaN sample was in the ultraviolet range. Thus, the energy gap covered a wide region of the electromagnetic radiation spectrum, which enhanced the characteristics of the solar cell. Reducing the thickness of the AlGaN layer led to improved solar cell performance due to a greater amount of light energy crossing the absorption layer of the solar cell. The optimum thickness of the solar cell layer was 100 nm for AlGaN. Consequently, the following values were obtained for the best cell at the temperature of 300K: V_{OC}=0.17 V, J_{SC}=36.62 mA/cm^2, FF=42.89% and η=2.68%. The results exhibited a clear decrease in the values of short-circuit current with an increase in thickness due to the increase because of the decrease in the amount of light energy crossing the absorption layer of the solar cell and the increase in the electric resistance of the layer, hence leading to a decrease in the contribution to the generation of electron hole pair and an increase in the thickness of this layer increases undesirable recombination because of major diffusion.

References

[1] M. Rais-Zadeh, et al. "Gallium Nitride as an Electromechanical Material", *J. Microelectromech. Sys.*, 23(6) (2014) 1252-1271.

[2] A. Pandey et al., "Growth, structural and electrical properties of AlN/Si (111) for futuristic MEMS applications", *Mater. Sci. Semicond. Process.*, 123 (2021) 105567.

[3] S. Zhao et al., "Aluminum nitride nanowire light emitting diodes: breaking the fundamental bottleneck of deep ultraviolet light source", *Sci. Rep.*, 5 (2015) 8332.

[4] M. Nur Koçak et al., "*in-situ* and *ex-situ* face-to-face annealing of epitaxial AlN", *Vacuum*, 203 (2022) 111284.

[5] D. Walker et al., "High-speed, low-noise metal–semiconductor–metal ultraviolet photodetectors based on GaN", Appl. *Phys. Lett.*, 74(5) (1999) 762-764.

[6] X.W. Sun, J. Wang and A. Wei, "Zinc oxide nanostructured biosensor for glucose detection", *J. Mater. Sci. Technol.*, 24(4) (2008) 649-656.

[7] J.H. Park et al., "Polymer/Gold nanoparticle nanocomposite light-emitting diodes: Enhancement of electroluminescence stability and quantum efficiency of blue-light-emitting polymers", *Mater. Chem.*, 16(4) (2004) 688.

[8] D.Y.H. Pui and D.R. Chen, "Guest Editorial: Nanometer Particles: A New Frontier for Multidisciplinary Research", *J. Aerosol Sci.*, 28(4) (1997) 539-544.

[9] E. Kabir et al., "The linkage between renewable energy potential and sustainable development: Understanding solar energy variability and photovoltaic power potential in Tibet, China", *Sustai. Ener. Technol. Assess.*, 82 (2018) 870–905.

[10] V. Bougrov et al., Book Chapter in **"Properties of Advanced Semiconductor Materials: GaN, AIN, InN, BN, Sic, SiGe"**, M.E. Levinshtein, S.L. Rumyantsev, and M.S. Shur (ed.), John Wiley & Sons (2001).

[11] H. Angerer et al., "Determination of the Al mole fraction and the band gap bowing of epitaxial $Al_xGa_{12x}N$ films", *Appl. Phys. Lett.*, 71 (1997) 1504.

[12] S.M. Sze, **"Physics of Semiconductor Devices"**, 2nd ed., Wiley (NY, 1981).

[13] E.H. Rhoderick and R.H. Williams, **"Metal-Semiconductor Contacts"**, 2nd ed., Clarendon Press (Oxford, 1988).
[14] J.H. Werner, "Schottky barrier and pn-junctionI/V plots - Small signal evaluation", *Appl. Phys. A*, 47 (1988) 291-300.
[15] P. Syed Abthagir and R. Saraswathi, "Electronic properties of polyindole and polycarbazole Schottky diodes", *Org. Electron.*, 5(6) (2004) 299-308.
[16] R.K. Gupta, R.A. Singh, "Schottky diode based on composite organic semiconductors", *Mater. Sci. Semicond. Process.*, 7(1-2) (2004) 83-87.
[17] E.T. Yu and M.O. Manasreh, **"III-V Nitride Semiconductors: Applications and Devices"**, Taylor and Francis Books, Inc. (2003), 16.
[18] Burgelman et al, SCAPS manual, no. May. 2014.
[19] T.L. Amu, "Performance optimization of tin halide perovskite solar cells via numerical simulation", MSc thesis, African University of Science and Technology, Abuja (Nigeria, 2014).
[20] O.D. Neikov, S.S. Naboychenko and N.A. Yefimov, **"Handbook of Non-Ferrous Metal Powders"**, Elsevier (2019).
[21] A.S. Hussein, "AlGaN Thin Films on Silicon Substrates for photodetector and Transistor Devices", PhD thesis, Universiti Sains Malaysia (2011).
[22] B. Hussain et al., "Electron Affinity and Bandgap Optimization of Zinc Oxide for Improved Performance of ZnO/Si Heterojunction Solar Cell Using PC1D Simulations", *mdpi Electronics*, 8(2) (2019) 238.
[23] B. Jayant Baliga, **"Fundamentals of Power Semiconductor Devices"**, Springer International Publishing AG (2019).

Table (1) C.B density of state, Electrical conductivity, and mobility of $Al_{0.3}Ga_{0.7}N$ and CdS

Sample	C.B density of state (cm^{-3})	Conductivity $(\Omega.cm)^{-1}$	Mobility ($cm^2/V.s$)	Type
$Al_{0.3}Ga_{0.7}N$	-3.97E+14	4.30E-02	6.77E+02	N
CdS	-1.59E+15	1.27E-01	4.97E+02	N

Table (2) The ideality factor, Saturation current, Series resistance, Barrier height and Electron affinity

Simple	Ideality factor n	Saturation current Is (mA)	Series resistance Rs (ohm)	Barrier height φ_B(eV)	Electron affinity χ (eV)
AlGaN	3.13	0.000877	13.27	0.55	4.65

Table (3) Simulation parameters for the different layers in AlGaN/CdS/p-Si thin film solar cells [22,23]

Parameters	Symbol (unit)	Si	CdS	AlGaN
Thickness	W	300µm	1042nm	640nm
Bandgap	Eg (eV)	1.12	2.63	3.62
Electron affinity	χ (eV)	4.5	4.2	4.65
Dielectric permittivity	єr	11.9	10	9.35
C.B density of state	N_c (cm^{-3})	2.80E+19	2.20E+18	3.97E+14
V.B density of state	N_V (cm^{-3})	1.04E+19	1.80E+19	1.00E+12
Electron thermal velocity	V_n (cm/s)	1.00E+07	1.00E+07	1.00E+07
Hole thermal velocity	V_p (cm/s)	1.00E+07	1.00E+07	1.00E+07
Electron mobility	µn ($cm^2/V.S$)	1.50E+03	1.00E+02	6.77E+02
Hole mobility	µp ($cm^2/V.S$)	4.50E+03	2.50E+01	6.16E+02
donor concentration	ND ($1/cm^3$)	0	1.00E+17	3.97E+14
acceptor concentration	NA ($1/cm^3$)	1.00E+16	0	0
defect	Normal	-	-	-

Duaa A. Uamran [1]
Hadeel O. Ismael [2]
Hammad R. Humud [2]

[1] *Department of Physics, College of Science, University of Karbala, 56001 Karbala, IRAQ*
[2] *Department of Physics, College of Science, University of Baghdad, Baghdad, IRAQ*

Synthesis and Characterization of Magnesium–Carbon Nanoparticles by Exploding Wire Method in Liquid

Fe_3O_4@C@Mg nanoparticles were prepared by the electro-exploding of C and Mg (C-Mg) wires in Fe_3O_4 colloidal solution nanoparticles respectively. The structural properties of the produced nanospheres have been examined via x-ray diffraction (XRD), field-emission scanning electron microscope (FE-SEM), and energy-dispersive x-ray (EDX). The XRD study revealed the gradual covering of the Fe_3O_4 by C-Mg nanoparticles, depending on the explosive current C and Mg. The FE-SEM analysis revealed a heavily decorated surface of the Fe_3O_4 nanoparticles with the (C-Mg) nanofibers (NFs) of 50±20nm in diameter. The EDX spectrum has detailed the weight percentages of the elements as evidence of a successful construction of Fe_3O_4@C@Mg microsphere.

Keywords: Electrical exploding wire; Fe_3O_4; Nanoparticles, Core-shell
Received: 15 May 2024; **Revised:** 16 June 2024; **Accepted:** 23 June 2024

1. Introduction

The main cause of the diverse nanomaterial production methods is to control the produced material characteristics. The physical methods are characterized by a high degree of purity, fast preparation, and limitless production sources [1-5]. One of the most prominent physical methods is the underwater electro-explosion wire (UEEW) technique, which on top of all the qualities mentioned above is an inexpensive straightforward, and efficient method [3,6,7].

The characteristics of the NPs produced by the UEEW are reliant on many parameters, including the material and dimensions of the wires, electrical circuit characteristics, and the surrounding medium. All control the shape, size, and morphologies of the nanoparticles which in turn determine the suitable applications. Targeted medication transfer are the most suited for the nanomaterial prepared in this work [8-13].

This study focuses on Iron oxide nanoparticles specifically magnetite (Fe3O4). Fe3O4 is a non-toxic biocompatible, which qualifies them to be utilized in a broad range of applications, such as high-density information storage and electronic devices. Both iron oxides represent crystal graphic isomorphs [14–17].

Carbon and Magnesium are used as explosive wires, where carbon nanofibers (CNFs) are a compelling nano-material to study due to their superior mechanical, surface, and electrical characteristics. The broad range of applications of CNFs includes sensors [8,9], structural materials [6,7], displays for field emission [10,11], scanning probe microscopy tips [14,15], and nm-size semiconductor devices [16,17].

In this study, Fe3O4 NPs were coated by C@Mg NPs respectively by exploding the C-Mg wire in the colloidal Fe3O4 NPs. where a high current pulse is transferred by the metal wire in a split second which causes the wire to vaporize, then instantly decreases its temperature to form the nano-particles [18]. On the other hand, to ensure a more, spherical, even NPs and a smaller distribution of the particle sizes, The colloidal suspension of those nano-particles has been exposed to thermal ablation (thereby the plasma or vapor phase formation) with the following interactions with liquid [19–23]. Several approaches have been utilized to study the characteristics of those nanoparticles such as XRD, EDX, and FE-SEM.

2. Experimental part:

The experimental setup to synthesize decorated Fe_3O_4 with Carbon (C) and Magnesium (Mg) is depicted in Fig. 1. This process has been accomplished through the explosion of thin C and Mg wires (0.3mm in diameter) with a purity of 99.99% (supplied by Zhongnuo Advanced Material Technology Co. Ltd. China) against C and Mg plates respectively, that has been held (plates) at 80V regarding the wire, trying pulse 150A of current. The explosions were conducted in a vessel reactor that contains 50mg of the Fe_3O_4 NPs, with a mean particle size of 40nm, ultrasonically dispersed in 100ml of distilled water. The electrical circuit stays open until the wire touches the plate, which leads to the wire explosion. In turn, this opens the circuit to repeat the process 30 more times. The metal wire has been liquefied, vaporized, and then converted to plasma due to a high current density pulse passing through the wire. Metal plasma expands at a super-sonic

speed, which results in creating a shock wave in the liquid medium that surrounds it. At last, the NPs have been created by interacting with the liquid. Due to explosions of C@Mg wires in Fe_3O_4 colloidal solution, Fe_3O_4 NPs have been decorated with the C@Mg NPs.

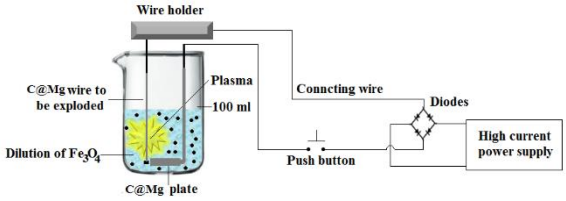

Fig. (1) Experimental set-up that has been utilized for the synthesis of C@ Mg decorated Fe_3O_4 NPs

3. Results and discussion

The XRD analysis of the sample has been depicted in Figure 2. , It was observed that all samples with different concentrations of magnesium and nanocarbon showed the same behavior, so in this research, we are presenting the result of (20% Carbon and 10% Magnesium), where the main reflection, illustrates the presence of 2 broad peaks that have been centered at 35° and 43°, which represent (002) and (100) planes for the graphite, The characteristic of numerous carbon products which include the crystalline component with different basal plane alignment degrees [24]. In this case, the peak has been related to C presence. The pattern of the sample diffraction is after the carbon fiber growth step. We note the total coverage of carbon for each of the Mg and Fe_3O_4, where a carbon nanofiber triple network is formed.

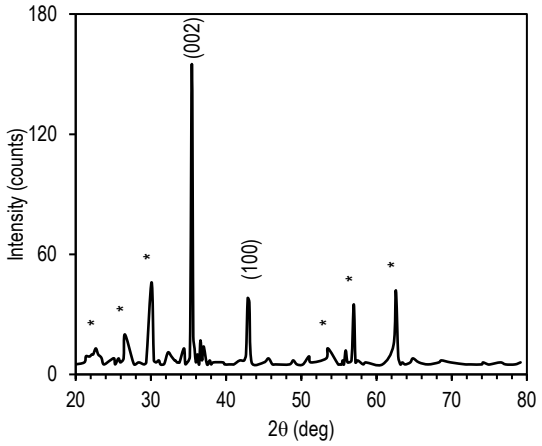

Fig. (2) XRD pattern of C@Mg decorated in Fe_3O_4 (20% C and 10% Mg)

Morphologies of the obtained nanoparticles have been identified using FE-SEM for the samples prepared from different concentrations of carbon (C) and magnesium (Mg) as shown in figures (3), (4) and (5) (where sample (a) pointing to 25% C and 5% Mg, (b) 20% C and 10% Mg, (c) 10% C and 20% Mg, (d) 5% C and 25% Mg, (e) 14% C and 16% Mg and finally sample (f) pointing to 15% C and 15% Mg). We observed that all samples with different concentrations of magnesium and nanocarbon displayed the same behavior, whereas nonwoven C consists of long nano-fibers that have been packed randomly, producing micrometer-size pores.

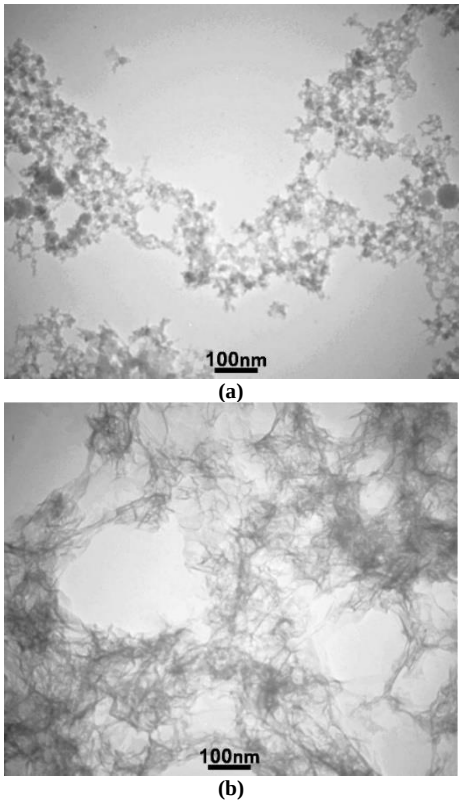

Fig. (3) FE-SEM micrographs of C@Mg decorated Fe_3O_4 NPs at different concentrations of carbon (C) and magnesium (Mg) (a) 25% C and 5% Mg, and (b) 20% C and 10% Mg

The high magnification image has revealed that CNFs have smooth surfaces. Those inter-connected CNFs have produced a porous 3D network that includes Mg as well as Fe_3O_4 (sample c) favoring the formation of a high interfacial surface area for the transfer of reactions. The magnified images of FE-SEM of nanofibers have been depicted in Fig. (3) show the surface of nano-fibers is heavily decorated with NPs with diameters of 50±20nm. This confirms the XRD results. Where uniform distribution of the four elements (Fe, C, O, and Mg) had been exhibited within the microsphere structures, exhibiting the existence of the Mg on the carbon-encapsulated Fe_3O_4 surface.

Figure (6) shows the EDX spectra and the weight percentages for the elements in the prepared samples. It has been observed distinctly that the percentages of Fe is between 2.96 and 0.25%, O is between 44.97 and 51.92%, C is between 12.11 and 8.85%, and Mg is between 19.55 and 38.98%, which confirms the expected successful construction of Fe_3O_4@C@Mg micro-sphere.

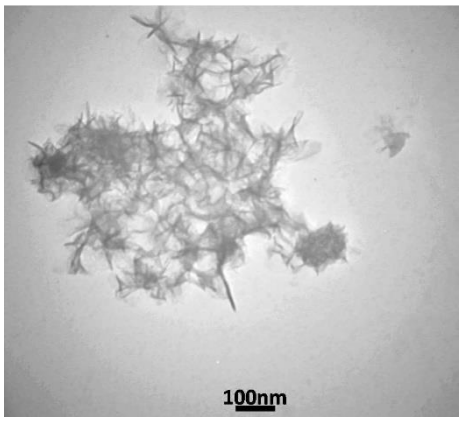

(a)

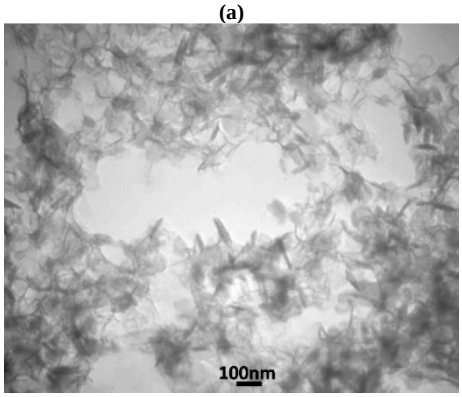

(b)

Fig. (4) FE-SEM micrographs of C@Mg decorated Fe_3O_4 NPs at different concentrations of carbon (C) and magnesium (Mg) (a) 10% C and 20% Mg, and (b) 5% C and 25% Mg

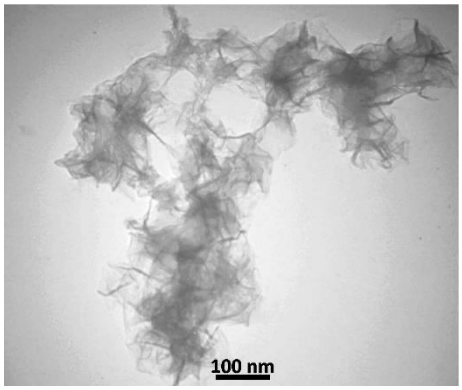

(a)

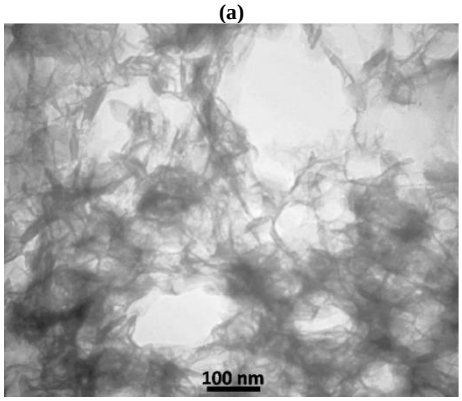

(b)

Fig. (5) FE-SEM micrographs of C@Mg decorated Fe_3O_4 NPs at different concentrations of carbon (C) and magnesium (Mg) (a) 14% C and 16% Mg, and (b) 15% C and 15% Mg

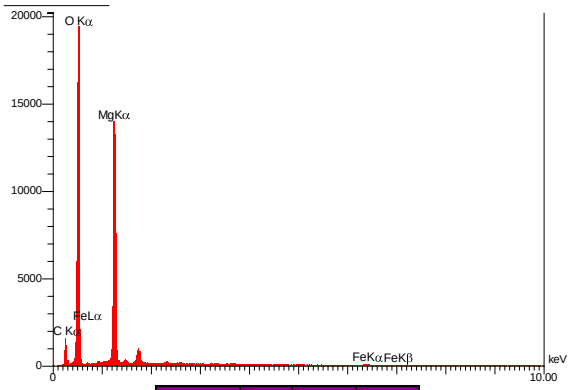

Element	Line	W%	A%
C	Ka	12.11	18.33
O	Ka	44.97	51.12
Mg	Ka	19.55	14.63
Fe	Ka	2.96	0.96

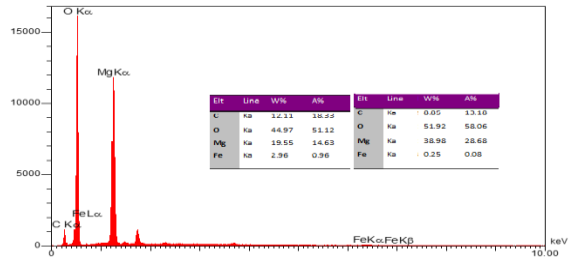

Element	Line	W%	A%
C	Ka	8.85	13.18
O	Ka	51.92	58.06
Mg	Ka	38.98	28.68
Fe	Ka	0.25	0.08

Fig. (6) EDX spectra of C@ Mg decorated Fe_3O_4 nanoparticles

4. Conclusions

The main goal of this research is to obtain carbon nanofibers in the simple inexpensive method, of the explosive wire using simple materials. Fe_3O_4@C@Mg nanomaterials have been synthesized successfully and the structural properties suggest using them as Eu(III) and U(VI) elimination adsorbents of the water waste, via sticking the polluted materials to the prepared carbon nanofibers network and then pulling them using an electromagnet due to the presence of Fe_3O_4 on which the carbon nanofibers grew, and this is confirmed by the results of both XRD and FE-SEM.

Acknowledgment

We appreciate the support for this work from University of Kerbala, College of Science and Department of Physics, and University of Baghdad, College of Science and Department of Physics.

References

[1] K. Ibrahim, S. Khalid and K. Idrees, "Nanoparticles: Properties, applications and toxicities", *Arabian J. Chem.*, 12(7) (2019) 908-931.
[2] J.D. Mackenzie, E.P. Bescher, "Chemical routes in the synthesis of nanomaterials using the sol-gel process", *Acc. Chem. Res.*, 40 (2007) 810-818.

[3] E.T. Thostenson, Z. Ren and T.-W. Chou, "Advances in the science and technology of carbon nanotubes and their composites: a review", *Compos. Sci. Technol.*, 61 (2001) 1899-1912.
[4] K.L. Klein et al., "Surface characterization and functionalization of carbon nanofibers", *J. Appl. Phys.*, 103 (2008) 061301-061326.
[5] H. Dai, "Carbon nanotubes: synthesis, integration, and properties", *Acc. Chem. Res.*, 35 (2002) 1035-1044.
[6] N.M. Rodriguez, "A review of catalytically grown carbon nanofibers", *J. Mater. Res.*, 8(12) (1993) 3233-3250.
[7] P.K. Dash ad Y. Balto, "Generation of nano-copper particles through wire explosion method and its characterization", *Res. J. Nanosci. Nanotechnol.*, 1 (2011) 25-33.
[8] G.S. Yun et al., "Preparation and dispersive properties of Ag colloid by electrical explosion of wire", *J. Alloys Compd.*, 509 (2011) S348-S352.
[9] J.W. Song et al., "Effect of variation in voltage on the synthesis of Ag nanopowder by pulsed wire evaporation", *J. Nanomater.*, 2012 (2012) 1-5.
[10] Y. Wei et al., "Synthesis of Fe_3O_4 nanoparticles and their magnetic properties", *Procedia Eng.*, 27 (2012) 632-637.
[11] S. Eustis and M.A. El-Sayed, "Why gold nanoparticles are more precious than pretty gold: noble metal surface plasmon resonance and its enhancement of the radiative and nonradiative properties of nanocrystals of different shapes", *Chem. Soc. Rev.*, 35 (2006) 209-217.
[12] M. Stefan et al., "Synthesis and characterization of Fe_3O_4@ZnS and Fe_3O_4@Au@ZnS core-shell nanoparticles", *Appl. Surf. Sci.*, 288 (2014)180-192.
[13] Y.Y. Dong et al., "Ag@Fe_3O_4@cellulose nanocrystals nanocomposites: microwave-assisted hydrothermal synthesis, antimicrobial properties, and good adsorption of dye solution", *J. Mater. Sci.*, 52 (2017) 8219-8230.
[14] D. Wang et al., "Preparation of magnetic Fe_3O_4@ SiO_2@mTiO_2–Au spheres with well-designed microstructure and superior photocatalytic activity", *J. Mater. Sci.*, 51 (2016) 9602-9612.
[15] A.S. Wasfi, H.R. Humud and N.K. Fadhil, "Synthesis of core-shell Fe_3O_4-Au nanoparticles by electrical exploding wire technique combined with laser pulse shooting", *Opt. Laser Technol.*, 111 (2019) 720-726.
[16] B. Duane y al., "Core-Shell Structurized Fe_3O_4@C@MnO_2 nanoparticles as pH responsive T-1-T-2* dual-modal contrast agents for tumor diagnosis", *ACS Biomater. Sci. Eng.*, 4 (2018) 3047-3054.
[17] Y. Xiong et al., "Preparation of magnetic core-shell nanoflower Fe_3O_4@MnO_2 as reusable oxidase mimetics for colorimetric detection of phenol", *Anal. Methods*, 7 (2015) 1300-1306.
[18] S. Yang et al., "Rapid and highly efficient Preconcentration of Eu(III) by core-shell structured Fe_3O_4@humic acid magnetic nanoparticles", *ACS Appl. Mater. Interfaces*, 4 (2012) 6890-6899.
[19] H.R. Humud and S.J. Kadhem, "Laser-Induced Modification of Ag and Cu Metal Nanoparticles Formed by Exploding Wire Technique in Liquid", *Iraqi J. Sci.*, 56 (2015) 3135-3140.
[20] Y.A. Kotov, "Electric explosion of wires as a method for preparation of nanopowders", *J. Nanoparticle Res.*, 5 (2003) 539-550.
[21] P. Ranjan et al., "Thermodynamic analysis of ZnO nanoparticle formation by wire explosion process and characterization", *Ceram. Int.*, 43 (2017) 6709-6720.
[22] K. Lazar et al., "Electric explosion of steel wires for production of nanoparticles: reactions with the liquid media", *J. Alloys Compd.*, 763 (2018) 759-770.
[23] D.A. Uamran, H.Q. Ubaid and H.R. Humud, "Core-Shell SiO_2/Ag Composite Spheres Prepared by Electrical Exploding Wire Plasma Technique : Synthesis and Characterization", *NeuroQuantol.*, 19 (2021) 82-88.
[24] H. Wang et al., "Synthesis of carbonencapsulated superparamagnetic colloidal nanoparticles with magnetic-responsive photonic crystal property", *Dalton Trans.*, 39 (2010) 9565-9569.

Effect of Acidity on Electrodeposition of Nickel Manganese Alloy

Hizia Merkoune
Kamel Hachama

The Laboratory for the Valorization of Natural Substances, University of Khemis Miliana, Khemis Miliana, ALGERIA

Nickel and manganese have good ability to conduct electricity for those reason they are used and many industrial application and researchers do not stop to optimize the methods of deposing them. Electrodeposition process is used for those goal, it recovers conductive materials like copper, steel, aluminum. Numerous industrial applications use this procedure to enhance the coated material's hardness, wear resistance, and visual appeal. This electrochemical process is influenced by experimental parameters. The chemical and physical parameters effect the electroplating such as temperature, pH, appliqued current, agitation, composition nature of electrolyte, nature of substrate; etc. can be controlled by several electrochemical methods. Our article is interested by the effect of PH values on nickel manganese alloy's electrodeposition behavior on copper, using the cyclic voltammetry analysis. To control it. The electrodeposition of nickel and manganese alloy is done by bath composed from nickel and manganese ions, in our work we used: Nickel(II) sulfate hexahydrate, Nickel(II) sulfate hexahydrate, Manganese dichloride tetrahydrate and Manganese Sulfate Tetrahydrate. The PH was justified by drops of HCl (0,1M) and NaOH (0,1M).

Keywords: Electrodeposition; Ni-Mn alloys; pH influence; Cyclic voltammetry
Received: 12 May 2024; **Revised:** 30 July 2024; **Accepted:** 05 August 2024

1. Introduction

Thin film materials containing ferromagnetic elements such as Ni, Mn, Zn, Al, and Co have long piqued attention because of their improved chemical stability and specific physical characteristics [1].

Thin films of nickel and its alloys, as well as manganese and its alloys, have garnered considerable interest in research due to their resistance to corrosion. These materials are being researched for use in magnetic recording and magnetic processes, as well as their capacity to provide good electrocatalytic activity for a variety of reactions, involving the production of hydrogen and oxygen [2-5].

Several techniques can prepare these materials with vacuum deposition like sputtering, epitaxy, etc., but that exert costly high laboratory conditions to realize [6]. Electrodeposition present advantages in domain of recuperation of many active materials because of the purity of deposits and their uniformity and stability [7]

During and after electrodeposition, structure of deposited materials and their morphology are influenced by many factors such as ion source, particle load, surfactants, pH, agitation, temperature, agitation speed, nature of substrate and others [8].

A notable influence on the electrodeposition process is caused by the potential hydrogen (pH) value. The pH has an important impact on the effectiveness, deposit rate, and final quality of the coating.it can effect ions solubility where metal ions are more soluble in solution at low (acidic) pH levels, which can improve the effectiveness of deposition however, the hydroxides of previously exposed metals precipitate rather than establish a metal purity at basic pH values [9].

Depositary teeth can also be influenced where, the electrochemical deposit rate may be higher due to the direct chemical reaction that occurs in an acidic environment between metal ions and electrons. But in a basic bath, the unfavorable formation of hydroxide compounds may cause the rate of deposit to decrease. The pH effect also the metal coatings which is usually more cohesive and pure at mild to intermediate pH levels; nevertheless, at very acidic or basic pH values, coatings may become brittle and uneven [10].

Appearance of secondary reactions can be result of pH modification values; the high pH may cause secondary reactions to occur before the deposit process, such as the formation of gas bubbles (oxygen or hydrogen) and electrode corrosion could happen in low pH environments, which would be detrimental to the process [11].

The electrochemical society is continuing to optimize the quality of deposited materials by controlling this factors, some of the works of detecting pH influence on electrodeposition of nickel and manganese and their alloys are resumed in table (1).

Finally, protons cause an increase in tension and present a challenge to metals with a higher negative tension than hydrogen, pH has a significant impact on the structure of deposits. Increased pH at the cathode level results in the development of hydroxides, which degrade the deposit's quality. So, in order to maintain a consistent pH, buffer solutions must be used [17]. The pH indicates electrochemical equilibrium in mass and concentration of several compounds formed by electroactive species.

2. Experimental Work

Cyclic voltammetry is used for the analysis of electrochemical behavior during electrodeposition of nickel manganese alloy, the used software was VoltaMaster4 installed on pc linked by a potentiostat

voltalab G201. We used a double recovered electrochemical cell and three electrodes; electrode of reference: saturated calomel and the work electrode copper attached to the electrical source by electrical tuna thread counter electrode (platinum)

First, we started by preparing the surfaces of the parts to be coated is an important step that improved the quality of the coating it was started by mechanical polishing of the substrates is carried out using abrasive paper. A rotary polisher, small abrasive disc of different grain sizes was used (800, 1000, 1200, and 1400). Then an electrolytic degreasing must be done where a static voltage circuit was installed for degreasing operations; the electrode to be cleaned (the copper plate) is taken as a cathode in the electrolyte an alkaline solution containing a mixture of sodium hydroxide (NaOH) and sodium carbonate (Na_2CO_3), which acts as a surfactant, it lowers interfacial tension of the room, ensures its wetting and facilitates the drainage of dirt.

The chemical stripping of the samples was carried out in hydrochloric acid boiling in 10% (by volume).

The steel plates were completely immersed in the acid solution for 3 min, the stripping time is considered as a function of the degree of contamination of the sample.

Rinsing is the final step; once the samples are stripped, they are rinsed immediately by distilled water, octane then with our bath solution. The conditions of manipulation are resumed in the table (2).

Table (2) Experimental conditions of nickel manganese alloy electrodeposition

Electrolyte Bath Composition	T (K)	Scanning Capacity (mV)	Scan Speed (mV/s)	pH
$NiSO_4.6H_2O$ $NiCl_2.6H_2O$ $MnSO.4H_2O$ $MnCl_2.4\ H_2O$	293	-600,500	8	from 1.7 to 6.12 (modified carefully by drops of HC and NaOH)

3. Results and Discussion

Voltamograms of electrodeposition of nickel manganese alloy are presented by Fig. (1). The voltamogrmas give the highest current density for the pH=4.7, it increases from 0.00492 at pH=1.7 to 0.01229 at pH=2.7, then 0.01281 at pH=3.81, 0.02286 at pH=4.7. This can be interpreted by the invasion of protons whish pounce the electrons at the cathode interface and raise the possibility of hydrogen gas formation which impedes the reduction of nickel and manganese ions at the cathode.

Current density started to decrease more than pH value of 4.7 until the final value test of (pH=6.12) where the current density was 0.00931, which can be justified by the low movement of ions in the electrolyte

The following oxydo-reduction reactions state describe our electrodeposition process:

• **Oxidation**: A dissociation of Ni and Mn oxides that release their ions on the anode

$NiSO_{4\,(s)} \rightarrow Ni^{2+}_{(aq)} + SO_4^{2-}{}_{(aq)}$

$MnSO_{4\,(s)} \rightarrow Mn^{2+}_{(aq)} + SO_4^{2-}{}_{(aq)}$

$NiCl_{2\,(s)} \rightarrow Ni^{2+}_{(aq)} + 2Cl^{-}_{(aq)}$

$MnCl_{2\,(s)} \rightarrow Mn^{2+}_{(aq)} + 2Cl^{-}_{(aq)}$

• **Reduction of Ni^{+2} and Mn^{+2}**

Here are the reactions goal of our work

$Ni^{2+} + 2\ e^- \rightarrow Ni$

$Mn^{2+} + 2\ e^- \rightarrow Mn$

$2H^+ + 2\ e^- \rightarrow H_2$

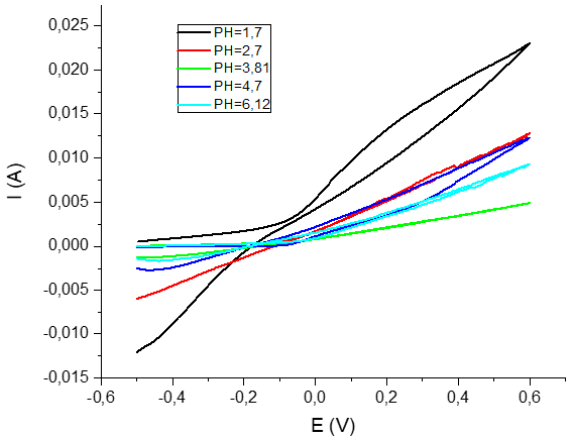

Fig. (2) Influence of pH value on current density during the electrodeposition NiMn on copper

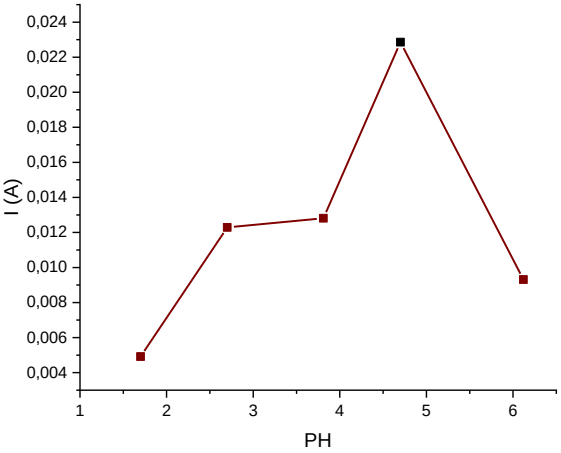

Fig. (3) Variation of current density with bath pH value

The software Tafel information are resumed corrosion behavior of the studies system in table (3).

Table (3) Electrochemical properties offered by Tafel's Data

pH	1,7	2,7	3,81	4,7	6,12
R_p (Ω.cm)	34,45	787,67	191,78	4720	113,08

The highest polarization resistance (R_p) was recorded for electrolyte with pH=4.7, which accord to the previous result of the biggest current density of electrodeposition that significates that perfect pH

gives perfect deposition, which in turn, gives the best protection for the copper.

4. Conclusion

The performance polarization obtained by cyclic voltammetry was at pH=4.7. Acidic baths found difficulty in the reduction of the cations because of the possibility of dihydrogen. The possibility of hydroxide of nickel and hydroxide of manganese is also existing because the hydroxide ions attacked the $Ni^{+2}Mn^{+2}$ and push them to be reduced, which decreases the electrochemical deposition on copper that exposes the substrate surface for more corrosion. The pH value of the electrolyte solution can be adjusted to strike the perfect balance between the deposition process's efficiency and rate as well as the final product's quality, or revetment. The relation between the electrodeposition of nickel manganese alloy and the corrosion behavior of copper against the environment of operation conditions is clear and direct where the electrolytes alloys of the same conditions given less nobility from for the pH=4.7, it increases from R_p at pH=1.7 to pH=6.12 then at pH=3.81 than the R_p at pH=2.7. The effect of pH on the copper corrosion behavior can be observed by its strong direct influence on quality of formed film of NiMn alloy.

Buffer solutions such as boric acid can save the electrochemical process and avoid the secondary reaction during its unfolding. It will be good job if other researchers finish this study with same electrolytes at the same operating conditions with values of pH higher than 6.12. Producing materials must by selective process such as electrodeposition; it insures the coating for all shapes of all substrate for many applications and the strongest cause wish make it a process of choice from industrials is that is can be controlled with modifying the chemical and physical parameters that manage it. Protons and hydroxide ions push the formation of coating on areas of vised cathode or this reason we must choose carefully the additives for solving the accumulation of atoms on the surface of electrodes.

References

[1] P.N. Solovev et al., "Magnetic anisotropy and ferromagnetic resonance in inhomogeneous demagnetizing fields near edges of thin magnetic films", *J. Phys.: Cond. Matter*, 36 (2024) 195803.

[2] Y. Chen et al., "Efficient Catalysis of Acetylene Semi-Hydrogenation through Synergistic Action of Supported Ionic Liquid-Nickel Catalyst", *Appl. Catal. A: Gen.*, 681 (2024) 119775.

[3] L. Behrouzi et al., "Exploring an Electrochemical Route for Water-Enhanced Oxygenation Reactions Utilizing Nickel Molecular Structures: A Case Study", *Inorg. Chem.*, 63(4) (2024) 2268-2274.

[4] F. Wiedemaier et al., "The crucial role of ligand deprotonation in manganese catalyzed hydrogenation reactions", *J. Catal.*, 429 (2024) 115252.

[5] M. Lautens and C.E. Johnson, "Selective C–H Oxidation Enabled by Manganese Catalysis", *Synfacts*, 20(6) (2024) 0615.

[6] P.K. Saxena, P. Srivastava and A. Srivastava, "Dislocations/Defects analysis in III-V nitrides-a cost effective MOCVD epitaxy solution", *J. Cryst. Growth*, 630 (2024) 127584.

[7] C. Liu et al., "Directional controllable electrodeposition growth of homogeneous Au nano-rampart arrays and its reliable SERS applications", *J. Electroanal. Chem.*, 909 (2022) 116120.

[8] F. Nasirpouri et al., "Electrodeposition of anticorrosion nanocoatings", Ch. 24, S. Rajendran et al. (ed.), in **"Micro and Nano Technologies, Corrosion Protection at the Nanoscale"**, Elsevier (2020).

[9] A. Pohl, "Removal of heavy metal ions from water and wastewaters by sulfur-containing precipitation agents", *Water Air Soil Poll.*, 231(10) (2020) 503.

[10] K. Hermange et al., "Effect of hydrophobicity in hybrid sol-gel coating for enhanced barrier property on mild steel", *Surf. Coat. Technol.*, 485 (2024) 130876.

[11] M.P. Rayaroth et al., "Advanced oxidation processes (AOPs) based wastewater treatment-unexpected nitration side reactions-a serious environmental issue: A review". *Chem. Eng. J.*, 430 (2022) 133002.

[12] H. Zhu et al., "Ni-Mn_3O_4 Composite Coating by Electrophoresis/Electrodeposition for Metallic Interconnects Applications", *J. Electrochem. Soc.*, 166 (2019) F423.

[13] Z. Abdel Hamid et al., "Influence of electrodeposition parameters on the characteristics of NiMoP film", *Surf. Coat. Technol.*, 212 (2012) 37-45.

[14] M. Mortaga et al., "Influence of pH on the Composition, Morphology and Corrosion Resistance of Zn-Ni-Mn Alloy Films Synthesized by Electrodeposition", *Int. J. Electrochem. Sci.*, 10 (2015) 2972-2987

[15] M. Boubatra et al., "The influence of pH electrolyte on the electrochemical deposition and properties of nickel thin films", *Ionics*, 18 (2012) 425-432.

[16] I. Djaghout, « Study of The Influence of Organic Additives on the Properties of Nickel Electrolytic Deposits", PhD thesis (in French), Université 8 Mai 1945 Guelma (2016).

[17] E. Aidaoui, 'The effect of electrolysis parameters on the behavior of electrodeposited Ni-Cr composite deposits', PhD thesis (in French), Université Mohamed Khider – Biskra (2020).

Table (1) Some studies on effect of bath pH on electrodeposition of Ni and Mn and their alloys

Materials	Work	Ref.
MnNi (electrodeposited on steel substrate)	The pH 5 given the biggest mass fraction of $MnO_{3\ that}$ was incorporated at the Ni matrix where the interval study whish was from 4 to 6 by the scale of 0.5 of pH	[12]
NiMoP (electrodeposited on steel substrate)	The pH 6 given smooth and nonporous surfaces from than pH 6 to 7,5 it was formation of pore and cracked surfaces of NiMnP from 7.5 to 10. So the quantities formed of Mo and P decreased	[13]
NiMnZn (electrodeposited on steel substrate)	Electrodeposited films at high pH values (2.5~5) are often relatively smooth, uniform, and compact but the films formed at low pH values exhibit very poor quality and a rough surface.	[14]
Ni films (electrodeposited on Au glass substrates)	As pH grows, an anodic shift in the discharge potential detected. SEM observations show that the morphology, shape, and size of the crystallites x rays are significantly influenced by the bath pH. Additionally, the average particle size of Ni ranges between 49 and 153 nm based on the electrolyte's pH	[15]
NiCoP (electrodeposited on copper)	Based on EDAX tests, the concentration of Co and P increased while the concentration of Ni fell when the pH value of the solution was raised from 1.5±0.1 to 5.0±0.1	[16]

IRAQI JOURNAL OF APPLIED PHYSICS

Volume (20) Issue (3B) August 2024

CONTENTS

Contents

Sponsored and Published by
American Quality for Scientific Publishing, Inc.